STRESS CORROSION CRACKING AND CORROSION OF CARBON STEEL IN SIMULATED FUEL-GRADE ETHANOL

A Dissertation
Presented to
The Academic Faculty

by

Xiaoyuan Lou

In Partial Fulfillment
of the Requirements for the Degree
Doctor of Philosophy in the
School of Materials Science and Engineering

Georgia Institute of Technology
December, 2010

STRESS CORROSION CRACKING AND CORROSION OF CARBON STEEL IN SIMULATED FUEL-GRADE ETHANOL

Approved by:

Dr. Preet M. Singh, Advisor
School of Materials Science and Engineering
Georgia Institute of Technology

Dr. Lawrence A. Bottomley
School of Chemistry and Biochemistry
Georgia Institute of Technology

Dr. Meilin Liu
School of Materials Science and Engineering
Georgia Institute of Technology

Dr. Richard W. Neu
The George W. Woodruff School of Mechanical Engineering
Georgia Institute of Technology

Dr. W. Brent Carter
School of Materials Science and Engineering
Georgia Institute of Technology

Date Approved: October 29, 2010

[To my great parents Jiaxing Lou and Xiuying Jin, and my beloved wife Xing Wang]

ACKNOWLEDGEMENTS

The days during my PhD study are enjoyable and memorable. At first, I would like to thank my advisor, Dr. Preet M. Singh, for his advice and support throughout my research. This thesis is a result of his inspiration, encouragement and discussion. I have learned so much from him in both technical and non-technical aspects of life. I also want to thank Dr. Meilin Liu who leads me into the field of electrochemical research during the early part of my graduate study. Dr. Larry Bottomley's great classes provide me a basic understanding of electrochemical process and analysis. Some discussion with Dr. Richard Neu solved my questions on the mechanical behavior of material. I would also like to express my appreciation to Dr. Carter to serve on my committee. Valuable discussions and suggestions by Dr. Rudy Buchheit (Ohio State University), Dr. Narasi Sridhar (DNV), Jake Haase (Colonial Pipeline Company), Mark Hereth, Chuck Corr (ADM), throughout this work, are also greatly appreciated.

In the lab, I want to thank Jamshad Mahmood's help for preparing samples and setting up testing equipments. His help accelerated my research progress. I would further like to thank the support and help from all the members in Dr. Singh's group. They made my life in the lab enjoyable.

Lastly, but the most importantly, I want to express my deep appreciations to my beloved family, my father Jiaxing Lou, my mother Xiuying Jin, and my wife Xing Wang. Their endless love, encouragement and support are greatly cherished and part of my life.

This work was sponsored by the Colonial Pipeline Company (project No. 3306F49) and US Department of Transportation PHMSA program (contract No. DTPH56-08-T-000013 and DTPH56-09-T-000004).

TABLE OF CONTENTS

LIST OF TABLES

LIST OF FIGURES

SUMMARY

Today, ethanol, as well as other biofuels, has been increasingly gaining popularity as a major alternative liquid fuel to replace conventional gasoline for road transportation. Currently, less than 10% of fuel-grade ethanol (FGE) is blended into the gasoline to reduce the pressure from gas shortage. One of the key challenges for the future use of bioethanol is to increase its availability in the market via an efficient and economic way. Pipelines are normally used for transporting and distributing traditional petroleum products. However, ethanol, so far, is transported primarily by tanker trucks. One major concern in using the existing gas-pipelines to transport fuel-grade ethanol or blended fuel is the potential corrosion and stress corrosion cracking (SCC) susceptibility of carbon steel pipelines in these environments. The key technical challenge for ethanol fuel transportation is to understand the mechanisms of metal degradation in such an environment.

In this thesis, both phenomenological and mechanistic investigations have been carried out in order to address the possible degradation phenomena of X-65 pipeline carbon steel in simulated fuel-grade ethanol (SFGE). Firstly, the susceptibilities of stress corrosion cracking of this steel in SFGE were studied. Ethanol chemistry of SFGE was shown to have great impact on the stress corrosion crack initiation/propagation and the corrosion mode transition. Inclusions in the steel can increase local plastic strain and act as crack initiation sites. Secondly, the anodic behavior of carbon steel electrode was investigated in detail under different ethanol chemistry conditions. General corrosion and pitting susceptibility under unstressed condition were found to be sensitive to the ethanol

chemistry. Low tendency to passivate and the sensitivity to ethanol chemistry are the major reasons which drive corrosion process in this system. Oxygen plays a critical role in controlling the passivity of carbon steel in ethanol. Thirdly, the detailed study was carried out to understand the SCC mechanism of carbon steel in SFGE. A film related anodic dissolution process was identified to be a major driving force during the crack propagation. Fourthly, more detailed electrochemical impedance spectroscopy (EIS) studies using phase angle analysis and transmission line simulation reveal a clearer physical picture of the stress corrosion cracking process in this environment. Fifthly, the cathodic reactions of carbon steel in SFGE were also investigated to understand the oxygen and hydrogen reactions. Hydrogen uptake into the pipeline steel and the conditions of the fractures related to hydrogen embrittlement were identified and studied.

This study, for the first time, systematically investigated the stress corrosion cracking and corrosion of carbon steel in simulated fuel-grade ethanolic environment, which provides useful information on material degradation and selection in biofuel environments.

CHAPTER 1

INTRODUCTION

1.1 Motivation of This Research

With the increasing demand for alternative energy sources to reduce carbon emission and the dependence on petroleum products, finding a stable and environmentally friendly liquid fuel becomes more and more important, especially for the road and air transportation. Biomass products, such as bioethanol, biobutanol and biodiesel, provide a possible way to realize carbon neutral fuel supply. Currently, compared with other alternative energy sources, biofuel is the only liquid fuel which can be immediately used in current combustion engine systems. Due to the production cost and efficiency, fuel-grade ethanol (both corn-based and cellulosic ethanol) is the most common biofuel that has been commercialized. Nationwide, less than 10% FGE is blended into the gasoline to reduce the dependence on foreign petroleum. Further increasing the availability of FGE and reducing its cost become critical.

Currently, the petroleum products, such as gasoline and natural gas, are transported throughout the country, primarily via pipelines. Such infrastructure dramatically reduces the cost and increases the efficiency of the distribution process. Since the pipelines are usually buried underground and subjected to local stresses due to internal pressure and external environmental pressure, corrosion and stress corrosion cracking are the major failures. Coating and cathodic protection are used to protect the pipelines from corrosion. However, fuel-grade ethanol is still transported primarily by

railroad tanker cars and tanker trucks. With the increasing demand of bioethanol, fast, cheap and safe transportation by pipelines is needed to satisfy the demand.

However, stress corrosion cracking has been reported in user terminals and storage tanks of FGE. Recent studies have shown that the SCC is the major failure mode for ethanol transportation through carbon steel pipelines. [1-3] Previous studies of metallic materials in methanol and ethanol also show that significant pitting corrosion can be initiated in these alcoholic solvents. [4, 5] These corrosion failures can strongly cause the degradation of in-service equipment, in either pipeline transportation industry or biofuel manufacturing industry. With the huge investment for biomass energy production (e.g. cellulosic ethanol) and application (e.g. fuel cell), one of the key technical challenges for the future use of bioethanol is to understand both phenomenon and mechanism of material degradation in such environments and the prevention methods. Compared to the aqueous corrosion, much less work has been done to understand the corrosion process in ethanol environments. Most of the published work is based on phenomenological study of factors which may affect the material. Arguments in the literature usually address which factors are important for causing or preventing the corrosion failure. Environmental and stress effects on the failure initiation and growth, the anodic and cathodic activities, and the passivity and dissolution largely remain unclear. The possible degradation modes of metallic materials in various FGE conditions are also unknown. Better understanding of corrosion phenomena in FGE is a critical step toward large scale application of biomass based energy source.

1.2 Research Objective and Technical Approaches

Due to the limited knowledge about the ethanol corrosion in literature, the goal of this work primarily focuses on understanding the stress corrosion cracking, pitting corrosion, and other corrosion related phenomena on carbon steel in simulated fuel-grade ethanol environment. The specific technical objectives are:

(1) To systematically investigate the possible degradation phenomena of carbon steel, such as stress corrosion cracking, general corrosion, and pitting corrosion, in SFGE environments. Factors influencing corrosion susceptibility, such as ethanol chemistry, aeration level, stress, and potential range, have to be determined.

(2) To understand the anodic behavior of carbon steel in SFGE. The anodic behavior includes the passivation and dissolution. The effect of environmental factors on electrochemical activities can provide useful information in order to understand the corrosion mechanisms.

(3) To address the mechanism for the stress corrosion cracking of carbon steel in SFGE. The focus is to understand how the cracks initiate and propagate on the surface and identify the driving force of this process.

(4) To investigate the cathodic reactions, such as oxygen reduction and hydrogen evolution, on carbon steel in SFGE. Cathodic activities in SFGE also play an important role in controlling the corrosion kinetics and possible hydrogen production. Hydrogen uptake and its effect on hydrogen embrittlement are also studied.

(5) To understand the role of microstructure on dissolution and localized corrosion initiation.

In order to achieve these objectives, various mechanical, electrochemical, and characterization analysis were carried out in this study. Slow strain rate test (SSRT) and constant immersion test were used to characterize SCC and corrosion susceptibility in different ethanol environments. Different *dc* and *ac* electrochemical tests, such as potentiodynamic polarization, potentiostatic polarization, open circuit potential (OCP) monitoring, and electrochemical impedance spectroscopy (EIS), were used to understand the anodic and cathodic responses of carbon steel in SFGE, with the changes in ethanol chemistry, aeration level, potential range, stress state. The surface chemical and structural evolution processes during cracking or pitting were also studied by interrupted test and characterized using scanning electron microscopy (SEM), energy dispersive X-ray spectroscopy (EDX), X-ray diffraction (XRD), and back-scattered electron (BSE). Transmission line model (TLM) and its simulation were also used to provide a clear physical picture during cracking propagation.

1.3 Organization of Upcoming Chapters

In the following, Chapter 2 will provide a general review of the mechanisms of environmentally induced fracture (stress corrosion cracking and hydrogen embrittlement), pitting corrosion, and the previous understanding of corrosion in alcoholic environments. Chapter 3 will summarize all the main experimental techniques, materials, and the testing conditions used in this study. Chapter 4 will present the ethanol chemistry effects on the stress corrosion cracking susceptibility of carbon steel in SFGE. Chapter 5 will present the electrochemical study to understand the anodic behavior of carbon steel in SFGE. Corrosion and pitting corrosion susceptibilities under unstressed condition will be

discussed. Chapter 6 will give the mechanism which drives the crack initiation and propagation on carbon steel in SFGE. Chapter 7 will present a detailed physical picture during crack propagation using phase angle analysis and transmission line model simulation. Chapter 8 will present the systematical investigation of the corrosion related cathodic activities of carbon steel in SFGE. The study of hydrogen uptake and hydrogen embrittlement fracture on carbon steel will also be discussed. Chapter 9 will summarize all the presented conclusions and present a global picture of the corrosion of carbon steel in SFGE. The mitigation methods for corrosion and stress corrosion cracking in fuel-grade ethanol, which are derived based on this research, will be suggested. Some recommendations for the future research in this area will also be provided.

CHAPTER 2

BACKGROUND

2.1 Stress Corrosion Cracking

2.1.1 General Definition

Stress corrosion cracking is a type of environmentally-assisted cracking (EAC) where the material experiences a brittle fracture failure due to the combined effect of corrosive environment and tensile stresses. As shown in Figure 2-1, in order for this brittle fracture to occur, three conditions must be present simultaneously: a susceptible material, a corrosive environment, and local tensile stress. Within this triangle, stress corrosion cracking is a complex phenomenon that involves a large number of material and environment related variables, such as corrosion potential, solution chemistry, stress intensity factor, cold work, etc.

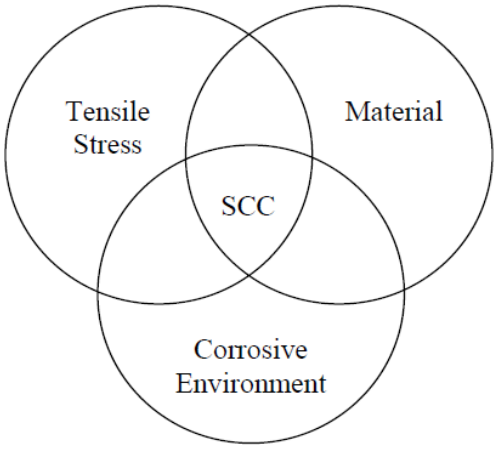

Figure 2-1. Conditions for Stress Corrosion Cracking

Among these factors, alloy composition and microstructure plays an important role in controlling the SCC susceptibility. Especially in stainless steel and nickel alloy, sensitization, grain boundary Cr depletion, and inclusion are usually preferential crack initiation sites, depending on the alloy microstructure and composition. Temperature is another important factor which affects the SCC. Temperature activation process may set a threshold for SCC to occur. The tensile stress which induces the SCC can be below or above the yield stress of the material. In many cases, the existing residual stress due to the fabrication process or welding process may be sufficient to overcome the threshold stress needed for SCC initiation.

Stress corrosion cracking can be either intergranular type or transgranular type. As shown in Figure 2-2(a), intergranular stress corrosion cracks propagate along the grain boundaries. But in Figure 2-2(b), transgranular stress corrosion cracks propagate through the grains. Such a difference in crack growth path is usually due to alloy composition and microstructure. Grain boundary composition, e.g. Cr depletion or carbides, can be a major reason for the intergranular cracking to occur.

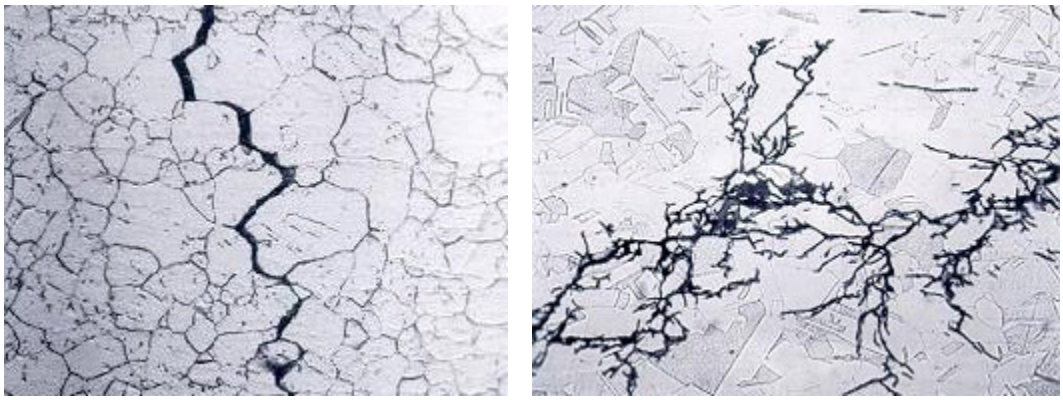

(a) (b)

Figure 2-2. Types of stress corrosion cracking: (a) Intergranular SCC (Inconel heat exchanger tube); (b) Transgranular SCC (316 stainless steel) [6]

2.1.2 Initiation of SCC

SCC initiation on the metal requires many pre-existing factors: an unstable passivity in an aggressive environment, surface defects, and the local tensile stress. Cracks typically initiate from certain surface defects. These defects can be scratches, pits, and inclusions. Some defects, especially in stainless steel, can generate Cr depletion region which changes the local passivity. Corrosion activities on these defects are usually higher than other areas. Certain chemical environment on the surface creates a right chemistry/electrochemistry to promote the reaction for local passivity breakdown. A local mechanical loading threshold, either a threshold stress or a critical concentration factor K_{ISCC}, needs to be met in order to initiate SCC.

There are many mechanisms reported to explain the crack initiation process for SCC. Cracks can initiate at the scratches and dents on the metal surface due to the high local stress intensity. As shown in Figure 2-3, pit initiation under certain stress condition can cause SCC to initiate if the local stress threshold is reached [7, 8]. Selective dissolution of certain inclusions, grain boundary and phases are normally the most important mechanisms in many alloys for SCC initiation. During such a selective dissolution process, galvanic corrosion may play an important role in promoting the corrosion rate. Free hydrogen atom on the surface, produced by hydrogen evolution reaction, can also participate in crack initiation which leads to hydrogen embrittlement. This type of environment assisted cracking is different from the normal SCC and will be discussed separately.

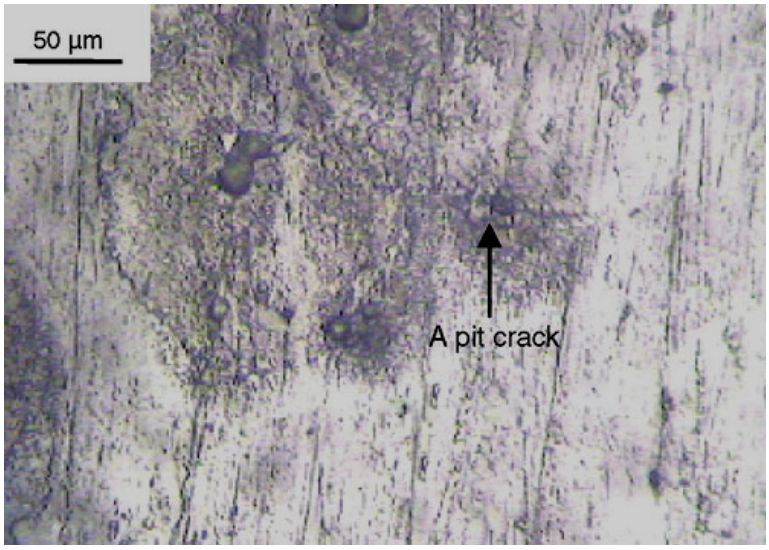

Figure 2-3. Crack initiation at a pit [7]

The rupture of surface film, which lasts for less than 1 second, is usually considered as the initial step of crack initiation. This process can be activated by all mechanisms described above. Slip steps produced by local plastic deformation on the surface can weaken the surface film stability and promote the film breakdown [9]. A certain amount of time, which is called induction time or incubation time, is needed before the fracture starts.

2.1.3 Propagation of SCC

After the SCC initiation, the further growth of the crack is controlled by the combined effect from crack tip chemistry/electrochemistry, local stress/strain, and microstructure. The chemistry or electrochemistry at the crack tip affects the crack tip passivity. The continuous passivation and breakdown can be a major driving force for the brittle failure propagation. Local stress usually produces a plastic zone at the crack tip

which assists the lattice straining. Microstructure and defects usually determine the direction of crack growth.

There are a number of proposed SCC mechanisms, which differ in the sequence of events and causes of local embrittlement. Figure 2-4 gives a schematic of the rate-determining steps involved in the SCC propagation. Crack tip usually undergoes fast anodic reaction in order to support the crack propagation. Oxidation, film breakdown and repassivation are common reactions at crack tip. In order to support the anodic process, cathodic reaction, such as oxygen reduction or hydrogen evolution, takes place near the crack tip and on the crack wall. Mass transport of the reactants from the bulk solution to the crack tip can be a limiting step for SCC propagation. The mechanical property ahead of crack tip is modified by the plastic zone or process zone ahead of crack tip, which controls the crack growth and local stress/strain. Clearly, the behavior at the crack tip controls the SCC process.

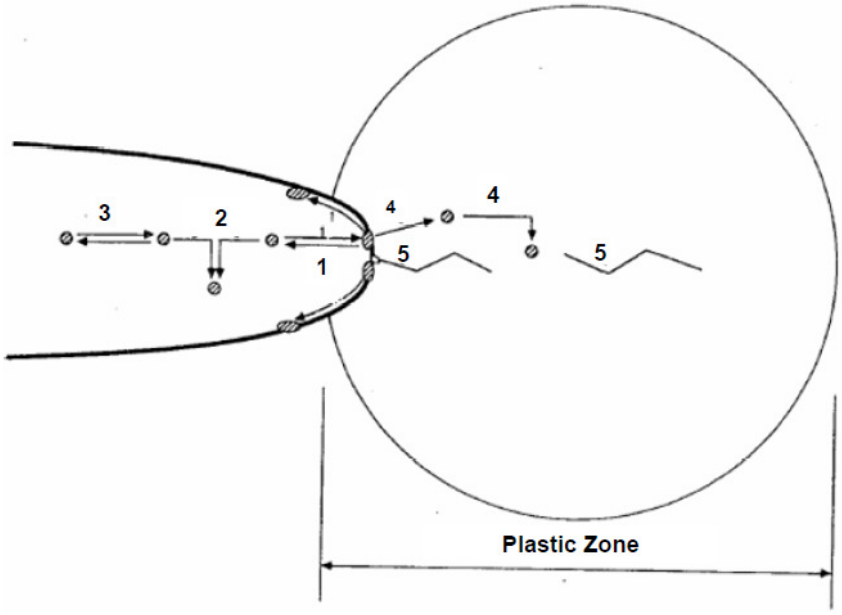

Figure 2-4. Rate-determining steps in stress corrosion crack: (1) surface reaction and diffusion; (2) solution reaction; (3) mass transport; (4) atomic diffusion in material; (5) mechanical failure [10]

2.1.4 SCC Mechanisms

Fundamentally, majority of SCC phenomenon can be explained by four different mechanisms: crack tip anodic dissolution, film induced cleavage, atomic surface mobility, and absorption induced embrittlement. Anodic dissolution is governed by the preferential dissolution at the crack tip on the pre-existing active paths in the material, such as grain boundary. With local plastic deformation, the stress ruptures the relatively brittle passive film. The exposed metal at the crack tip experiences the active corrosion and fast dissolution along some active paths. Then, oxide film can form again in order to passivate the crack tip. These two processes repeat and produce a brittle path for the stress corrosion crack to propagate. [11] Anodic dissolution mechanism highly depends on the specific environment and material. Crack walls form passive film and the dissolution rate

at the crack wall is usually orders of magnitude slower than that at the crack tip. Therefore, a much higher value of current is expected from the crack tip area. This dissolution controlled mechanism of SCC mostly occurs in a narrow potential range where the passivity is thermodynamically unstable.

In comparison, film induced cleavage mechanism is mostly based on a brittle passive film that is formed at the crack tip. Film induced cleavage is also called slip dissolution mechanism. Local plastic strain at the crack tip ruptures the passive film and results in the fast corrosion of the underlying metal and the crack propagation into the base material. In this mechanism, the passivation process is thermodynamically stable and kinetically fast. The major driving force is the local mechanical damage of the brittle passive film due to staining, such as slip step. The brittle passive film at the crack tip breaks down and reforms during the crack growth [12].

Compared with the two mechanisms above, the mechanism of atomic surface mobility is unique. According to this mechanism, SCC is only possible if the materials are exposed to the corrosive environments at temperatures less than half of the melting temperatures of the corrosion products formed at the surface. During the corrosion process, atoms at the crack tip diffuse away and create the movement of vacancies towards the crack tip, which results in the crack propagation. According to this proposed mechanism, low melting point materials and material/environment combinations that form low melting point corrosion products are more suitable for this mechanism because the surface mobility of metal is usually high in such systems.

Another mechanism, adsorption induced embrittlement, proposes that the selective adsorption of chemical species decreases the bond energy at the crack tip

thereby decreasing the mechanical integrity at the crack tip. Hydrogen embrittlement falls into this category. The details of hydrogen embrittlement will be described separately later.

2.2 Pitting Corrosion

2.2.1 General Definition

Engineering alloys, such as carbon steels, stainless steels and aluminum alloys etc., are useful only because of the passive films. Nanoscale oxide layers formed on the surface by corrosion reactions can protect alloys from further corrosion. Different from the stress corrosion cracking, pitting corrosion is an accelerated dissolution of metals due to the localized passive film breakdown in specific environments without local stress/strain. The passive film breakdown during pitting is usually because of the defects present on the metal surface and the chemical/electrochemical conditions. If the passive film is broken down and the local corrosion activity can be sustained without repassivation, it can result into pitting corrosion.

2.2.2 Basic Mechanism of Pitting Corrosion

Fundamental studies related to pitting corrosion usually focus on one of the following stages [8]: (1) passive film formation and its characteristics; (2) the earliest stage of passive film breakdown; (3) metastable pit growth and its repassivation; (4) the growth of stable pits. Pitting corrosion is a complex but important issue for material degradation. Sometimes, it is the reason for many corrosion failures. For instance, active pits may lead to leaks in pressure vessels or may even become an initiation site for stress corrosion cracking. [7]

Many factors can be a critical for pit initiation and growth. Environment and local chemistry is the major reason for pitting corrosion. Pits can only initiate and grow when aggressive anionic species are present. Most of the time, chloride ions are the major anions causing pitting. Hydrolysis of metal chloride products inside a pit may lead to strong acidity which further leads to active dissolution on alloys that normally show active-passive behavior. With the presence of oxidizing agents, chloride can enhance localized corrosion significantly. In addition, chloride is a small anion with a high diffusivity. It can easily adsorb and diffuse into the passive film to cause localized attack. Pitting is an autocatalytic process which means that once a pit initiates on the surface, the conditions form for its further growth. Depletion of local cathodic reactant (e.g. oxygen) inside an active pit may results in a shift of cathodic reaction to large exposed surface, outside the pit. Enrichment of metal cations inside the pit further attracts anionic species, such as chloride ions, from the bulk solution. Therefore, local pH value goes down while the anion concentration increases inside the pit. Such acidic environment again drives the pit growth.

Besides the environment, other factors such as potential, alloy composition and microstructure, temperature, stochastic processes related to microstructure, and potential inhibitors in the solution may all influence the pitting corrosion. Studies showed that the pitting corrosion only occurs under certain characteristic potential range. Pits initiate at potentials above the pitting potential (E_p), and grows at the potentials above repassivation potential (E_r), which is usually lower than E_P. The locations of E_p, E_r, and corrosion potential (E_{corr}) are shown in Figure 2-5.

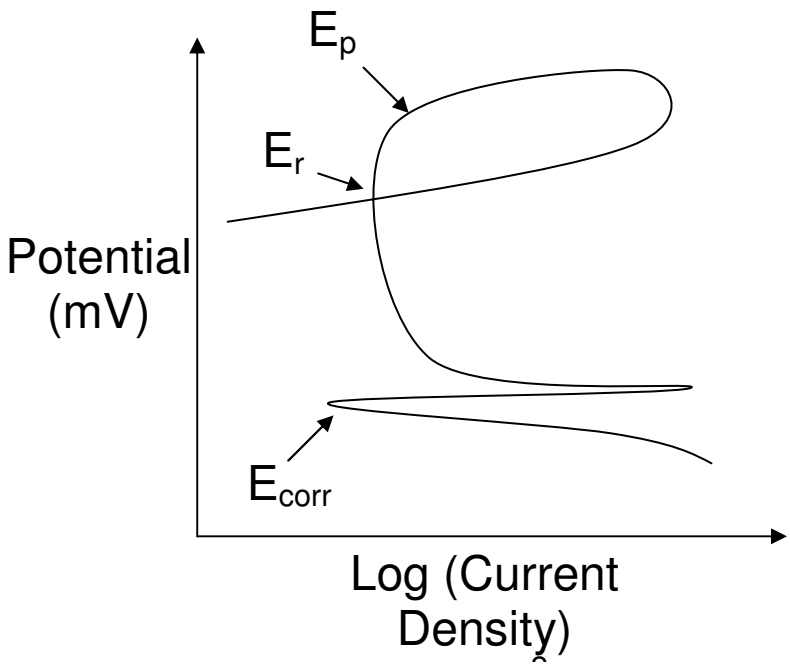

Figure 2-5. Schematic of a typical cyclic polarization curve

Regarding the material composition and microstructure, pits almost always start at the surface sites where exhibit chemical or physical heterogeneity, such as inclusions, second phase particles, grain boundaries, mechanical defects and dislocations. For instance, pitting in stainless steel is often associated with MnS inclusion, while pitting in Al alloys is more related to inter-metallic particles.

2.3 Hydrogen Embrittlement

2.3.1 General Definition

Hydrogen embrittlement is the most important type of absorption induced failure phenomenon in metals. During selective absorption, specific species may be adsorbed on the surface and diffused into the metal lattice in order to reduce the surface energy. Such

a process can interact with the strained bonds ahead of the crack tip and induce a reduction in the bond strength.

Hydrogen embrittlement process is due to the absorption of atomic hydrogen on the surface. Since hydrogen atom is small, it presents a higher diffusivity in the metal lattice. The atomic hydrogen tends to diffuse to the area with higher tensile strain and triaxial stresses, like the crack tip. Any dislocation or imperfection at the crack tip can act as an initiation site for hydrogen absorption. Brittle fracture of the local area causes the crack to propagate. Hydrogen may also react with alloying elements and make brittle phases that may cause embrittlement.

2.3.2 Mechanism of Hydrogen Embrittlement

Figure 2-6 shows the local chemistry and electrochemistry inside a crack which may be related to the hydrogen generation [13]. Though the solution is under aeration, the solution close to the crack tip tends to be depleted of oxygen due to its consumption in the reduction reaction on the crack wall. Due to the de-aeration inside the crack, the corrosion potential of the metal surface inside the crack is more negative than that of the external surface. In this case, the cathodic reactants in the external solution, including hydrogen (H^+), hydrogen sulfide (H_2S), and bicarbonate (HCO_3^-) will tend to be consumed by reaction in the crack. Under some specific conditions, the production of hydrogen by chemical or electrochemical reactions will become dominant and promote the anodic activity.

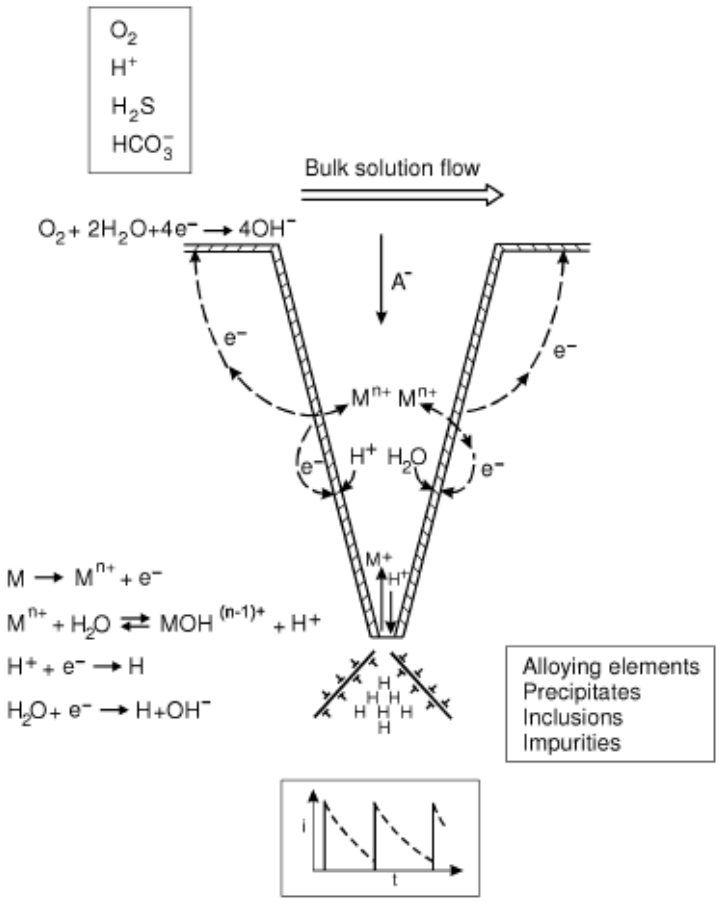

Figure 2-6. Schematic of the chemistry and electrochemistry inside a crack [13]

Throughout the whole hydrogen embrittlement process, three key components are necessary in order to understand the crack evolution. Firstly, in an established environment, the generation of hydrogen and its kinetics is critical to establish a stable hydrogen flow to embrittle the metallic material. In some cases, hydrogen-producing cathodic reaction is not a thermodynamically favorable reaction during the corrosion process. Secondly, the transport stage of atomic hydrogen is very important for the initial embrittlement. Hydrogen has to be adsorbed at the surface and then absorbed into the material by either lattice diffusion or dislocation transport to internal defects. The kinetics of surface recombination reaction, leading to molecular hydrogen, and passivation may

also affect this process. Thirdly, a proper local stress condition and strain change has to be maintained in order to support the brittle crack propagation.

There are a number of mechanisms proposed to explain the hydrogen embrittlement process. These mechanisms highly depend on the type of material, environment, and the stress condition. Three major mechanistic models are: (1) hydride mechanism; (2) hydrogen enhanced decohesion; (3) hydrogen enhanced local plasticity.

Hydride mechanism is controlled by the formation and cleavage of hydride under stressed condition [14]. In systems such as titanium, tantalum, zirconium, uranium, and niobium, the formation of hydride is thermodynamically favorable under certain condition. Since hydride is usually brittle, the local tensile stress can breakdown the hydride and lead to a crack propagation. Then, hydride can reform. These two processes repeat and result in the fracture of material.

Hydrogen enhanced decohesion mechanism is one of the oldest model for hydrogen embrittlement. According to this mechanism, under the tensile strength field, such as crack tip area, welding region, and dislocation clusters, the solubility of hydrogen can increase. The increased hydrogen concentration in those regions can result in a decrease in the atomic binding forces of the metal lattice, which leads to a crack growth along pre-determined paths, such as grain boundary or other weakly passivated matrix.

Hydrogen enhanced local plasticity (HELP) is another popular model which has been observed in a variety of materials with BCC, FCC, and HCP lattice structures. It is the most recent mechanism proposed for explaining hydrogen embrittlement [15-17]. Similar to hydrogen enhanced decohesion mechanism, the pre-requisite of this model is that hydrogen tends to accumulate in the field of stress at crack tip and dislocations.

According to this mechanism, the presence of hydrogen inside the lattice decreases the barrier to dislocation movement and increases the plastic deformation ahead of the crack tip. Hydrogen tends to surround the crack tip due to the facilitated slip process or the effect of stress on the chemical potential of the hydrogen. Due to the shielding effect of hydrogen, the dislocation movement takes place at low shearing stress, which is caused by the local decrease in the yield stress by hydrogen. This enhances local plasticity in the region of crack. Micro-cracks can be produced by the formation of micro pores and shearing.

Hydrogen permeation test is the most common method for hydrogen study [18]. The hydrogen flux through a membrane is measured to determine the availability and concentration of hydrogen. The permeation can be divided into three stages. Each stage provides its own resistance to the measured hydrogen flux. The first stage is hydrogen entry. The thickness of the permeation membrane must be sufficiently large to minimize the resistance of this first stage. The second stage is hydrogen diffusion through the membrane. Larger membrane thickness makes this stage the largest resistance for permeation process. The final stage is the hydrogen exit from the membrane. A suitable anodic potential has to be applied in order to ionize all the exiting hydrogen and generate measurable anodic current.

2.4 Previous Research on Corrosion in Alcoholic Environments

Compared to the corrosion research in aqueous environments, corrosion behavior of metallic materials in non-aqueous, especially alcoholic, environments are much less understood. The main reason is that most industrial applications of structural materials are related to the aqueous environments. Corrosion in alcoholic environmnets was not a

major concern in industry. However, in recent years, with the increasing demand for alternative energy to reduce carbon emission and dependence on petroleum products, biofuels, such as bioethanol, biobutanol and biodiesel, become possible sustainable energy sources. Among them, bioethanol (sugarcane, corn-based, and cellulosic ethanol) is immediately available for use in current combustion engine systems. In the United States, up to 10% fuel-grade ethanol (FGE) is blended into the gasoline. Due to the increasing demand for FGE, understanding the possible degradation behavior of metallic materials, especially the pipeline carbon steel, which may come in contact with these fuels, becomes crucial.

2.4.1 Stress Corrosion Cracking in Alcoholic Environments

Stress corrosion cracking in ethanolic environments has been reported and investigated since the 1980s [19-23]. Most of these early studies on alcoholic SCC in literature were based on phenomenological observations. In recent years, fuel-grade ethanol attracts a lot of interests in the corrosion community. One critical concern in using the existing gas-pipelines to transport the fuel-grade ethanol or blended fuel is the potential stress corrosion cracking susceptibility of carbon steel pipelines in these environments.

The first report, published by American Petroleum Institute (API) in 2003, provides a survey of published literature and service experience with SCC of carbon steel in FGE in industry [1]. As shown in Figure 2-7, the report suggests that pipeline carbon steel is susceptible to stress corrosion cracking in FGE especially close to the welding region which contains higher residual stress.

Figure 2-7. Crack observed under the ethanol pipeline [1]

Since then, a number of groups worked on the phenomenological study of SCC in FGE. These studies have confirmed that the SCC is the major failure mode for ethanol transportation through carbon steel pipelines. [2, 3] As shown in Figure 2-8, SCC of carbon steel can be reproduced in the lab using ethanol fuel and simulated fuel-grade ethanol. Both transgranular and intergranular SCC have been reported in different labs.

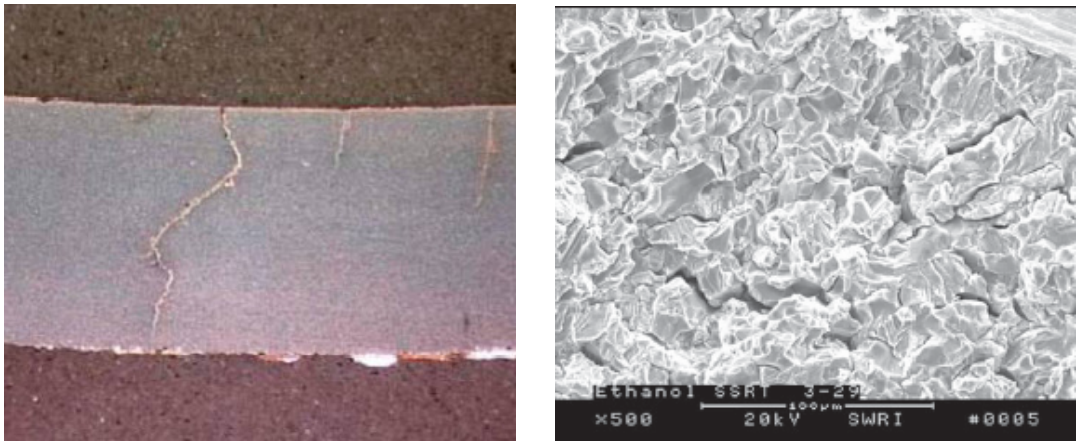

(a) (b)

Figure 2-8. Stress corrosion crack research from various labs: (a) SCC of steel equipment in fuel ethanol; (b) SCC in SFGE

Impurities such as chloride, water, and methanol have been reported to influence the SCC susceptibility as well as the SCC mode. Methanol and chloride were observed to be important for determining the crack morphology, intergranular or transgranular [3]. Laboratory studies on the simulated fuel grade ethanol have typically shown a mixed mode SCC (both transgranular and intergranular) on pipeline steels. The dissolved oxygen level in the ethanol controls the SCC initiation and the surface electrochemical potential. Most of the impurities and other constituents in the FGE originate from the source, production processes used, storage, or transportation. However, degradation of ethanol by either electrochemical or chemical reactions is also considered as a reason that may generate impurities and affect the SCC of carbon steel [24]. Jiang et al. [25] reported that the acetic acid produced by ethanol degradation provided protons and promoted stress corrosion cracking of titanium alloys in ethanolic environments. As shown in Figure 2-9, SCC was found to occur in a narrow range of potential (0V to 200mV vs.

Ag/AgCl/ethanol) [3]. In addition, the open circuit potential varies with environmental factors.

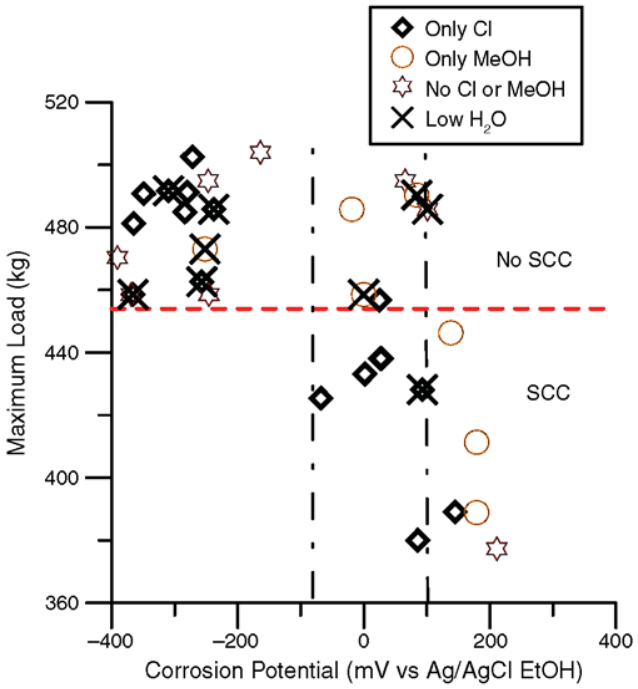

Figure 2-9. Effect of corrosion potential on SCC susceptibility [3]

While some phenomenological understanding of bioethanol SCC slowly emerged from the published research [1-3], the basic stress corrosion cracking mechanism governing the crack initiation and growth remained unclear. Mechanisms of stress corrosion cracking have been thoroughly studied in various aqueous environments. [12, 26-31] In most of these systems, local breakdown of the passive film and repassivation under certain stress conditions are critical to SCC initiation. [32-34] Crack propagation is mainly dominated by two kinds of mechanisms: one controlled by the anodic dissolution at the crack tip within a certain potential range [11], the other possibility is due to the embrittlement by hydrogen produced from cathodic reactions. [35] However, very few

studies were designed to understand the fundamental mechanism in alcoholic environments. Corrosion work on alcoholic solvents was generally carried out in methanol-based environments rather than in ethanol-based environments [19-21]. The repassivation kinetics has been considered as one important factor to determine SCC activity in methanol. A good correlation between SCC transition potential and repassivation potential was reported in methanolic solution [19]. SCC occurs only when the specimen potential is higher the repassivation potential.

In ethanolic environment, the only published mechanistic study is the theoretical review by Newman [24]. The work suggested that the anodic dissolution is more likely a controlling factor for stress corrosion cracking in ethanol instead of the hydrogen related mechanisms. Newman [24] also suggested that the oxidation products of ethanol could drive corrosion of the crack tip and its complex effects can possibly lead to intergranular SCC. Transgranular SCC in ethanol could be more close to the SCC in CO-CO_2-H_2O system.

2.4.2 Corrosion and Electrochemistry in Alcoholic Environments

Similar to SCC study, relatively small volume of work has been reported in literature on the corrosion behavior in non-aqueous alcoholic environments. Most prior corrosion work focused on methanol system [36-40]. The work by Heitz [23] showed that metals usually exhibit different and complicated electrochemical behavior in non-aqueous solvent compared to that in aqueous solution. Corrosion potential, passivity and passive film breakdown are easily varied by the impurities in the solution. In ethanolic environments, corrosion and pitting, as well as their related anodic and cathodic

electrochemical behavior, have been documented since 1980s [4, 5, 41]. Water concentration, sulphate, and acidity have been reported as critical factors increasing the pitting corrosion susceptibility [4, 5, 19]. Repassivation kinetics is slowed by impurities, e.g. water, resulting in an increase in the pitting susceptibility [42]. Role of water has also been widely studied in alcoholic environment. Water may act as oxygen donor to promote passivation process on metal surface and stabilize the passive layer. [36, 43] Brossia et al. [37] have shown that even a small amount of water is effective in the formation of a passive film in the acidic methanol solutions.

The major difficulty in studying the electrochemical corrosion behavior of alloys in ethanol system is the high solution resistivity [3, 44]. Although work has been done to understand metal electrochemistry in ethanolic solution, most of them required either high salt impurity concentration or supporting electrolyte [41, 42, 45]. It was reported that supporting electrolyte could possibly influence the passivity of metal in ethanolic solution [44]. As shown in Figure 2-10, the supporting electrolytes in ethanol usually play a critical role in changing the electrochemical conditions during corrosion process. Anodic behaviors of tested metals were easily changed due to the supporting electrolyte.

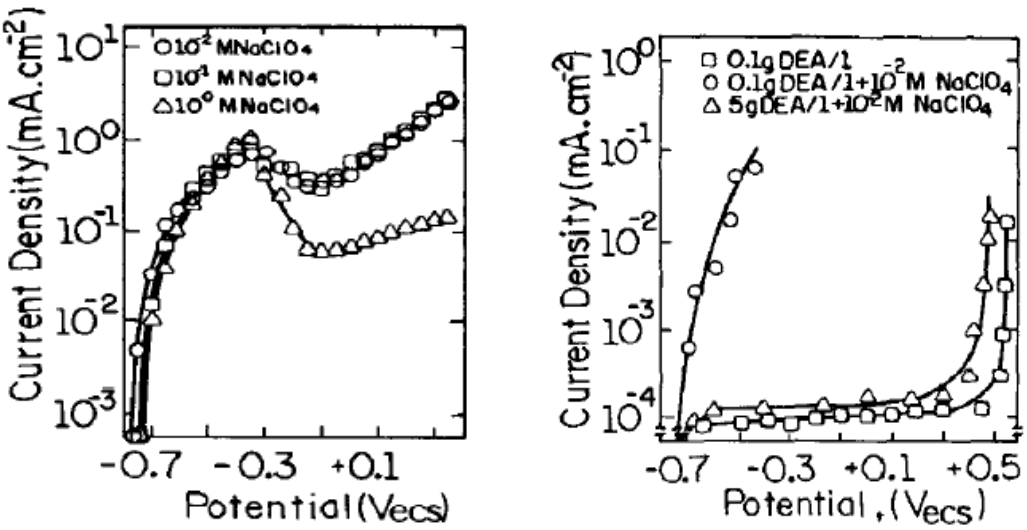

(a) (b)

Figure 2-10. The effects of different supporting electrolytes on the corrosion electrochemical behaviors in ethanol: (a) effect of perchlorate; (b) the differences between DEA and perchlorate

In reality, a commercial fuel-grade ethanol usually contains minimum amount of impurities, which results in an extremely low ionic strength. Work with high concentrations of impurities easily alter the surface behavior of metals and cannot explain the reaction mechanism in FGE. IR compensation (automatic and manually adjusted) has been used in FGE to accommodate for the high solution resistance [3], which showed some difficulties in data interpretation. Up to now, limited systematic work has been reported to address the corrosion related electrochemistry in ethanolic solutions with a low ionic strength.

Thermodynamics of iron in ethanol is quite different from that in water. Shown in Figure 2-11 are the Pourbaix diagram calculated for pure ethanol and ethanol with 400

ppm water [3]. Clearly, even with a small amount of water addition, the thermodynamic equilibrium state on iron surface changes. This suggests that the electrochemistry and corrosion behavior of carbon steel in ethanol can change dramatically by a little water present.

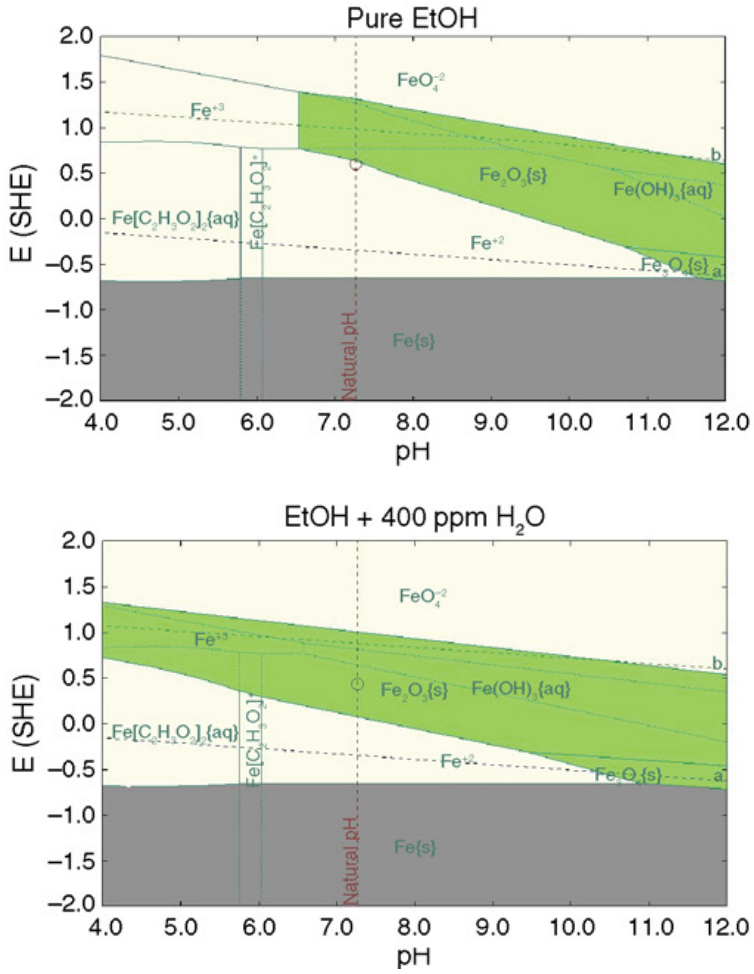

Figure 2-11. Calculated Pourbaix diagram for pure ethanol and ethanol with 500 ppm water addition

2.4.3 Cathodic Reactions and Hydrogen Uptake in Alcoholic Environments

As the counter part of corrosion reaction, cathodic activities in the solution also play an important role in controlling the corrosion kinetics and possible hydrogen

production. The latter reaction may further induce the hydrogen related embrittlement fracture under certain conditions. However, compared to the anodic behavior, no systematic work has been reported on understanding the cathodic corrosion reactions in ethanolic environments, specially oxygen reduction and hydrogen evolution. Although the oxygen and hydrogen related electro-catalytic activities in alcohols (both methanol and ethanol) have brought lots of attentions due to the fuel cell research in recent years [46, 47], the cathodic electrocatalytic reactions in those systems exhibit very different mechanisms and kinetics and can not be used to interpret the ethanol corrosion of steel. Regarding the metallic corrosion process, most of the early cathodic studies still focused on methanol. The cathodic polarization study reported by Bellucci et al. [38] showed the discharge of free protons and the reduction of residual oxygen generate a wide range of limiting current densities in methanol under de-aeration. As shown in Figure 2-12, hydrogen reduction can only be reached below -1 V vs SCE under de-aeration. This value is far below the normal corrosion potential. Neither the discharge of water nor that of methanol can significantly contribute to the corrosion process. In comparison, in oxygen saturated methanol, the cathodic reactions are not affected by additions of water and acid.

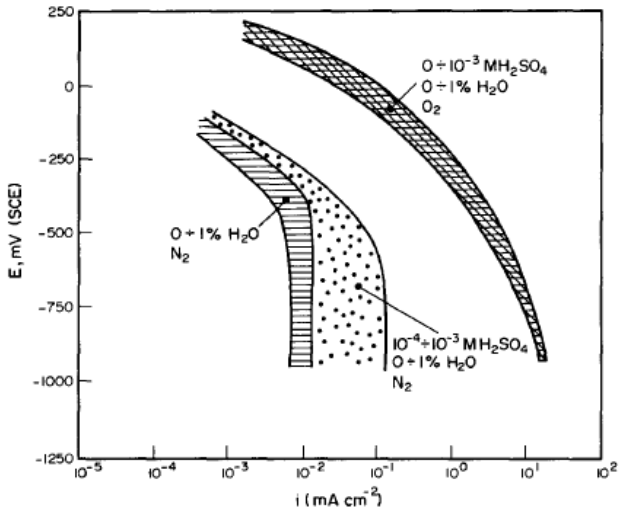

Figure 2-12. Cathodic polarization curves for platinum in CH_3OH+10^{-1} M $LiClO_4$ [38]

Heitz [23] proposed that water, produced by cathodic reaction, may play a more significant role on the corrosion in organic solvents. Further study by Bellucci et al. [48], as shown in Figure 2-13, reported that the first cathodic reaction below the free corrosion potential of various metallic materials in methanol corresponds to the reduction of pre-existing oxides.

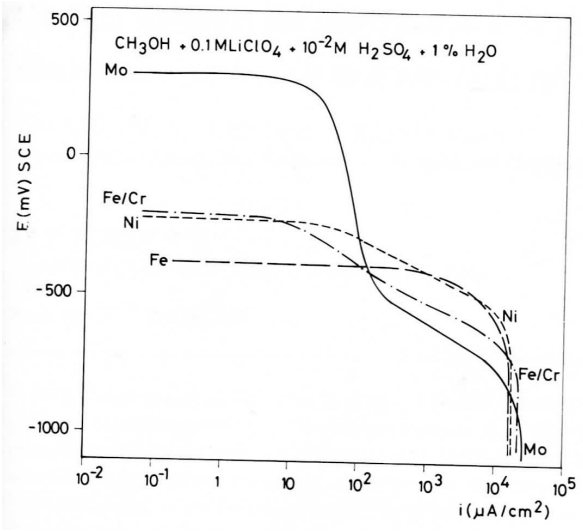

Figure 2-13. Cathodic polarization of ferritic stainless steel in methanolic solution [48]

The investigation by Brossia et al. [37] reported that water is not electro-active in the potential range relevant to iron corrosion in methanol. Their results also indicated that the proton reduction kinetics is faster than oxygen reduction in methanol. In the methanol environment with the addition of hydrochloric acid (HCl), Brossia et al. [37] proposed a preferential protonation mechanism which causes the decrease of proton mobility due to the slight increase (< 0.5 wt%) in water content. This process may result in the decrease in corrosion activity.

CHAPTER 3

EXPERIMENTAL

3.1 Materials and Testing Environments

3.1.1 Materials and Sample Design

The pipeline steel used for this study is X-65 carbon steel. The nominal chemical composition of this low-carbon steel is shown in Table 3-1. The mechanical properties of this grade of steel is also shown in Table 3-2. Samples used in this work were machined out of a new X-65 pipe under as-received condition.

Table 3-1. The chemical composition of as-received X-65 carbon steel.

Type	C wt%	Mn wt%	P wt%	Al wt%	Si wt%	S wt%	Cr wt%	Ni wt%	Cu wt%	Fe wt%
X-65	0.08	1.26	0.01	0.041	0.24	0.002	0.03	0.01	0.015	Bal.

Table 3-2. The mechanical properties of as-received X-65 carbon steel

Type	Yield Stress		UTS	
	ksi	MPa	ksi	MPa
X-65	69.3	478	81.3	561

Various sample geometries were fabricated for different purposes. Two different kinds of tensile samples (smooth and notched) were machined for the slow strain rate

tests based on the ASTM standard G 129 [49]. The schematics of sample geometries are shown in Figure 3-1. The smooth tensile sample provides an opportunity to get the random crack initiation, which is critical for studying initiation site. In comparison, the notched tensile sample fixes the crack initiation at the notch root where the stress intensity is the maximum, which helps to monitor crack propagation process. In addition, a notched tensile sample with the shorter gauge length, 0.25 inch, were also applied in some tests, as shown in Figure 3-1(c). The purpose of this short gauge length sample is to minimize the corrosion activity from the gauge shoulder and maximize the signal from the crack at the notch root. This design benefits the EIS study during crack propagation, which will be described in detail later. All tensile samples were machined along the rolling direction and the pipe axis. The surfaces of tested specimens were dry-polished up to 2000 grit and degreased with acetone, and dried in blowing air. Tensile specimens were polished longitudinally to prevent the SCC initiation due to the circumferential polishing scratches.

(a)

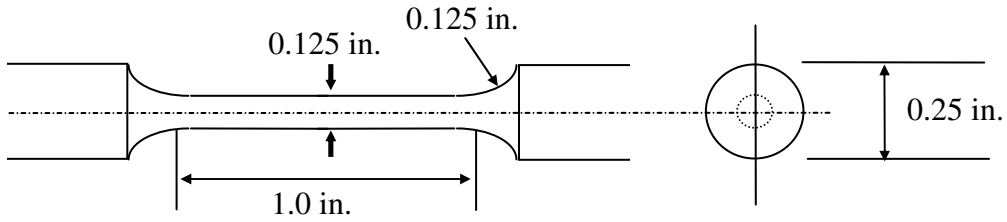

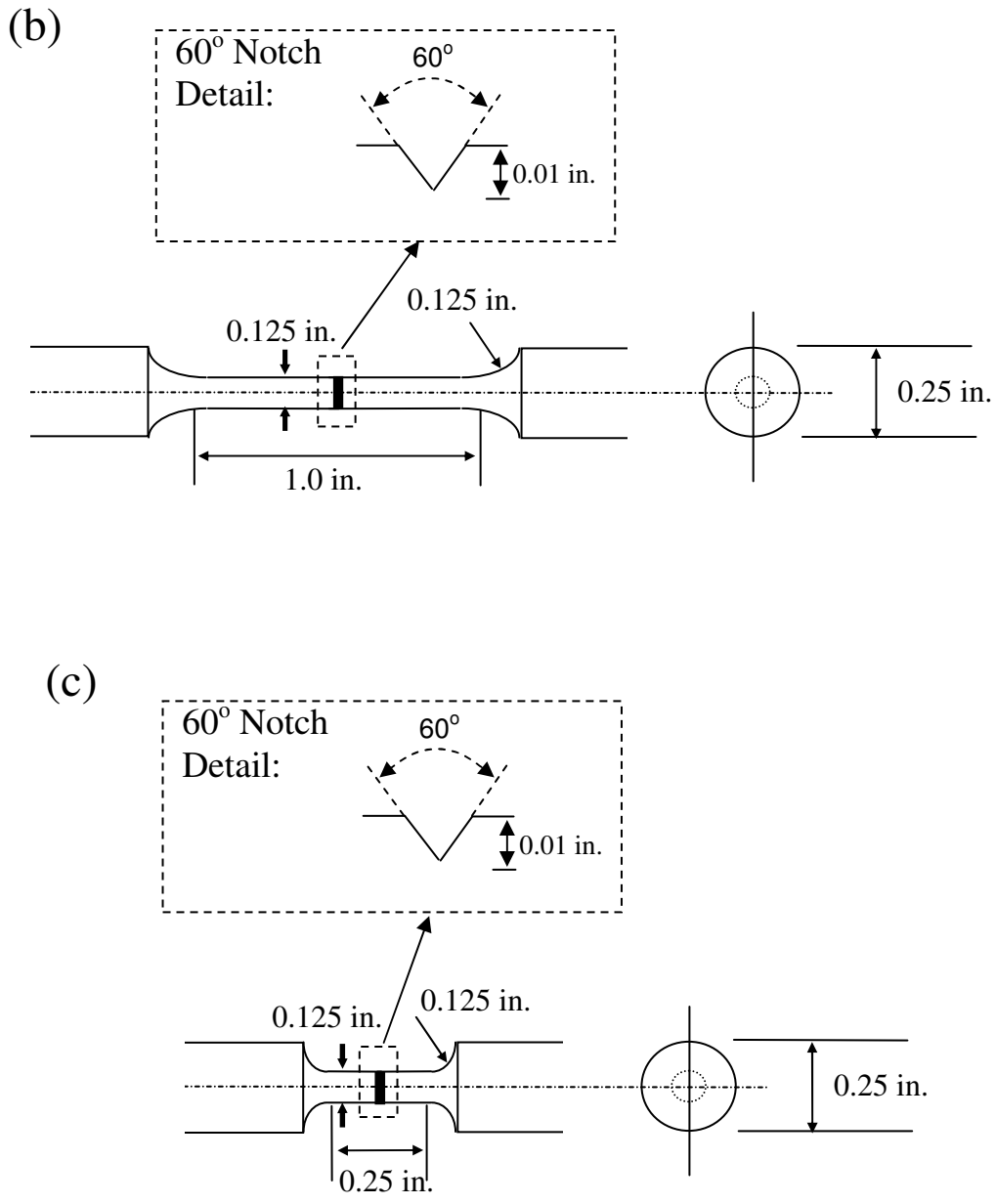

Figure 3-1. SSRT round tensile sample gauge geometry: (a) smooth sample; (b) notched sample; (c) short-gauge notched sample

Cylindrical samples (6.2 mm in diameter, 15 mm in length) and flat square coupons (14 mm x 14 mm x 4 mm) were machined for electrochemical tests and long-

term exposure tests, respectively. The flat square membrane specimens (40 mm in length and width, 1.5 mm in thickness) were machined for hydrogen permeation test. All specimens were dry-polished up to 2000 grit and degreased with acetone, and finally dried in blowing air. The actual dimension of each sample after polishing was measured before the test for current density calculation. All electrochemical tests were started immediately after the polishing and cleaning.

3.1.2 Testing Environments

Since the commercial fuel-grade ethanol from different refineries may show various compositions, a standardized testing environment is necessary for consistent mechanistic study. Based on the ASTM standard D-4806 for fuel-grade ethanol, the simulated fuel-grade ethanol solution was made using 200 proof ethanol, pure methanol, glacial acetic acid, pure NaCl and NaOH (purities >99%), and ultra pure water (~18 MΩ/cm) [3, 50]. All test solutions were prepared using analytical grade reagents and deionized water. Sodium chloride used for making the SFGE was dried at 150^{o}C to remove any adsorbed water. Chemical composition of the baseline simulated fuel-grade ethanol (SFGE) used in this study is shown in Table 3-3.

Table 3-3. Composition of simulated fuel-grade ethanol (SFGE) used in this study based on ASTM D 4806.

Ethanol (vol%)	Methanol (vol%)	Water (vol%)	NaCl (mg/L)	Acetic Acid (mg/L)
98.5	0.5	1.0	53	56

The ethanol chemistry variables of SFGE were adjusted in order to investigate their effects on corrosion susceptibility. Without any further description, the name "SFGE" in this paper refers to a baseline composition standardized in Table 3-3. In some parts of this thesis, the names "acidic SFGE", "neutral SFGE", and "alkaline SFGE" were also used to distinguish the pHe in the solution, which were formulated with 56 mg/L acetic acid, no added acetic acid and NaOH, and 50 mg/L NaOH, respectively. NaOH was first dissolved into water, and then added into ethanol to reach the specified NaOH and water concentrations. Aeration and de-aeration of SFGE solutions were carried out by bubbling dry air or nitrogen through the test solution. The oxygen level in the tested SFGE solutions were controlled by bubbling dry oxygen and nitrogen mixture under certain ratio through the test solution. The flow rate of the purging gas was always fixed at 100 ml/min.

3.2 Slow Strain Rate Test

Stress corrosion cracking of carbon steel in ethanolic environments was studied using the slow strain rate test method with and without the electrochemical measurements. Although the in-service pipelines do not experience loading conditions like SSRT, but this accelerated test provides reliable information on SCC susceptibility and has been used to study SCC of carbon steels in FGE [3, 51] and other environments. A glass cell with PTFE end caps was used to form a reaction chamber, as shown in Figure 3-2. SFGE solutions were aerated during tests by passing dry-air through the testing solution. The testing cell and the gas-purge system were designed to eliminate the evaporation of the ethanol and the adsorption of water from atmosphere. The variation in the ethanol

chemistry was maintained within 5% of the values during a 6-day test (based on the post chemical analysis). Smooth and notched tensile samples were used for different purposes, as described before. Initial strain rate was controlled based on the crack tip creep property of the carbon pipeline steel. For SCC susceptibility test, the range of initial strain rate used for the tensile tests was from $1x10^{-7}$ /sec to $2x10^{-6}$ /sec. For the mechanistic study, the smooth samples were tested under a constant extension rate giving an initial strain rate of $2x10^{-6}$ /sec, while the notched sample was tested under an extension strain rate of $8x10^{-7}$ /sec. The choices of these strain rates offer two things: (1) reasonable cracking susceptibility; (2) short testing time to eliminate the effect of chloride leakage from reference electrode [52].

For the notched sample, all the stress curves reported in this thesis is the notch-root maximum stress. Based on the initial sample and notch geometry, the initial stress concentration factor (K_t) at the notch root is calculated using the K_t plot in literature [53]. It should be noted that K_t normally changes with an increase in the crack depth. Therefore, after the large crack forms, the plot of this stress only represents the evolution of loading.

Electrochemical measurement during SSRT test has been proven to possibly affect the cracking susceptibility determination due to the small chloride leakage from the reference electrode [51]. We observed a significant amount of chloride leakage through a standard vycor glass frit from Princeton Applied Research. Electrophoresis analysis of SFGE after electrochemical tests revealed that the chloride leakage through the vycor glass frit was of the order of 43.5mg/L after one week. However, the liquid volume in the salt bridge, which contained a 1M LiCl ethanol supporting electrolyte, did not change

during the same testing duration. At room temperature, the surface tension of ethanol in air is about 22 dynes/cm, while that of water is about 72 dynes/cm. [54] Such chloride ion leakage may be due to the better wetting property of the ethanol supporting electrolyte in a porous glass structure. Therefore, the SCC susceptibility tests in this study are pure tensile test without the electrochemical measurement, unless otherwise specified. During the mechanistic study, electrochemical measurements were carried out. However, the test durations for those SSRT were limited to a relatively short period.

The picture in Figure 3-2 shows the detailed setup for the SSRT test with electrochemical measurement. The test rig applied a constant extension rate on the tested sample. The air purged into the test solution was kept dry from the inlet to outlet of the test cell.

Figure 3-2. Experimental setup for SSRT test in the lab

3.3 Electrochemical Measurements

Potentiodynamic polarization, in-situ open circuit potential (OCP) monitoring, potentiostatic current acquisition and electrochemical impedance spectroscopy (EIS) were used to understand the electrochemical behavior of carbon steel in this study.

Electrochemical tests without stress were carried out using a Gamry PC4 or Gamry Reference-600 electrochemical measurement system in a sealed three-electrode electrochemical testing cell. A silver-silver chloride based reference electrode for ethanol (SSCE), noted with the configuration of Ag/AgCl/1M LiCl,EtOH, was used in this study [3, 51, 55]. The vycor glass frit from Princeton Applied Research was used to construct the glass reference electrode. The pure silver wire was chloridized by galvanostatically polarized at 0.4 mA/cm2 in 1M HCl aqueous solution for 2 hours. The obtained wire (with AgCl coating) was stored in the sealed 200 proof ethanol beaker for 24 hours before the construction of reference electrode. Pure ethanol with 1M LiCl (from Mettler Toledo) was filled in reference electrode as electrolyte.

All samples were dry-polished to 2000 grit and then immediately immersed in the test cell. Tested SFGE solutions usually exhibit high solution resistances. To avoid any possible influence on the corrosion potential and the anodic behavior of carbon steel [44], supporting electrolytes were not added to the SFGE test solutions in this study. Due to the low ionic strength of SFGE, the test cell and specimen geometries were optimized, as shown in Figure 3-3. With this design, the working electrode (WE) had a reasonably large surface area with minimum distance from both the counter electrode (CE) and the reference electrode (RE). The distances between the counter electrode, the testing sample, and the reference electrode were kept constant for every test. Therefore; automatic IR

compensation could be applied even at a relatively high polarization potential. Detailed effects of ohmic drop, or IR drop, on electrochemical measurements are discussed later. This cell design, with automatic IR compensation, enabled us to overcome the high solution resistivity and perform reliable electrochemical tests using the voltage control capability of a standard potentiostat.

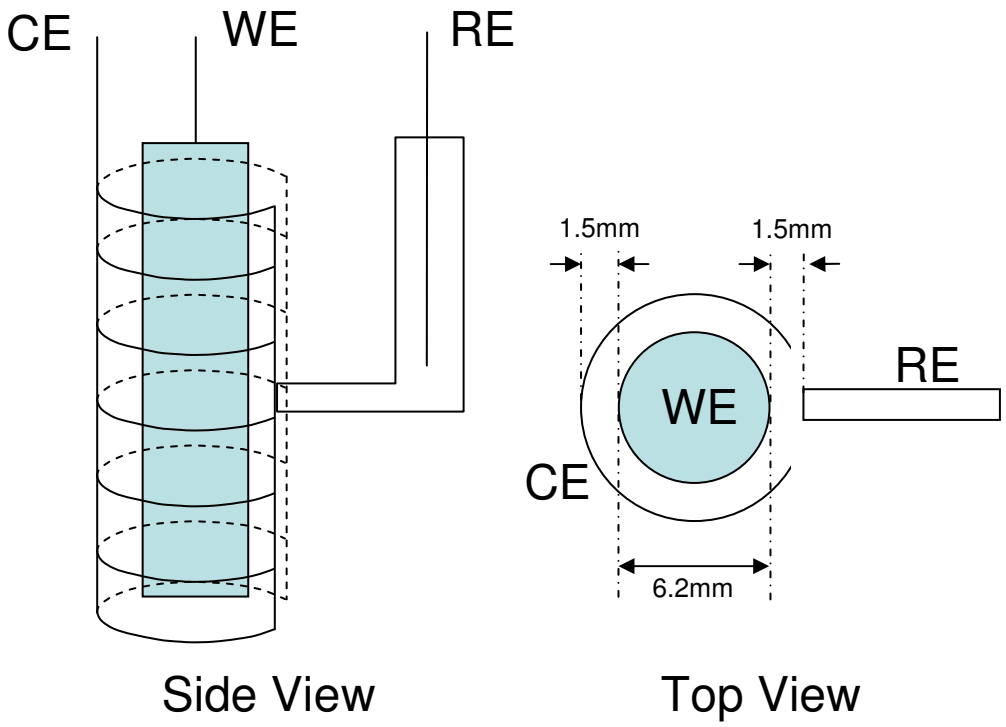

Figure 3-3. Schematic of the electrochemical cell design for an ethanolic solution with a low ionic strength (WE, CE, and RE refer to working electrode, counter electrode, and reference electrode, respectively)

Figure 3-4 shows the geometry of the testing cell for the electrochemical measurement during SSRT test. The distance between the counter electrode (CE) and the

working electrode (WE) is fixed at 2mm, and the distance between the reference electrode (RE) and the working electrode (WE) is fixed at 5mm for every test.

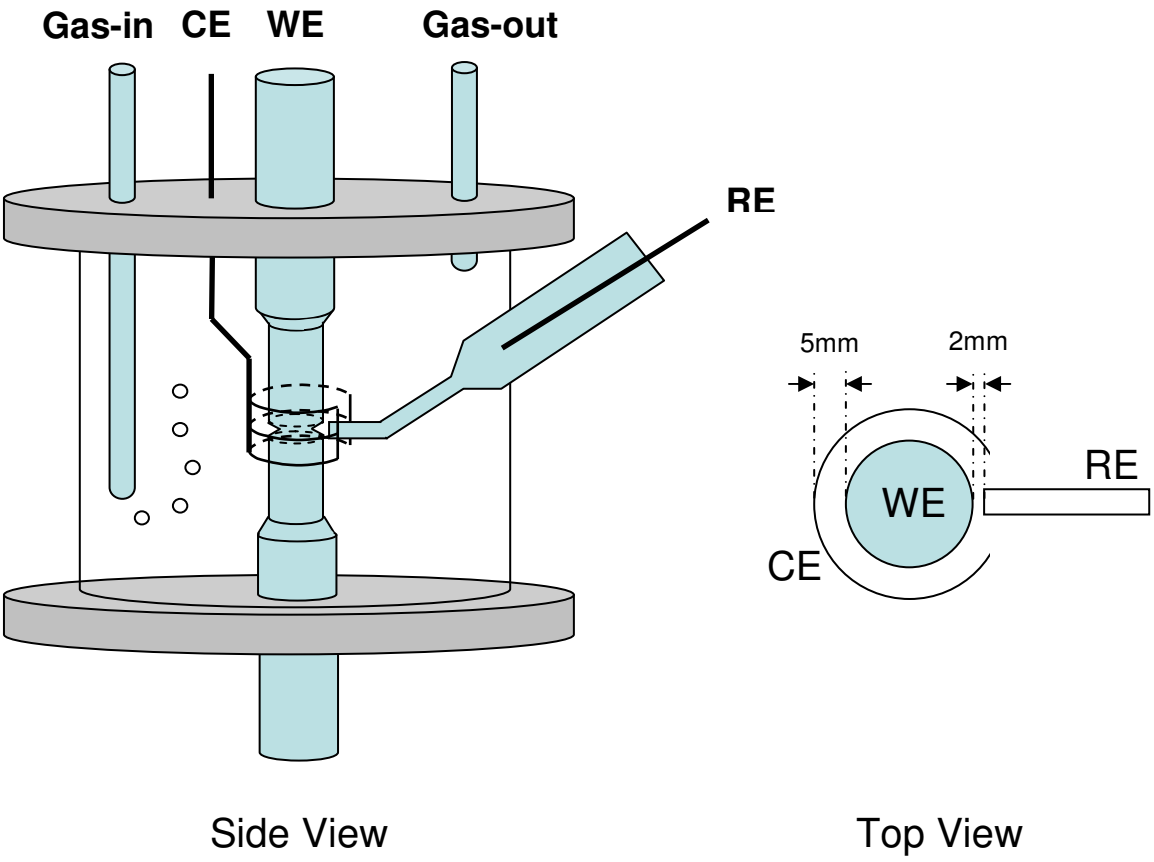

Figure 3-4. Electrochemical cell geometry with characteristic dimensions for SSRT test

Phase angle analysis using EIS was also used in this study in order to understand the detailed mechanism during the crack propagation. During EIS measurement, the electrochemical measurements were carried out continuously in such a way that every 50 minutes of OCP or potentiostatic measurement was followed by an EIS measurement, throughout the SSRT. The automatic IR compensation was applied for all tests due to the

high resistivity of SFGE. The impedance was measured with an applied *ac* voltage of 10 mV in the frequency range from 100 Hz to 0.01 Hz.

To study the cathodic reactions possible in ethanol environment, cathodic polarization tests were carried out with different environmental conditions. If no additional description was made in the figure, the cathodic potentiodynamic scan was carried out from OCP to negative cathodic potentials at a scan rate of 1 mV/s with automatic IR compensation. EIS measurement does not have the automatic IR compensation function. Therefore, pre-calculation for IR correction is needed to determine the real applied *dc* potential value before EIS test. All EIS tests were started with a cathodic pre-polarization at the tested potential for 500 seconds to ensure a steady state. The applied ac amplitude was 10 - 20 mV with an analysis frequency ranging from 0.01 Hz to 100 kHz. The EIS curve fitting was carried out using ZView® by Scribner Associates Inc.

3.4 Long-term Exposure Corrosion Tests

Long-term exposure corrosion test was used in this study to evaluate the corrosion susceptibility of carbon steel coupon in SFGE with different ethanol chemistry and dissolved oxygen level. These tests were carried out in 250mL glass flasks for 8 days at room temperature. Compositional changes in the prepared solution for exposure tests were reported in the results and discussion section. A special circulating gas-purge system was designed to avoid the evaporation of the ethanol and the adsorption of water from atmosphere. Flat square samples (14 mm x 14 mm x 4 mm) were placed in glass sample holders, designed to minimize the contact area. After test, the specimens were

immediately cleaned with acetone, dried, and stored in vacuum box. Overall weight loss, pit size and pit density were measured after 8-day exposure by removing the corrosion film from the surface. Pitting data reported for each test condition is from ten randomly selected areas on two identically tested samples. The average value and the standard deviation are both given in the figures in this paper. Surface and the polished cross-section were characterized using optical and scanning electron microscopes.

3.5 Hydrogen Permeation Test

The electrochemical hydrogen permeation tests were carried out using a modified Devanathan-Stachurski hydrogen permeation cell based on ASTM standard G-148 [18]. The schematic of the permeation cell is shown in Figure 3-5.

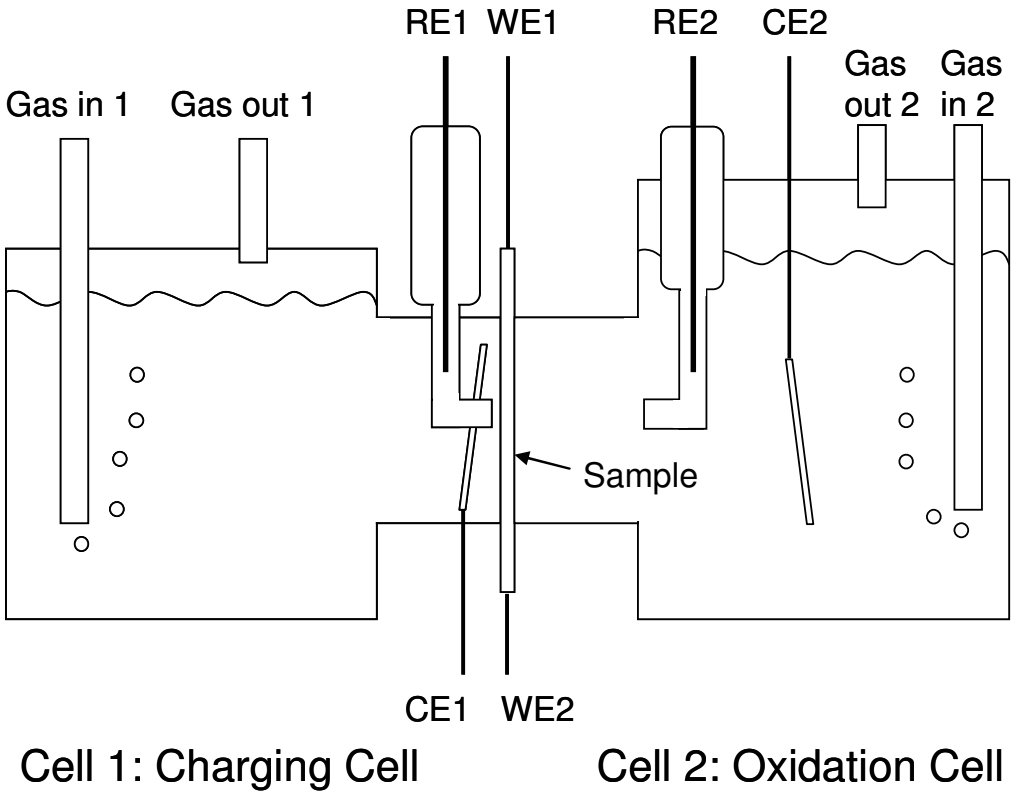

Figure 3-5. Schematic of the hydrogen permeation cell

Thickness of the X-65 carbon steel membrane specimen, which was sandwiched between the oxidation cell and the charging cell, was around 1.5 mm. Due to the high resistivity in SFGE, both counter and reference electrodes in the charging cell were placed very close to the permeation membrane to reduce the effect of IR drop during polarization. Similar to the electrochemical testing cell described earlier, the circulating gas-purge system was used so that no ethanol evaporation and moisture absorption took place during the permeation test. The specimen was dry-polished to 2000 grit finish and immediately assembled into the cell. The sample exposure area was around 3.1 cm^2. The charging cell was filled with the SFGE solution under various potentials and oxygen partial pressures. The charging was conducted at OCP or constant applied potential. The ethanol reference electrode, Ag/AgCl/1M LiCl, EtOH, was used in hydrogen charging cell. In the oxidation cell, the membrane specimen was immersed in 0.1 M NaOH solution and polarized at a constant potential of 300 mV vs a standard saturated calomel electrode (SCE) with nitrogen bubbling.

3.6 Chemical Analysis

Analytical chemistry tools were used to determine and control the chemical composition of the test solution. Water concentration in ethanol solutions, before and after the test, was measured by the Karl-Fisher titration using an Aquastar titrator V-1B. The value of pHe, which stands for the pH value in ethanol, was used to quantify the acid strength in SFGE. pHe is an engineering term defined by ASTM standard to quickly estimate and compare acid strength (proton strength) in ethanol fuel. An Orion ROSS^{TM} sure-flow pH electrode was used for this purpose. Based on the ASTM standard [56],

pHe measurement was carried out in a 50mL beaker under stirring. After immersing the electrode in solution for 30 seconds, the value was recorded as the pHe value for the tested solution. The dissolved oxygen concentration in SFGE was measured using Polestar^{TM} DSP 3000 optical oxygen probe (for ethanol). With the optical oxygen probe, the partial pressure of oxygen was measured. The dissolved oxygen concentration was calculated using Henry's law, with the mathematical formula of C=P/k. C is the dissolved oxygen concentration in ethanol. P is the partial pressure of oxygen in ethanol. k is Henry's constant and equal to 10360 Pa m^3 mol^{-1} at 293 K [57]. Concentrations of cations such as iron and sodium were determined using inductively coupled plasma (ICP) spectroscopy, and anions such as chloride were determined using electrophoresis method.

3.7 Microstructure and Physical Characterization

Surface morphology was characterized using a Nikon Optiphot-2 optical microscope. A LEO 1530 thermally-assisted field emission scanning electron microscope (SEM) coupled with energy dispersive spectrometry (EDS) was employed to characterize the surface microstructure and chemical composition. Surface film characterization and phase identification were done using Philips XRG 3100 X-ray diffraction (XRD) system.

Crack density and crack growth velocity for the carbon steel X-65 were quantified after each SSRT. The failed tensile samples were sectioned, mounted, and polished to 0.5 μm finish. A 2% Nital solution was used to etch the microstructure to show the grain structure and to determine the mode of the stress corrosion crack path. On the fracture surface, the crack depth after SSRT was characterized by measuring 10 equally-spaced

positions around the fracture surface. Their average and an error bar with maximum and minimum values are reported in this thesis.

CHAPTER 4

PHENOMENOLOGICAL INVESTIGATION OF STRESS CORROSION CRACKING OF CARBON STEEL IN SIMULATED FUEL-GRADE ETHANOL: THE EFFECTS OF ETHANOL CHEMISTRY, TESTING CONDITION AND MATERIAL

In order to understand the stress corrosion susceptibility of carbon steel in simulated fuel-grade ethanol environment, slow strain rate test was used to evaluate the crack initiation and propagation rate. The key factor which affects the SCC susceptibility in this environment is the ethanol chemistry and the testing condition. In this chapter, ethanol chemistry as well as other testing conditions, such as oxygen level and strain rate, was systematically reported. Chemical and mechanical factors which contribute to the SCC were studied in detail. The study also includes typical crack morphology and crack-to-pitting transition. Inclusions were identified as possible sites for crack initiation.

4.1 Effect of Strain Rate

Initial strain rates were varied between $1x10^{-7}$ /sec to $2x10^{-6}$ /sec. Figure 4-1 shows the effect of strain rate on the crack density and crack velocity in aerated standard SFGE which contains 1% water. The crack density was found to increase with a decrease in the initial strain rate, while the crack velocity decreased with a decrease in the strain rate. Although the sample tested at the lowest strain rate, $1x10^{-7}$ /sec, exhibited the

slowest crack velocity, it also resulted into the deepest crack for the tested strain rates. The lower crack velocity at lower strain rates is consistent with the longer testing time.

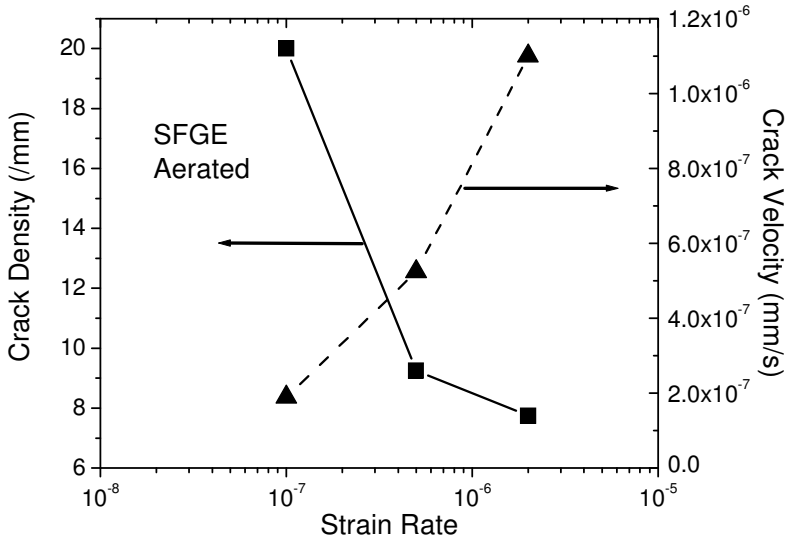

Figure 4-1. Evolution of crack density and crack growth velocity with strain rate in SFGE

The reduction in area and %-elongation under three different strain rates are shown in Figure 4-2. Results show that both the reduction in area and the %-elongation decreased with a decrease in the strain rate. Nishimura and Maeda also reported a linear relationship between the %-elongation and log (strain rate) and interpreted this effect to indicate that SCC is the predominant process within this strain rate range. [9] An increased tendency for brittle fracture indicates that the SCC susceptibility is higher at lower strain rates. SCC is strongly controlled by the interplay between the creep rate ahead of the crack tip which breakdowns the passivity, and the repassivation at the crack tip. [58] The low kinetics of crack tip repassivation in this system may be the reason for the higher SCC susceptibility at lower strain rates.

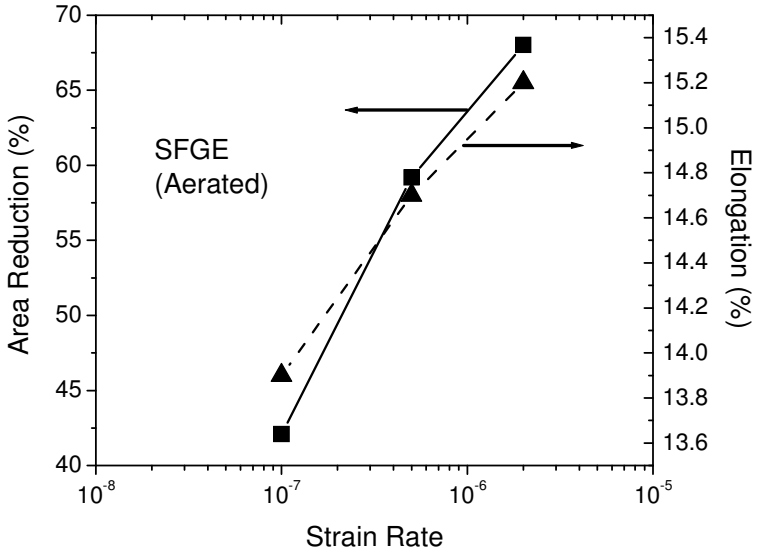

Figure 4-2. Area reduction and %-elongation as a function of applied initial strain rate in SFGE

4.2 Effect of Chloride

To study the effect of chloride in SFGE with 1% water on the SCC behavior of carbon steels, the chloride concentration was varied between 0 mg/L to 70 mg/L. Results in Figure 4-3 show the crack density and the crack growth velocity for the SFGE vs. chloride concentration. Results indicate that both the crack density and the crack velocity increased with an increase in the chloride concentration in the SFGE. Duplicate SSRT samples tested in the SFGE solution without chloride did not show any signs of SCC. However, the rate of increase in the crack density and the crack velocity decreased as the chloride concentration increased. Even a small amount of chloride can generate a strong effect on SCC of carbon steel in SFGE. Chloride is an active anion which reduces the stability of passive film of various alloys in ethanolic solution. [19, 59] This explains its role in the initiation and growth of stress corrosion cracks in the SFGE containing chlorides.

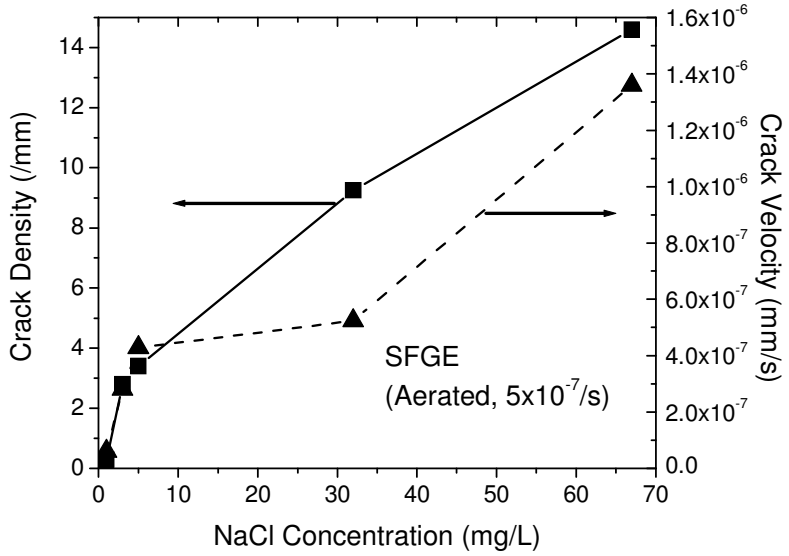

Figure 4-3. Evolution of crack density and crack growth velocity with chloride concentration in SFGE

Reduction in area and %-elongation for the SSRT samples as a function of chloride content in SFGE are shown in Figure 4-4. Both the area reduction and %-elongation decrease with an increase in the chloride concentration.

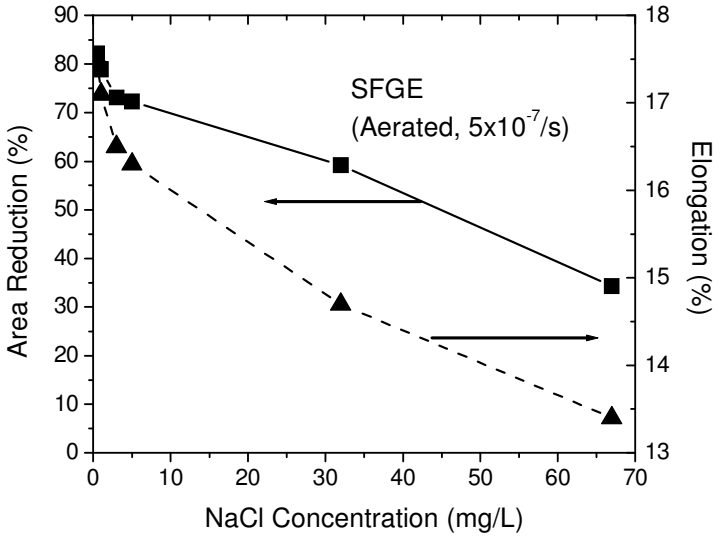

Figure 4-4. Evolution of area reduction and %-elongation with chloride concentration in SFGE

Figure 5 shows that the iron concentration (both dissolved and suspended) in solution, measured using ICP method after the test, changed with the chloride concentration. The results indicate that, in addition to stress corrosion cracking, an increase in the chloride content can also increase the metal dissolution rate in SFGE.

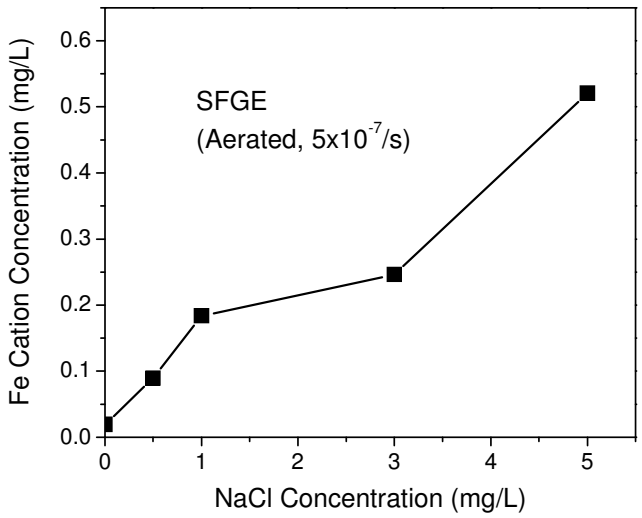

Figure 4-5. Concentration of dissolved iron in solution with the change of chloride amount after SSRT

4.3 Effect of Water

Typically, water is present in fuel grade ethanol, and it may affect its reactivity and corrosivity towards carbon steel. To investigate this, the extra water, zero to 5 vol.%, was added to make various SFGE solutions. Pre-analysis showed that SFGE without adding water had ~500 ppm water in it. Water has been shown to be an important factor in the passivation of various alloys in different alcoholic environments. [36, 37, 43, 48] Water is a polar molecule similar to the ethanol. However, electrochemically, aqueous solvents are significantly different from ethanolic solvents due to the differences in molecular solvation. The thermodynamics and kinetics of metal passivation also change with the addition of water in ethanolic environments. [36, 60, 61] Results in Figure 4-6 show the changes in the crack density and velocity as a function of water concentration in SFGE. SFGE with 1% water showed the highest crack density and crack velocity for the tested environments. Carbon steel in SFGE without water exhibited lower SCC susceptibility than in SFGE with 1% water. The results also show that carbon steel did not show signs of SCC when the water content of SFGE was increased to 5%. Although the carbon steel did not show SCC in the SFGE with 5% water, the samples showed a higher tendency for pitting corrosion and general corrosion.

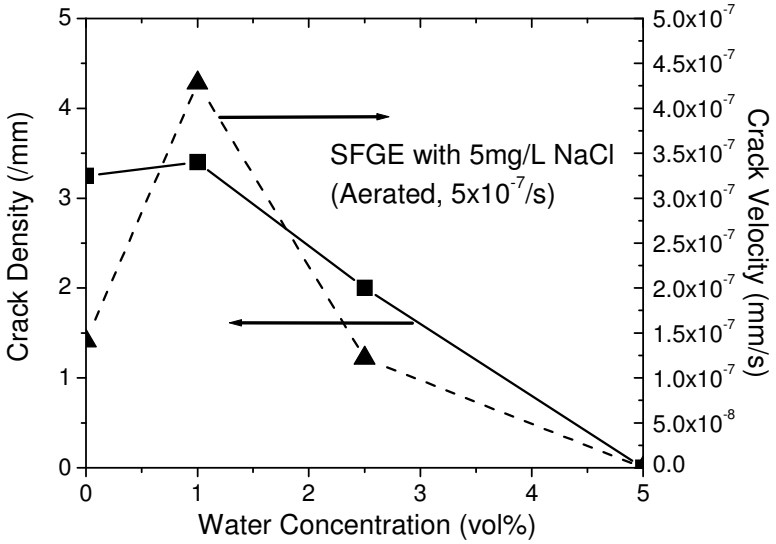

Figure 4-6. Evolution of crack density and crack growth velocity with water concentration in SFGE

Figure 4-7 shows the changes in the area reduction and %-elongation vs. water concentration, which indicate a similar SCC susceptibility trend as shown by more direct measurements in Figure 4-6.

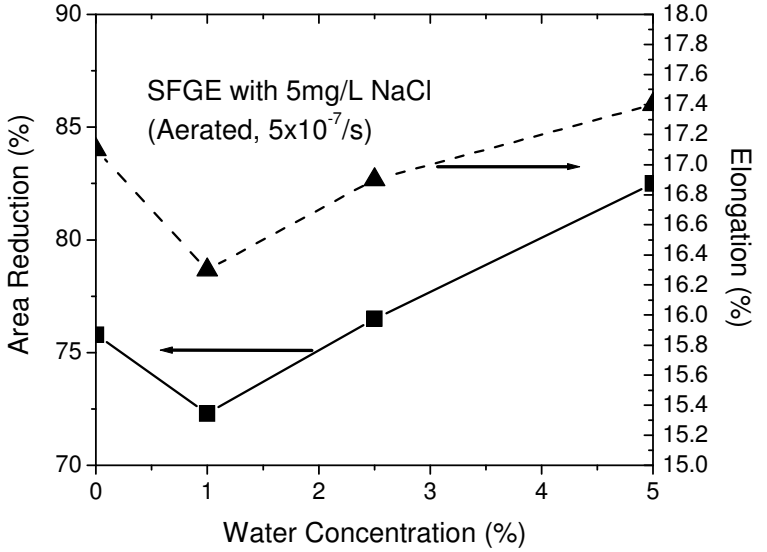

Figure 4-7. Evolution of area reduction and %-elongation with water concentration in SFGE

In Figure 4-8, ICP analysis of SFGE solutions after SSRT revealed that the solutions with no added water and 5% water both had higher concentration of dissolved iron than the SFGE with 1% water content. It has been reported that the water can act as an oxygen donor in the passivation process on metal surface, which stabilize the passive layer. [36, 43] In an anhydrous solution, a stable oxide film may not form to passivate the surface well, causing a fast dissolution rate for carbon steel. Poor passivity at the crack tip of the carbon steel in SFGE without water may also decrease its susceptibility to the SCC, possibly due to the blunting of the crack tip. The addition of a small amount of water (~1%) in the SFGE mixture seems to increase the anodic film kinetics [48], resulting in less general dissolution, but increasing the SCC susceptibility. Much higher water content (~5%) in ethanolic solution results in a thicker film, causing pitting and general corrosion, but eliminating SCC.

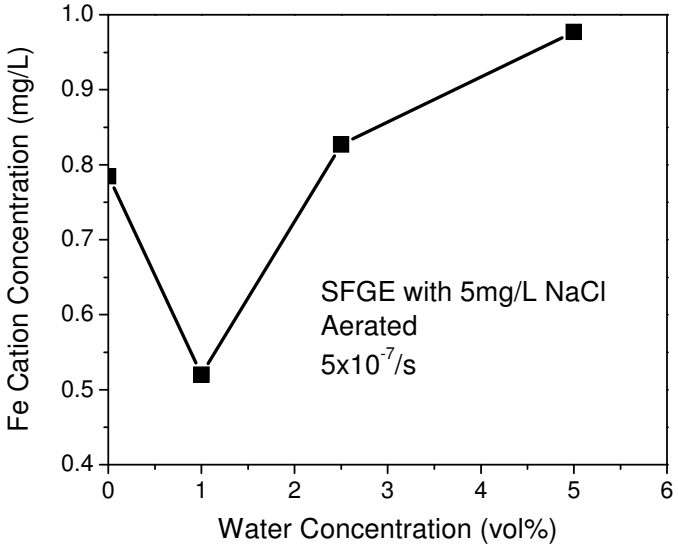

Figure 4-8. Concentration of dissolved iron in solution with the change of water amount after SSRT

4.4 Effect of pHe

pHe in a water/ethanol mixed system strongly depends on the concentration of water in ethanol. In an organic solution mixed with water, such as ethanolic solution, strong solvation may change the electrolyte structures on the electrode/solvent interface and in the solution. [36] Such behavior can strongly affect the mobility and concentration of free protons. [37] Figure 4-9 shows the change of pHe vs. water concentration in SFGE. Results show that with the same amount of acetic acid (5.6mg/L) present, the pHe decreases as water concentration is increased in SFGE. Molecule ionization strongly depends on the water/ethanol solvation. It has been reported that the passive film on a metal in alcoholic environments can be destabilized as the acidity is increased. [36]

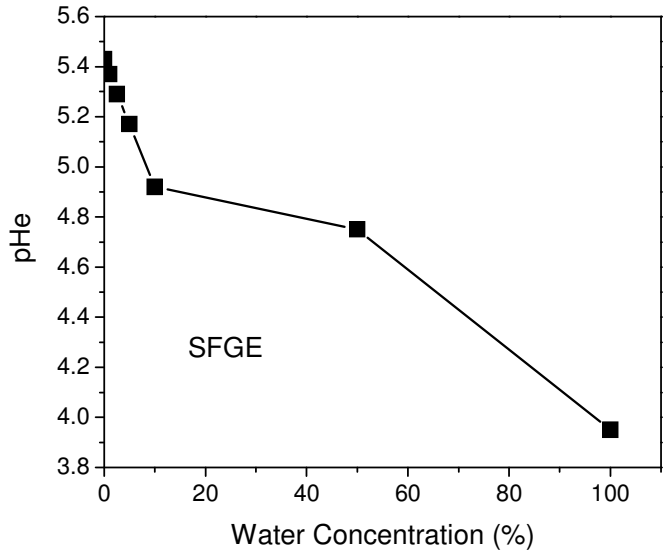

Figure 4-9. pHe change with water concentration

Figure 4-10 shows the failed X-65 carbon steel samples tested by SSRT method in normal-SFGE and alkaline-SFGE under the same testing condition. The pHe for the two solutions were 5.4 and 8.9, respectively. There was no indication of SCC in the

higher pHe SFGE even in the necked region of the tensile samples with high deformation. SSRT results suggest that the pHe control can be used to control the SCC susceptibility of carbon steel (X-65) in SFGE environments. Examination of the fracture surfaces using SEM also indicated a ductile mode of failure in the alkaline-SFGE environment.

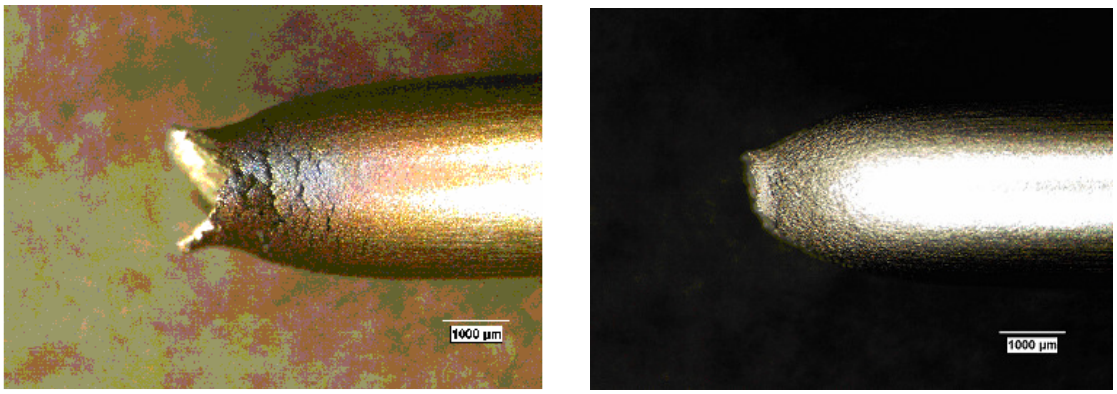

(a) (b)

Figure 4-10. Optical images of samples in SFGE with different pHe after SSRT: (a) pHe=5.4; (b) pHe=8.9

4.5 Effect of Oxygen

The role of oxygen in SCC in SFGE has been studied by Sridhar et al. [3] As shown in Figure 4-11, our study confirmed that removal of oxygen by purging nitrogen stopped the initiation of SCC on carbon steel.

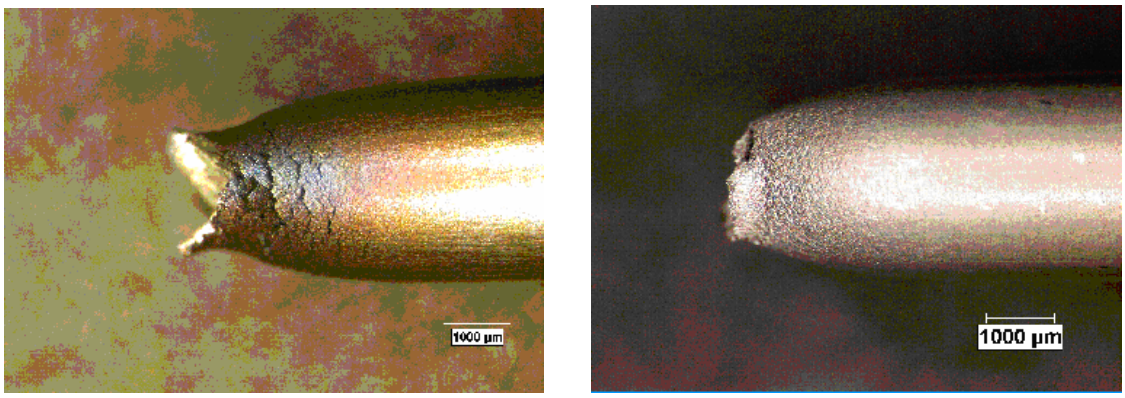

(a) (b)

Figure 4-11. Optical images of samples in SFGE with different oxygen conditions after SSRT: (a) Aerated; (b) De-aerated

4.6 Crack and Surface Morphology

Figure 4-12 shows the cross section of etched X-65 steel SSRT samples tested in SFGE with 1mg/L, 5mg/L, and 32mg/L NaCl concentrations. The crack morphologies were predominantly transgranular for the samples tested in this study, even at very low chloride concentration. As described earlier, a decrease in the chloride concentration in the SFGE resulted in a lower crack density and velocity. In the low-chloride SFGE solutions, most of the stress corrosion cracks were concentrated closer to the necked region of the tensile sample, indicating that large plastic deformation is needed for crack initiation. As shown in Figure 4-12 (a), the crack-like features very close to the final fracture may not be stress corrosion cracks, as highly deformed plastic zone was associated with these fissures.

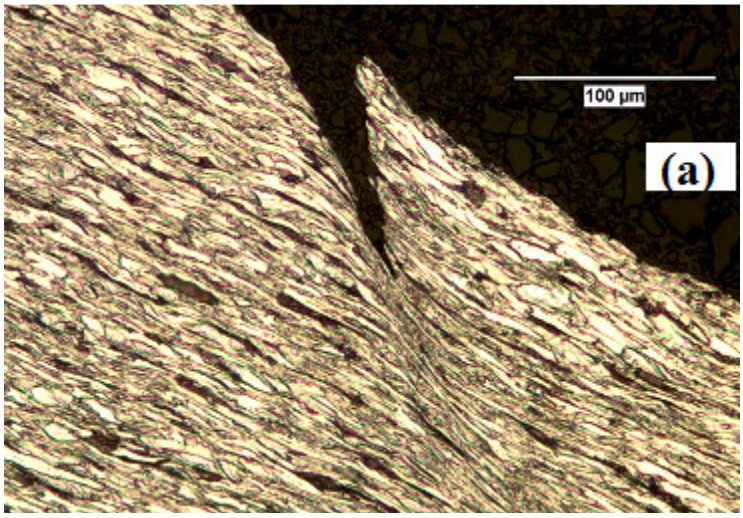

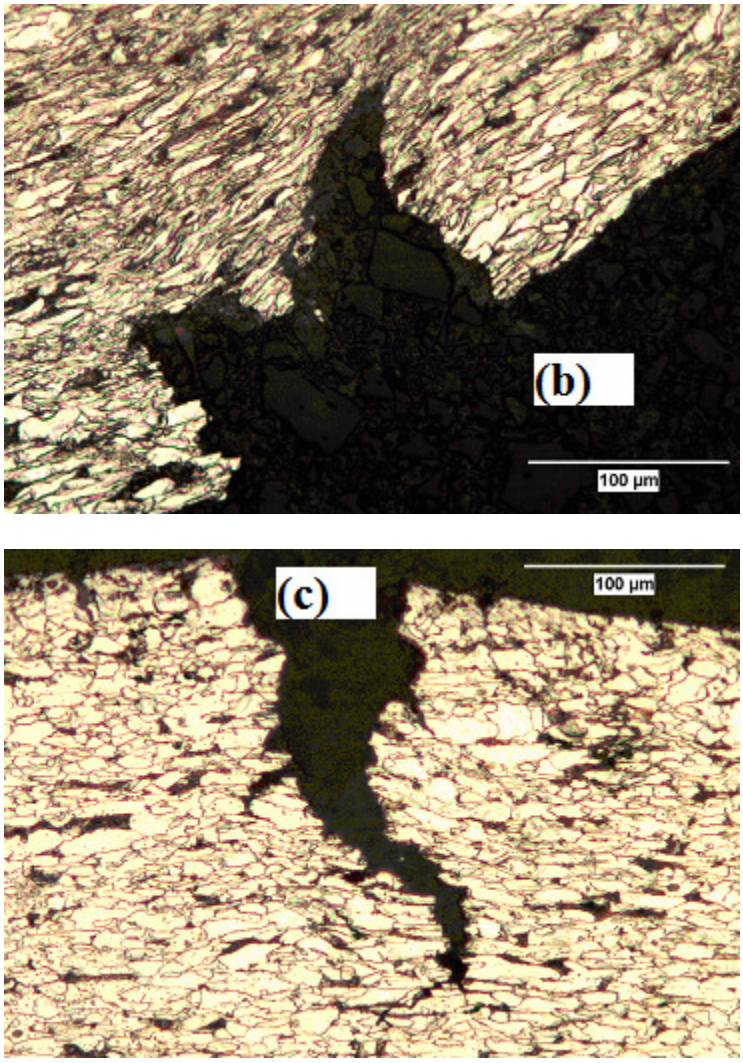

Figure 4-12. Optical images of crack morphology in SFGE with different chloride concentrations: (a) 1mg/L NaCl; (b) 5mg/L NaCl; (c) 32mg/L NaCl

SEM examination of the fracture surfaces was carried out for each SSRT sample to determine the size of the final fracture surface affected by SCC and to determine the mode of cracking. Examination revealed that without chlorides in SFGE, no SCC was observed at the fracture surface or on the side of the tensile samples. The fracture surface for this sample exhibited a typical ductile failure behavior, as shown in Figure 4-13(a). SEM micrographs in Figure 4-13 (b to d) show the effect of SFGE chloride content on crack morphology. With an increase in the chloride concentration, the SCC area at the

fracture surface increased. However, examination of fracture surfaces by SEM showed transgranular mode was the predominant mode of SCC for all chloride containing SFGE environments. The sample tested in the SFGE with low chloride concentration showed small areas with grain-like features at the fracture surface; however, it was difficult to categorize those areas as intergranular mode.

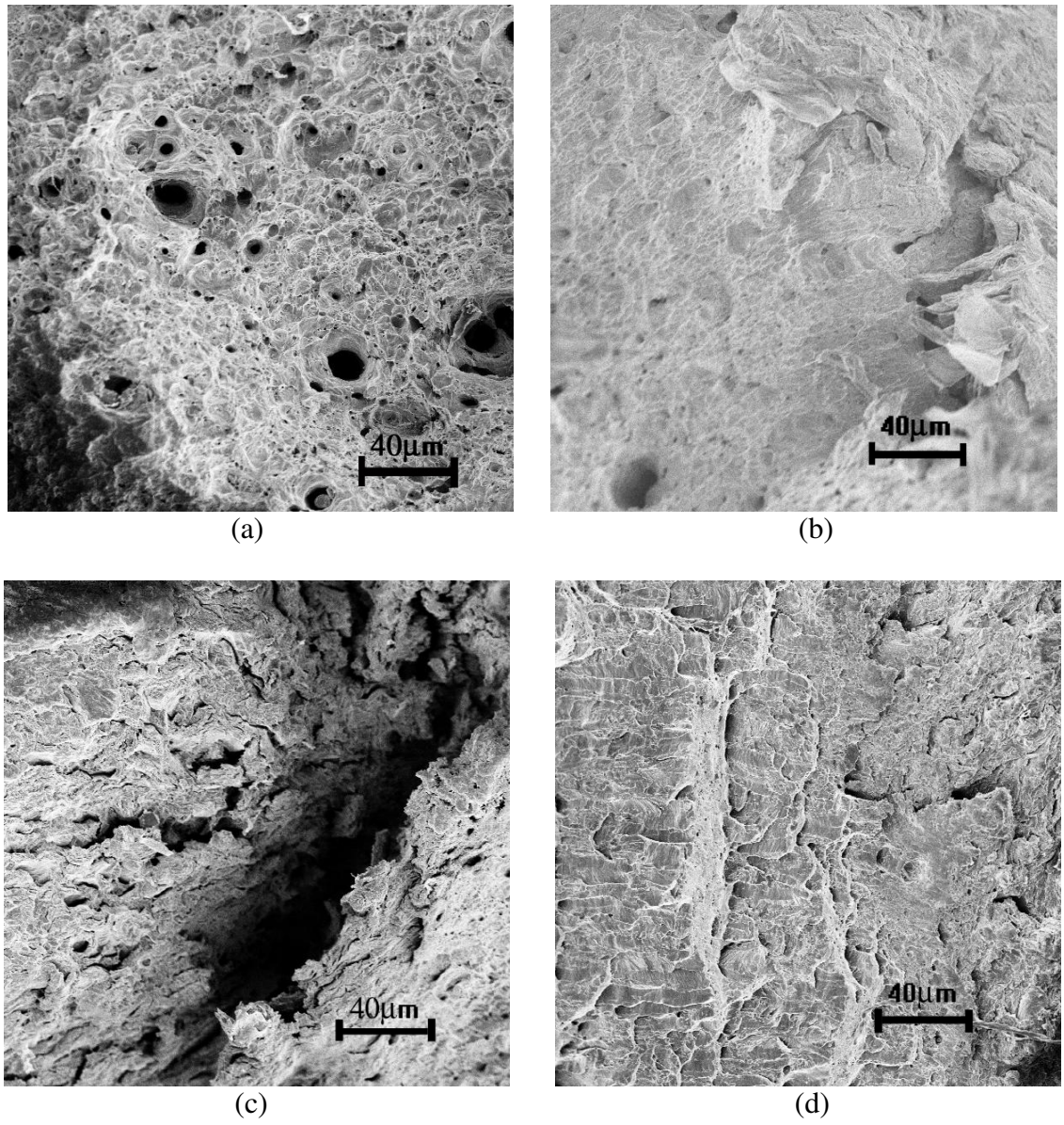

(a) (b)

(c) (d)

Figure 4-13. SEM images of fracture surface close to the edge in SFGE with different chloride concentration: (a) no NaCl; (b) 1mg/L NaCl; (c) 5mg/L NaCl; (d) 32mg/L NaCl

The water content in SFGE had a significant effect on crack initiation and the type of corrosion. Figure 4-14 shows the cross sections of tensile samples tested in SFGE with different amounts of water. The sample tested in SFGE with 2.5% water exhibited transgranular SCC as shown in Figure 4-14 (a). Although most of the cracks were typical SCC in this sample, some SCC had initiated from the corrosion pits at the surface. By increasing the water concentration to 5%, pitting corrosion became dominant and stress corrosion cracks were not visible. Figure 4-14 (b) shows the pit morphology on a SSRT sample tested in SFGE containing 5% water. Pit opening was typically smaller at the surface than the pit size under the surface, as shown in Figure 4-14 (b). This pit morphology indicates a strong autocatalytic process involved under the stagnant solution inside these pits.

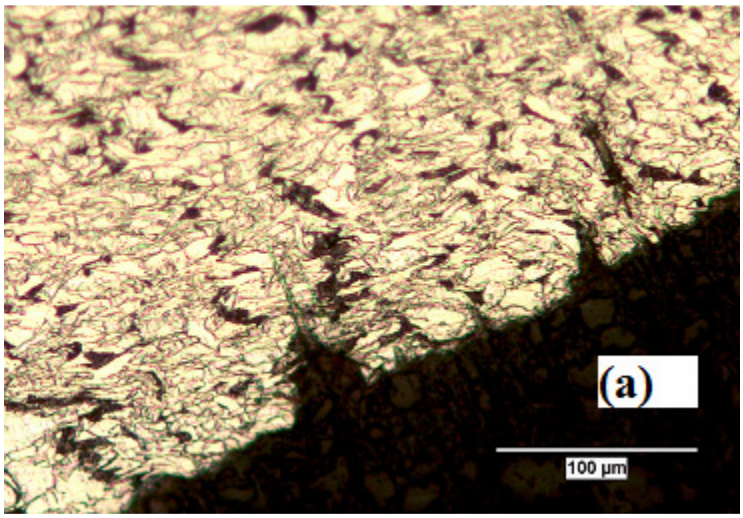

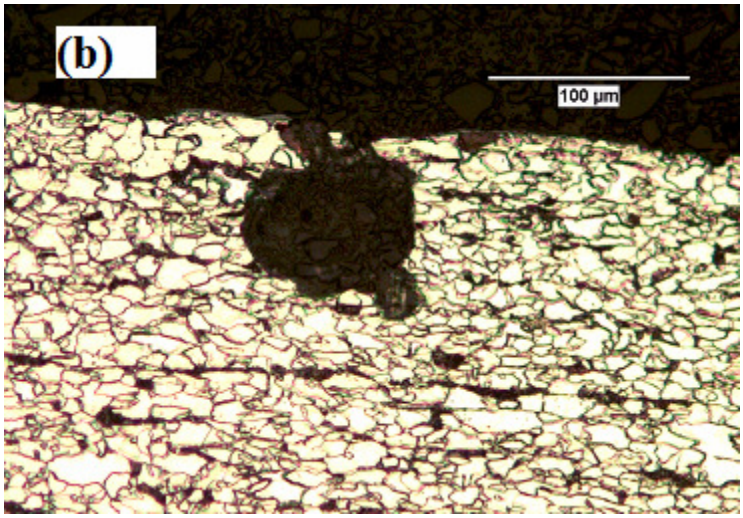

Figure 4-14. Optical images of cross section in SFGE with different water concentrations: (a) 2.5% water; (b) 5% water

SEM examination of the side surface of the tensile SSRT sample tested in 5% water SFGE indicated that the pitting tendency was different in the different parts of the sample. Figure 4-15 shows the surface attack on the tensile sample with respect to the distance away from the necked tip. It indicates that the formation of pits was predominant in the areas away from the necked region, where the damage of the passive film under heavy deformation may have led to general corrosion rather than localized corrosion attack. In the region of heavy plastic deformation closer to the fracture surface, (Figure 4-15 (a)) no corrosion pits were observed. As shown in Figure 4-15 (b) and (c), farther away from the fracture surface, local breakdown in the passive film was visible, as crazed cracks, and pit initiation became visible. In the region about 4mm or more away from the fracture surface, strong signs of pitting corrosion dominated the whole surface. Large pits were observed on the sample surface beyond this region. Previous work indicated that water can strongly affect the surface passivation of metal in ethanolic environment [36, 37, 43]. In SFGE with 5% water, such unique passivation behavior changed the failure

mode from SCC to pitting corrosion. At the region close to fracture surface, heavy deformation kept the metal surface active, which did not provide the right condition for the pit initiation.

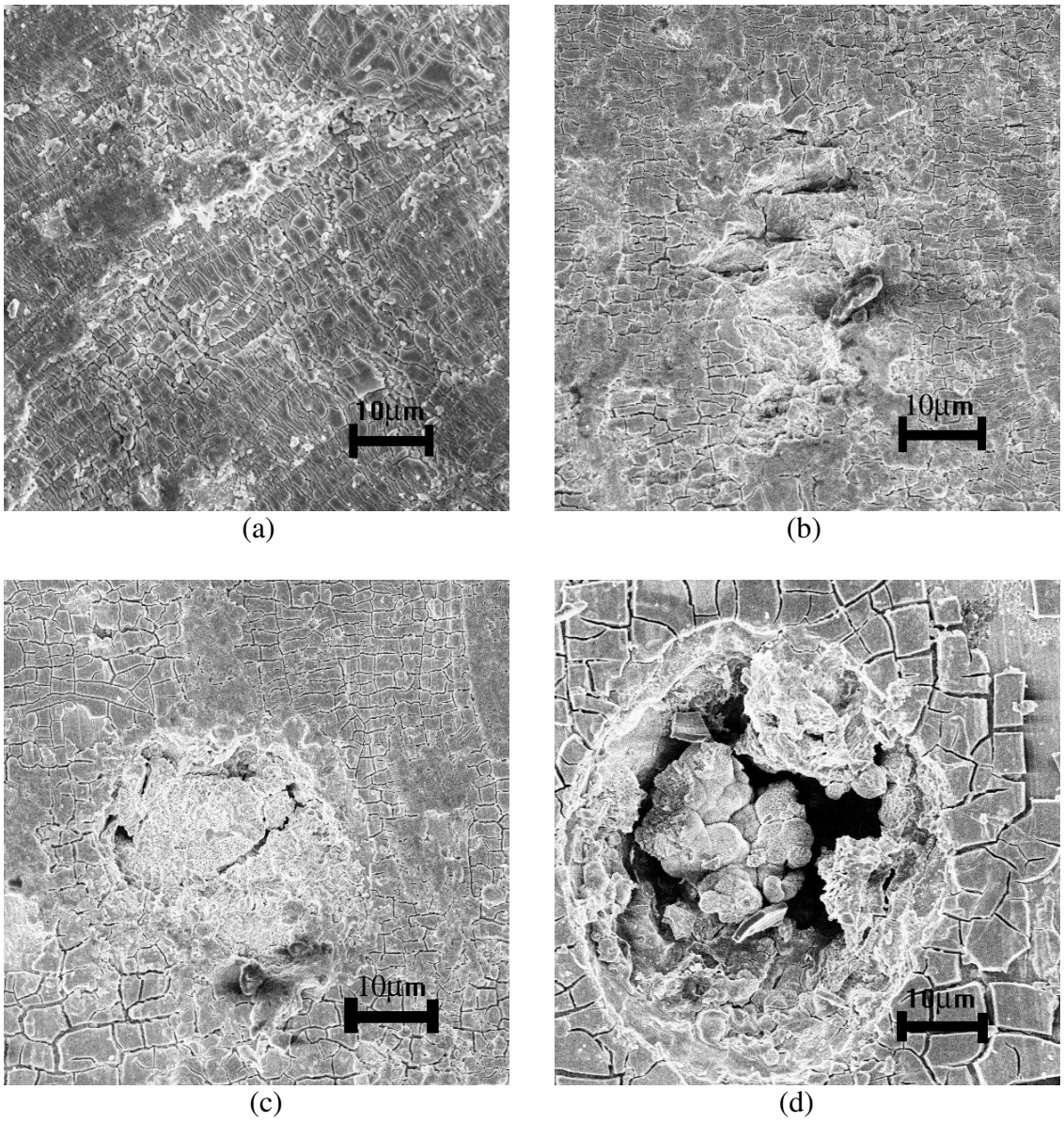

(a) (b)

(c) (d)

Figure 4-15. Surface morphologies on samples after SSRT in 5% water SFGE with various distances away from necking region: (a) 1mm; (b) 2mm; (c) 3mm; (d) 4mm

Removal of dissolved oxygen is considered effective in preventing SCC in fuel grade enthanolic environments. [3] To investigate this, deaerated tests were performed by

bubbling N_2 through the test solution. Figure 4-16 shows the SEM image of an X-65 carbon steel sample tested in deaerated SFGE. Similar to published results [3], the carbon steel sample did not show any signs of SCC in deaerated SFGE. However, SEM examination revealed a significant metal dissolution at the sample surface, as shown in Figure 4-16. EDS analysis of the corroded sample showed carbon rich phases at the surface, which was not observed on other carbon steel samples tested in the SFGE with dissolved oxygen. This suggests that the ferrite phase was selectively attacked under deaerated SFGE conditions, leaving the carbon-rich cementite at the surface.

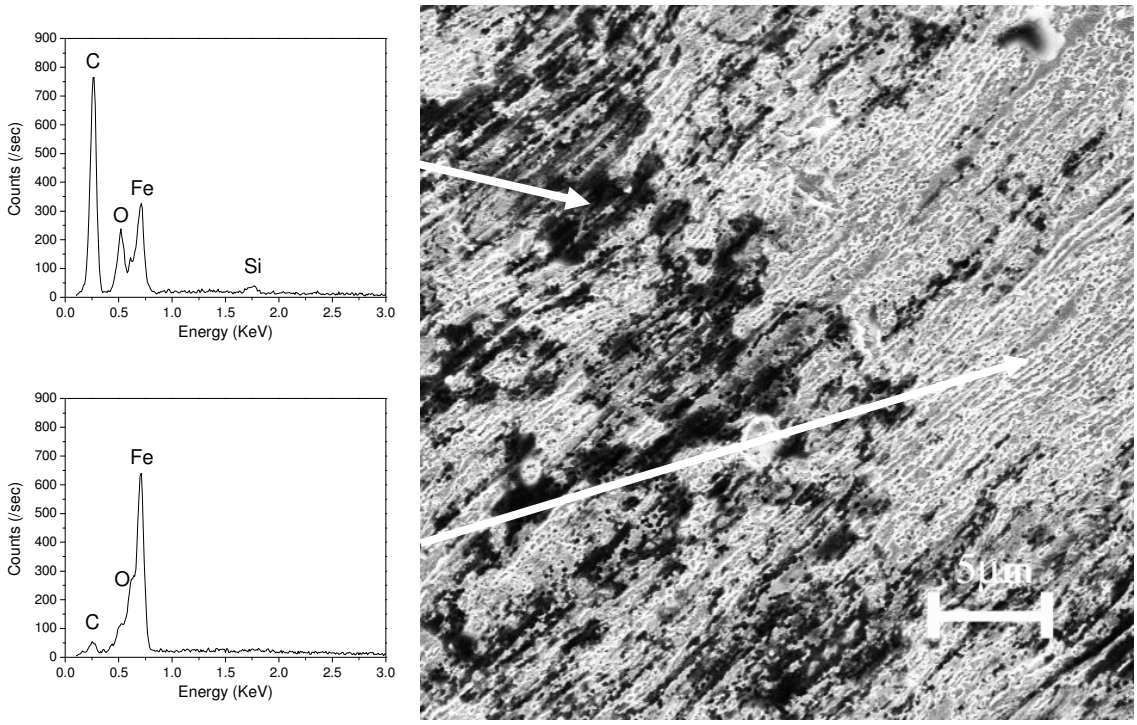

Figure 4-16. Surface morphology and EDS spectrums on the sample after SSRT in de-aerated SFGE

4.7 Relationship between SCC Susceptibility and Mechanical Parameters

Maximum tensile stress (σ_m) and strain to failure (ε_m) for the tensile samples tested in corrosive environments can usually be used to quantify their SCC susceptibility.

[9] Figure 4-17 shows the maximum stresses for SSRT samples tested in SFGE with different chloride concentrations and water concentrations. As shown in Figure 4-17(a) and (b), σ_m did not change vs. chloride or water in the SFGE. However, previous discussion showed that chlorides and water both strongly affected the SCC susceptibility. This suggests that the majority of stress corrosion crack propagation takes place after the maximum stress. Therefore, SCC of carbon steel in SFGE does not influence the maximum stress for the tested samples. Thus, high plastic deformation is one of the major factors which controls cracking in SFGE.

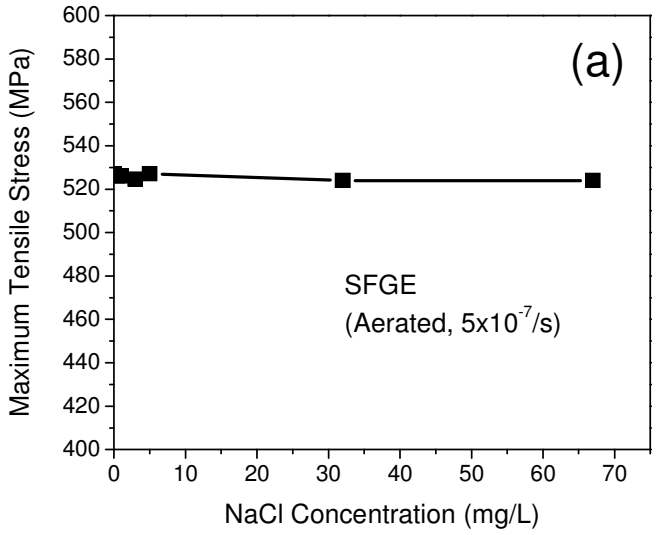

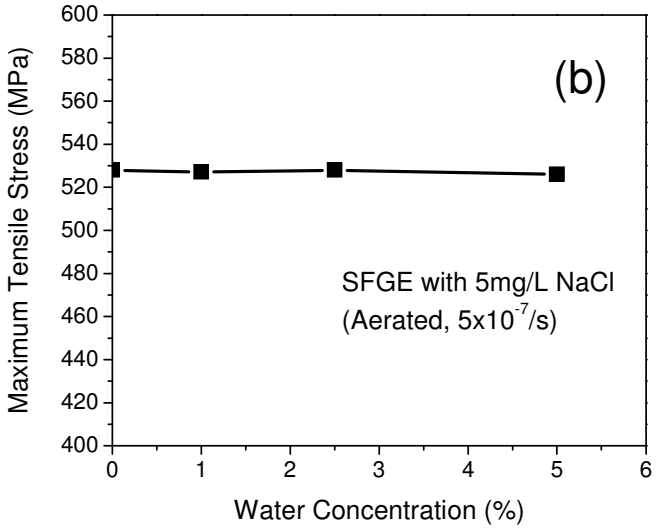

Figure 4-17. Maximum tensile strength with (a) chloride concentration; (b) water concentration

Figure 4-18 shows the relationships between the ratio of ε_m to ε_f vs. chloride and water concentration, where ε_m is the strain at the maximum stress, and ε_f is the fracture strain. Both figures show that the ratio of ε_m to ε_f increases with increasing SCC susceptibility, which indicates that the strain after the maximum stress dropped faster with an increase in the SCC susceptibility. These results suggest that the localized plastic deformation after maximum stress contributes more to the crack propagation and final failure of carbon steel in SFGE environment.

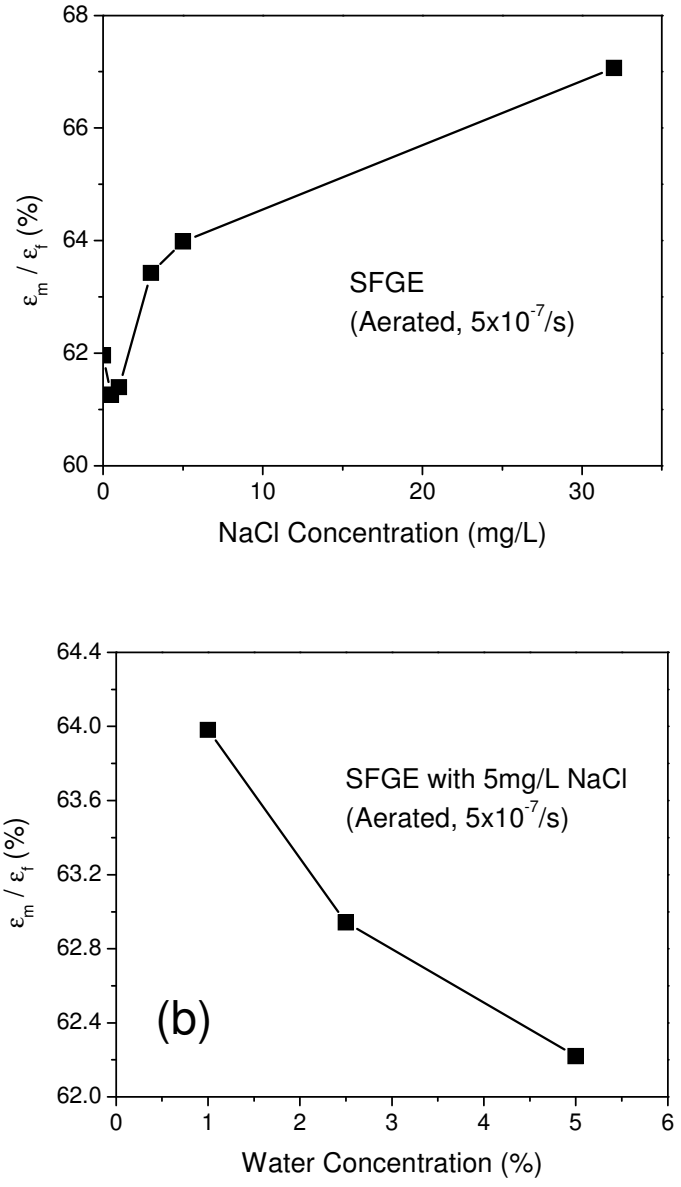

Figure 4-18. The relationship between $\varepsilon_m / \varepsilon_f$ and (a) chloride concentration; (b) water concentration in SFGE

4.8 Early SCC Due to Inclusions

Examination of carbon steel samples with SCC in SFGE environment indicated that some microstructural features facilitate crack initiation in this system. Figure 4-19

shows a crack initiating from an inclusion that caused early stress corrosion cracking in tested X-65 pipeline steel in SFGE. EDS analyses on the inclusion residue, associated with the early crack initiation sites, showed high concentrations of aluminum and silicon in these inclusions. Alumina and silicates are common inclusions in carbon steel, especially for aluminum killed or silicon killed steels. Based on the previous discussion, the local plastic deformation is a critical factor in the initiation of SCC in SFGE. Hard inclusions at the surface lead to local accumulation of stresses at the inclusion/steel interface, which may induce local plasticity and film damage, leading to SCC initiation. Figure 4-19 clearly shows localized slip bands and crack lines around the alumino-silicate inclusions. The electrochemical effect of Al-Si containing inclusions on crack initiation in SFGE is not clear.

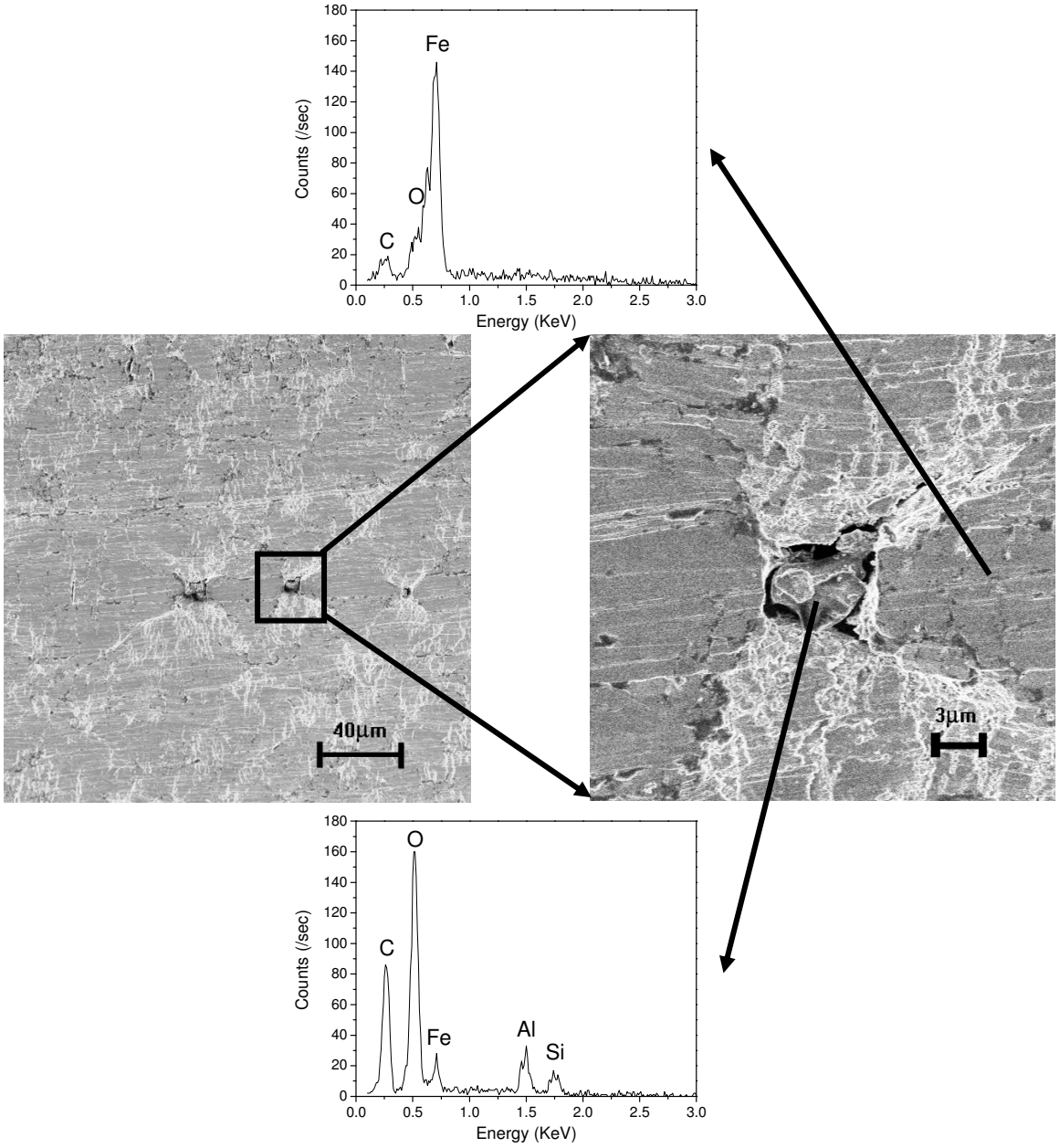

Figure 4-19. SEM images and EDS spectrums of inclusions causing SCC early initiation

4.9 Transition from Non-SCC to SCC in A Commercial Fuel-grade Ethanol

Tests in this work were mostly carried out in various SFGE environments, which used 200-proof ethanol along with other constituents listed in Table 3-3. To evaluate the

ethanol chemistry effect on a real fuel-grade ethanol system, the chemical composition of a commercial fuel-grade ethanol was modified to study their effects on SCC susceptibility of carbon steel. The results of pHe analysis in various FGE samples are shown in Table 4-1.

Table 4-1 Comparison of pHe in various FGE and SFGE

	pHe
200 proof ethanol	7.06
SFGE	5.37
FGE	7.65
FGE with 56mg/L acetic acid	6.8
FGE with 112mg/L acetic acid	6.6
FGE with 168mg/L acetic acid	6.3

Three different FGE samples were evaluated for this purpose: (1) as-received FGE; (2) FGE with 32mg/L NaCl; (3) FGE with 32mg/L NaCl and 16.8mg/L acetic acid. Figure 4-20 shows the SCC susceptibility of X-65 pipeline steel in these environments. The addition of chlorides and acetic acid transformed the commercial FGE from a non-SCC causing environment to a SCC causing environment. The addition of the acetic acid dramatically increased SCC susceptibility. Although the pHe change was only from 7.65 to 6.3, the crack density and velocity increased by ~5 times. Such a strong effect of pHe on SCC susceptibility is due to a lower stability of the surface film in acidified SFGE environment. The ability to change the SCC susceptibility in FGE by impurity

modification indicates that mitigation of SCC of carbon steel in the commercial FGE environments is feasible.

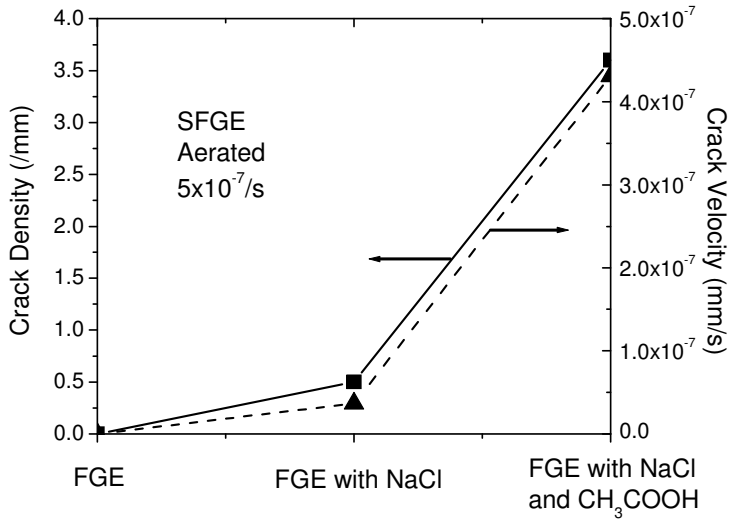

Figure 4-20. Crack density and velocity changes from modified commercial fuel-grade ethanol

4.10 Conclusions

Effects of ethanol chemistry in SFGE were studied using the slow strain rate test method. The conclusions include:

(1) SCC of carbon steel (X-65) in SFGE depends on the initial strain-rate within the tested range from 2E-6/s to 1E-7/s. Crack density increased with decreasing strain rate. Although the crack velocity decreased with a decrease in the strain rate, the crack length was higher at the lower strain rate.

(2) Environmental parameters like chloride, water content, pHe, and dissolved oxygen affect the SCC susceptibility of carbon steel in SFGE.

(2a) Chloride promotes both SCC initiation and growth.

(2b) A transition from SCC to pitting was observed with an increase in the water concentrations in SFGE. Sample tested in the SFGE with 2.5% water showed signs of pit initiated cracks whereas the sample tested in 5% water containing SFGE did not show any signs of SCC but had significant pitting attack at the surface.

(2c) Higher pHe inhibits SCC of carbon steel in SFGE.

(2d) Dissolved oxygen is an important factor in SCC in this system and lack of it can also stop the crack initiation. However, deaeration of SFGE can still lead to a similar amount of metal dissolution as observed in aerated SFGE. Selective dissolution of ferrite phase, leaving carbon-rich cementite at the surface, was observed in the deaerated environment.

(3) The mode of SCC for the carbon steel in SFGE was predominately transgranular under tested environments.

(4) Plastic deformation was found to influence both SCC and pitting corrosion. For SCC, high plastic deformation was needed for crack initiation especially in low chloride SFGE. In SFGE with high water content, pitting corrosion does not take place in the fast straining region. Relative low plastic deformation and a thick passive film were found to favor pit initiation.

(5) Maximum stress did not change with the compositional changes in the SFGE, whereas the ratio of ε_m to ε_f increased with increasing SCC susceptibility. Theses results indicate that the SCC propagates after the maximum stress during SSRT on smooth tensile samples.

(6) Aluminum and silicon containing inclusions in the X-65 carbon steel were found to promote early initiation of SCC in the SFGE environments.

(7) By modifying the chloride content and the pHe, a non-SCC causing commercial FGE could be transformed into a SCC causing FGE, and vice versa.

CHAPTER 5

CORROSION AND ELECTROCHEMISTRY OF CARBON STEEL IN SIMULATED FUEL-GRADE ETHANOL

It has been shown that the changes in ethanol chemistry in SFGE play critical roles in the stress corrosion cracking susceptibility of carbon steel and can lead to corrosion mode transition. Therefore, the investigations of electrochemical behavior and corrosion behavior of carbon steel in SFGE are important for understanding the detailed corrosion process, e.g. passivity and localized corrosion. In this chapter, electrochemical tests using modified electrochemical cell were carried out to understand the general corrosion behavior and corrosion related electrochemistry. Uniform corrosion, localized corrosion and surface corrosion product layer were characterized in order to understand the corrosion process under un-stressed condition.

5.1 IR Drop and Its Compensation in Low Ionic Conductivity Ethanolic Solutions

Measured solution resistivity values, for all ethanolic solutions tested in this study, are listed in Table 5-1. The measurements were carried out using Cole-Parmer resistivity meter model 19100-20. The results show that the tested SFGE solutions exhibit high solution resistivity. Therefore, IR drop in these solutions can be significant during electrochemical polarization tests [62].

Table 5-1. Solution resistivities for selected ethanolic solvents with varied ethanol chemistry of SFGE

(a) Changes in water content (ethanol, methanol, NaCl and acetic acid contents are fixed as shown in Table 3-3)

Water Content (vol%)	0	1	2.5	5	10	50	100
Solution Resistivity (KΩ-cm)	4.40	4.40	4.25	4.20	3.50	2.85	1.20

(b) Changes in acidity (ethanol, methanol, NaCl and water contents are fixed as shown in Table 3-3)

	56 mg/L Acetic Acid	Neutral	50 mg/L NaOH
Solution Resistivity (KΩ-cm)	4.40	4.40	3.80

(c) Changes in NaCl content (ethanol, methanol, water and acetic acid contents are fixed as shown in Table 3-3)

NaCl Content (mg/L)	0	1	5	10	32	160
Solution Resistivity (KΩ-cm)	100.00	80.00	25.00	12.85	4.40	0.82

The supporting electrolyte was not used in this study to avoid any possible effect on the corrosion activity of carbon steels and therefore on the measured OCP and polarization behavior [44]. With high IR drop in the solution, the difficulty of carrying out electrochemical measurement is raised due to two major problems: (1) the ohmic

drop between WE and RE increases the difference between the applied potential and the actual potential on the sample's surface, which has to be compensated; (2) the ohmic drop between WE and CE can affect the potential compensation and drive the compliance voltage beyond the voltage control capability of a potentiostat, especially at the high polarization potential. By adopting the cell geometry shown in Figure 3-3, both problems are mitigated for the tests in the potential range of interest by minimizing the WE/RE distance and the WE/CE distance. A platinum-mesh counter electrode surrounding the working electrode is necessary for this design to eliminate the non-uniform current distribution.

For this defined cell geometry, the solution resistance R between WE and RE can be estimated using a simplified expression, described as following:

$$R = \rho \frac{L}{A} \qquad (5\text{-}1)$$

where ρ is the solution resistivity, L is the distance between the working electrode and the reference electrode, and A is the working electrode's surface area. By knowing the solution resistivity (given in Table 5-1) and the cell geometry, the actual polarization potential of the working electrode can be calculated by subtracting the IR from the applied potential. With the interruption method [63], the automatic IR compensation offered by most modern potentiostats can also do IR correction during the test.

Using the baseline SFGE as an example (see Table 3-3 for composition), Figure 5-1 shows the potentiodynamic polarization of carbon steel with and without IR correction. Both manually-corrected and automatic IR compensations are shown for comparison. At the current density range below 10^{-5} A/cm^2, the ohmic drop does not affect the electrochemical measurement using the adopted cell geometry. However, at

higher polarization region where the current density is above 10^{-5} A/cm^2, IR drop starts to influence the polarization. IR drop increases as the polarization increases. The similarity between the automatic IR-compensated and the manually IR-corrected polarization curves indicate that both correction methods are effective within the tested polarization range. Since the local solution resistivity around the working electrode may change with time due to the anodic dissolution, the automatic IR compensation by the potentiostat is applied in all presented data in this study hereafter.

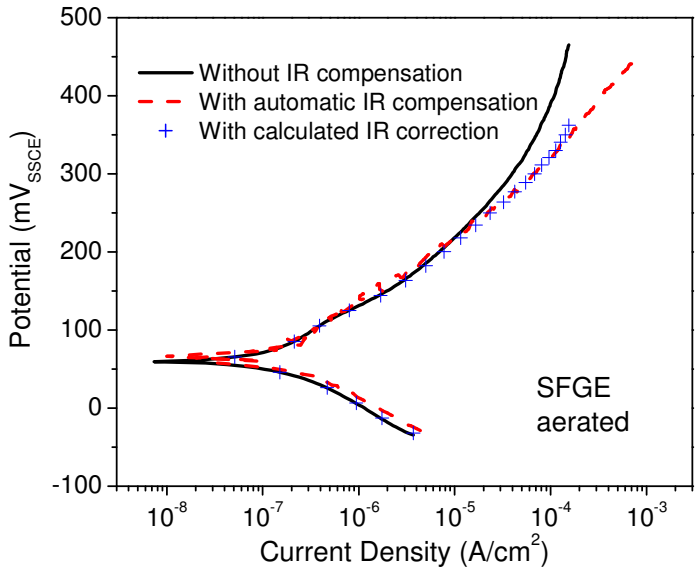

Figure 5-1. Effect of IR drop on potentiodynamic polarization curve in aerated SFGE with the electrochemical cell shown in Figure 3-3

5.2 Effect of Water on Corrosion Mode

Water can be introduced to FGE easily during manufacturing and transportation. Therefore, water is the most important factor which needs to be understood. Shown in Figure 5-2 are the average pit density and pit size as a function of water concentration in

SFGE after immersion for 8 days. With low water content (below 5 vol%), both pit density and pit size increase as the water concentration increases. No distinguishable pits are found on the carbon steel surface exposed to the SFGE with less than 1 vol% water. As the water content increases from 5 vol% to 10 vol%, the pit size increases dramatically, by 5 times, and the pit density reduces by 3 times. Optical microscopic images showed that the increase in the pit growth rate and pit coalescence at the surface, while the cathodic reaction region around the large pits further reduced the initiation of new pits, thus reducing the pit density. When the water concentration reaches 50 vol%, surface pitting behavior is eliminated although uniform corrosion is strong. Effect of water in non-aqueous solvents, such as methanol and ethanol, has been widely studied. Some researchers have concluded that the greater solubility of corrosion product and increase of the hydrated proton concentration in presence of water result in aggressive pitting corrosion [5, 36, 37]. However, contradictory data showed that the water acts as an inhibitor for iron in methanol [4]. Such complicated influence of water on pitting corrosion susceptibility of carbon steel in SFGE is mainly due to the solvation in ethanol/water mixture and the balance between the surface passivation reactions and the passivity breakdown in such system.

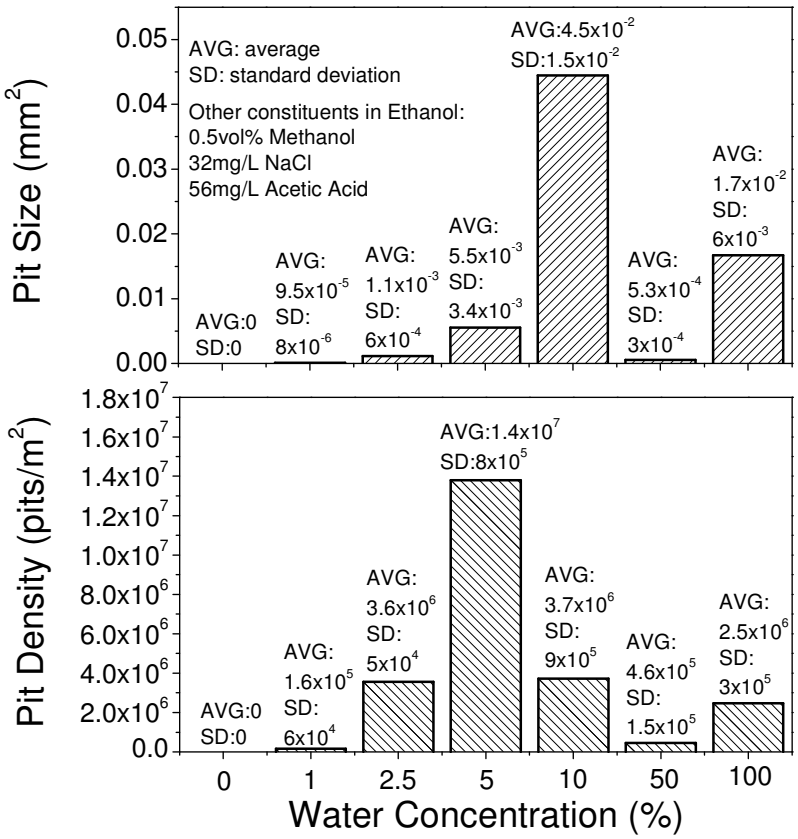

Figure 5-2. Effect of water on pit size and pit density in aerated SFGE after 8 days

Figure 5-3 shows the effect of water concentration in SFGE on weigh loss of carbon steel. It clearly shows that the weight loss increases due to multiple effects from the increase of the water content. Aqueous solution, without any ethanol, with the same amount of SFGE impurities, results in the highest metal loss, which is around $8.5x10^{-3}$ g/cm^2 after 8 days.

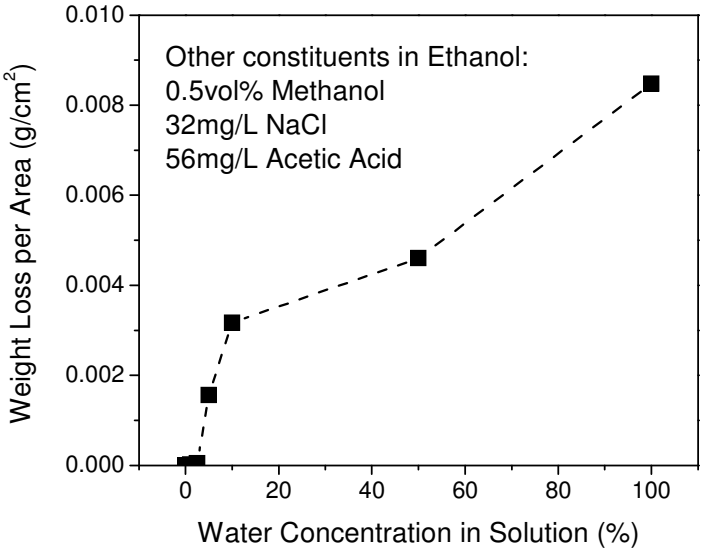

Figure 5-3. Effect of water on weight loss in aerated SFGE after 8 days' exposure

Changes in open circuit potential (OCP) with time for the carbon steel, as a function of water concentration in the SFGE, are shown in Figure 5-4(a). SFGEs with no water and 1 vol% water exhibit continuous increases in the OCP. These increases in the OCP can be explained as the growth of surface film, although such film may not be fully passive [5, 40]. As the water content increases, the OCP decreases. In SFGE with 2.5 vol% water, potential quickly levels and reaches equilibrium at around 50 mV_{SSCE}. Under these conditions, some areas on the metal surface generated small and isolated pits, while other areas remained passive. SFGE with 2.5 vol% water exhibits a competition between the film growth and breakdown. SFGE solutions with 5 vol% and 10 vol% water contents produce a fast decrease in the OCP of carbon steel, due to the fast pitting corrosion as well as the uniform corrosion. Although metal in the 5 vol% water-containing SFGE starts with a higher potential, it exhibits a much faster potential drop rate and reaches a

lower OCP after 900 minutes. Post characterization showed that the carbon steel sample tested in the SFGE with 5 vol% water exhibited the highest pit density. Therefore, the faster pit initiation rate may be the reason for the faster rate of the OCP decrease in the SFGE with 5 vol% water. As the water content increases to 50 vol%, the OCP of carbon steel increases with time. Characterization of steel surface showed a thicker surface film, and this corrosion product formed a protective layer to eliminate pit initiation. Although the OCP decreases slightly at the end, the final potential is still much higher than that in SFGE with 5 vol% or 10 vol% water. Minimum number of pits was recorded for the sample tested in SFGE with 50 vol% water, as shown in Figure 5-2. Duplicate OCP vs time measurements were carried out for all tested conditions presented in this paper to verify the reproducibility. General trend and the range of potential change with time were used to judge the reproducibility of OCP data under given conditions. Tests showed that the changes in the OCP with time were reproducible for all the tested ethanolic environments. As a typical example, Figure 5-4(b) presents the results from two identical tests in SFGE with 50 vol% water. It shows that the trend and the potential range for the two tests are almost the same under identical conditions, though a slight difference in the time scale can be observed from the duplicate tests. Changes in the OCP of carbon steel also indicate that the surface reaction and oxide film characteristics in ethanolic environment are altered by the addition of water, as reported in literature [37, 41]. Presence of water in ethanol also plays a role in changing the solvent structure and its physical properties, such as dielectric constant, oxygen content [64] and proton activity [37]. Shchukarev et al. [64] reported that the concentration of dissolved oxygen decreased as the water content increased in an ethanol-water mixture. Lou et al. [51] also observed

an increase of acidity as the water content increased in SFGE. A combination of all these effects due to the presence of water in ethanol leads to a significant change in reaction rates and overall corrosion and passivation mechanism.

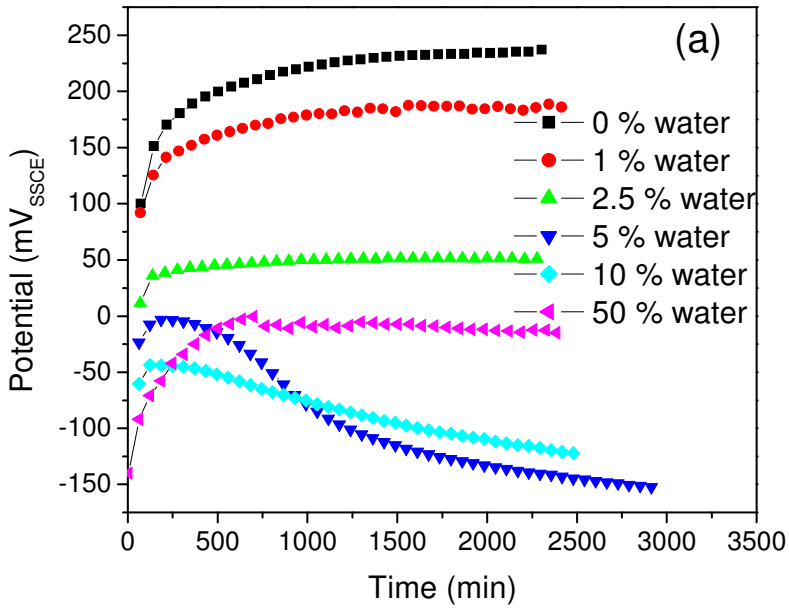

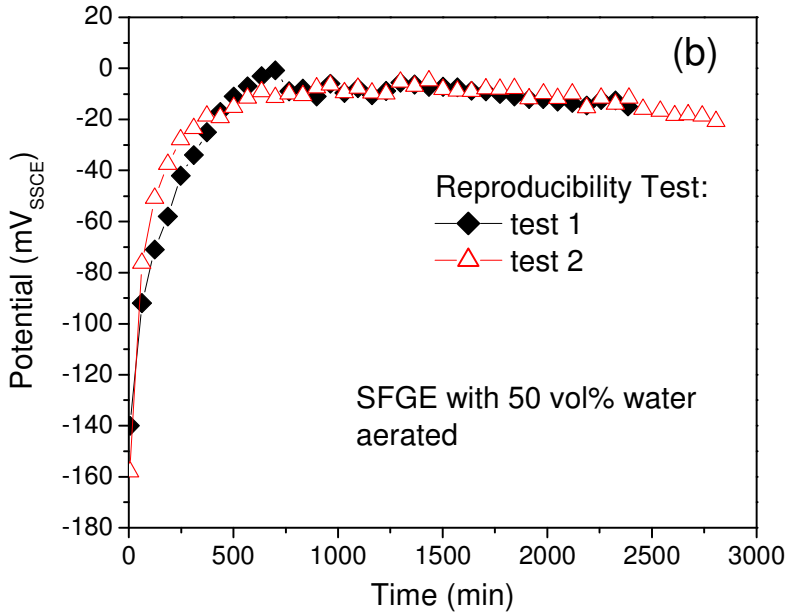

Figure 5-4. OCP evolution with time under various water concentrations in aerated SFGE: (a) effects of water concentrations; (b) example showing OCP test reproducibility. (other constituents: 0.5 vol% methanol, 32 mg/L NaCl, 56 mg/L acetic acid)

The results of cyclic potentiodynamic polarization in SFGE with different water concentrations are shown in Figure 5-5. Since the surface reactions for carbon steel change with the water content, polarization to a fixed potential in these environments may involve different chemical reactions. Therefore, for the cyclic polarization data shown in Figure 5-5, the carbon steel samples are anodically polarized with the same potential difference (150 mV_{SSCE}) from their initial OCPs, to simulate a similar effect of potential disturbance from equilibrium in all SFGE environments. Data in Figure 5-5 shows that carbon steel does not exhibit clear passivation behavior and pitting potential

with anodic polarization under a wide range of ethanol-to-water ratio, from pure ethanol solution to pure aqueous solution.

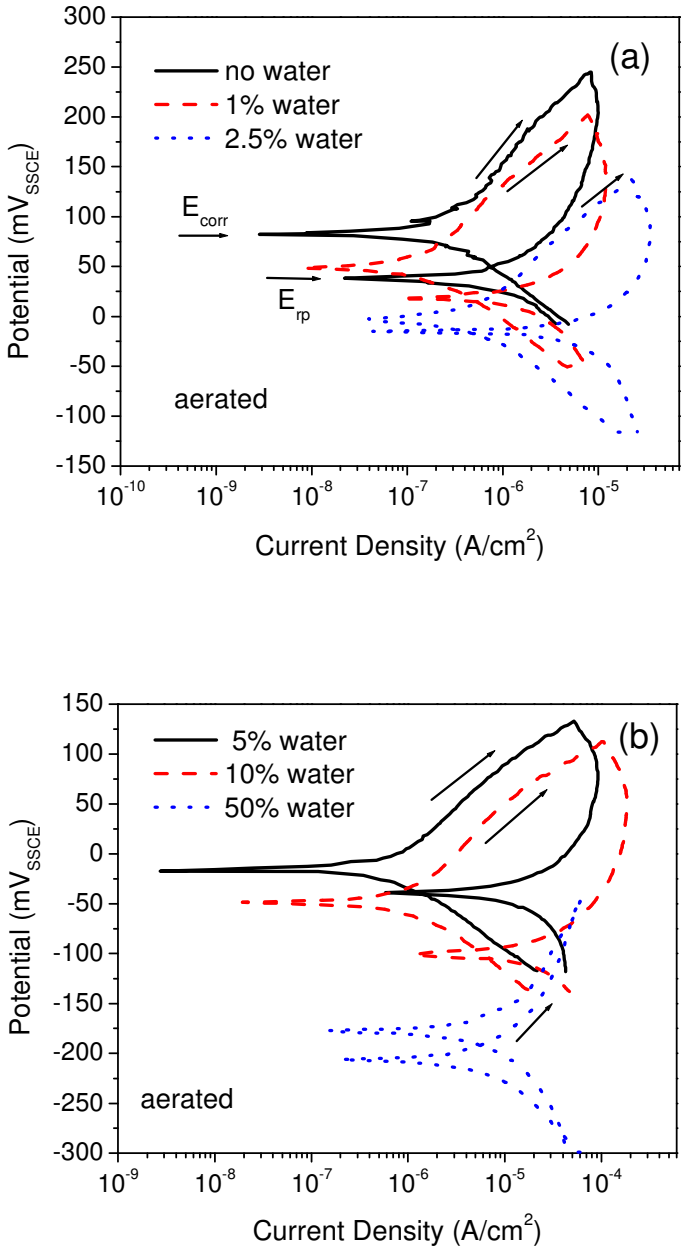

Figure 5-5. Cyclic potentiodynamic polarization in aerated SFGE with various water concentrations: (a) 0%, 1% and 2.5% water; (b) 5%, 10% and 50% water. (other constituents in ethanol: 0.5 vol% methanol, 32 mg/L NaCl, 56mg/L acetic acid)

Figure 5-6 summarizes the corrosion potential (E_{corr}), repassivation potential (E_{rp}) and estimated corrosion current density ($i_{corr\text{-}estimate}$) with different water contents. It should be noted that the E_{rp} is defined to be a potential during reverse scan where the current reaches zero, as shown in Figure 5-5(a). In this paper, all polarization tests were carried out at a scan rate of 2 mV/s to accommodate various corrosion kinetics and eliminate the effect of chloride leakage from the salt-bridge. Therefore, an estimated corrosion current density, $i_{corr\text{-}estimate}$, is reported especially for some environments with slow kinetics. The results show that under the testing condition, E_{corr} is always higher than E_{rp} when water content is below 10 vol%. In alcoholic solvent, metal usually exhibits a poor passivity [40]. These lower E_{rp} values are mostly due to the poor repassivation kinetics, which can lead to the localized corrosion or fast uniform corrosion. However, with 50 vol% water, E_{rp} is higher than E_{corr}, and no current hysteresis is shown by the reverse potential scan. Therefore, for the SFGE with 50 vol% water, localized corrosion should not be a major corrosion, which is also seen from the long-exposure test results shown in Figure 5-2. Water has been reported to have a corrosion-inhibiting effect in some non-aqueous system [37]. With low water content, the decrease in the difference between E_{corr} and E_{rp} suggests that very small amount of water can increase the repassivation behavior in FGE, although such increase may not result in a protective passive film. Estimated corrosion current density $i_{corr\text{-}estimate}$, measured from the polarization curves, increases due to the multiple effects from the water addition, which presents a trend similar to the weight loss data shown in Figure 5-3.

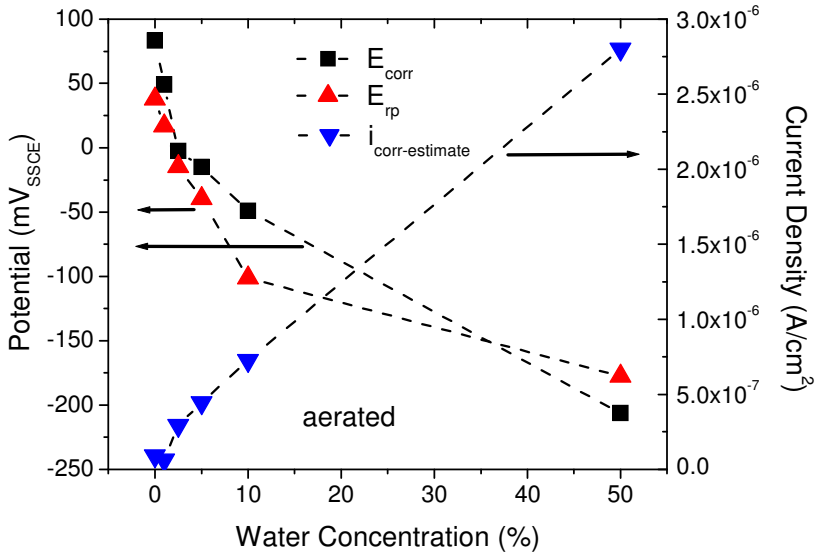

Figure 5-6. Effect of water on E_{corr}, E_{rp} and $i_{corr\text{-}estimate}$ in aerated SFGE. (other constituents in ethanol: 0.5 vol% methanol, 32 mg/L NaCl, 56mg/L acetic acid)

5.3 Effect of pHe

The effects of acidic, neutral and alkaline conditions under long-term exposure tests are shown in Figure 5-7. Both pit density and pit size decrease as the acidity decrease. Under alkaline conditions, no pits are present.

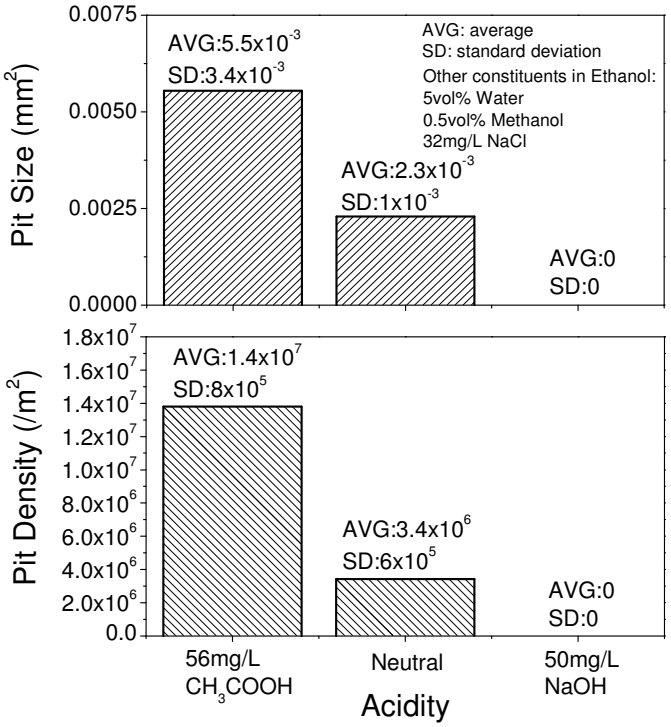

Figure 5-7. Effect of acidity on pit size and pit density in aerated SFGE with 5 vol% water for 8 days' exposure

Data in Figure 5-8 shows that the weight loss of carbon steel decreases with a decrease of acidity in the SFGE solution containing 5 vol% water. Alkaline environment inhibits the carbon steel from the general or localized corrosion behavior in SFGE environments. However, for all tested conditions, an increase in the water concentration increases the corrosion activity of carbon steel, primarily due to the increased proton activity, as shown in Figure 5-8.

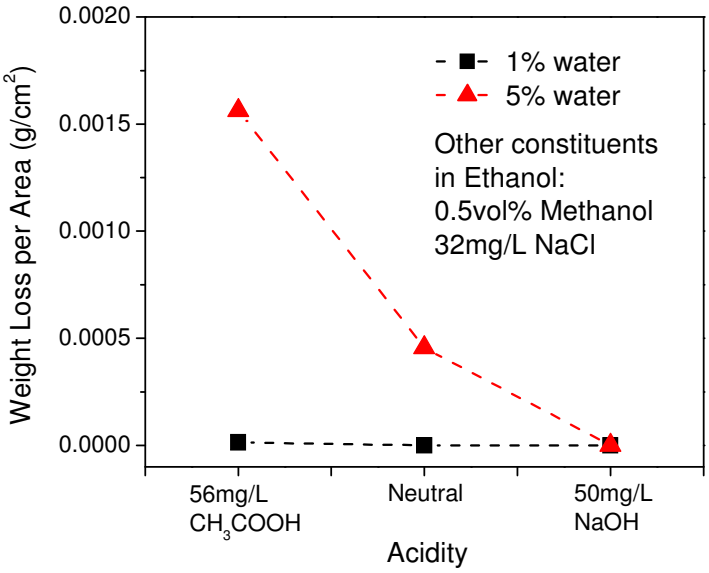

Figure 5-8. Effect of acidity on weight loss in aerated SFGE (1% and 5% water) for 8 days' exposure

Shown in Figure 5-9 are the evolutions of the OCP under various acidity conditions in SFGE containing 1 vol% water. OCP for carbon steel samples increase with time and finally reach equilibrium, which indicates that the surface film growth took place in all these tested conditions. However, the amount of potential increase in alkaline condition is much larger compared with the ones in neutral and acidic conditions, indicating that the alkaline condition generates better surface protective film or faster film growth kinetics on the carbon steel surface. It should be noted that the OCP decreases as the acidity decreases. Such a large drop on the OCP suggests a change in surface reaction from acidic SFGE to alkaline SFGE [3]. Also, the nature and kinetics of the cathodic reaction in SFGE could also be influenced by the acidity [37, 38]. For ethanolic system, thermodynamic stability diagram of iron has been reported by Sridhar et al.[3], showing

that the acidic ethanolic solution promotes iron oxide formation while the alkaline one promotes iron hydroxide formation.

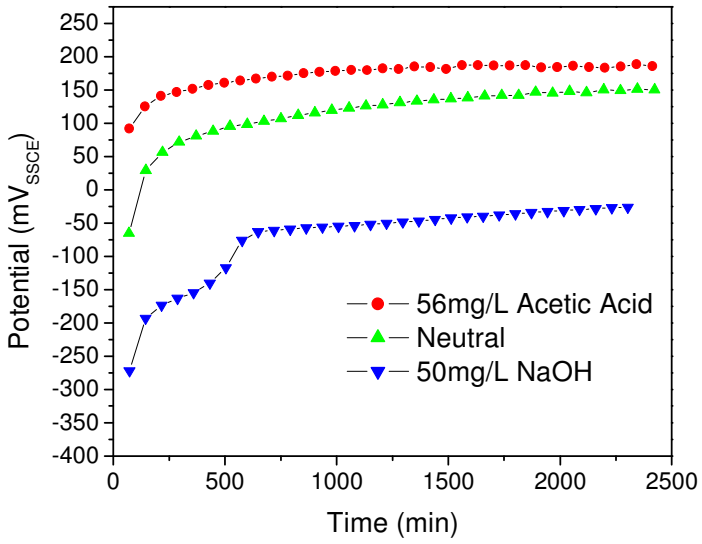

Figure 5-9. OCP evolution with time under various acidity of aerated SFGE (other constituents in ethanol: 1 vol% water, 0.5 vol% methanol, 32 mg/L NaCl)

Cyclic polarization behavior of carbon steel under the acidic, neutral and alkaline conditions are shown in Figure 5-10. Results show that the corrosion potential decreased as the acidity decreased, which was due to different reaction mechanisms. Acidified SFGE shows a different behavior upon potential reversal compared to both the neutral and alkaline SFGEs. The reverse loop produces a hysteresis loop in the acidified SFGE, suggesting slow repassivation kinetics.

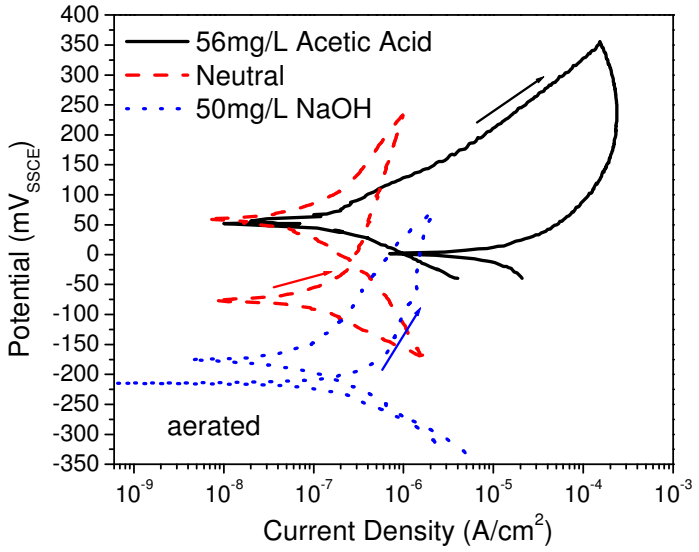

Figure 5-10. Cyclic potentiodynamic polarization in aerated SFGE with various acidity (other constituents in ethanol: 1 vol% water, 0.5 vol% methanol, 32 mg/L NaCl)

Figure 5-11 summarizes the effect of acidity on E_{corr}, E_{rp}, $i_{corr\text{-}estimate}$. E_{rp} exhibits lower values than E_{corr} in the acidified SFGE, while in the neutral and alkaline conditions, E_{rp} is higher than E_{corr}. Clearly, acidified SFGE destabilizes the surface film formation and decreases the film repassivation kinetics, which may lead to possible localized corrosion attack. Calculated $i_{corr\text{-}estimate}$ from the polarization curves also decreases as the acidity decreases, which is consistent with the decrease in weight loss shown in Figure 5-8.

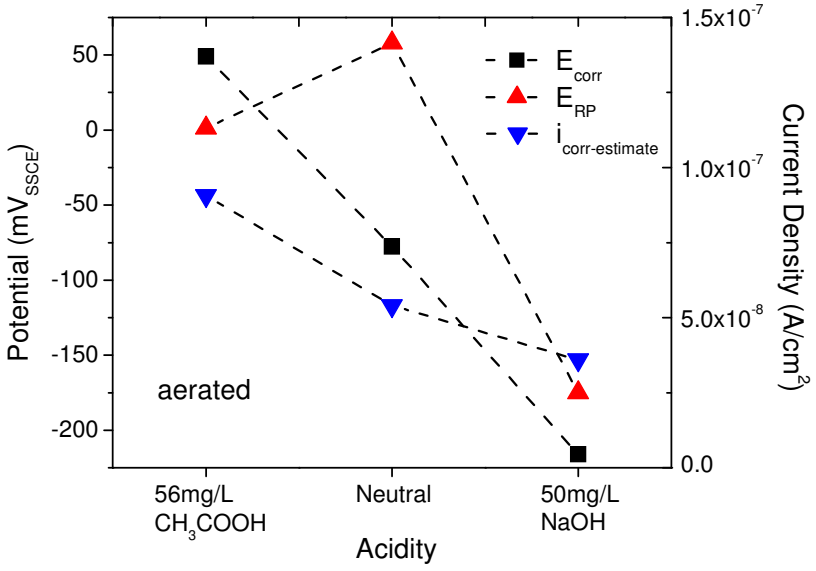

Figure 5-11. Effect of acidity on E_{corr}, E_{rp} and $i_{corr\text{-}estimate}$ in aerated SFGE (other constituents in ethanol: 1 vol% water, 0.5 vol% methanol, 32 mg/L NaCl)

In neutral and alkaline SFGE, the effects of water on polarization behavior in SFGE are shown in Figure 5-12. In both tested solutions, the increase in the water content of SFGE from 1 vol% to 5 vol% results in a decrease in the corrosion potential. Under the same extent of polarization, 300 mV_{SSCE} above their initial OCPs, the increase in the water content causes a breakdown of passivity in the neutral SFGE, resulting in a clear pitting potential at around 60 mV_{SSCE}. But the passivity of carbon steel in the alkaline SFGE remains protective as the water increases.

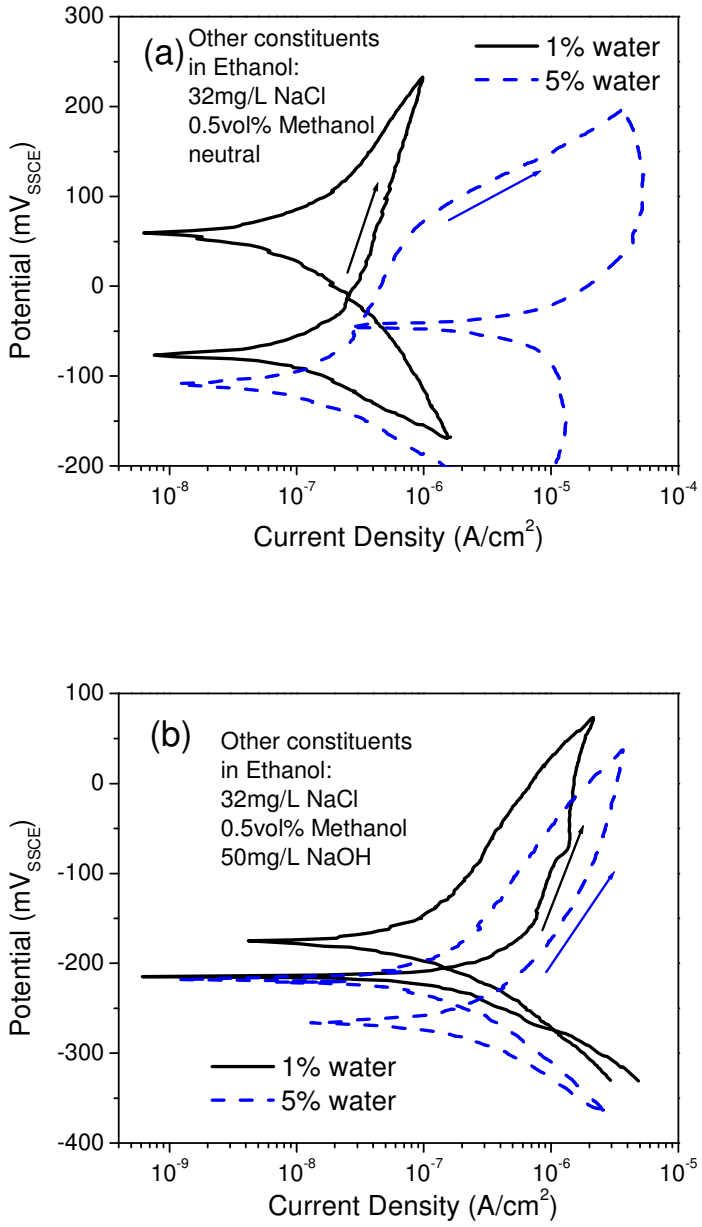

Figure 5-12. Effect of water on polarization behavior in aerated SFGE at neutral and alkaline conditions: (a) neutral; (b) 50mg/L NaOH

5.4 Effect of Chloride

Pit analysis after weight loss test, shown in Figure 5-13, indicates the pit size increases as the chloride concentration in SFGE increases. No pitting was observed on the sample tested in the SFGE without chlorides. However, the pit density decreases slightly at very high chloride concentrations (e.g. 160mg/L). Post-test characterization showed that such a decrease in the pit density is mostly due to the fast uniform corrosion and some pit growth coalescence.

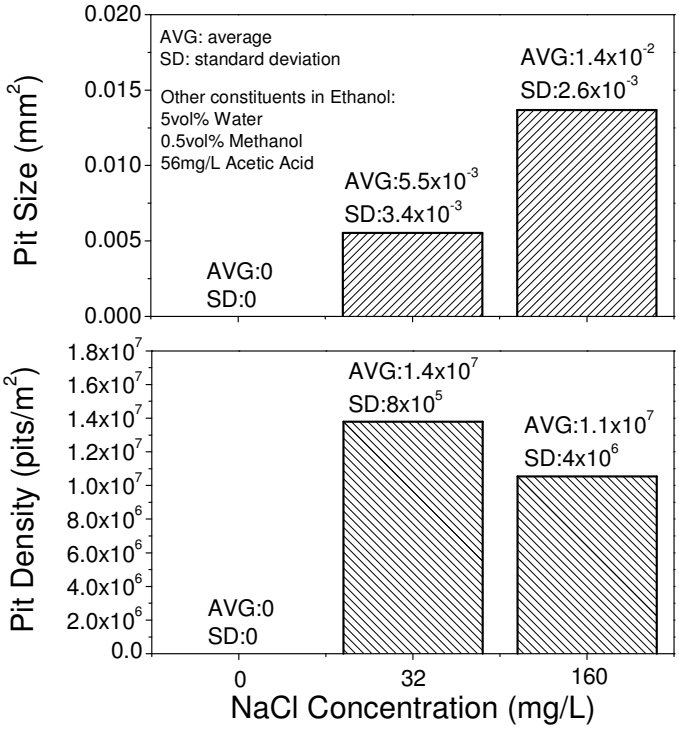

Figure 5-13. Effect of chloride on pit size and pit density in aerated SFGE with 5% water for 8 days' exposure

Figure 5-14 shows that the weight loss keeps increasing with the increase of chloride in 5 vol% water containing SFGEs. The observed metal loss is primarily due to

the increase of pitting corrosion. The sample tested in the SFGE with 1 vol% water exhibited negligible metal loss.

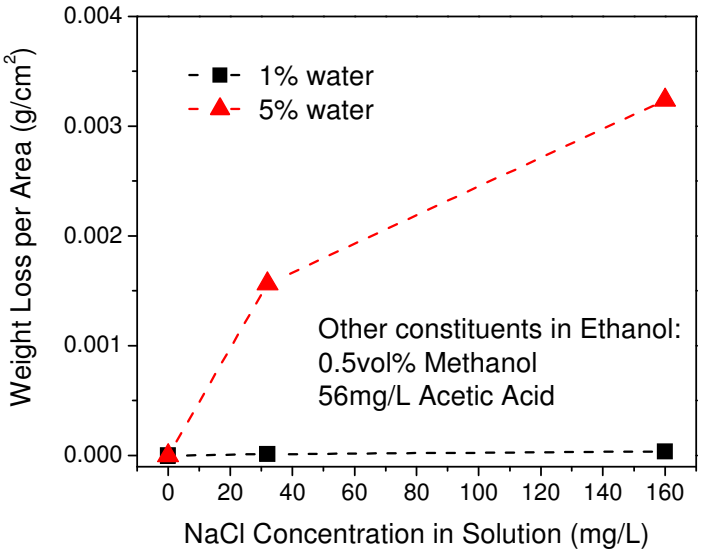

Figure 5-14. Effect of chloride on weight loss in aerated SFGE (1% and 5% water) for 8 days' exposure

Effects of chloride content on the cyclic polarization in SFGE are shown in Figure 5-15. Water and acetic acid concentrations were fixed at 1 vol% and 56 mg/L respectively. A potential difference of 300 mV_{SSCE} from initial OCP was chosen as a point for reverse-scan potential to compare the repassivation behavior under a similar extent of polarization for all environments. Without chloride addition, cyclic polarization curve does not show any hysteresis. The current density for the reverse potential scan is smaller than that for the forward scan, which suggests that the metal is not susceptible to the localized attack in this environment. Without chloride addition, the cyclic polarization signal shows oscillations due to a very low ionic strength. However, as the chloride

concentration increases, the reverse scan hysteresis appears and become stronger, indicating an increasing susceptibility to localized corrosion.

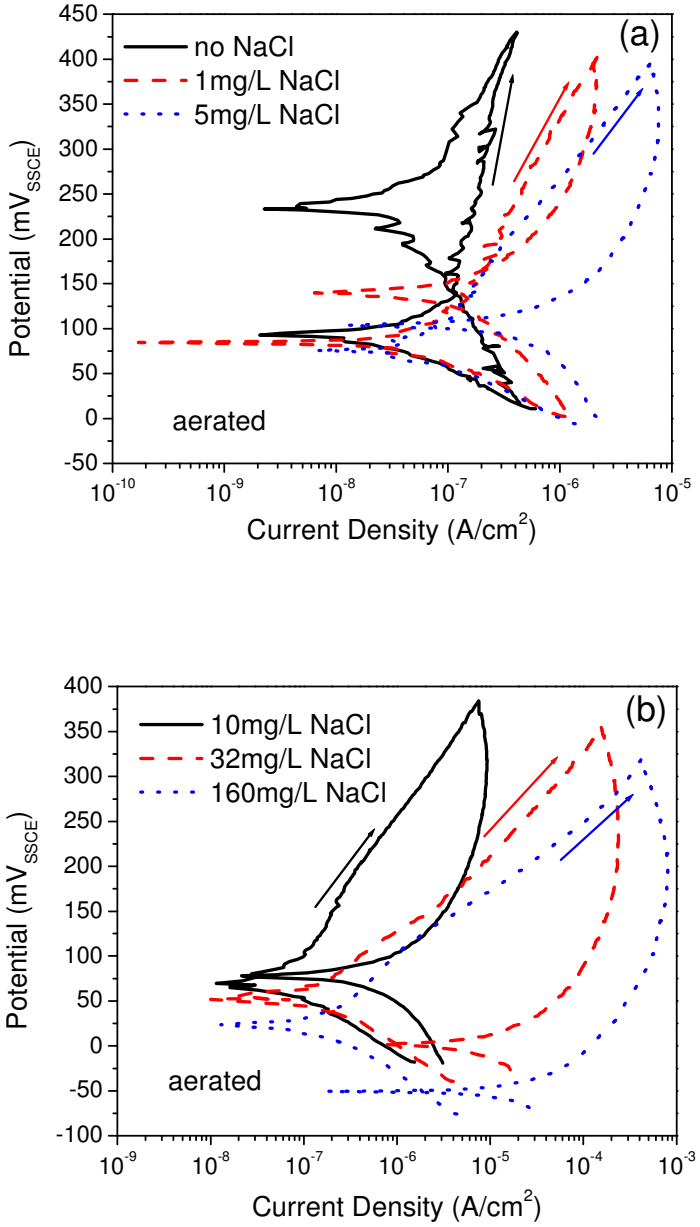

Figure 5-15. Cyclic potentiodynamic polarization in aerated SFGE with various chloride concentrations: (a) 0, 1 and 5 mg/L NaCl; (b) 10, 32 and 160 mg/L NaCl. (other constituents in ethanol: 1 vol% water, 0.5 vol% methanol, 56mg/L acetic acid)

Figure 5-16 summarizes the effects of chloride addition in SFGE on the E_{corr}, E_{rp}, and $i_{corr\text{-}estimate}$ for the carbon steel samples. Both E_{corr} and E_{rp} decreases with an increase in the chloride concentration. Since the surface reaction should not change with the same water and acidity conditions, such the decrease in the E_{corr} and E_{rp} suggests an increase in the corrosion activity. This is also supported by the increase in $i_{corr\text{-}estimate}$ shown in Figure 5-16. In SFGE with lower chloride concentration, the E_{rp} is higher than E_{corr}. However, after the NaCl concentration in SFGE reaches ~18 mg/L, E_{rp} exhibits lower values than E_{corr}. These results suggest an increased pitting susceptibility beyond a threshold chloride concentration in a given SFGE environment.

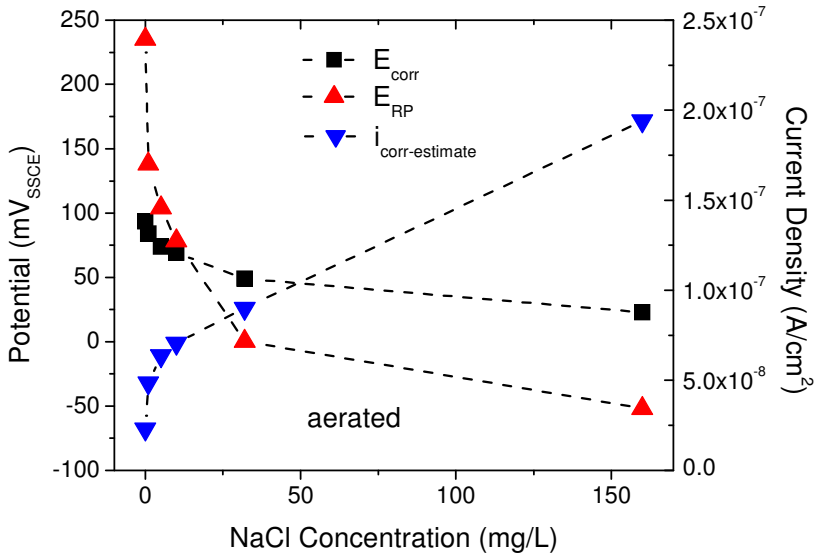

Figure 5-16. Effect of chloride on E_{corr}, E_{rp} and $i_{corr\text{-}estimate}$ in aerated SFGE. (other constituents in ethanol: 1 vol% water, 0.5 vol% methanol, 56mg/L acetic acid)

5.5 Effect of Dissolved Oxygen

The role of oxygen on stress corrosion cracking behavior of carbon steel in FGE has been widely documented in literatures [3, 51]. Shown in Figure 5-17 are the surface morphologies of samples tested in SFGE with 5 vol% water. Severe pitting corrosion and uniform corrosion are present on the sample surface under dry air bubbling, as shown in Figure 5-17(a). Pit density under these conditions is 1.38×10^{7} /m^2 and the pit size is 5.5×10^{-3} mm^2. In comparison, under de-aeration with dry N_2 bubbling through the solution, susceptibilities towards pitting and uniform corrosions are significantly reduced, as shown in Figure 5-17(b). Surface appears clean, except that some pit initiation sites are present along with light coloured cathodic reaction areas. Pit density and size are reduced to 2.64×10^{6} /m^2 and 1.1×10^{-4} mm^2.

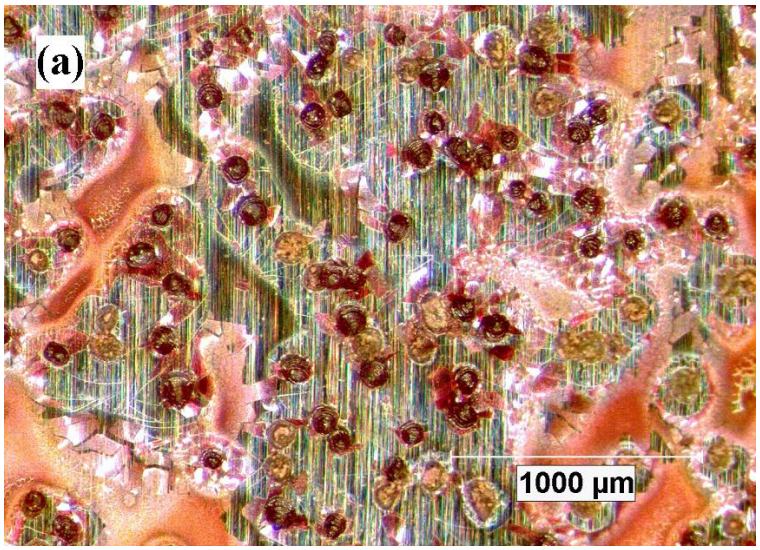

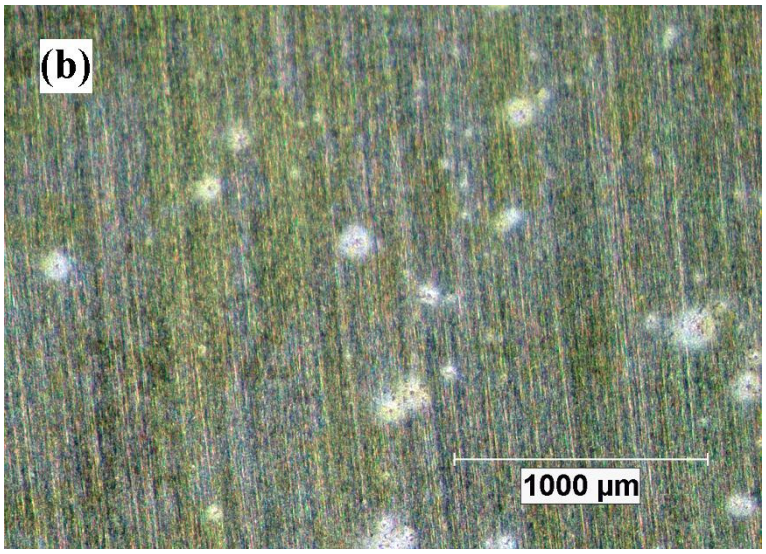

Figure 5-17. Optical micrographs of sample surfaces after 8-day exposure tests in SFGE with 5% water: (a) aerated; (b) de-aerated

However, in SFGE with 1 vol% water, no corrosion activity was observed on both aerated and de-aerated specimens after long-term exposure test, though the specimen in aerated condition shows thicker oxide layer on the surface than the de-aerated one. In order to further understand the role of oxygen, the potentiodynamic polarization with very slow potential scan rate was carried out on the carbon steel in various oxygen concentrations, as shown in Figure 5-18(a). The slow scan rate of 0.02 mV/s allows the slow surface film formation to participate into the electrochemical response. OCP is significantly reduced by the decrease in the dissolved oxygen concentration in the solution. Such a decrease in OCP is mainly because the cathodic reaction in alcoholic environment strongly depends on the degree of aeration [37]. Surprisingly, the anodic current dramatically increases as the oxygen level decreases. Such a phenomenon suggests that oxygen plays an important role in promoting surface film formation on

carbon steel in SFGE. Without oxygen, the poor passivity leads to a fast dissolution from base metal.

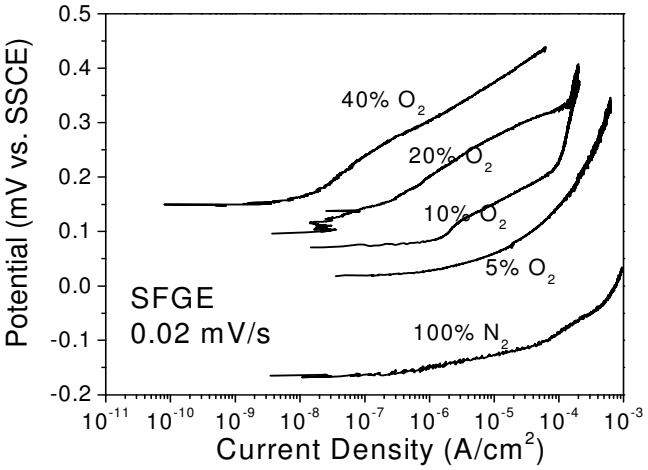

(a) Potentiodynamic polarization under various dissolved oxygen level

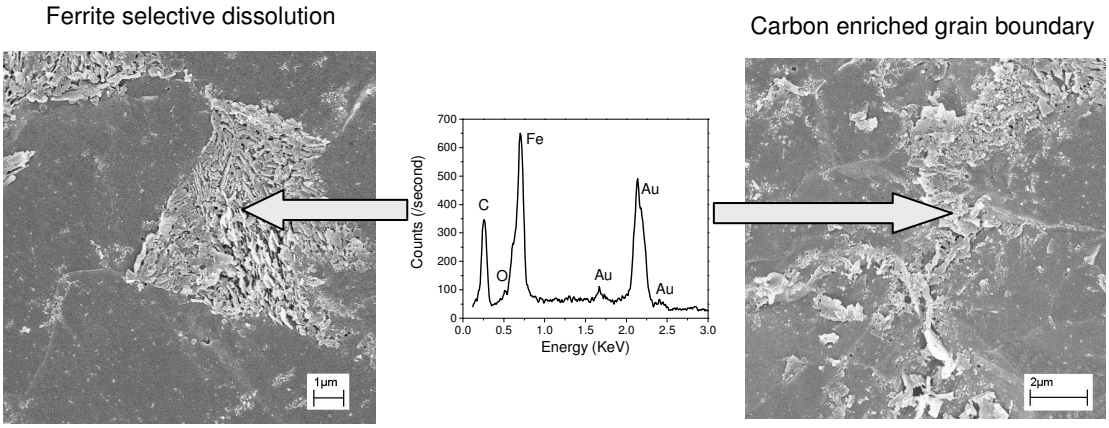

(b) SEM image and EDS spectrum on the carbon steel polarized at -50 mV vs Ref. in de-aerated SFGE

Figure 5-18. Electrochemistry and fast dissolution of carbon steel in de-aerated SFGE

The surface morphology and EDS chemical analysis from the sample in de-aerated SFGE polarized at -50 mV vs Ref. are shown in Figure 5-18(b). It is clearly that

ferrite is dissolved from the matrix which leaves cementite present on the surface. Fast dissolution of ferrite takes place in SFGE under de-aerated condition. On the right, carbide-rich grain boundary is also visible due to the fast dissolution. These grain boundaries may be possibly susceptible to some intergranular attacks in some low aeration environment.

5.6 Empirical Relationship of Chloride Concentration and Corrosion in SFGE

Results from this study, Figures. 5-6, 5-11 and 5-16, have clearly shown that the corrosion and repassivation potentials strongly depend on water, acidity, and chloride in SFGE. Solvent structure (water-to-ethanol ratio) and acidity not only change the reaction kinetics, but also influence the reaction mechanisms. The change in NaCl concentrations does not alter the surface reaction under the same potential. Therefore, in addition to Figure 5-15, polarization tests were also carried out with a fixed potential scan from -50 mV_{SSCE} to 400 mV_{SSCE} for all tested chloride environments. Empirical equations of E_{corr} and E_{rp} for fixed potential scans were developed using a linear regression method, as shown in Figure 5-19. The equations for the SFGE composition (1 vol% water, 56mg/L acetic acid, and 0.5 vol% methanol) under aerated condition are shown as following:

$$E_{corr} = -29.398 \cdot \mathrm{Log}[Cl^-] - 49.122 \qquad (5\text{-}2)$$

$$E_{rp} = -76.74 \cdot \mathrm{Log}[Cl^-] - 219.09 \qquad (5\text{-}3)$$

where, E_{corr} and E_{rp} have a unit of mV_{SSCE}, and $[Cl^-]$ has a unit of molar (M). R-square values for Equations. 5-2 and 3 are 0.983 and 0.974, respectively.

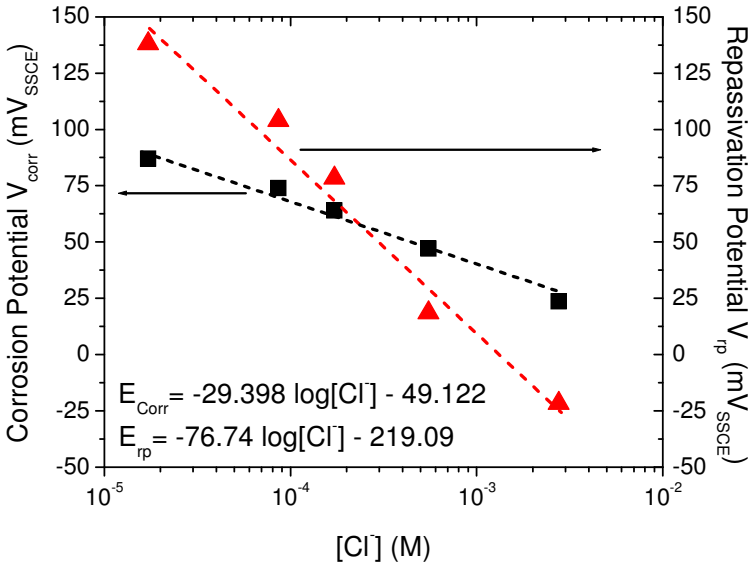

Figure 5-19. Data and empirical equations for E_{corr} and E_{rp} as a function of chloride molar concentration in aerated SFGE. (other constituents in ethanol: 1 vol% water, 0.5 vol% methanol, 56mg/L acetic acid)

5.7 Pits Morphology

Scanning electron micrographs in Figure 20 (a-c) show typical pit morphologies for carbon steel exposed to SFGE with various water concentrations. Pit size and pit depth increase as the water content increase. Pit depth was characterized from polished cross-sections of the tested samples. The polished cross-section confirms pit exhibits a wide and shallow morphology. Corrosion products are deposited inside the pits due to their low solubility in ethanol. EDS analysis of the deposits, shown in Figure 5-20(d), reveals that the corrosion products inside corrosion pits are mostly iron oxide and iron chloride. In some pits, aluminium and silicon peaks are also present, which are associated with the alumina and silicates inclusions in carbon steel, especially for aluminium killed

or silicon killed steels [51]. These inclusions may serve as preferential sites for pit initiation in these steels. The electrochemical effects of Al-Si containing inclusions are not clear at this stage.

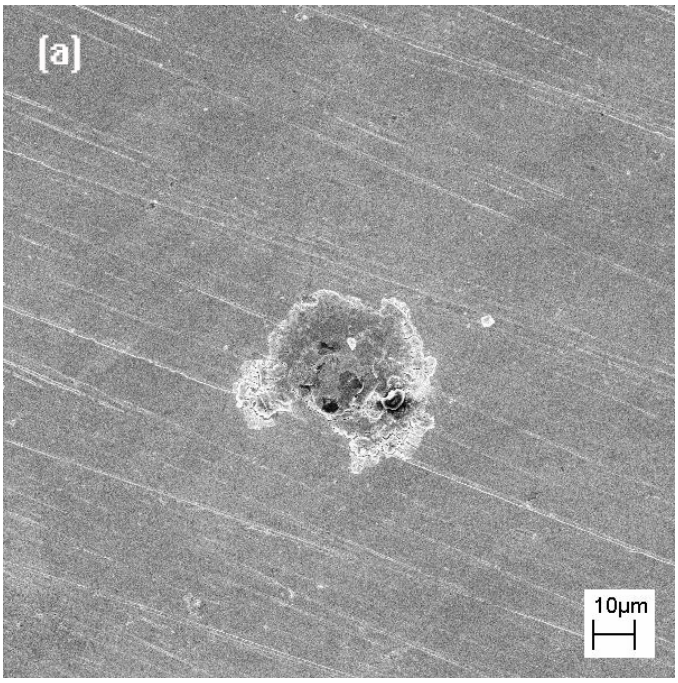

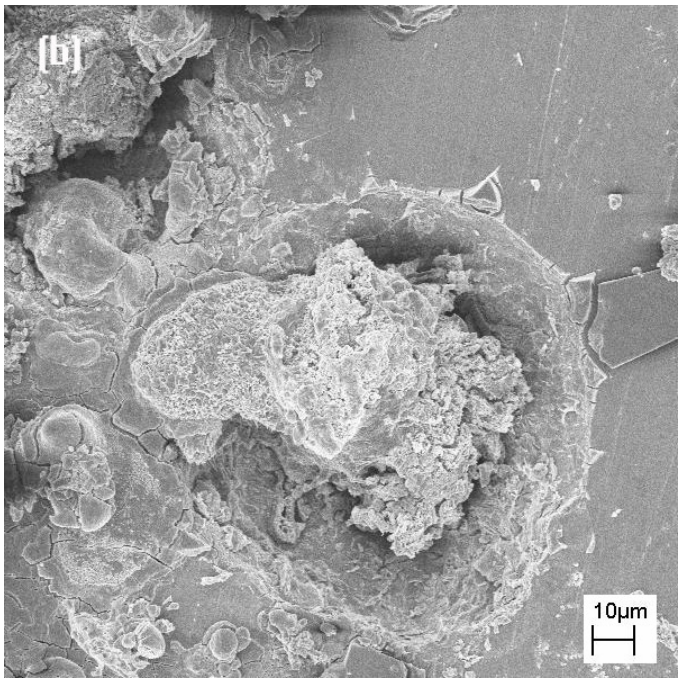

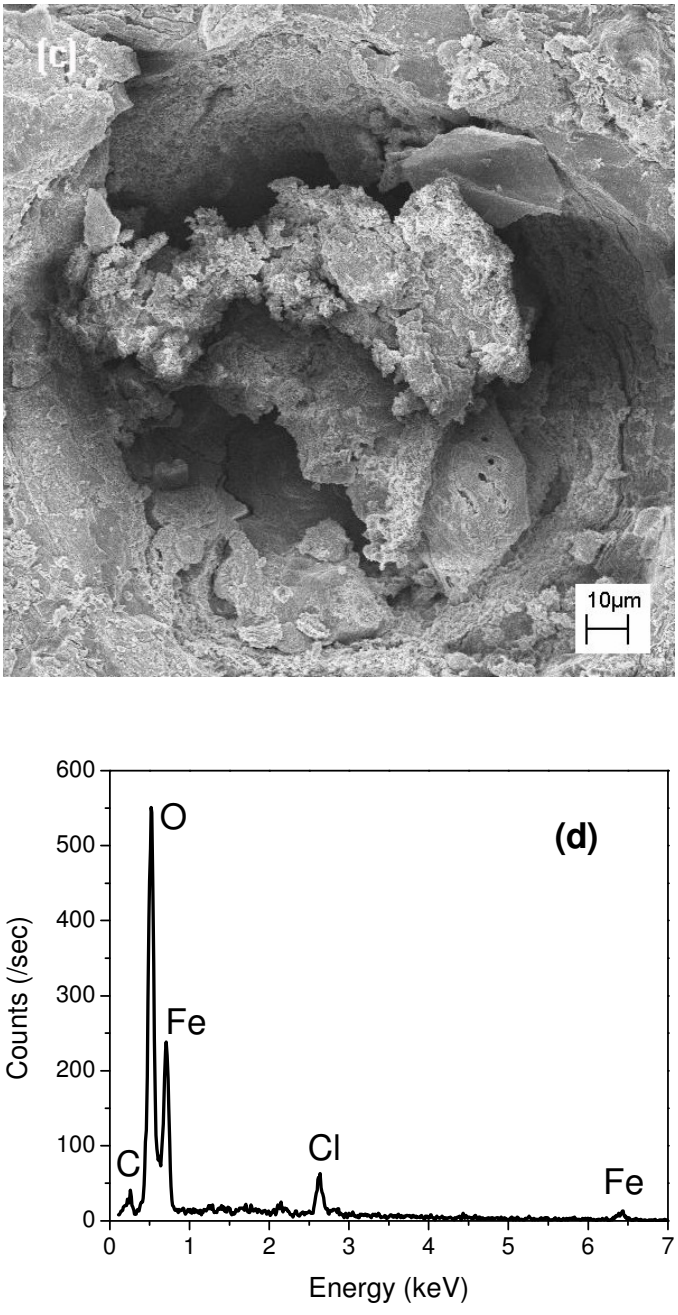

Figure 5-20. Pit morphologies and chemical compositions: (a) 2.5% water (SEM image); (b) 5% water (SEM image); (c) 10% water (SEM image); (d) typical EDS spectrum inside a pit

5.8 Corrosion Products

Surface film formed at the carbon steel surface, in SFGE with various water concentrations, was characterized using X-ray diffraction method. XRD results, in Figure 5-21, show that when the water concentration is below 10 vol% (Figure 5-21(a)), the major corrosion product phase is hematite (Fe_2O_3). XRD spectrum curve-fitting confirms its R-3c space group. Optically, the corrosion products exhibited very thin reddish layers on the top of the metal surface. Therefore, the substrate iron peaks also appear in the spectra in Figure 5-21(a). The short and broad peak shape of hematite may be due to the very thin film at the surface. It may also be due to the partially amorphous nature of this film formed in low-water ethanolic solution, which was also reported elsewhere [5].

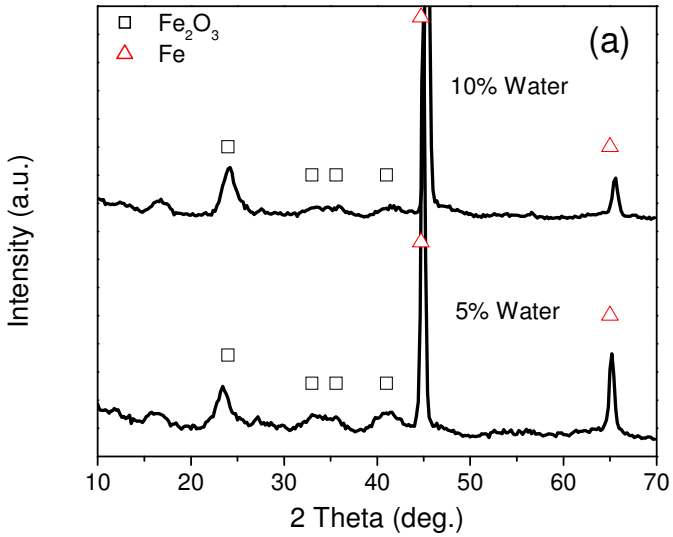

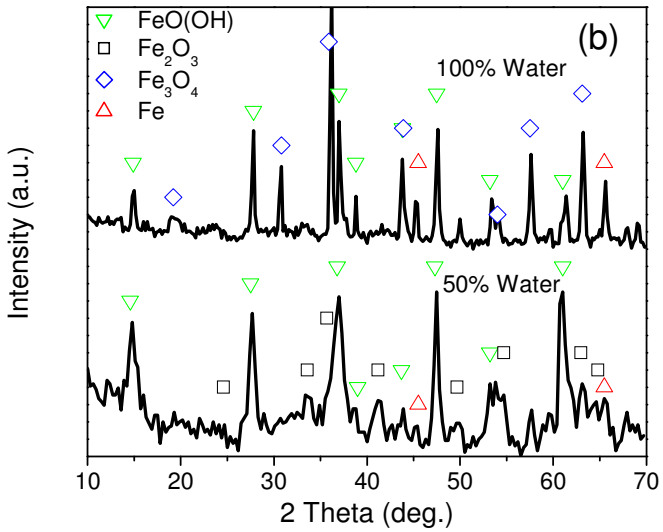

Figure 5-21. XRD spectra from surface corrosion products on X-65 carbon steel in aerated SFGE with various water concentrations: (a) 5% and 10% water; (b) 50% and 100% water

As the water concentration reaches 50 vol% (Figure 5-21(b)), lepidocrocite (FeO(OH)), with a space group of Cmcm, becomes a dominant phase in its corrosion products. The presence of water in SFGE promotes the formation of iron hydroxide. Hematite also forms under this condition, although its peak intensity is significantly reduced. A much thicker corrosion layer also weakens the XRD peak from iron substrate. For comparison, an aqueous solution (100 vol% water) with similar impurities (32mg/L NaCl and 56 mg/L acetic acid) was also used for the corrosion product study. Similar to other studies in drinking water system [65], the magnetite (Fe_3O_4) and lepidocrocite (FeO(OH)) are two major corrosion products formed in water with impurities.

A duplex-layer corrosion film structure can be found in ethanol-water mixed SFGE, as shown in Figure 5-22. Outer layer consists of both lepidocrocite and hematite. Outer

layer has a weak mechanical bonding to the substrate and can be easily removed by a water jet. After mechanically removing the outer layer products, XRD spectrum shows that the inner layer is mostly a thin layer of hematite.

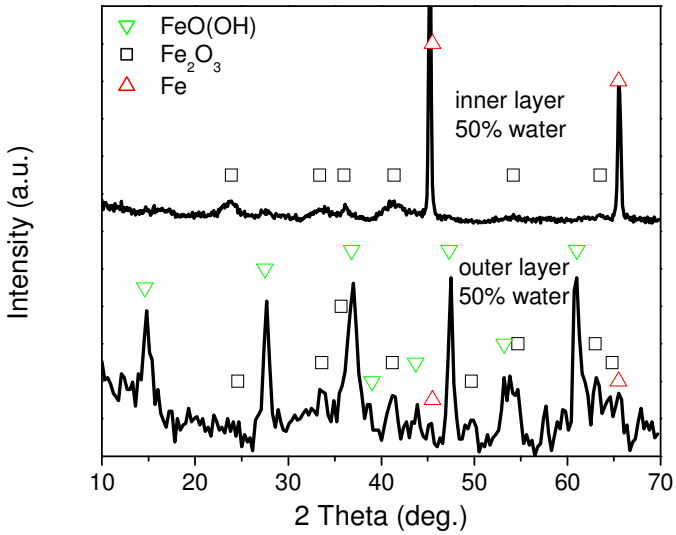

Figure 5-22. XRD spectra showing duplex layer structures of corrosion products on X-65 carbon steel in aerated SFGE

5.9 Conclusions

Corrosion and pitting behavior of carbon steel was systematically studied with variations in FGE constituents. In the absence of the supporting electrolyte, modified cell geometry enabled us to carry out reliable electrochemical analysis of carbon steel behavior in the low-conductivity ethanolic solutions. The surface electrochemical properties of carbon steel are found to be sensitive to the impurities in FGE. The specific conclusions are as following:

(1) Weight loss increases with an increase in the water concentration. Below 5 vol% water, pitting susceptibility increases as the water content increases. However, much higher water content (above 10 vol%) reduces pitting corrosion. SFGE with 2.5 vol% exhibits a state of competition equilibrium between passivation and its breakdown. Electrochemical measurements in SFGE environments exhibit no clear passivity and breakdown potential.

(2) The decrease in pHe reduces both pitting and general corrosion in SFGE. Alkaline condition stimulates a good surface inhibition towards corrosion in SFGE.

(3) Chloride increases the weight loss and pitting tendency of carbon steel in SFGE. Without chlorides, no pitting corrosion is observed. Chloride was also found to play a significant role on destabilizing the surface film, resulting in the decreases of both E_{corr} and E_{rp}.

(4) A decrease in the dissolved oxygen in SFGE is found to reduce, but not eliminate, the pitting susceptibility in high water content SFGE. However, in SFGE with 1 vol% water, de-aeration can lead to fast dissolution of ferrite from carbon steel. Carbide-rich phase or grain boundary appears on the surface.

(5) With lower water content in SFGE, iron oxide is identified as a major corrosion product on carbon steel surface. As the water concentration in SFGE increases, iron hydroxide film is present on the surface of carbon steel.

CHAPTER 6

FILM BREAKDOWN AND ANODIC DISSOLUTION DURING STRESS CORROSION CRACKING OF CARBON STEEL IN SIMULATED FUEL-GRADE ETHANOL

The phenomenological investigation has been reported in Chapter 4. However, the physical mechanism of the stress corrosion cracking of carbon steel in SFGE is still unclear. In this chapter, in-situ electrochemical measurements of crack initiation and growth were carried out along with SSRT test. Under plastic stress, film breakdown and film related anodic dissolution were characterized and identified as the major mechanism for SCC on carbon steel in SFGE.

6.1 Stress Corrosion Crack Evolution during SSRT

Slow strain rate tests were carried out where the tests were intercepted at certain strain values to examine the sample for SCC. The samples were examined in SEM to identify the crack initiation and morphology change as a function of applied strain. Figure 6-1 shows the SEM images of cracks at the tensile sample surface under different applied strains. Strain values indicated in this paper were calculated from the machine displacement rates, therefore, the actual strain at the sample gage were smaller, especially at the initial stages of the test. At the strain (ε) value of 0.026, the tensile sample just exceeded the yield point for this material. No surface cracks were observed on the sample

below or just at the yield stress. SEM observations revealed that the sample surface was smooth and without any indication of film rupture, as shown in Figure 6-1. At the strain value of 0.102, crack initiation and film breakdown were visible throughout the gauge area of the sample. The crack initiation and growth at the surface continued to increase as the plastic strain increased. After the ultimate tensile stress (UTS), initiation and growth of the cracks were mostly limited to the highly deformed necked region of the tensile sample. Coalescence of multiple cracks, to form larger cracks, was observed throughout the surface. Finally, at the strain value of 0.142, which was close to the sample's final fracture strain, localized plastic deformation caused the existing cracks to open, as shown in Figure 6-1.

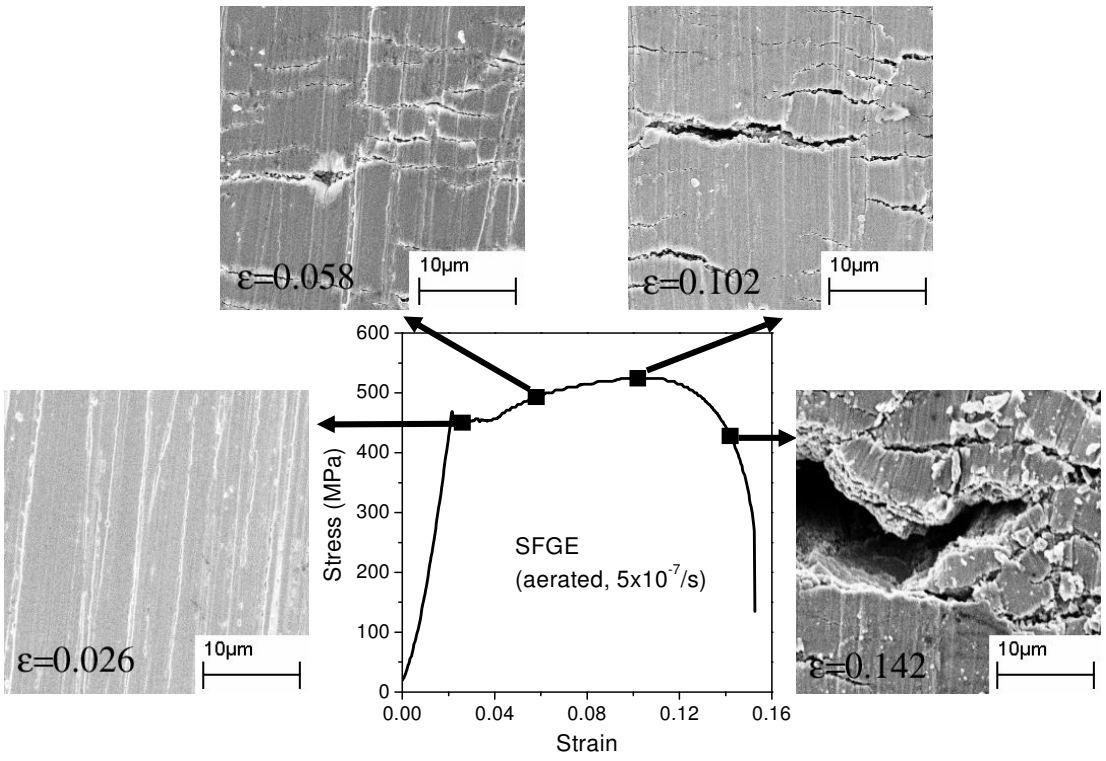

Figure 6-1. SEM images of X-65 sample surface showing the crack evolution in SFGE under aerated condition during slow strain rate tests.

The evolution of surface micro-crack density and crack velocity during SSRT are plotted in Figure 6-2. The surface micro-crack density was characterized based on the average number of micro cracks per unit distance along the random lines drawn on the SEM micrographs of the sample surface. The intercepted tensile samples with different strains were also polished for the crack depth and morphology characterizations. The crack velocity was calculated from the deepest crack on the polished sample cross-section. As shown in Figure 6-2, the micro-crack density increased with strain from 0 to 220 cracks /mm before the maximum stress, but decreased to 120 cracks /mm after the maximum stress. This decrease in the micro-crack density after necking was mostly due to the coalescence of multiple cracks and the increase of the crack size during the necking of the sample. Crack velocity kept increasing during the SSRT. A large increase in the crack velocity, from 8×10^{-9} to 1.6×10^{-7} mm/s took place after UTS in the necked region , predominately due to the fast crack propagation under the large plastic deformation. However, in the area away from the necked region, both the micro-crack density and the crack velocity did not change after the necking started on these samples. It can be concluded from the Figure 6-2 that, during SSRT in SFGE, crack initiation mostly takes place between the yield stress and UTS, while the crack growth rate increases significantly after necking.

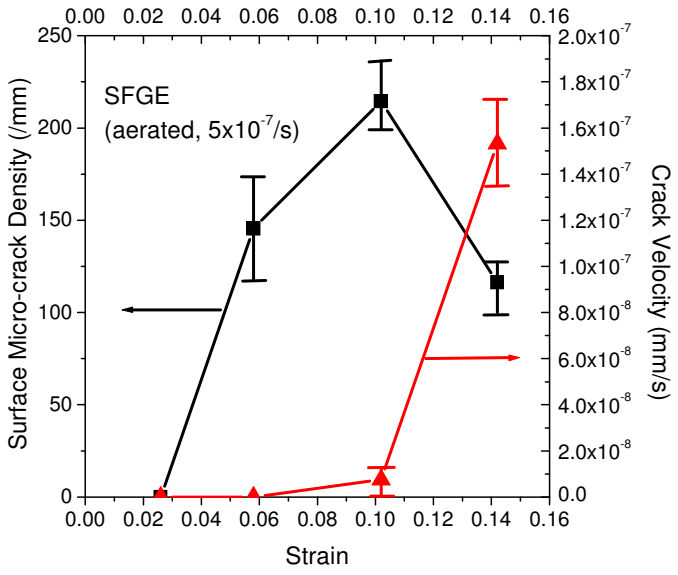

Figure 6-2. The evolutions of surface micro-crack density and crack velocity during SSRT

To illustrate the onset of the crack initiation at the close-to-yield region, the long-term constant-strain tests were carried out on the smooth tensile samples in aerated SFGE. As shown in Figure 6-3, the strain before and after the yield point was held for 5 days to study the effect of time on crack initiation and propagation. The results showed that the plastic deformation played a critical role on crack initiation. At the strain value of 0.02, no crack initiation was observed even after holding the sample under a constant strain for 5 days. However, at the strain of 0.025, which was beyond the upper yield point for this material, crack initiation was observed. Yielding of the material promoted the crack initiation on the surface, although the propagation kinetics was very slow in the low strain range.

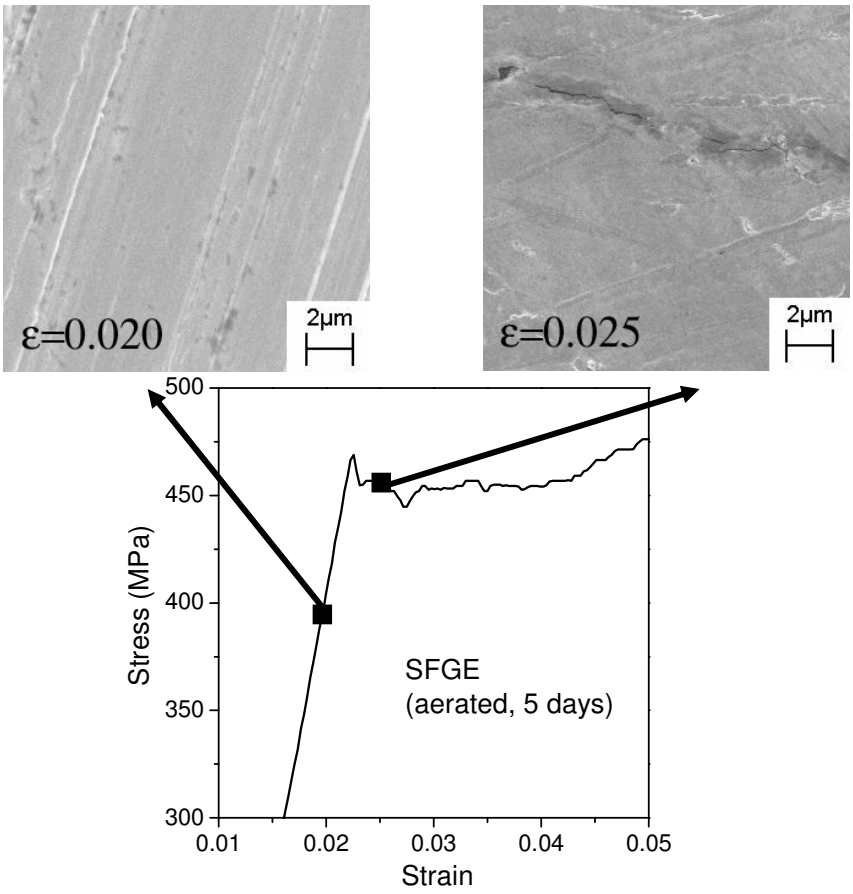

Figure 6-3. SEM images of sample surface after long-term constant strain tests at close-to-yield region

6.2 Potentiodynamic Polarization

Potentiodynamic polarizations with automatic IR compensation were carried out in aerated SFGE with three different potential sweep rates: 0.2 mV/s, 0.07 mV/s and 0.02 mV/s, as shown in Figure 6-4. The potential sweep started from the initial OCP for each sample. The results show that the anodic behavior of the carbon steel in SFGE was dependent upon the potential sweep rate. It has been widely accepted [27, 58] that, for the systems where the SCC mechanism involves an active dissolution at the crack tip, a fast

potential sweep simulates the active crack tip undergoing anodic dissolution whereas a slow sweep simulates the crack wall or sample surface with surface/passive film. In the tested potential range, a faster sweep rate resulted in a higher anodic current density. For instance, at 200mV vs. SSCE, the current density under a sweep rate of 0.2 mV/s was one order of magnitude higher than that under a sweep rate of 0.02 mV/s. At around 75mV vs. SSCE, the polarization with 0.02 mV/s sweep rate exhibited signs of passivation or barrier-film formed at the sample surface. The observation of the passivation under such a slow sweep rate suggested that the film formation kinetics in SFGE was much slower than that in the aqueous environments.

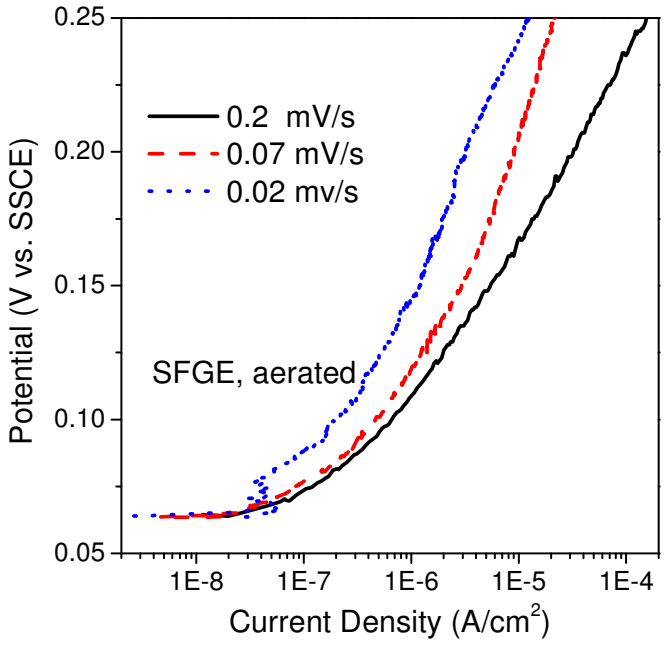

Figure 6-4. Potentiodynamic polarization with automatic IR compensation (starting from initial OCP) of X-65 carbon steel at different sweep rates

6.3 Surface Potential and Impedance Measurement

To study electrochemical activities at the metal surface during stress corrosion crack initiation and growth, the changes in the electrochemical potential and the impedance were studied on both the smooth and the notched tensile samples during long-term static immersion as well as slow strain rate tests. Figure 6-5 shows the changes in the potential and the electrochemical impedance during a long-term immersion of the carbon steel in the aerated SFGE. Figure 6-5(a) shows that the OCP increases continuously with the immersion time. Since the oxygen level and ethanol chemistry were constant throughout the test, this increase in the OCP indicated the growth of the surface film on the carbon steel surface. The potential reached equilibrium at ~210mV vs. SSCE. Water was shown to influence the passive film stability and characteristics in alcoholic environments. [36, 37, 43, 48] The impedance spectra during immersion, shown in Figure 6-5(b), also increased with time, which confirmed the film growth process. The polarization resistance kept increasing, indicating a continuous film growth on the surface. Such a slow kinetics of film growth in SFGE also suggests a poor passivity of carbon steel in ethanol with low water content. [36]

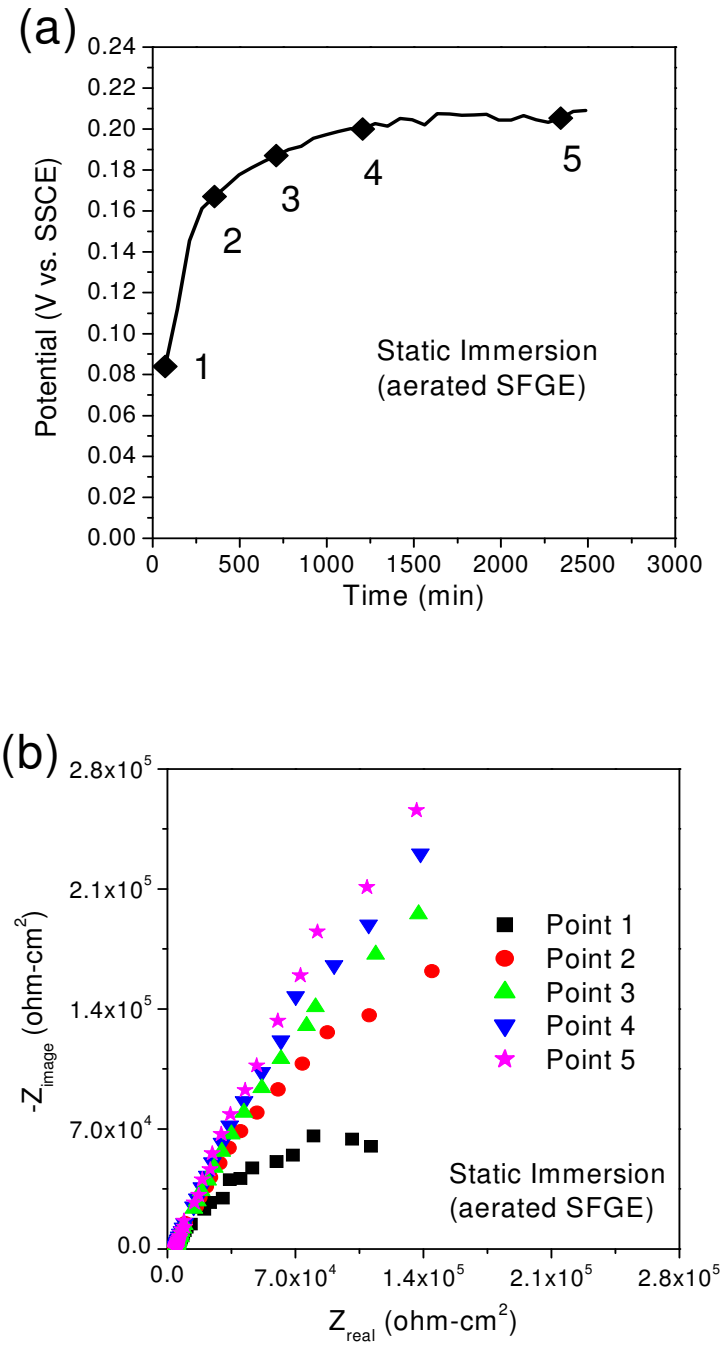

Figure 6-5. Static immersion in aerated SFGE under OCP: (a) potential evolution with time; (b) impedance spectra at selected points shown in Figure 6-5(a)

Figure 6-6 shows the change in the open circuit potential and electrochemical impedance measured on a smooth tensile sample during SSRT in SFGE. OCP data in Figure 6-6(a) shows that the potential values increased with time to around 150mV vs. SSCE until the yield point was reached. The corresponding impedance data in Figure 6-6(b) also shows an increase in the polarization resistance before the yield point for the sample. Without any changes in the environmental parameters, such a potential increase for a SSRT sample can be related to the film growth on the surface under low strain conditions. Just after the yield point, the OCP dropped quickly from 150mV to 10mV (vs. SSCE), indicating the film breakdown and the polarization resistance values also dropped. The intercepted SSRT tests (Figure 6-3) also showed that the stress corrosion cracks on the carbon steel in SFGE initiated after the yield point. Crack initiation was associated with the film breakdown and anodic activity at the steel surface. At point 3 (around 600 minutes into the test), the OCP and polarization resistance began to increase gradually with time and strain. The increasing rate of potential change between point 3 and the UTS was slower than the rate of potential change between points 1 and 2 in the elastic-plastic region. These results suggest that although the surface film might breakdown locally beyond the yield stress, the overall film growth and repassivation on the smooth sample surface dominated the average potential in the strain-hardening region. Strain localizations in the necked area and crack initiation sites reduced the further straining in other areas of the tensile sample and led to a fast repassivation in areas with strain relaxation. After the UTS, the OCP values stopped increasing further. This flattening of the OCP curve after the UTS was associated with the necking or strain localization which led to the fast propagation of existing cracks in the necked region.

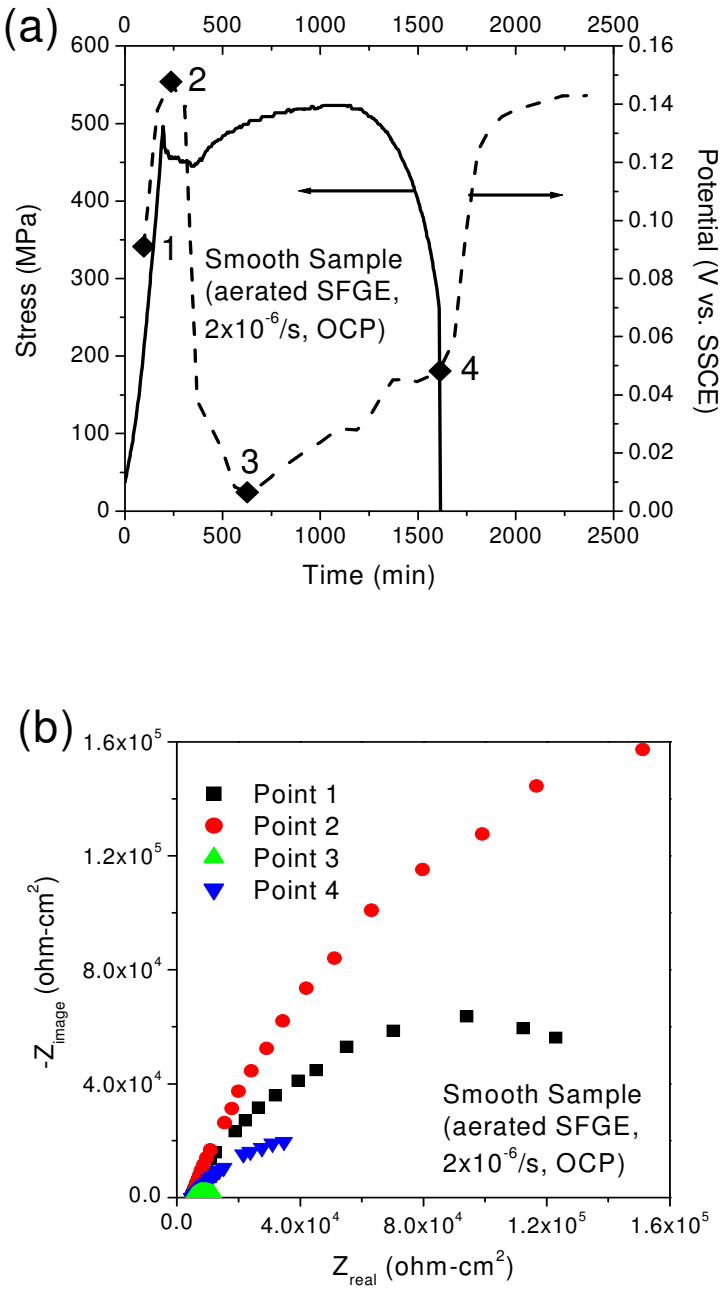

Figure 6-6. SSRT using smooth tensile sample in aerated SFGE: (a) potential evolution with time; (b) impedance spectra at selected points shown in Figure 6-6(a)

To monitor the electrochemical behavior of a single crack, a notched tensile sample was used to localize crack initiation at the notch tip. The tip of the salt bridge was

placed very close to the notch root. A slower strain rate of $8x10^{-7}$/s was chosen due to the higher local strain rates ahead of the notched root. To avoid the electrochemical signal from the areas other than near an active stress corrosion crack, only the notch area was exposed to the SFGE solution. The rest of the sample was covered with PTFE film. The OCP and the impedance changes as well as the maximum stress at the notch-root during the SSRT are shown in Figure 6-7. The stress concentration factor (K_t) at the notch-root was calculated based on a V-notch round sample model. [53] For the sample geometry used in this study (Figure 3-1), the calculated K_t was 2.8. Because the value of K_t normally changes with an increase in the crack depth, the short dashed curve is plotted after the yielding of the whole notch gauge to finish the corresponding stress-strain curve. Initially, there was a fast increase in OCP to ~100mV vs. SSCE in the notched area, as shown in Figure 6-7(a). The initial rate of this increase in OCP for the notched sample was similar to that for the smooth sample, indicating that the passivation kinetics for the two was similar under the unstressed or low-stress conditions. With further loading on the notched sample, there was a decrease in the slope at which the potential-increase started after 50 minutes until the potential reached its peak at around 350 minutes (point 2). In Figure 6-7(b), the polarization resistance also increased from point 1 to point 2 in the figure, suggesting a surface film growth. Further increase in strain, beyond the point of the peak potential, led to a gradual decrease in the OCP until the final failure of the tensile sample. The notched sample did not show any increase in the OCP during the plastic deformation, which was different from the smooth sample data in Figure 6-6(a). The polarization resistance in Figure 6-7(b) also decreased until the end of the test, indicating a continuous process of film breakdown and anodic dissolution activity on the

notched sample during SSRT. As the activity in the “non-active” part on the notched tensile sample was blocked by covering that area with the PTFE film, electrochemical data suggest that the high stress concentration kept the crack tip mostly free of passive film throughout the test. This behavior is also expected at each growing stress corrosion crack in this system, even for the smooth samples. However, the electrochemical behavior for the non-active region on the smooth sample dominated the average electrochemical signal measured globally, as shown in Figure 6-6. It should be noted that the onset of film breakdown on the notched sample was detected at point 2 in the figure. The corresponding notch-root maximum stress was around 650MPa, which was higher than the yield stress on the smooth sample in Figure 6-6. This requirement for stresses, higher than the surface yielding, to breakdown surface film on the notched geometry was also reported elsewhere. [66] Detection of a singular-point passive film breakdown at the notch tip can be difficult due to the instrument’s resolution. A significant accumulation of the surface film damage, associated with growth of plastic zone or surface strain rate ahead of the notch tip are needed for the initial electrochemical change to register for the notched sample. [66, 67]

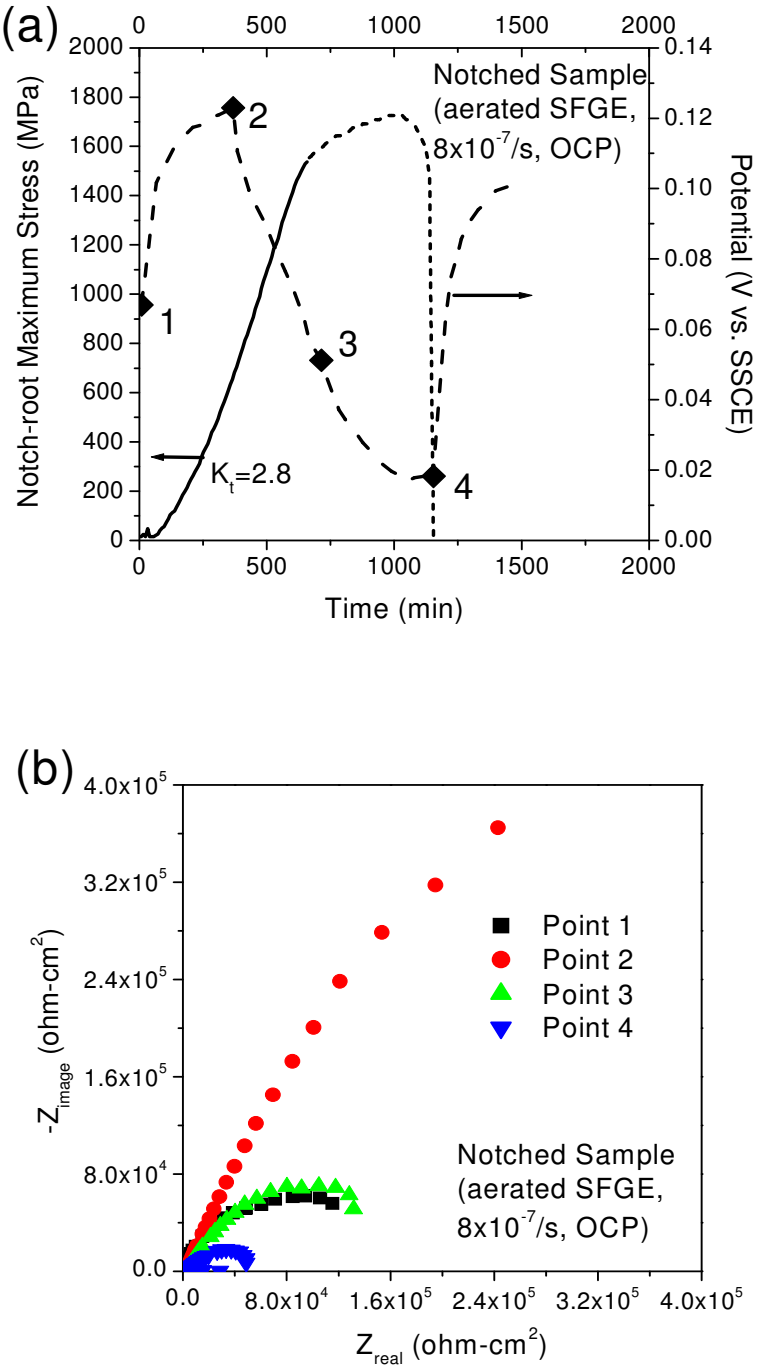

Figure 6-7. SSRT using notched tensile sample in aerated SFGE: (a) potential evolution with time; (b) impedance spectra at selected points shown in Figure 6-7(a)

6.4 Surface Current Evolution under Potentiostatic Condition

Changes in the electrochemical current generated at the sample gauge or notch were also measured using potentiostatic method. The current transient has been proven as an effective parameter to detect film rupture on the surface. [34, 66] An anodic potential close to the initial OCP (85mV vs. SSCE) was applied on both the smooth and the notched tensile samples. Figure 6-8(a) shows the change in current density for a smooth sample during SSRT. As shown in the inset, a sudden increase in the current density from 0 to 3×10^{-6} A/cm^2 was observed after the upper yield point, which indicated a start of film breakdown and active dissolution. This observation was consistent with the previous results from both OCP and EIS measurements. After this onset point, the current density continuously increased until the time reached 530 minutes. A strong oscillation in the surface current density was visible during this period. This current oscillation was attributed to an unstable passivity and a competition between the film breakdown and repassivation. After reaching a peak value at around 530 minutes, the surface current density tended to decrease as the strain increased. Such a change in the current was similar to the change in potential shown in Figure 6-6(a), which was also an averaged measured value from the sample surface due to the competition between the film breakdown and repassivation. A transition point with a change in the rate of current decrease was exhibited at 950 minutes where the stress reached the UTS. The rate of the film breakdown increased after the UTS, due to the fast crack propagation in the necked region. Upon failure, a small increase in the current density could be observed because of the increased exposure of the fresh metal surface to the environment after final fracture.

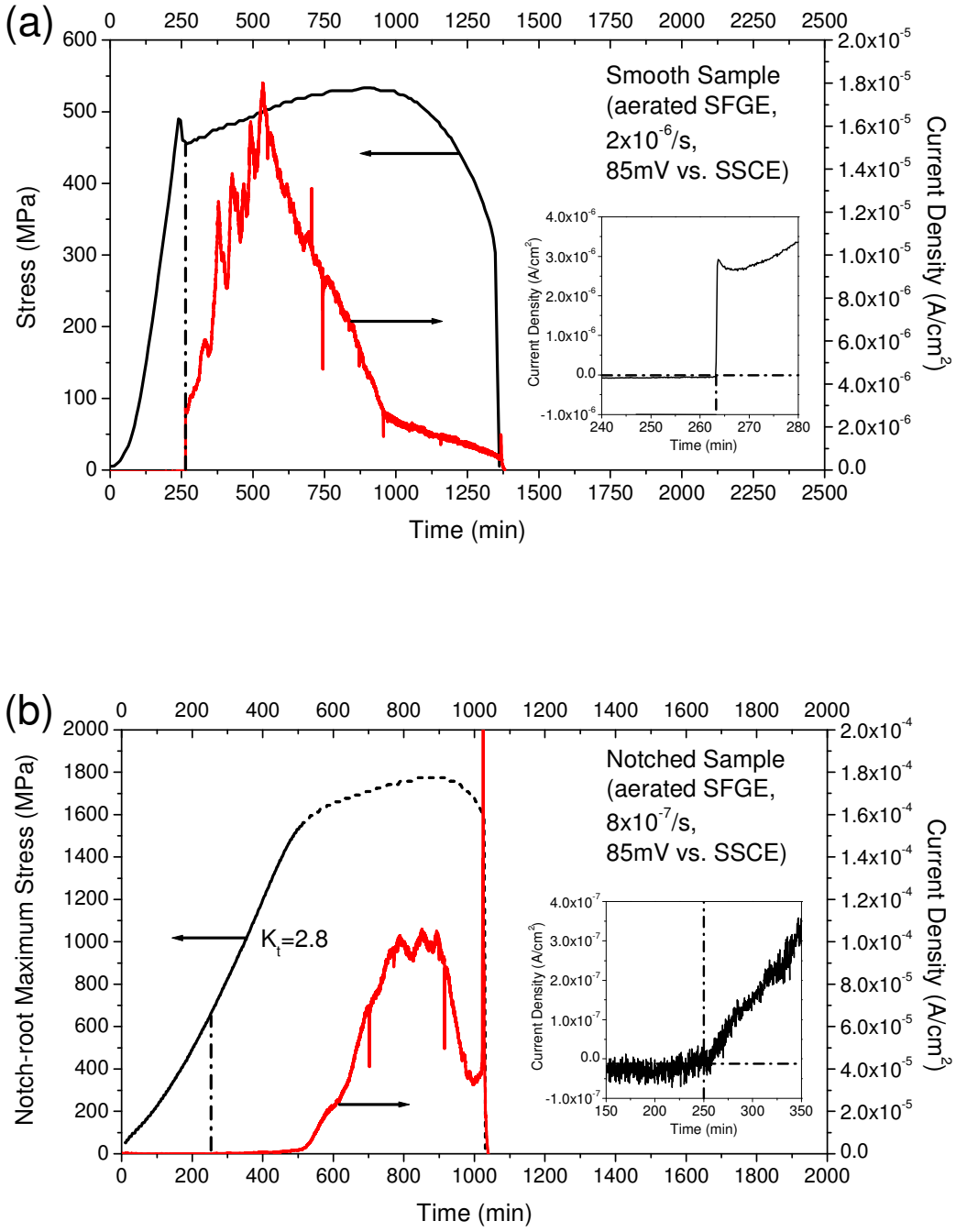

Figure 6-8. Potentiostatic current monitoring with 85mV vs. SSCE during SSRT: (a) for a smooth sample; (b) for a notched sample

Figure 6-8(b) shows the current density for a notched tensile sample tested under SSRT. A constant potential of 85mV vs. SSCE was also applied throughout the potentiostatic test. The inset shows a start of current increase took place at around 250 minutes where the notch-root maximum stress was around 650MPa. This current change indicated the onset of film breakdown and anodic dissolution was detected at the notch root. Different from the smooth sample, the onset of anodic current was not sharp for the notched sample, which indicated only a very small region ahead of the notch tip was active at this moment. Similar to the potential measurement in Figure 6-7, the maximum notch-root stress at this point was also higher than the yield stress on the smooth sample, indicating the notch effect on the local strain accumulation and surface strain rate. [66] After that, the current density slowly increased with strain. A major increase in the current density was visible after 520 minutes where the bulk sample started to yield. Such a large increase in the current signal may come from the increasing film breakdown area due to the strain accumulation within the notch and the propagation of the main stress corrosion crack at the notch root. A maximum current density of around $1x10^{-4}$ A/cm^2 occurred between 750 minutes and 900 minutes when the stress slowly approached the maximum point. After a maximum notch-root stress, which was around 950 MPa, the current density quickly decreased as the strain increased. Damage localization ahead of the main stress corrosion crack, at this stage, caused fast crack growth. Considering that the machined notch geometry was not the ideal singular notch tip (Figure 3-1), the strain localization could also release the stress in other notch areas, which possibly promoted the repassivation in those areas to reduced the overall anodic current value. A large burst

in the current density, which was mostly due to the sudden increase in the bare-metal surface exposed to the solution, could be observed at the final fracture.

6.5 Potential Dependences of Stress Corrosion Cracking

Figure 6-9 shows the evolution of crack density and velocity with the applied potential. The crack density in Figure 6-9 was determined from the polished sample cross-section. It shows that both crack density and velocity increased as the potential increased within the tested range. Because the potentials within this range were closely related to the dissolution kinetics (Figure 6-4), initiation and propagation of these corrosion cracks were strongly controlled by the anodic polarization.

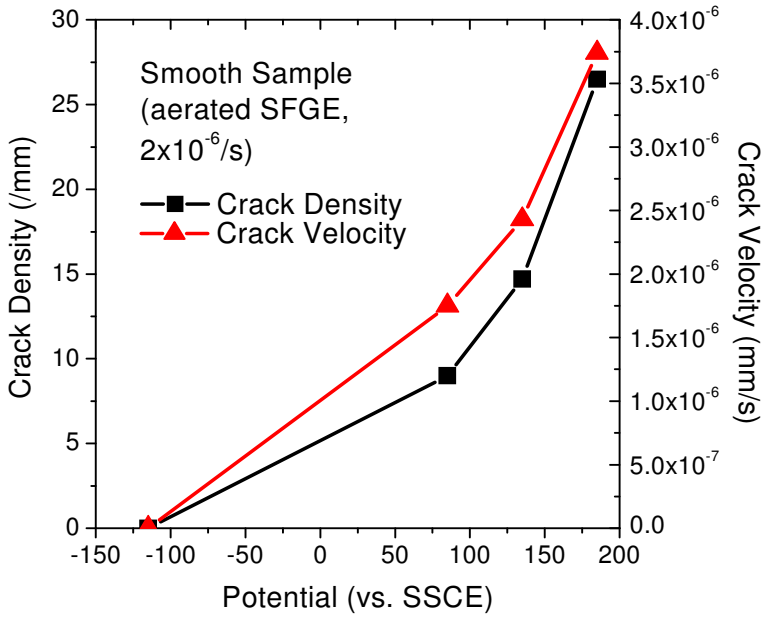

Figure 6-9. Potential dependences of the crack density and crack velocity

Figure 6-10 shows the relationship between the concentration of dissolved and precipitated iron in the tested solution, determined by ICP analysis after the test, and the

corresponding crack density/velocity. The results indicate that within the narrow potential range, an increase in the crack density and velocity correlated well with an increase in the metal dissolution in SFGE. Such correlation suggests that a fast anodic dissolution was associated with the SCC propagation. However, this trend in an increase in the dissolved iron with crack velocity and density is not expected to continue at higher applied potentials or dissolution rates, where the mode of attack will be general corrosion.

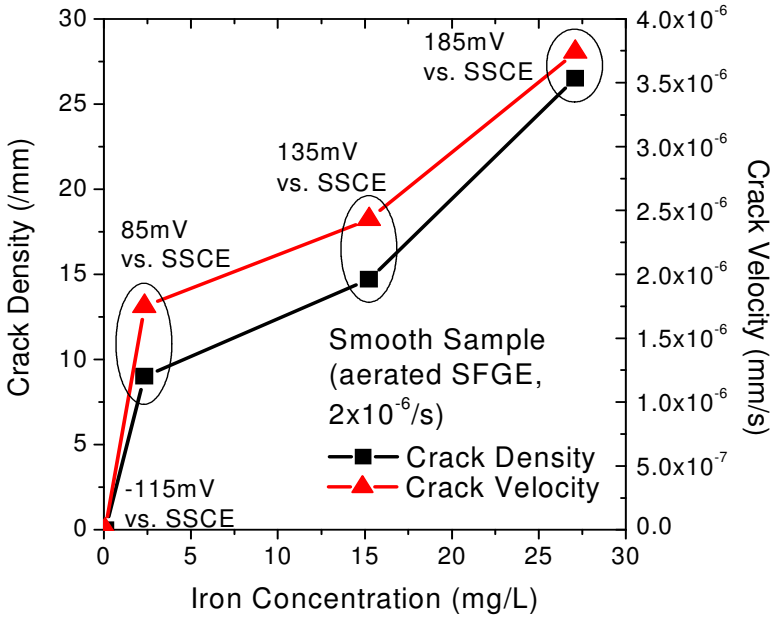

Figure 6-10. Relationships between iron concentration in solution and crack density/velocity under various potentials

It should be noted that, under the cathodic potential of -115mV vs. SSCE, no stress corrosion cracking was observed on either the sample surface or the fracture surface. A surface current change under the cathodic polarization (-115mV vs. SSCE) is shown in Figure 6-11. These results indicate that crack initiation can be stopped by eliminating anodic dissolution.

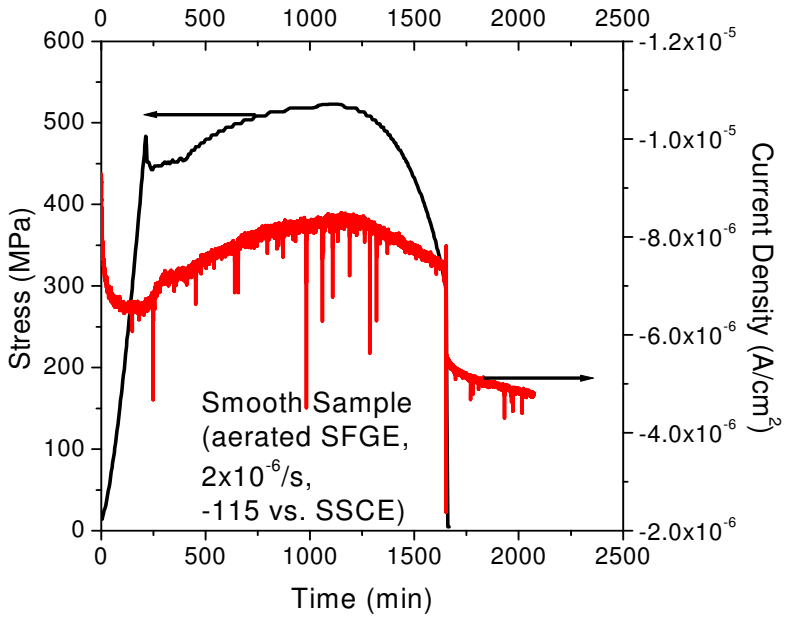

Figure 6-11. Current change during cathodic polarization (-115mV vs. SSCE)

6.6 Crack Morphology

The fracture surface morphologies of tested pipeline steel samples under various potentials were examined close to the edge using SEM, as shown in Figure 6-12. Figure 6-12 (a) shows the ductile type fracture surface without SCC on the steel sample polarized at cathodic potential (-115mV vs. SSCE). But, in Figure 6-12(b) and 6-12(c), brittle fractures caused by SCC were easily observed at various anodic potentials. The severity of SCC increased as the potential increased within the tested potential range. At 185mV vs. SSCE, no sign of ductile failure was observed on the fracture surface. The fracture morphology for the carbon steel in SFGE was predominantly transgranular, which was consistent with other reports.[3, 51] However, it has also been reported that

the intergranular mode or mixed mode could be observed under some specific SFGE testing conditions. [3] The reason for such phenomenon still remains unclear. [24]

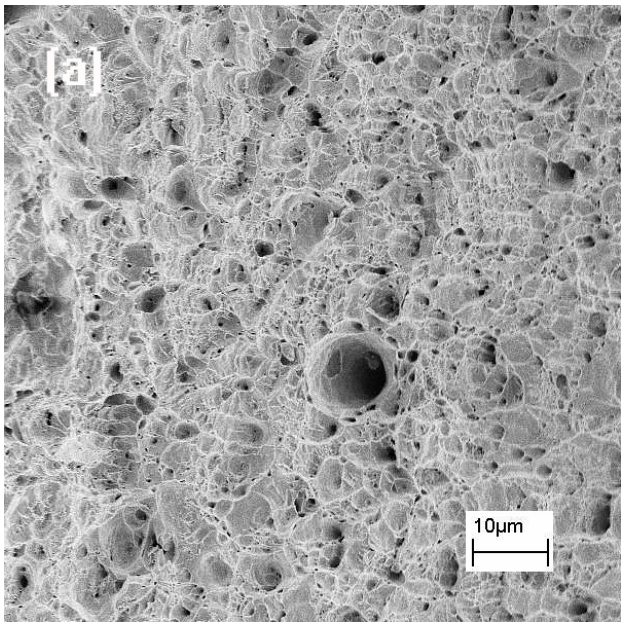

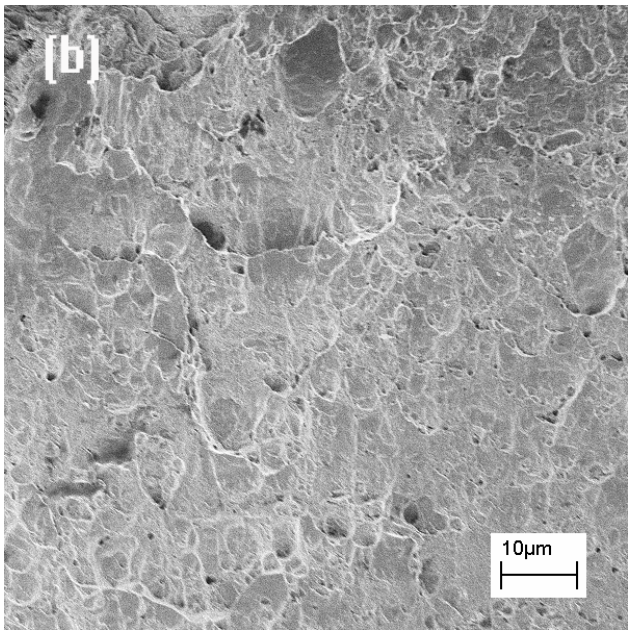

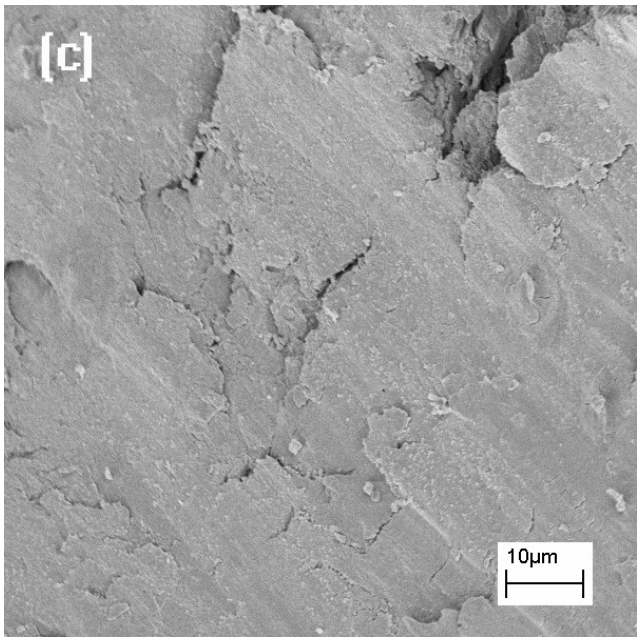

Figure 6-12. Fracture surface morphologies under various potentials: (a) -115 mVvs. SSCE; (b) 85 mVvs. SSCE; (c) 185 mV vs. SSCE. (OCP for carbon steel in SFGE is around 75 mV vs. SSCE

The cross-section view of a typical crack formed after SSRT with a strain rate of $2x10^{-6}$ /s is shown in Figure 6-13. The etched microstructure shows the ferrite–pearlite microstructure of carbon steel. Stress corrosion cracks did not show any preference for the microstructural features and exhibited a clear transgranular mode.

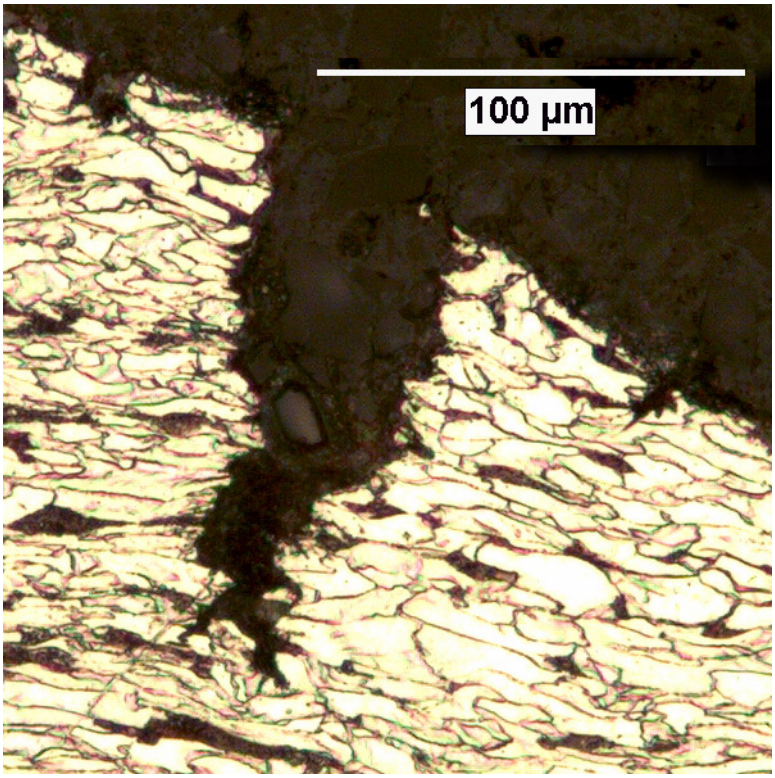

Figure 6-13. Optical image of a typical crack cross-section after SSRT under OCP with a strain rate of 2×10^{-6} /s

6.7 Role of Local Strain Accumulation in SCC Initiation and Growth

It has been shown previously that the film breakdown and crack initiation took place after the yield point for the carbon steel in SFGE. Results clearly indicate that the plastic strain is critical for the SCC nucleation and growth. Figure 6-14 shows the SEM images of the sample surface close to the necked area. Flow lines formed at certain angles to each other and the loading direction, were associated with the crack initiation. Enlarged image in Figure 6-14 shows that the stress corrosion cracks were larger along these lines. This observation suggests that these flow lines influence the SCC initiation, though the crack initiations can also be observed in the areas between those flow lines.

Macro flow lines are usually formed due to the high local strain on the sample surface and can serve as preferential initiation sites for the strain induced SCC initiation. These observations suggest that the local strain accumulation is a critical driving force in SCC initiation on the carbon steel in SFGE

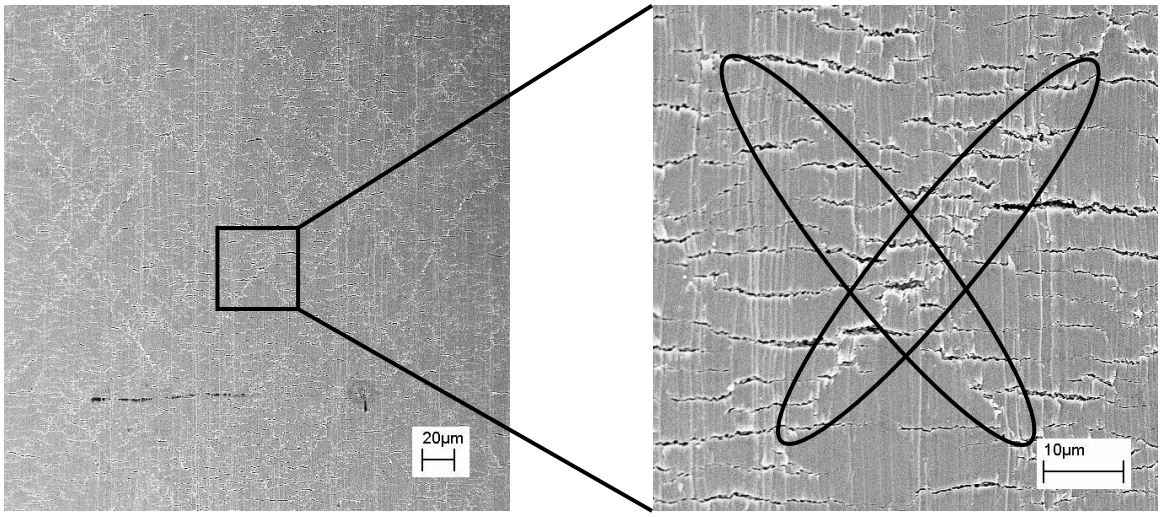

Figure 6-14. Macro flow lines on the sample surface after SSRT

6.8 A Mechanistic Model of Crack Initiation and Propagation in SFGE

Based on the results and earlier discussion, the schematic shown in Figure 6-15 represents a mechanistic understanding on the stress corrosion cracking of carbon steel in simulated fuel-grade ethanol during SSRT. Film breakdown and anodic dissolution is the most dominant mechanism in this process, although the surface film in the ethanolic environments may not be a stable passive film due to the limited amount of water. [36, 48] Figure 6-15 shows the local plastic deformation above yield stress is critical to the onset of film breakdown and crack initiation on both smooth and notched tensile samples. A certain plastic strain needed for film breakdown at the notch tip may produce even higher onset stress for the notched sample. Surface passivity of carbon steel in SFGE remains

stable under elastic deformation. Competition between the local strain accumulation and repassivation controls the crack initiation and growth. On the smooth sample, stress localization due to sample necking and slip band formation promotes the crack propagation around the highly strained region. The stresses in the other areas are relieved, resulting in a fast repassivation which stops the crack growth in those areas. The global surface potential is determined by the competition between the film breakdown and the repassivation. However, for the notched tensile samples, cracks formed at the notch root are always experiencing strain localization. Therefore, these cracks remain active throughout the test, although the crack walls may develop a passive film during the crack growth.

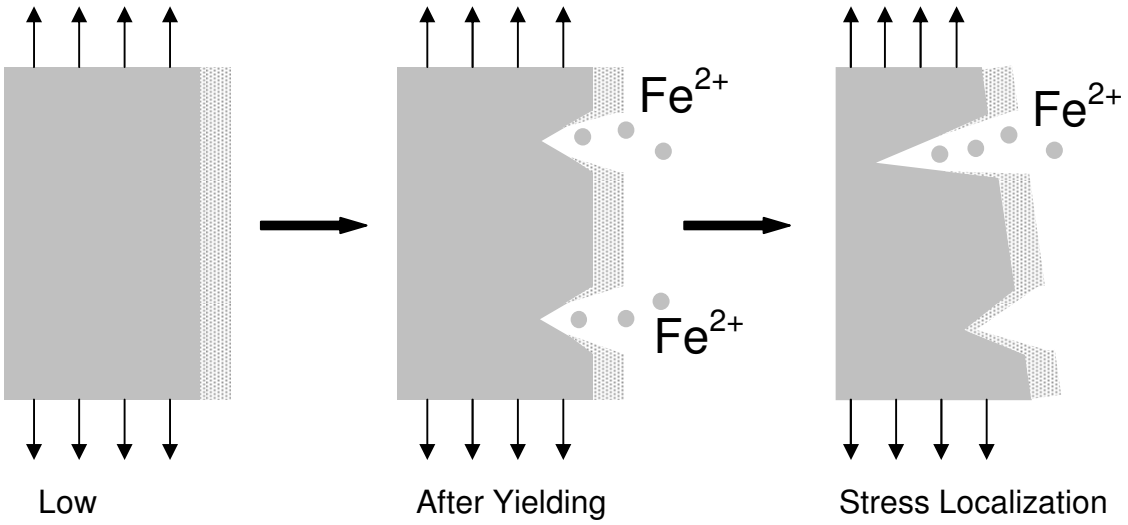

(a) Smooth Sample

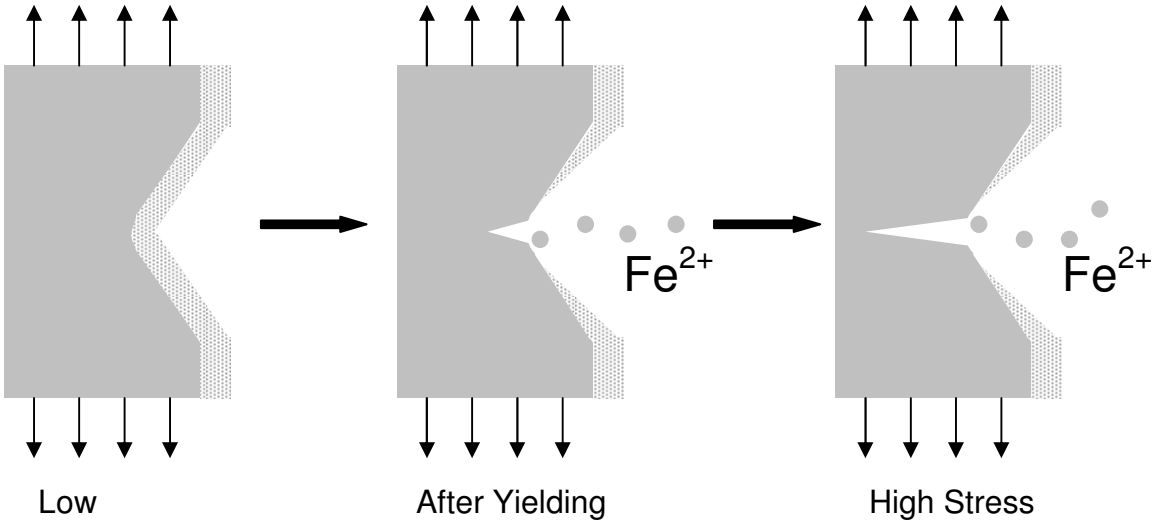

(b) Notched Sample

Figure 6-15. Schematic of a model describing the crack initiation and propagation for carbon steel in SFGE: (a) smooth sample; (b) notched sample

6.9 Conclusions

A mechanistic study was carried out towards understanding the stress corrosion cracking behavior of carbon steel in simulated fuel-grade ethanol environment. The onset of film breakdown under local plastic deformation initiates micro-cracks on the surface. The competition between the active anodic dissolution and the repassivation ahead of the crack tip controls the propagation of stress corrosion cracks. Some specific conclusions are addressed as following:

(1) Yielding of carbon steel and the onset of film breakdown cause stress corrosion crack initiation in simulated fuel-grade ethanol, which significantly decreases the open circuit potential and increases the surface current produced due to anodic activity.

(2) During SSRT, crack initiation (the increase of crack density) mostly takes place before the UTS, while crack growth (the increase of crack velocity) mostly takes place after UTS.

(3) Once the stress corrosion cracks are initiated, the competition between anodic dissolution and repassivation controls the crack growth rate.

(4) Within the anodic dissolution range, both the crack density and the crack velocity increase as the potential increases. SCC can be stopped by eliminating the anodic dissolution at the crack tip using a cathodic polarization.

(5) Transgranular SCC is the dominant crack morphology on the carbon steel samples in aerated SFGE environments tested.

(6) Local strain accumulation and its associated local film breakdown are important for the initiation of SCC on the carbon steel in SFGE.

CHAPTER 7

FURTHER INVESTIGATION ON SCC MECHANISM: PHASE ANGLE ANALYSIS AND SIMULATION

In previous chapter, film related anodic dissolution has been concluded as the major driving force for SCC on carbon steel in SFGE using *dc* technique. However, further understanding of the detailed electrochemistry in these corrosion cracks during the cracking process is needed to devise a clear mechanistic picture of SCC on carbon steel in FGE. In this chapter, in addition to the conventional *dc* technique, phase angle analysis using EIS was proposed as an *ac* technique to further understand the cracking mechanism in SFGE. For a dynamic process like stress corrosion cracking, EIS technique has to be used with caution due to the measurement stability with time. In this chapter, transmission line model simulation is proposed to simulate the cracking process. The simulation provides information about how to reduce the measurement time during SCC in order to reduce the instability. Though TLM simulation can not retrieve all the physical details from cracking due to the model complexity and the instability of cracking process during measurement, the simulated changes in phase angle under various conditions can still be correlated with the experimental observation during SSRT in order to give some explanation about the detailed behaviors inside a crack during propagation.

7.1 Static Immersion Tests

Carbon steel sample was exposed to the SFGE solution. No stress was applied to the sample. Shown in Figure 7-1 are the evolutions in the OCP and the phase angle of EIS with time. OCP slowly increased during immersion. Because the oxygen concentration and ethanol chemistry are similar throughout the test, this increase in OCP suggests a slow kinetics of film growth on the surface. EIS phase angle evolutions with time are analyzed for four different frequencies, as shown in Figure 7-1. The values of phase angle for the selected frequencies increase with the immersion time, primarily due to the increase in film resistance and the decrease in film capacitance. Phase angles at 10 Hz exhibit the lowest values (20^o ~ 30^o) and slowest increasing rate among these four frequencies. In contrast, the results from 1 Hz and 0.1 Hz produce high phase angles between 50^o to 70^o. Though the phase angles from 0.01 Hz shows relatively low values (20^o ~ 40^o), it presents the fastest increasing rate. Since the OCP increases quickly during the early stage of immersion, the slow EIS measurement at 0.01 Hz may generate a polarization effect. Post analysis showed that the increase in OCP during the first EIS spectrum was around 4 mV vs (Ag/AgCl/1M LiCl,EtOH). After the first spectrum, the OCP increase during EIS measurement was negligible. Therefore, in the static immersion test, EIS measurement with frequencies from 100 Hz to 0.01 Hz provides both good EIS spectrum and reasonable OCP behavior.

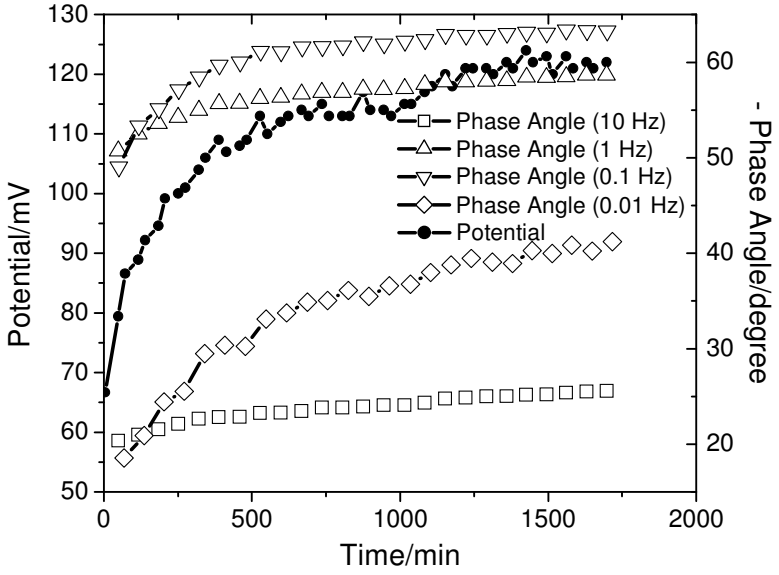

Figure 7-1. Open circuit potential (vs Ag/AgCl/1M LiCl,EtOH) and phase angle evolution under static immersion in aerated SFGE

Based on the equivalent circuit given in Figure 7-2(a), area-specific surface resistance $R_{surface}$ and surface capacitance $C_{surface}$ were obtained using the Simplex fitting algorithm with the software package Echem Analyst™ by Gamry Instrument. Some selected Bode plots and their fitting results are shown in Figure 7-2(b). A constant phase element (CPE) is used to fit experimental EIS data with depressed semi-circle. The impedance of CPE is defined as following:

$$Z_{CPE} = \frac{1}{Y(i\omega)^n} \qquad (7\text{-}1)$$

where Y is a parameter with a unit of s^n/Ω, and n is an adjusted exponent between 0 and 1. When n=1, it represents a perfect capacitor; when n=0, it represents a perfect resistor. Considering Y does not have the unit of capacitance, the mathematical expression developed by Brug et al. [68, 69] is used to calculate $C_{surface}$, shown as following:

$$C_{surface} = Y^{1/n}(R_{ohm}^{-1} + R_{surface}^{-1})^{(n-1)/n} \quad (7\text{-}2)$$

Figure 7-2(a) shows the fitted surface resistance $R_{surface}$ and the calculated surface capacitance $C_{surface}$. Here, $C_{surface}$ was calculated from the fitted CPE value Y using Eq. (1). In Figure 7-2(a), the increase in $R_{surface}$ and the decrease in $C_{surface}$ suggest a slow film growth on the carbon steel surface over time, when exposed to aerated SFGE. Generally speaking, the electric double layer usually shows a capacitance in a range of $2x10^{-5}$~$2x10^{-4}$ F/cm^2. The oxide film usually has the capacitance in the range of $1x10^{-7}$~$2x10^{-5}$ F/cm^2. The magnitude of $C_{surface}$ in SFGE is between the double layer controlled process and oxide controlled process, which suggests the metal exhibits a unique surface film character in SFGE. Based on other studies in methanol system [40, 70], it is possible that an unstable ethoxy-iron film may be the in-situ surface film formed in slightly acidic ethanol. This membrane type surface film may show a slightly higher capacitance value than the normal pure oxide film. The change in the $C_{surface}$ with time suggests that the system undergoes a slow process towards a film controlled behavior. This also suggests that the stress corrosion cracking of carbon steel in SFGE may involve a film-related process. It should also be noted that the increase in the $R_{surface}$ is much faster than the decrease in the $C_{surface}$ within the tested time range. Therefore, the system gradually changed towards one with more characteristic of capacitance during immersion, which leads to the increase in phase angle for all the frequencies, as shown in Figure 7-1 and Figure 7-2(b).

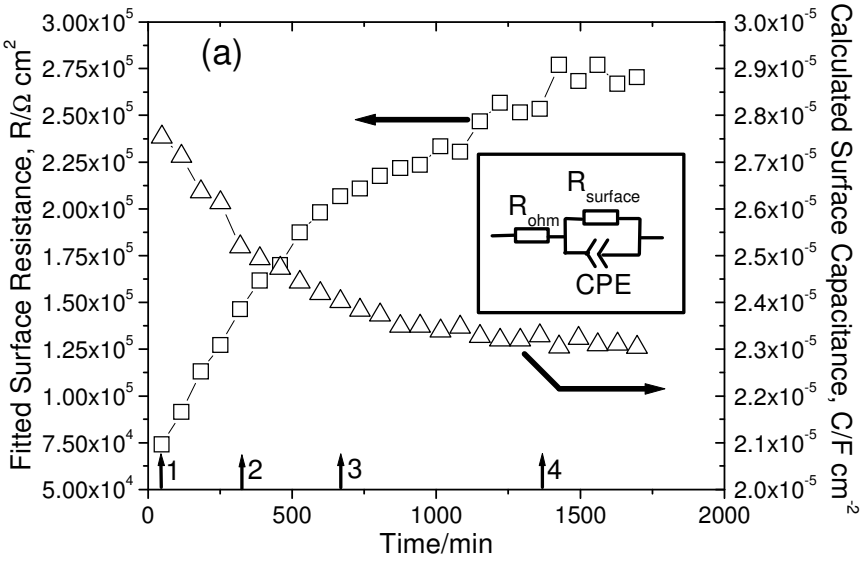

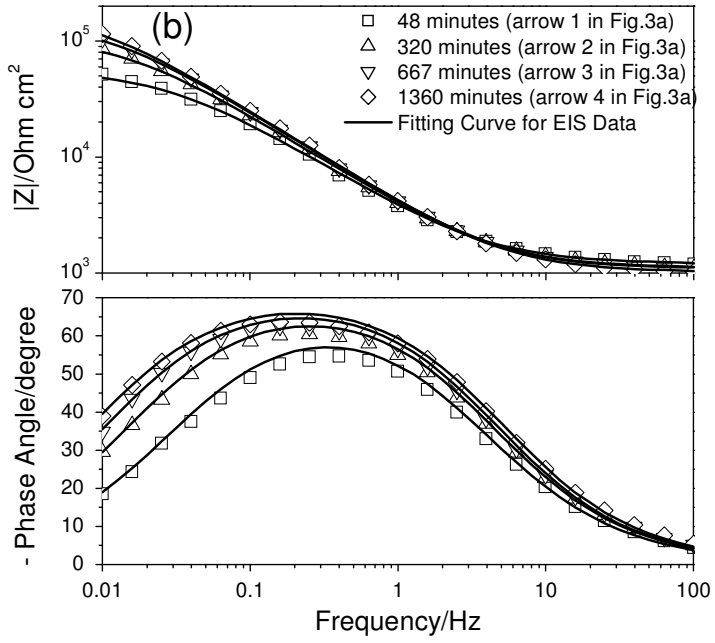

Figure 7-2. EIS spectra under static immersion: (a) regressed results of area-specific surface resistance and capacitance based on the equivalent circuit in the inset (note: surface capacitance was calculated from the fitted CPE value using Equation (7-2)); (b) selected Bode plots and their fitting curves

7.2 Stress Corrosion Cracking on a Notched Sample during SSRT

The crack morphology and the crack evolution on the smooth sample in SFGE have been reported in various papers [3, 51, 52]. Shown in Figure 7-3 is the change in stress corrosion crack depth on the notched sample during SSRT, measured using the interrupted tests. On the smooth tensile sample, it was reported that the crack initiation of carbon steel in SFGE took place upon the yielding of the material [52]. On the notched sample, the motion of dislocation is more difficult due to the triaxial stress state ahead of the notch. Higher stresses are needed to develop a sufficient plastic zone and initiate a crack at the notch root. Therefore, crack initiation will require a notch-root stress higher than the yield stress of carbon steel. Figure 7-3 shows the crack growth rate is small before the global yielding. Within the range between global yielding and maximum stress, SCC exhibits the fastest growth rate in SFGE. After the maximum stress, the crack growth rate decreases with time.

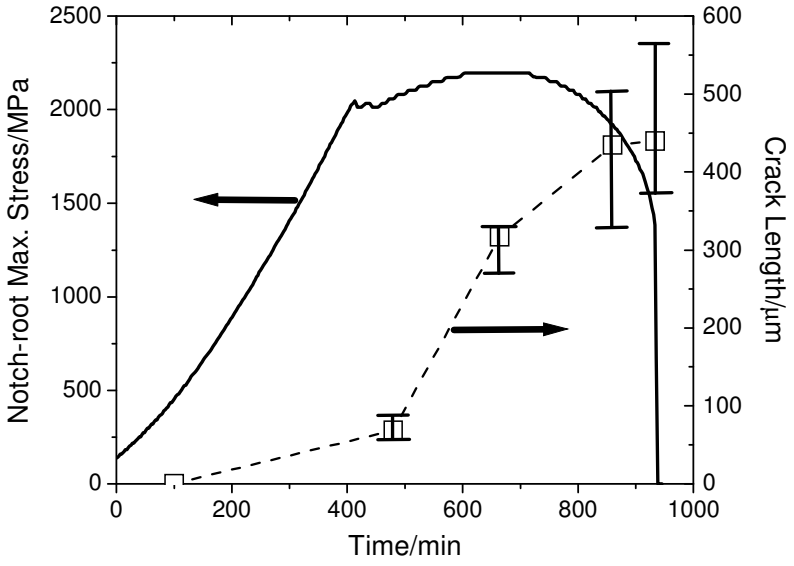

Figure 7-3. Measured crack length on the fracture surface using interrupted method during SSRT under OCP in aerated SFGE

Figure 7-4 represents a typical SEM image of the fracture surface after SSRT in SFGE. The fracture morphology for the carbon steel in SFGE is predominantly transgranular. After the tensile test, three characteristic regions are visible on the fracture surface: outside SCC brittle fracture region, a transition region of shear fracture, and a ductile fracture region with microvoids at the center. The latter two regions are usually formed after the maximum stress, where the crack blunting takes place due to final microvoid formation and coalescence. Therefore, as shown in Figure 7-3, the corrosion activity and SCC growth rate decrease after the maximum stress.

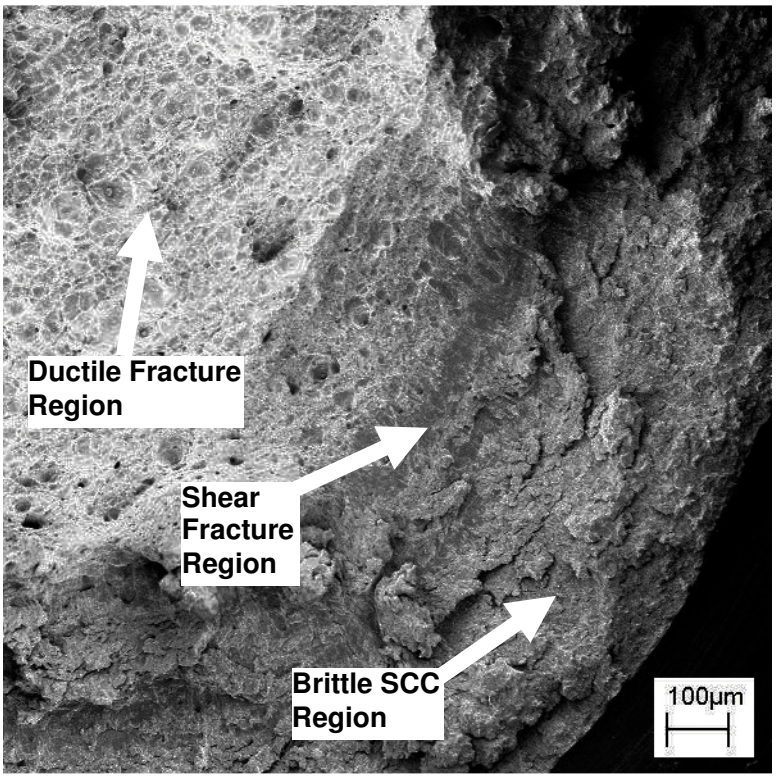

Figure 7-4. SEM image of a typical fracture surface

7.3 Phase Angle Evolution during Stress Corrosion Cracking

As shown in Figure 7-5, in-situ EIS and OCP monitoring were carried out on a notched tensile sample during SSRT. The notched tensile sample with the geometry shown in Figure 3-1(c) was used to study the crack initiation and growth. At the bottom of Figure 7-5, the OCP of the tensile sample during SSRT is shown with time. A tensile curve is also shown as a reference of stress state. An increase in the OCP from 80 to 110 mV vs (Ag/AgCl/1M LiCl,EtOH) is visible within the first 250 minutes. This increase can be attributed to the film growth in the low applied stress region during SSRT [52]. After that, the OCP continuously decreases till the maximum stress at point 4 in Figure 7-5. The detailed characterization in Chapter 6 suggested that the process of such a potential drop after yielding is related to the onset of crack initiation and crack propagation**.** A slight increase in the OCP can be observed after the maximum stress (point 4). Based on the crack evolution study in Figures. 7-3 and 7-4, the slight increase in the OCP, which suggests a decrease in corrosion activity, is mostly due to the final shear and ductile fractures caused by the sample necking. Compared to the average signal from OCP, the phase angles at different frequencies provide more information and characteristic signature, depending on the applied perturbation frequency. Shown in Figure 7-5 is the evolution of phase angles under four selected frequencies. Similar to the unstressed situation in Figure 7-1, 1 Hz and 0.1 Hz exhibit higher phase angles, while 10 Hz and 0.01 Hz exhibit lower phase angles. At low stress state from point 1 to point 2, all frequencies show increases in phase angle though their increasing rates are slightly different. Detailed EIS curve fitting further confirms that the stressed sample at this stage exhibits similar changes in $R_{surface}$ and $C_{surface}$ as the unstressed sample in Figure 7-2. Film

growth kinetics is not influenced by the low applied stress. With the further increase in strain, phase angles decrease significantly. Such a decrease in the phase angle can be correlated to the stress corrosion cracking process, as reported elsewhere [71-73]. Different from the other three frequencies, the decreasing rate of phase angle in 10 Hz is much smaller. After the maximum stress (point 4), lower frequencies at 0.1 Hz and 0.01 Hz exhibit the increases in phase angle with time while the phase angles at 10 Hz and 1 Hz still keep decreasing. Generally, the analyzed range of frequencies in EIS should reflect the dynamics of the electrochemical process. For example, the response from a higher frequency perturbation represents a faster electrochemical process, which is more close to a non-faradaic process. Therefore, the data clearly shows that a frequency which is lower than 1 Hz reflects the electrochemical behavior after the maximum stress. It should also be noted that the slower frequency analysis, such as 0.01 Hz, can generate higher instability during the dynamic cracking process. Therefore, the phase angle from a frequency between 1 Hz and 0.1 Hz better presents the cracking behavior at that moment with reasonable spectrum stability.

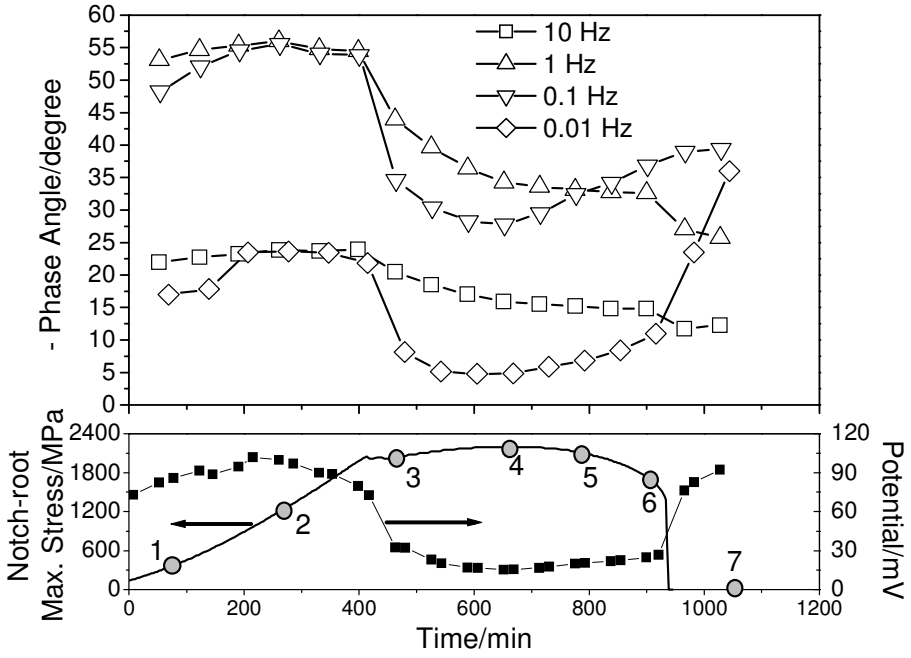

Figure 7-5. Evolutions of phase angle at various frequencies (10Hz, 1Hz, 0.1Hz and 0.01Hz) and potential (vs Ag/AgCl/1M LiCl,EtOH) during SSRT under open circuit potential in aerated SFGE

Figure 7-6 shows the Bode plots of the selected points in Figure 7-5. These plots represent typical changes in the physical process of cracking during SSRT. Only one time constant is present for both passivation process and cracking process. The Kramers-Kronig Transform (KKT) fits the experimental spectra well over the tested frequency range. When cracks form, KKT fitting is slightly different from the experimental data at low frequency range, which is mostly due to the cracking instability over a longer period of measurement. Therefore, data fitting based on EIS equivalent circuit model is not suitable for analyzing the cracking process. In this paper, simulation approach is used to study the SCC behavior. In Figure 7-6(a), the spectra before the maximum stress were presented. Both phase angle and impedance increase during early film formation and decrease after the crack initiation and growth. From these Bode plots, two conclusions

can be made: (1) during film growth process (point 1 to point 2), the lower frequency (< 0.3 Hz) exhibits a larger change in phase angle; (2) during the cracking process, the phase angle at slightly higher frequency also becomes sensitive towards cracking process. In the mean time, the shift of maximum phase angle towards higher frequency is also visible during SSRT. Figure 7-6(b) shows the spectra after the maximum stress. The maximum phase angle increases and shifts towards lower frequency from point 4 to point 6. Such a change in phase angle after maximum stress suggests a decrease in corrosion activity, which will be discussed later. When the deformation is close to fracture, a second time constant with a form of a long tail appears at the high frequency range (1-100Hz). After fracture, the sample exhibits very different EIS responses (phase angle and impedance magnitude) compared to the initial passive state. The second time constant with the long tail at the high frequency range becomes clearer. And the impedance magnitude curve shows a concave shape instead of a convex shape within the tested frequency range. The reason causing these changes upon fracture will be discussed later with the simulation results.

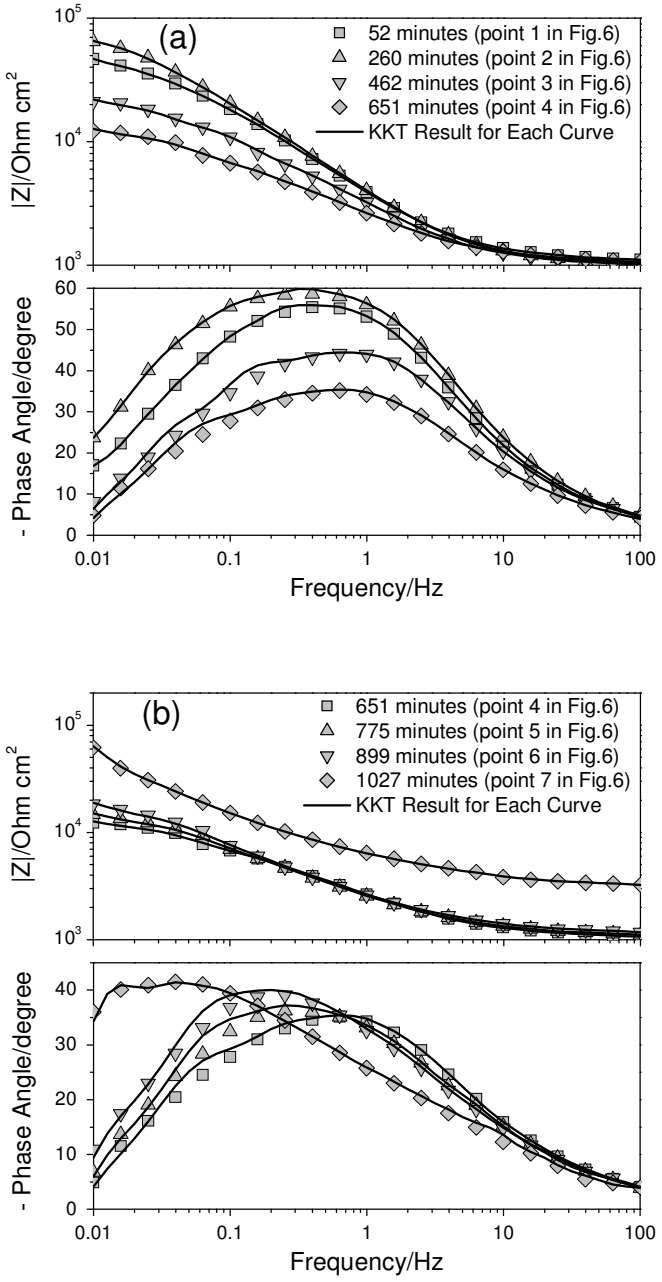

Figure 7-6. Experimental and KKT results of *ac* impedance Bode plots for selected points in Figure 7-5: (a) before the maximum stress of SSRT; (b) after the maximum stress of SSRT

7.4 Maximum Phase Angle (θ_{max}) and Frequency at Maximum Phase Angle ($f(\theta_{max})$)

The characteristics of maximum phase angle, either magnitude or frequency, can be meaningful to interpret an electrochemical process because it represents the maximum capacitor state. Any faradaic process can induce the current leakage, thus change the maximum phase angle. Shown in Figure 7-7 are the changes in θ_{max} and $f(\theta_{max})$ with time on a notched sample during SSRT. At the early stage without cracking activity, the frequency at maximum phase angle is located within a range of 0.3 to 0.4 Hz. After the global yielding of the notched sample, $f(\theta_{max})$ quickly increases to a region around 0.8 Hz. As shown in Figure 7-3, active crack growth takes place after the global yielding. Therefore, higher $f(\theta_{max})$ is related to the fast corrosion activity due to SCC. After the maximum stress, $f(\theta_{max})$ slowly decreases from 0.8 Hz to 0.3 Hz due to the ductile and shear fractures shown in Figure 7-4. Less corrosion activity takes place at this stage. Moreover, the final fracture of the sample drives the peak frequency below 0.1 Hz. Therefore, the cracking dynamics of carbon steel in SFGE can be at least categorized into two different frequency regions: (1) passive or early cracking at around 0.4 Hz; (2) active cracking at around 0.8 Hz. EIS response at a frequency can often be related to a certain type of reaction. Though the change in $f(\theta_{max})$ is not very sensitive, such a correlation between $f(\theta_{max})$ and cracking dynamics can be used as a fingerprint for characterizing the cracking stage and will be further discussed later.

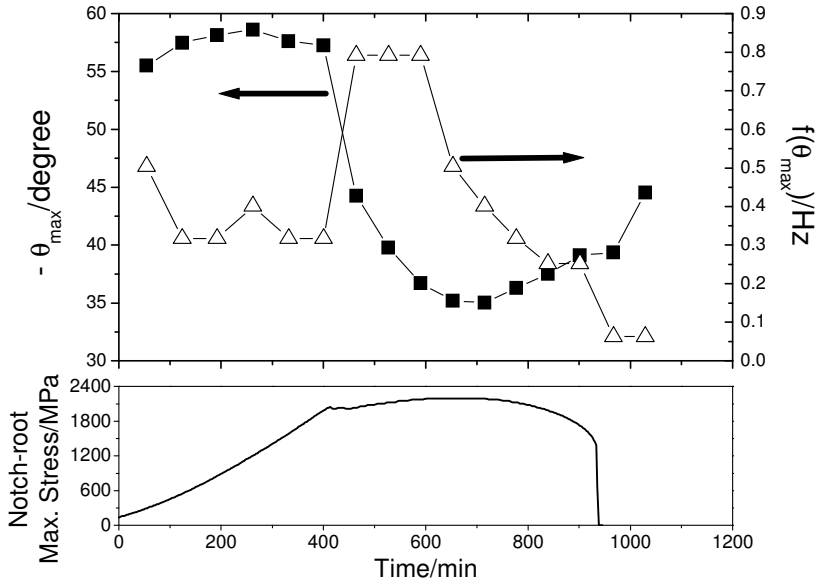

Figure 7-7. Evolution of maximum phase angle (θ_{max}) and frequency at maximum phase angle ($f(\theta_{max})$) from *ac* impedance Bode plots during SSRT under OCP in aerated SFGE

Compared with $f(\theta_{max})$, more time-resolved EIS response can be obtained from θ_{max}, as shown in Figure 7-7. θ_{max} increases initially due to the surface film growth. At around 250 minutes, θ_{max} starts to decrease till the maximum stress on the SSRT curve. Fast decreasing rate is visible after the global yielding. Such a decrease in θ_{max} is mainly due to crack initiation and growth. After the maximum stress, an increase in θ_{max}, similar to behaviors at 0.1 and 0.01 Hz in Figure 7-5, is present before the final fracture. After fracture, a re-passivation related increase in θ_{max} shows the film growth on a corroded fracture surface.

7.5 Effect of Applied Potential on SCC Behavior and EIS Response

Shown in Figure 7-8 is the stress corrosion crack depth on the fracture surface after SSRT under OCP or with a constant applied potential. It shows that the crack

growth rate increases as the applied anodic potential increases. Potentiodynamic polarization in SFGE [52, 74] has showed that the applied potential in Figure 7-8 falls into a range where the anodic dissolution current quickly increases with the potential. Thus, it can be reasonably concluded that the cracking process is closely related to a strong anodic dissolution process. With the applied cathodic potential of -115 mV vs (Ag/AgCl/1M LiCl,EtOH), the cracking is inhibited, which also supports an anodic mechanism for SCC in this system.

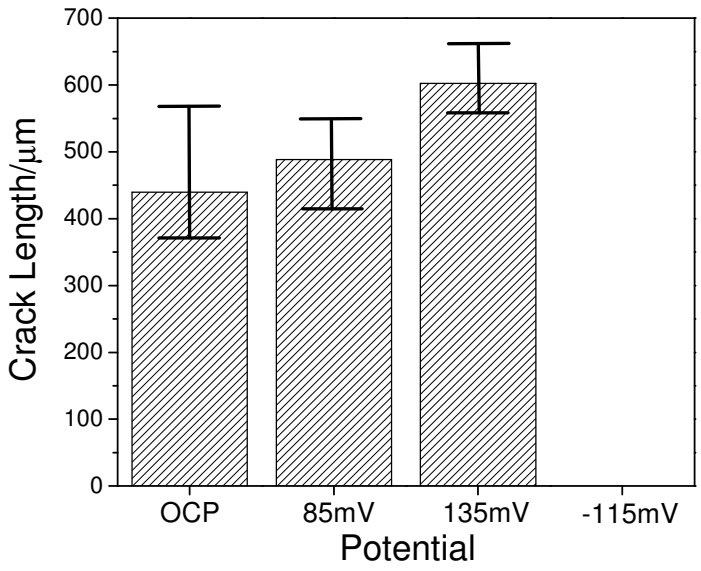

Figure 7-8. Stress corrosion crack depth on the fracture surface after SSRT under various applied potentials (vs Ag/AgCl/1M LiCl,EtOH) in aerated SFGE

The evolutions of θ_{max} and $f(\theta_{max})$ under various applied potentials are shown in Figure 7-9. Anodic current and calculated notch-root stress are also shown at the bottom of each plot as references. At 85 and 135 mV vs (Ag/AgCl/1M LiCl,EtOH), $f(\theta_{max})$ shows 0.3~0.4 Hz when there is no stress and 1.3 Hz when the stress reaches the maximum. Compared to Figure 7-7, higher $f(\theta_{max})$ is presented during crack growth. This

phenomenon can be easily related to a faster corrosion activity ahead of the crack tip which has been shown in Figure 7-8 and other literature [52]. At the same time, a lower θ_{max} is also present as the potential increases. From 85 to 135 mV vs (Ag/AgCl/1M LiCl,EtOH), anodic current increases by four times. Clearly, the anodic dissolution reduces the charge-transfer resistance, which leads to the increase in $f(\theta_{max})$ and the decrease in θ_{max}. If the anodic dissolution is stopped by a cathodic polarization at -115 mV vs (Ag/AgCl/1M LiCl,EtOH), no change in $f(\theta_{max})$ and θ_{max} is present during the tensile test. Similar to the conclusion from other literature [52], the anodic dissolution plays an important role in the SCC process.

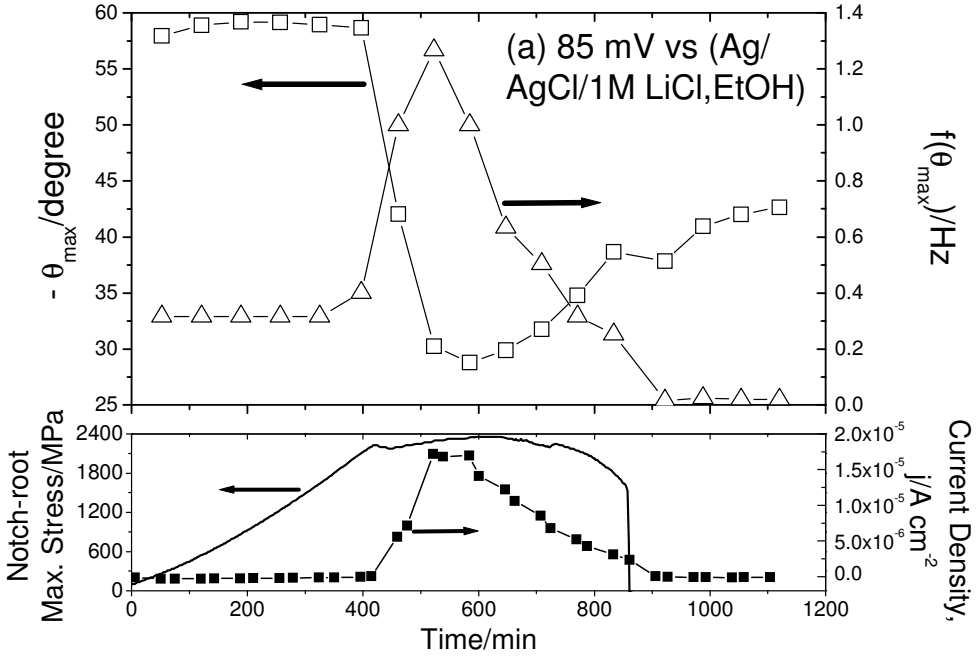

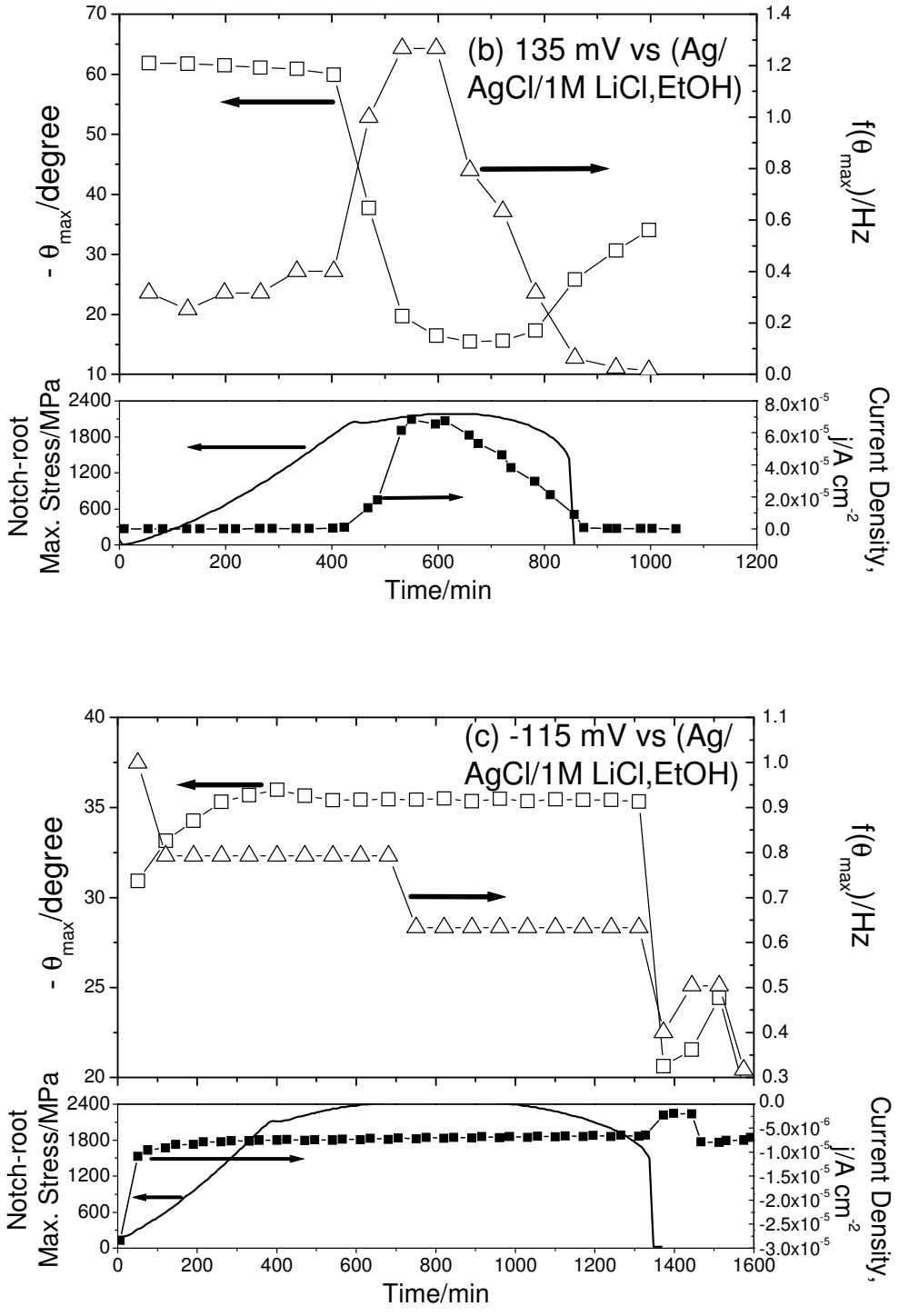

Figure 7-9. Evolutions of maximum phase angle (θ_{max}), frequency at maximum phase angle ($f(\theta_{max})$) and current density during SSRT under various applied potentials in aerated SFGE: (a) 85mV; (b) 135mV; (c) -115mV vs (Ag/AgCl/1M LiCl,EtOH)

7.6 Single Frequency Monitoring of Phase Angle during SSRT

With the detailed understanding of phase angle behavior under SCC (both magnitude and frequency changes), a single frequency monitoring was used to characterize the cracking process with the phase angle shift under a certain frequency during SSRT. Shown in Figure 7-10 is the 1 Hz phase angle monitoring with 85 and 135 mV vs (Ag/AgCl/1M LiCl,EtOH). The frequency of 1 Hz is chosen to accommodate both the cracking-related physical response and the fast test speed. The measurement time for each data point is about 1~2 seconds. Though this test duration is still longer than a film rupture process (a time scale of millisecond), it is still good enough to monitor the changes in the related electrochemical process during the crack initiation and propagation, such as the crack tip dissolution and repassivation. As shown in Figure 7-10, the applied anodic potentials at 85 and 135 mV vs (Ag/AgCl/1M LiCl,EtOH) result in a similar trend of phase angle change with respect to stress. Before the global yielding, the phase angle under 85 mV vs (Ag/AgCl/1M LiCl,EtOH) increases initially, then fluctuates and slightly decreases after 200 minutes. This suggests an electrochemical related crack initiation process. In contrast, 135 mV vs (Ag/AgCl/1M LiCl,EtOH) results in a continuous increase in phase angle before the global yielding, which may be due to the better initial passivation under higher potential. However, during the SCC propagation, 135 mV shows a significant lower phase angle than 85 mV vs (Ag/AgCl/1M LiCl,EtOH). And the sample elongation under 135 mV is shorter. Therefore, higher anodic polarization enhances the crack dissolution, which leads to higher SCC susceptibility.

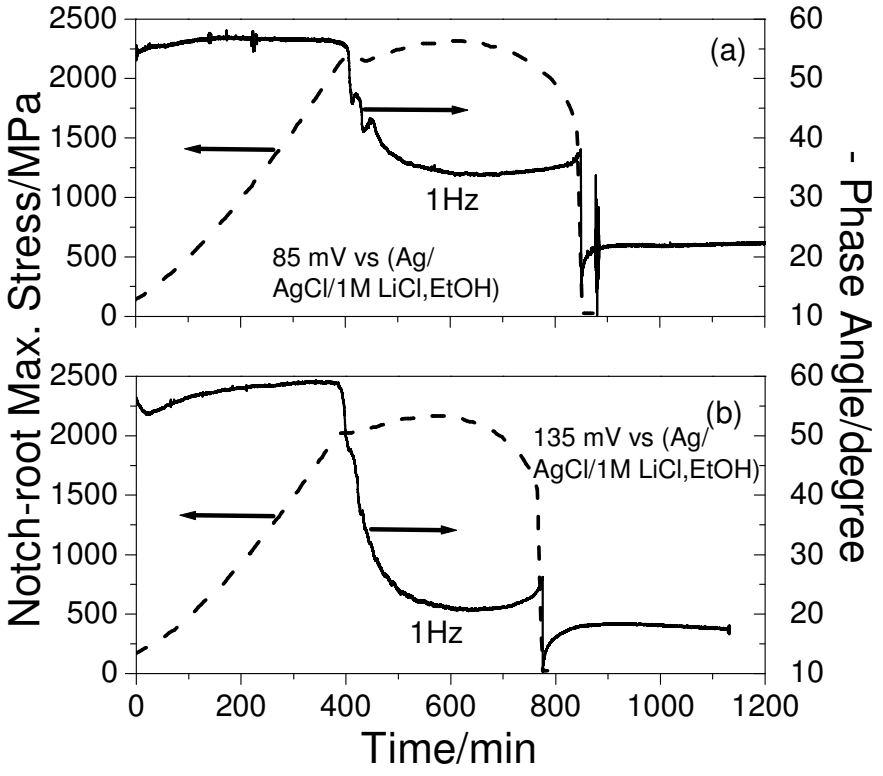

Figure 7-10. 1 Hz single frequency phase angle monitoring during SSRT under different anodic potentials: (a) 85 mV; (b) 135 mV vs (Ag/AgCl/1M LiCl,EtOH)

7.7 Physical Meaning of Phase Angle Parameters in Stress Corrosion Cracking Process

For a stress corrosion crack, many factors can be involved to interpret its EIS response, such as crack tip behavior, crack wall behavior, solution chemistry in the crack, and crack propagation path. To understand the parameters of phase angle and their relations with the SCC steps, let's start with a simple Randles circuit (Figure 7-11). R_s, R_{ct}, and C_{dl} are the solution resistance, the charge-transfer resistance and the double layer capacitance, respectively. The total impedance of this circuit can be expressed as following:

$$Z_T = R_s + \frac{R_{ct}}{1+\omega^2 R_{ct}^2 C_{dl}^2} - j\frac{\omega R_{ct}^2 C_{dl}}{1+\omega^2 R_{ct}^2 C_{dl}^2} \qquad (7\text{-}3)$$

It is clear that total impedance has a complicated form. Its absolute value is still affected by R_{ct}, C_{dl}, R_s and their combinations. Just by simply using Z_T, it is difficult to reflect the individual corrosion-related elements without fitting.

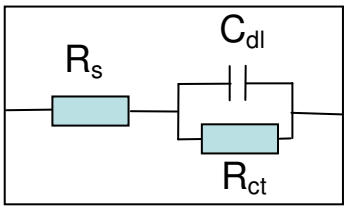

Figure 7-11. A simple Randles circuit

Based on Equation (7-3), the phase angle can be obtained as following:

$$\tan\theta = -\frac{\omega R_{ct}^2 C_{dl}}{R_s + R_{ct} + \omega^2 R_{ct}^2 C_{dl}^2 R_s} = \frac{1}{\frac{R_s + R_{ct}}{\omega R_{ct}^2 C_{dl}} + \omega C_{dl} R_s} \qquad (7\text{-}4)$$

This form in Equation (7-4) shows exactly what has been discussed in Figure 7-5. Generally speaking, the phase angle decreases as R_{ct} decreases. However, at different frequency, the changing trend in phase angle may be different. By considering ω term as a weight factor in the second part of Equation (7-4), two general conclusions can be made: (1) if ω is small, the change in $R_{ct}C_{dl}$ dominates the phase angle; (2) if ω is large, the change in C_{dl} dominates the phase angle. Since the SCC of carbon steel in SFGE is an anodic dissolution process, the change in R_{ct} is significant due to the dissolution. Therefore, low frequency range presents better sensitivity to monitor the SCC. This proves the observation in Figure 7-5.

By using the derivative $d(\tan\theta)/d\omega = 0$, the frequency at maximum phase angle and maximum phase angle can be expressed by the following Equations. (7-5) and (7-6):

$$f(\theta_{\max}) = \frac{1}{2\pi R_{ct} C_{dl}} \sqrt{\frac{R_s + R_{ct}}{R_s}} \qquad (7\text{-}5)$$

$$\theta_{\max} = -\tan^{-1}\left(\frac{R_{ct}}{2\sqrt{R_s (R_s + R_{ct})}} \right) \qquad (7\text{-}6)$$

Compared to the frequency-based phase angle expression in Equation (7-4), $f(\theta_{max})$ and θ_{max} clearly show much simpler relationships to R_{ct} and C_{dl}. Considering the fact that C_{dl} usually changes much slower than R_{ct} during fast corrosion process, $f(\theta_{max})$ should increase as R_{ct} decreases. In Equation (7-6), θ_{max} is not related to C_{dl}. It only exhibits a simple relationship with R_{ct}. And θ_{max} should decrease with the decrease in R_{ct} due to fast corrosion. As discussed in Figures 7-7 and 7-9, SCC behavior of carbon steel in SFGE leads to an increase in $f(\theta_{max})$ and a decrease in θ_{max}. Based on these expressions, it can be reasonably concluded that the cracking process induces a fast dissolution process which decreases R_{ct} for the system.

From Equations (7-4), (7-5) and (7-6), it can be concluded that the characteristics of the maximum phase angle ($f(\theta_{max})$ and θ_{max}) are good parameters to evaluate the corrosion process in a dynamic corroded system. The validity of using phase angle at a certain frequency to evaluate the corrosion process highly depends on the choice of the frequency range. Usually, a lower frequency can provide more sensitivity to the faradaic process.

7.8 Transmission Line Model

To retrieve physical significances from a crack based corrosion process, better equivalent circuit is needed to associate physical/chemical properties to mathematical variables. SCC during SSRT is a dynamic process. It involves changes in both crack geometry and electrochemical activity. Inside a single crack, these changes are contributed by crack growth, crack tip activity, crack wall activity, and crack chemistry. Therefore, a rigorous model which can accommodate geometry change and crack tip/wall activity changes is needed to relate the EIS signal to the cracking behavior. Transmission line model, initially developed for porous electrode by de Levie [75], provides a possibility to model a changing geometry by repeating certain electrochemical elements along the growth direction. It has been successfully used to understand SCC behavior [72, 73, 76] in various systems. In this study, TLM was utilized to describe the whole SCC process on a notched tensile sample during SSRT. However, as shown in Figure 7-6, the cracking process generates a high instability. The spectrum obtained from a long-time measurement is significantly averaged. Therefore, data fitting using equivalent circuit is not suitable for SCC study. In this paper, a simulation approach using TLM with real sample and crack geometry was used to understand the roles of different physical properties (or circuit elements) on the phase angle evolution during the cracking process. Furthermore, the comparison between the experimental spectra and the simulated spectra helps us derive a clearer picture of the activities inside a stress corrosion crack.

Figure 7-12(a) represents the total impedance from the tensile sample, which includes both surface impedance and crack impedance. As shown in Figure 7-12(b), the surface impedance includes a resistor and a capacitor. The crack impedance is modeled

by a TLM with a crack depth D shown in Figure 7-12(c), which includes repeated elements for solution resistance and crack wall impedance along the crack, and a crack tip impedance element. The TLM impedance used in this work is calculated based on Bisquert's enhanced model [77]. The derivations of TLM are described elsewhere [72, 73, 75, 77, 78]. The crack impedance can be described as equations (7-7) and (7-8):

$$Z_{crack} = R_{sol} \frac{1 + \frac{1}{\lambda}\frac{Z_{tip}}{R_{sol}} \coth\left(\frac{D}{\lambda}\right)}{\frac{1}{\lambda^2}\frac{Z_{tip}}{R_{sol}} + \frac{1}{\lambda}\coth\left(\frac{D}{\lambda}\right)} \tag{7-7}$$

$$\lambda = \sqrt{\frac{Z_{wall}}{R_{sol}}} \tag{7-8}$$

where R_{sol} is the length-specific solution resistance inside a crack (Ω/cm), Z_{tip} is the crack tip resistance (Ω), Z_{wall} is the crack wall length-specific impedance (Ω cm), and D is the crack depth (cm).

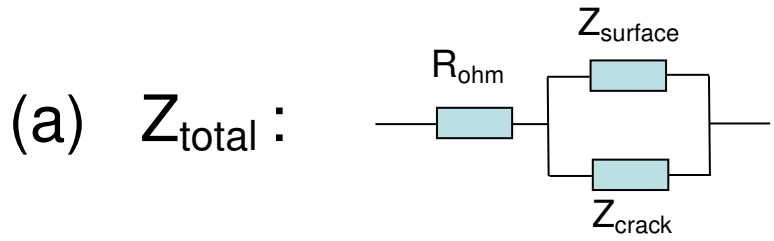

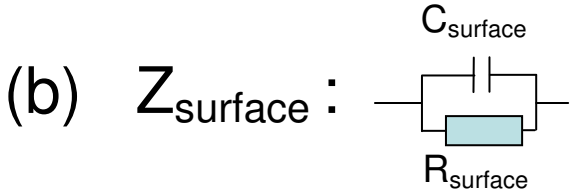

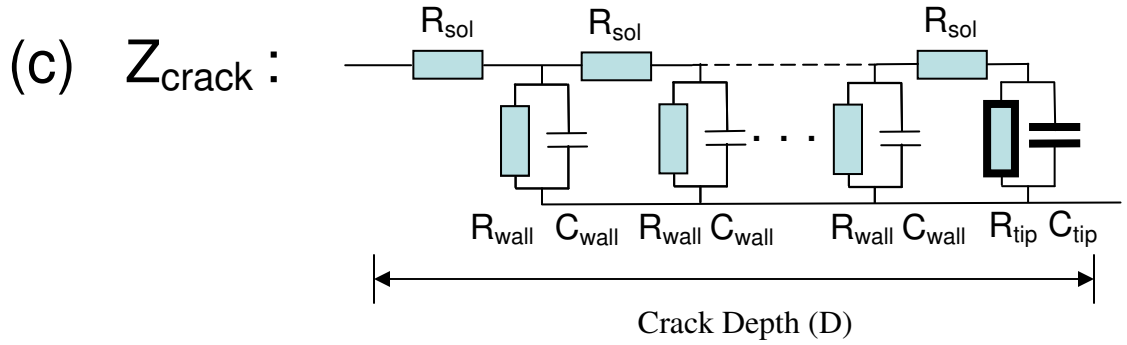

Figure 7-12. Equivalent transmission line circuit for a stress corrosion crack (including both crack and surface impedances): (a) Z_{total}; (b) $Z_{surface}$; (c) Z_{crack}. $R_{surface}$, $C_{surface}$, R_{wall}, C_{wall}, R_{tip}, and C_{tip} stand for resistance and capacitance components for sample surface, crack wall, and crack tip. R_{sol} represents the solution resistivity inside the crack.

7.9 Simplified Physical Model for a Stress Corrosion Crack

Figure 7-13 describes a physical picture of a propagating stress corrosion crack on carbon steel in SFGE during SSRT. As shown in Figure 7-4, the final fracture surface of a notched tensile sample exhibits three distinct regions: ductile fracture region, shear fracture transition region, and SCC brittle fracture region. SCC region forms like a continuous ring around the fracture surface on the notched tensile sample. Based on the experimental observations, stress corrosion crack growth on a notched sample can be categorized into two stages, shown respectively in Figures 7-13(a) and 7-13(b). At the early stage, a number of cracks initiate from the defects [51] and grow independently. With time, these independent stress corrosion cracks coalesce and form a continuous SCC ring which propagates towards the center of the sample.

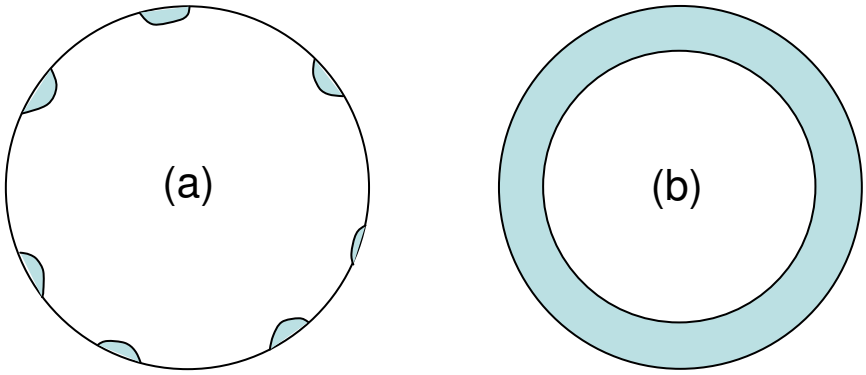

Figure 7-13. Crack evolution schematics on the fracture surface: (a) crack growth at early stage; (b) crack growth after full crack coalescence.

Based on the nature of a stress corrosion crack, the crack morphology is simplified to a rectangular cuboid geometry, as shown in Figure 7-14. Crack morphology includes crack surface length (L), crack mouth opening width at the surface (W), and crack depth (D). Compared to a cylindrical geometry, this cuboidal geometry makes a better visualization for the crack propagation, which usually has faster growth rate along the length and depth direction, but less growth rate along the crack opening width. The active zone of the crack tip is defined with a fixed width of 5μm and a length of L.

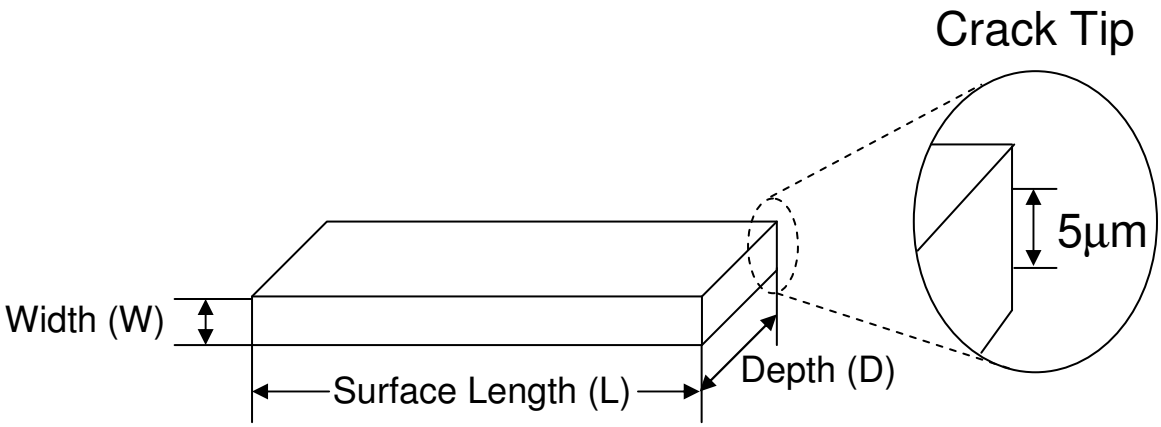

Figure 7-14. Simplified schematic of a crack with crack depth D, crack opening width W, crack surface length L, and active crack tip width 5μm.

Without further explanation in the figure caption, the values of some universal parameters used in crack simulation are shown Table 7-1, which are all obtained and estimated based on experiments. Based on Figure 7-2(a), a resistance magnitude of $1.6x10^5$ Ω cm^2 and a capacitance of $2.5x10^{-5}$ F/cm^2 are set as a passive state in TLM simulation.

Table 7-1. Universal parameters for the crack simulation.

Gauge Surface Area (cm^2)	2
Gauge Surface Resistance $R_{surface}$ (Ω cm^2)	$1.6x10^5$
Gauge Surface Capacitance $C_{surface}$ (F/cm^2)	$2.5x10^{-5}$
Solution Resistivity (Ω cm)	880

In the following simulation, the electrochemical elements ($R_{surface}$, $C_{surface}$, R_{wall}, C_{wall}, R_{tip}, C_{tip}) are changed from this passive state to a more actively corroded state in order to investigate their effects on EIS response. In addition to these values, three other assumptions are made in order to utilize the de Levie's transmission line model:

(1) the solution resistivity inside the crack keeps constant along the crack axis;

(2) the solid phase represents a metallic electrode behavior;

(3) the local crack tip and crack wall impedances are independent from the whole electrochemical system.

7.10 Effect of the Inactive (Non-cracking) Surface Area on EIS Response

The equivalent circuit in Figure 7-12 contains two major components: surface impedance and crack impedance. On a notched tensile sample like the one in Figure 3-1(c), the stress is concentrated at the notch root throughout SSRT. In contrast, the stress

on other surface areas, such as the notch side and the sample gauge, always remains below the yield stress. These regions remain in the passive state, similar to that for the unstressed static immersion sample, as shown in Figure 7-2 and elsewhere [52]. The effect of these non-cracking surface areas on the total impedance Z_{total} is simulated and shown in Figure 7-15. When we consider a crack with a fixed geometry and activity, the decrease in the exposed surface area outside the crack raises the total impedance at all frequencies. Most importantly, the maximum phase angle, which exhibits a strong correlation to SCC kinetics (Figures. 7-7 and 7-9), shifts towards the higher frequency range when the exposed area decreases. At the mean time, the magnitude of maximum phase angle increases as the surface area decreases. Since the higher frequency measurement requires much less testing time, the decrease in the sample surface area exposed to the SFGE could enable EIS to characterize faster cracking process with good spectrum stability.

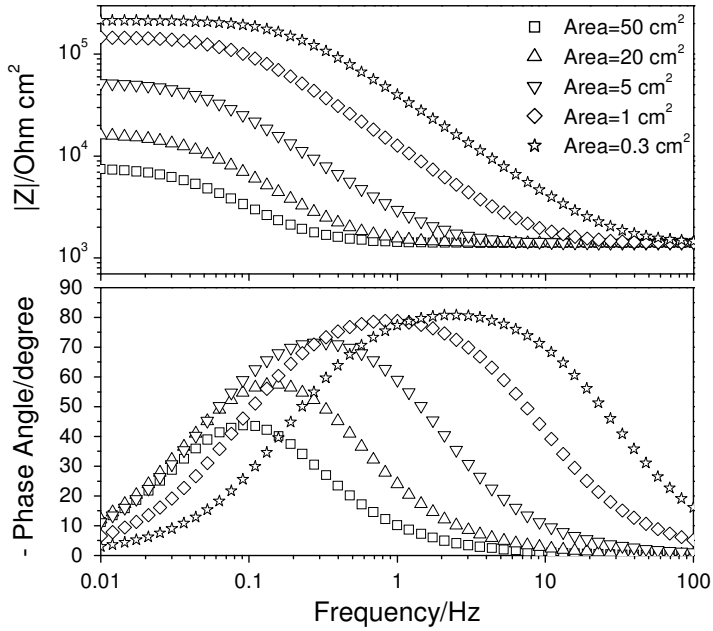

Figure 7-15. TLM simulation about the effect of unstressed gauge surface area on EIS response from an SSRT sample. Both the electrochemical and geometrical parameters are fixed as following: R_{wall}=1.6x10^5 Ω cm^2, R_{tip}=50 Ω cm^2, C_{tip}= C_{wall}=2.5x10^{-5} F/cm^2, D=100μm, W=50μm, L=7540μm.

7.11 Phase Angle Response at Two Stages of Crack Growth

The schematic in Figure 7-13 shows two stages of crack growth on a notched tensile sample tested by SSRT in the aerated SFGE. The major difference between the two stages is the change in the area of the active crack tip. At the early stage of independent crack growth (Figure 7-13(a)), both active crack tip length and crack depth increase with time. However, at the later stage when cracks coalesce to form a single circular ring, shown in Figure 7-13(b), the SCC ring propagation reduces the aspect ratio, resulting in a slight decrease in crack tip length with time. Figure 7-16 simulates the EIS responses from the same crack with an active crack tip at different crack growth stages. The crack geometry is calculated based on Figure 7-14. For the case of the independent

growth (Figure 7-13(a)), the relationships among crack length (L), depth (D) and width (W) are L/D=4 and D/W=2, which are obtained based on the interrupted SSRT using smooth sample. For the case of the ring growth, D/W=2, and L is calculated based on sample diameter reduction. As shown in Figure 7-16(a), ten cracks with the same size are simulated for the independent growth mode at the early stage. Various crack depths, from 10 μm to 300 μm, are simulated to show the EIS response at different crack growth stage, representing a dynamic change during the propagation of an active crack before coalescence. The results show that independent crack growth reduces the impedance at low frequency range (< 1 Hz). Furthermore, phase angles at low frequencies (< 1 Hz) also decrease as the crack depth increase. The maximum phase angle decreases and shifts slightly towards higher frequency region as the crack depth increases. However, after coalescence, crack growth as a form of ring, shown in Figure 7-16(b), generates almost similar EIS spectra from 10 μm to 200 μm depths. This is mostly because the crack growth as a form of ring makes little changes on the length of active crack tip. Therefore, Figure 7-16 suggests that crack initiation at the early stage with the increase in crack density can generate more changes in phase angle than ring-type crack propagation. Such a difference is primarily due to the multiple crack initiation at the early stage. This explains the experimental observation in Figures.7-5 and 7-7 where the decreasing rate in phase angle and θ_{max} shows the maximum value around the global yield stress. However, when the stress is close to the maximum stress, the value of phase angle keeps low and constant.

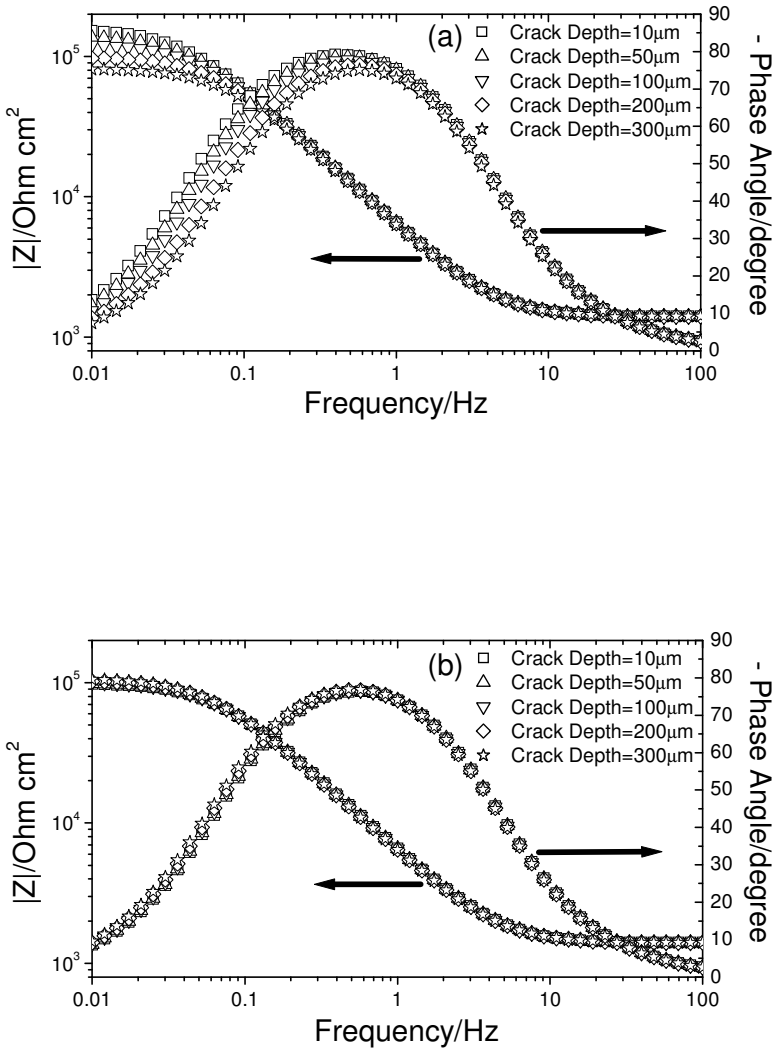

Figure 7-16. TLM simulation about the effect of crack depth on EIS response from an SSRT sample. The electrochemical parameters are fixed as following: R_{wall}=1.6x10^5 Ω cm^2, R_{tip}=50 Ω cm^2, C_{tip}= C_{wall}=2.5x10^{-5} F/cm^2. The crack geometry evolutions are set respectively as following: (a) independent crack growth, L/D=4, D/W=2; (b) crack growth in the form of ring, D/W=2, L is calculated based on ring propagation geometry.

Figure 7-17 shows the simulation results for the effects of an active crack tip vs. a passive crack tip during the early-stage crack initiation growth. The crack growth is an independence growth before coalescence, which means the active crack tip length keeps increasing. The changes in $f(\theta_{max})$ and θ_{max} are shown in Figure 7-17. When the crack tip

is active (Figure 7-17(a)), $f(\theta_{max})$ keeps increasing and θ_{max} keeps decreasing during the crack propagation. The experimental results in Figures. 7-7, 7-9(a) and 7-9(b) confirm this situation. However, once the tip keeps a non-corroding passive condition, as shown in Figure 7-17(b), the simulation shows there is no change in $f(\theta_{max})$ and θ_{max} during then tensile test. Figure 7-17(c) shows an interesting condition in which the crack tip, crack wall and sample surface are all active with low resistance. Although the EIS response shows low θ_{max} and high $f(\theta_{max})$, no change in $f(\theta_{max})$ and θ_{max} is visible during the extension of the crack depth. This also explains the experimental results in Figure 7-9(c), where cathodic polarization inhibits the corrosion and keeps $f(\theta_{max})$ and θ_{max} constant. Therefore, it can be concluded that the observed changes in $f(\theta_{max})$ and θ_{max} in the experiments are mostly due to an active local dissolution (usually a crack tip) on a large passive surface (usually a crack wall and sample surface).

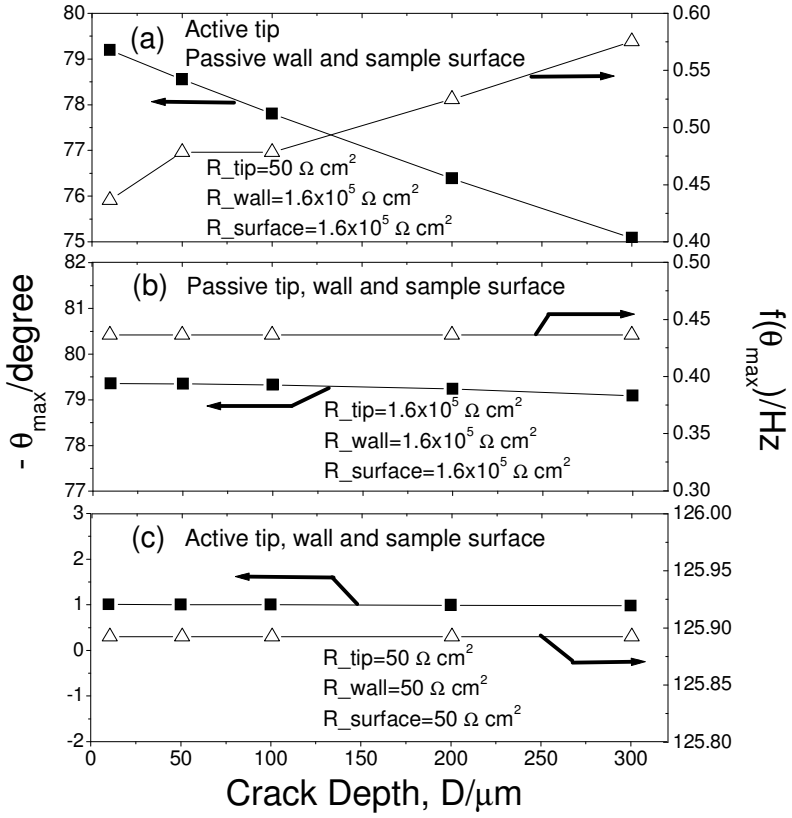

Figure 7-17. TLM simulation of maximum phase angle (θ_{max}) and frequency at maximum phase angle ($f(\theta_{max})$) under different crack tip, wall and sample surface activities at early-stage crack growth with various crack depths. The following electrochemical parameters are fixed: $C_{tip}=C_{wall}=C_{surface}=2.5x10^{-5}$ F/cm^2, independent crack growth (L/D=4, D/W=2). The values of resistor elements are following: (a) $R_{tip}=50\ \Omega$ cm^2, $R_{wall}=R_{surface}=1.6x10^5\ \Omega$ cm^2; (b) $R_{tip}= R_{wall}=R_{surface}=1.6x10^5\ \Omega$ cm^2; (c) $R_{tip}= R_{wall}=R_{surface}=50\ \Omega$ cm^2.

7.12 Effect of Solution Resistivity Inside The Crack on EIS Signal

Understanding the chemistry and electrochemistry inside a crack is always important for interpreting the cracking behavior [26, 79-81]. In Figure 7-18, we simulate the effect of solution resistivity inside the crack with an active crack tip and passive crack wall. SFGE has a high solution resistivity, which is around 4.4 KΩ cm [74]. According to the literatures, solution resistance inside a crack should be higher than that in the bulk solution, primarily due to the higher cation and anion concentrations [26]. In an anodic

dissolution type SCC, it is contributed by the fast local anodic dissolution and the autocatalytic activities. Solution resistivity is varied from 0.22 to 4.4 KΩ cm. No significant change is made on the EIS response. Therefore, the changes in phase angle in experiments are mostly related to the cracking behavior, not the change in the local resistivity inside the crack.

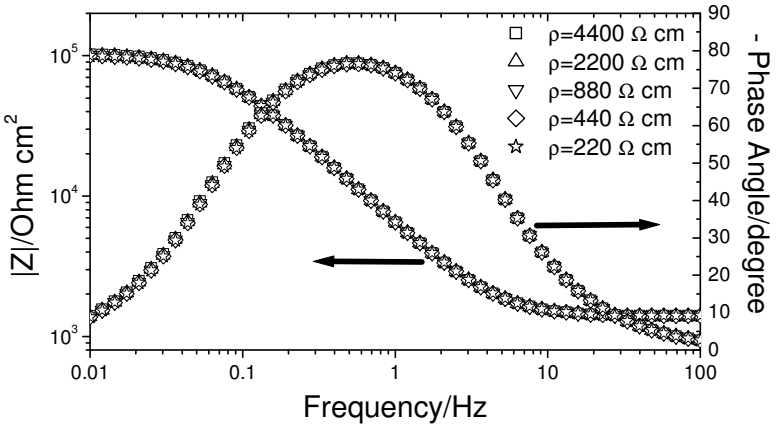

Figure 7-18. TLM simulation of the effect of solution resistivity inside the crack with an active crack tip and a passive crack tip. The following parameters are fixed: R_{wall}=1.6x10^5 Ω cm^2, R_{tip}=50 Ω cm^2, C_{tip}=C_{wall}=2.5x10^{-5} F/cm^2, D=100μm, W=50μm, L=7540μm.

7.13 Effect of Crack Tip and Crack Wall Resistance during Crack Propagation

The value of resistor is usually directly related to the dissolution process. Figure 7-19 shows the effect of crack tip resistance (R_{tip}) and crack wall resistance (R_{wall}) on EIS response from the same crack geometry. For a stress corrosion crack, the corrosion activity at the crack tip is usually significantly more active than that at the crack wall, which maintains the crack geometry and results in a growth of crack along the direction of crack tip. A passive surface of carbon steel in SFGE usually exhibits a polarization

resistance around 10^5 Ω cm^2, as shown in Figure 7-2(a). Therefore, the values of R_{tip} and R_{wall} for simulation are chosen below this passive value to study their effects. As shown in Figure 7-19(a), the increase in the crack tip activity (decrease in R_{tip}) reduces the total impedance of carbon steel in SFGE at low frequency range. The phase angle below 1 Hz also decreases as R_{tip} decreases. At the mean time, θ_{max} decreases and shifts towards the high frequency range. These simulation results present trends similar to the experimental observation in the previous part. Shown in Figure 7-19(b) is the effect of crack wall activity. Reduced by three orders of magnitude in R_{wall} from the passive state, EIS response shows a very slight change. Further reduction in R_{wall} to 500 Ω cm^2, which is close to an active crack tip behavior, significantly decreases both phase angle and resistance. Clearly, the crack wall activity in a stress corrosion crack can not be similar as the crack tip activity. Otherwise, it can blunt the crack tip and change a crack into a pit.

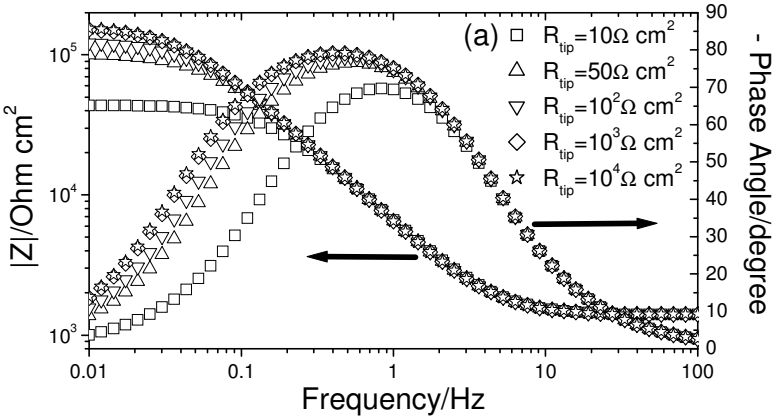

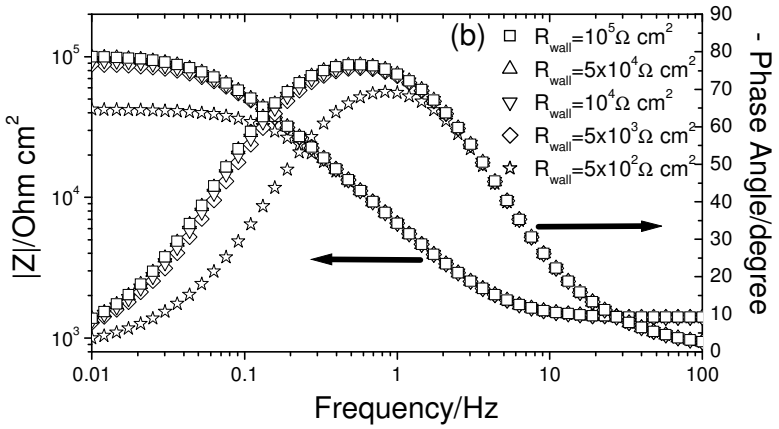

Figure 7-19. TLM simulation about the effect of the resistance of (a) crack tip and (b) crack wall on EIS response of a stress corrosion crack. The crack geometry is fixed as following: D=100μm, W=50μm, L=7540μm. The electrochemical parameters are set respectively as following: (a) $R_{wall}=1.6x10^5\ \Omega\ cm^2$, $C_{wall}=2.5x10^{-5}\ F/cm^2$, $C_{tip}=2.5x10^{-5}\ F/cm^2$; (b) $R_{tip}=50\ \Omega\ cm^2$, $C_{tip}=2.5x10^{-5}\ F/cm^2$, $C_{wall}=2.5x10^{-5}\ F/cm^2$.

The effects of a passive crack wall and an active crack wall against various crack tip activities are summarized in Figure 7-20 using simulation. When the crack wall is relatively passive, the crack tip dominates the EIS when R_{tip} reduces to below 1000 $\Omega\ cm^2$. However, when the crack wall is very active, such as the situation in a pit, EIS signal keeps constant. It should be noted that the simulated θ_{max} and $f(\theta_{max})$ in Figure 7-20(a) exhibits a more passive behavior than the experimental result in Figure 7-7. Therefore, it can be reasonably concluded that the actual R_{wall} on the crack wall should be lower than a passive value, but still much higher than an active value of crack tip. These simulated results suggest that an increase in corrosion activity at the crack tip serves as a main reason for the significant drop in phase angle during SSRT.

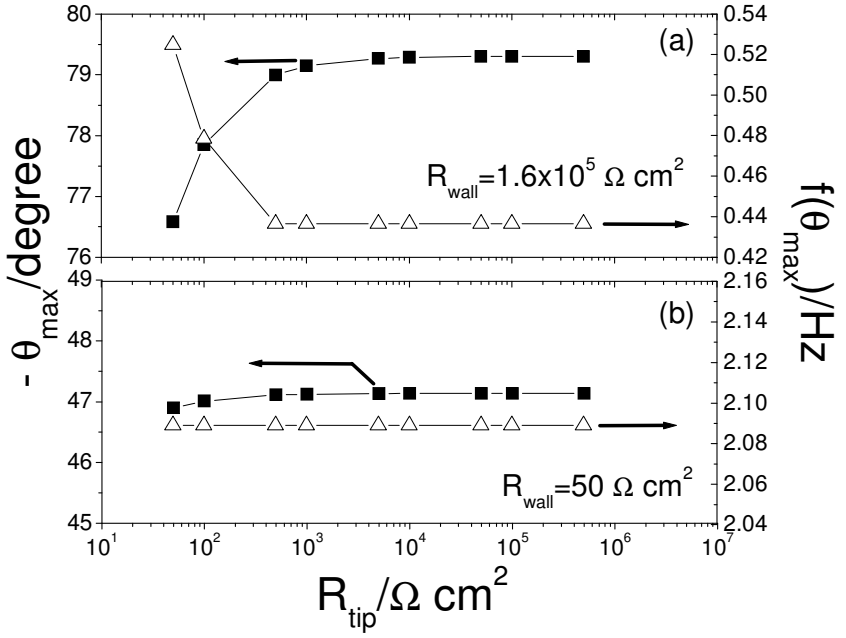

Figure 7-20. TLM simulation of the effect of crack tip area-specific resistance (R_{tip}) on maximum phase angle (θ_{max}) and frequency at maximum phase angle ($f(\theta_{max})$) in cracks with passive and active crack walls. C_{tip}=C_{wall}=2.5x10^{-5} F/cm^2, sample surface area = 2 cm^2, D=100μm, W=50μm, L=7540μm. The crack wall resistances are following: (a) R_{wall}=1.6x10^5 Ω cm^2; (b) R_{wall}=50 Ω cm^2.

7.14 Effect of The Crack Tip and The Crack Wall Capacitance on EIS Response

In all the simulations above, the capacitances in both crack tip and crack wall are considered to be the same as its passive value 2.5x10^{-5} F/cm^2. This assumption is made because the charge-transfer resistance usually plays a dominant role in a dissolution process. Furthermore, the change in the resistance is much faster than that in the capacitance, as shown in Figure 7-2(a). Here in Figure 7-21, the effect of the capacitance is studied in detail. In Figure 7-21(a), the increase in the crack tip capacitance (C_{tip}) does not change the EIS response. Only when C_{tip} increases to a very high value of 0.25 F/cm^2, the maximum phase angle shifts to a lower frequency. At the mean time, two time constants appear in the EIS response. In Figure 7-21(b), the increase in the crack wall

capacitance (C_{wall}) continuously shifts the whole phase angle curve to a lower frequency range. A second time constant, appearing as a flat tail in phase angle curve, is visible in the spectrum. The impedance magnitude curve presents a concave shape in the frequency range of 100~0.01 Hz. The shape of spectrum under high C_{wall} is very similar to what has been observed in Figure 7-6(b), where both the long-tail second time constant in phase angle and the concave shape in impedance are experimentally visible upon fracture. Therefore, the simulation in Figure 7-21(b) suggests that the dissolution and porous corrosion product formation also take place on the crack wall (see Figure 7-4), which changes the permittivity and increases the C_{wall} during the cracking process. This phenomenon becomes visible once the crack tip corrosion activity significantly decreases upon the final fracture.

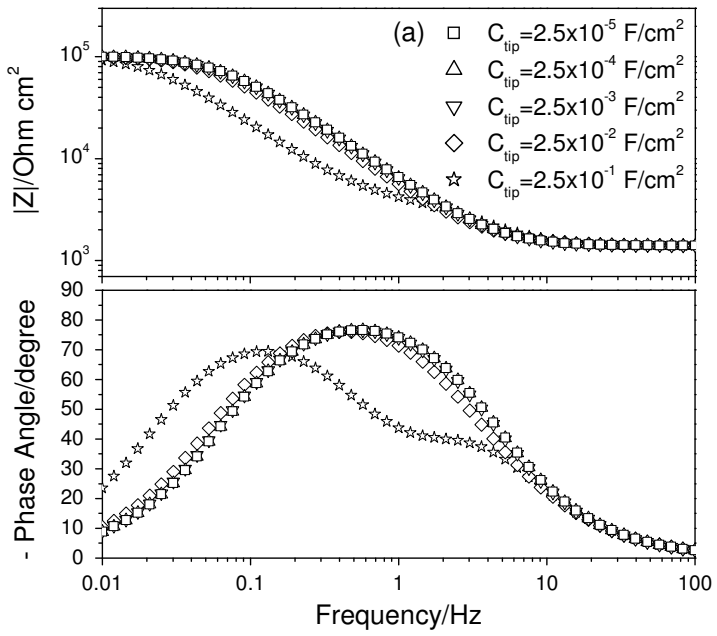

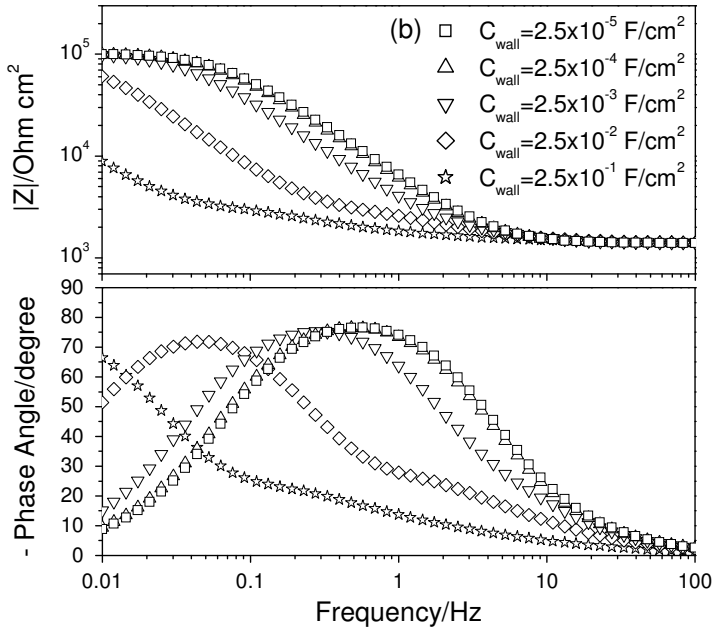

Figure 7-21. TLM simulation about the effect of (a) C_{tip} and (b) C_{wall} on EIS response of a stress corrosion crack. The crack geometries are fixed as following: D=100μm, W=50μm, L=7540μm. Sample surface area = 2 cm^2. The electrochemical parameters are set respectively as following: (a) R_{wall}=1.6x10^5 Ω cm^2, C_{wall}=2.5x10^{-5} F/cm^2, R_{tip}=50 Ω cm^2; (b) R_{tip}=50 Ω cm^2, C_{tip}=2.5x10^{-5} F/cm^2, R_{wall}=1.6x10^5 Ω cm^2.

7.15 Conclusions

The changes in electrochemical impedance, especially phase angle in Bode format, have been thoroughly studied to develop an understanding of the SCC of carbon steel in the SFGE. Compared to normal OCP measurement, Bode analysis of phase angle provides more variables, such as magnitude and frequency. Within a certain frequency range, phase angle is sensitive to the resistance change in the crack during SCC. Strong correlation between phase angle and SCC was observed within a frequency range from 0.1 Hz to 1 Hz. The electrochemical response from the cracking process can be studied using both phase angle at a single frequency and maximum phase angle. Frequency at maximum phase angle also suggests the cracking behavior, increasing towards an active

corrosion region at around 1 Hz. The behavior of maximum phase angle is mathematically more related to charge-transfer resistance. Though TLM model can not be used to retrieve full physical process during cracking due to the model complexity and the instability of the cracking process, the TLM simulation based on real geometry can still provide some understanding of stress corrosion crack growth in this system by correlating the changing trend of phase angle in simulation and in experiments. Several conclusions can be obtained: (1) small sample size shifts the SCC-sensitive frequency towards high frequency region, which can reduce the EIS measurement time and increase the stability; (2) multiple crack initiation at the early stage can produce more changes in the phase angle than the ring-type crack growth at the latter stage;(3) the crack tip is very corrosive with fast dissolution during SCC while the crack wall is less active; (4) the change in the solution resistivity inside the crack does not affect EIS response; (5) the crack wall capacitance may also increase during SCC.

CHAPTER 8

CATHODIC ACTIVITIES OF HYDROGEN AND OXYGEN ON CARBON STEEL IN SIMULATED FUEL-GRADE ETHANOL AND ITS IMPACT ON HYDROGEN EMBRITTLEMENT

Previous chapters have systematically discussed the corrosion and stress corrosion cracking of carbon steel in SFGE. The unique anodic behavior of carbon steel in ethanol system results in a lower passivity and higher dissolution rate, depending on ethanol chemistry. As the other part of corrosion reaction, cathodic activities in the solution also play an important role in controlling the corrosion kinetics and possible hydrogen production. Compared to the anodic behavior, no systematic work has been done towards understanding the cathodic corrosion reactions in ethanolic environments, specially oxygen reduction and hydrogen evolution. In this chapter, detailed electrochemical studies were carried out to understand the cathodic activities on carbon steel in SFGE. Oxygen and hydrogen activities were studied based on the changes in ethanol chemistry. Hydrogen uptake and its impact on hydrogen embrittlement were also studied.

8.1 Effect of Dissolved Oxygen on Cathodic Reactions

It is known that both oxygen and nitrogen have much higher solubility in ethanol than in water [82]. Figure 8-1 shows the measured dissolved oxygen concentration in 200-proof ethanol under the bubbling gas with various oxygen-nitrogen mixing ratios.

When the oxygen concentration in the gas is smaller than 21%, the measured value of dissolved oxygen exhibits a good linear relationship with oxygen concentration in the gas mixture. The value of dissolved oxygen in ethanol under 21% O_2+79% N_2 gas flow is around 79.8 ppm, which is very similar to other reported values in literature [57, 82, 83]. However, higher oxygen partial pressure in gas, e.g. 50%, results in a slight deviation from the linear relationship given by Henry's law with the mathematical formula of C=P/k. Here, C is the dissolved oxygen concentration in ethanol. P is the partial pressure of oxygen in ethanol. k is Henry's constant and equal to 10360 Pa m^3 mol^{-1} at 293 K [57]. Such a deviation at higher oxygen partial pressure region is probably due to the influences of the adopted gas flow rate and the optical sensing mechanism. Nevertheless, the data shown in Figure 8-1 exhibits a clear range of dissolved oxygen present in ethanol under various O_2-N_2 mixing ratios in the gas flow used in this study.

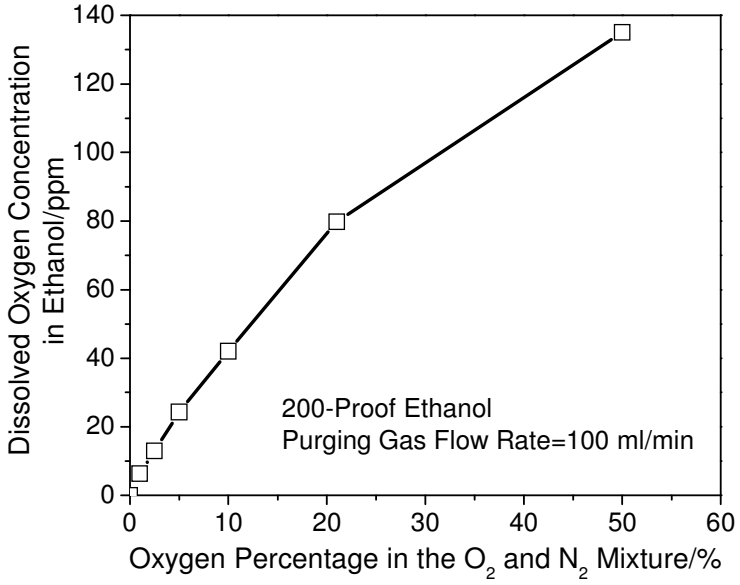

Figure 8-1. Measured dissolved oxygen concentration (ppm) in 200-proof ethanol, under 100 ml/min purge-gas flow rate, with various oxygen concentration in the gas mixture.

The cathodic polarization behavior of carbon steel in acidic SFGE under different aeration conditions are shown in Figure 8-2. The oxygen percentage in the bubbling gas changes from 0% to 50%. As the oxygen concentration decreases, OCP also decreases. Four major slopes of cathodic reaction, marked from I to IV, are visible in acidic SFGE. Clearly, they represent four different major cathodic reactions. The presence of oxygen plays an important role in reduction reaction. With even 1% O_2, Reaction III quickly changes to Reaction I, undergoing a significant decrease in the overpotential. The limiting current density of Reaction II decreases as the oxygen concentration decreases. When the oxygen concentration reaches 1%, Reaction II disappears and the limiting current density of Reaction I starts to decrease. Clearly, Reactions I and II represent the reduction activities involve oxygen. At very high cathodic overpotential, where the diffusion of oxygen to the metal surface becomes a limiting step, all curves converge at Reaction IV. The deficiency of oxygen, close to surface, stops the oxygen reduction reaction. Without oxygen present as a reactant (100% N_2 in gas-mixture), it can be reasonably concluded that hydrogen evolution or other reduction reactions contribute to Reactions III and IV in Figure 8-2.

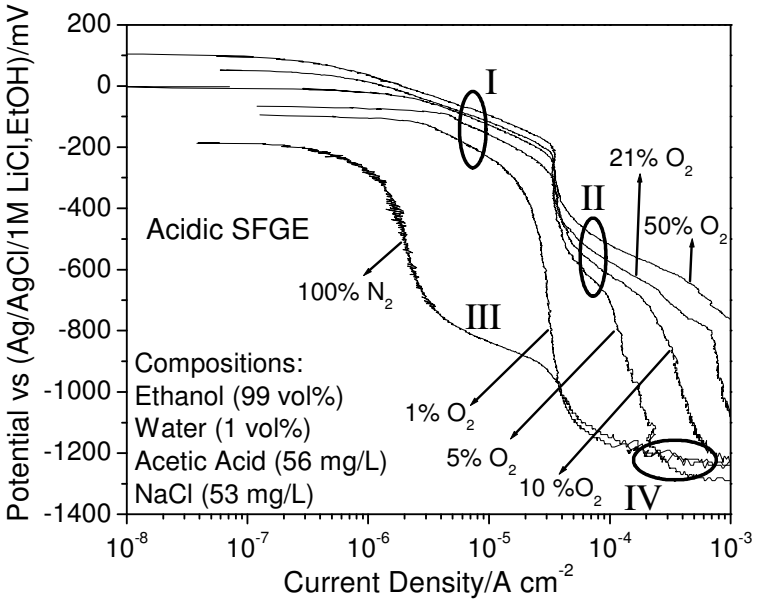

Figure 8-2. Cathodic polarization behavior of carbon steel in acidic SFGE (ethanol (99 vol%), water (1 vol%), acetic acid (56 mg/L), NaCl (53 mg/L)) with different aeration conditions

8.2 Effect of Acetic Acid on Cathodic Reactions

In the FGE standard [84], acetic acid is included as an oxidation byproduct present in fuel-grade ethanol. Shown in Figure 8-3 are the effects of acetic acid on the cathodic behaviors of carbon steel in 200-proof ethanol under aerated and de-aerated conditions. In Figure 8-3(a), under aeration (21% O_2 + 79% N_2), OCP slightly decreases with an increase in the acidity. A huge drop in the OCP is visible with the addition of 280 mg/L acetic acid. The limiting current density after the initial slope (similar to Reaction I in Figure 8-2) decreases as the acetic acid concentration decreases. However, the limiting current density after the 2nd slope (similar to Reaction II in Figure 8-2) does not change with the acetic acid concentration. It suggests that protons dissociated from acetic acid only participate in Reaction I at a low cathodic overpotential. Since both Reactions I and

II are oxygen dominated reduction processes, the possible reactions can be reasonably summarized as following for 200-proof ethanol:

For Reaction I:

$$O_2 + 4CH_3COOH + 4e^- \Leftrightarrow 2H_2O + 4CH_3COO^- \quad (8\text{-}1)$$

For Reaction II:

$$O_2 + 2C_2H_5OH + 4e^- \Leftrightarrow 2C_2H_5O^- + 2OH^- \quad (8\text{-}2)$$

With the presence of acetic acid, proton assists oxygen reduction at lower cathodic overpotentials (Equation 8-1). At the high overpotential region, the deficiency of free proton close to the surface limits the kinetics of Equation 8-1. Then, ethanol itself is further dissociated to promote the oxygen reduction in Equation 8-2.

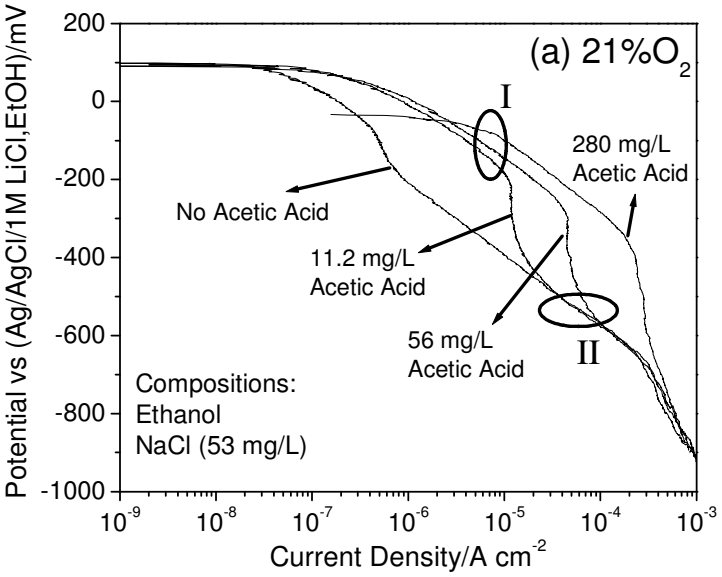

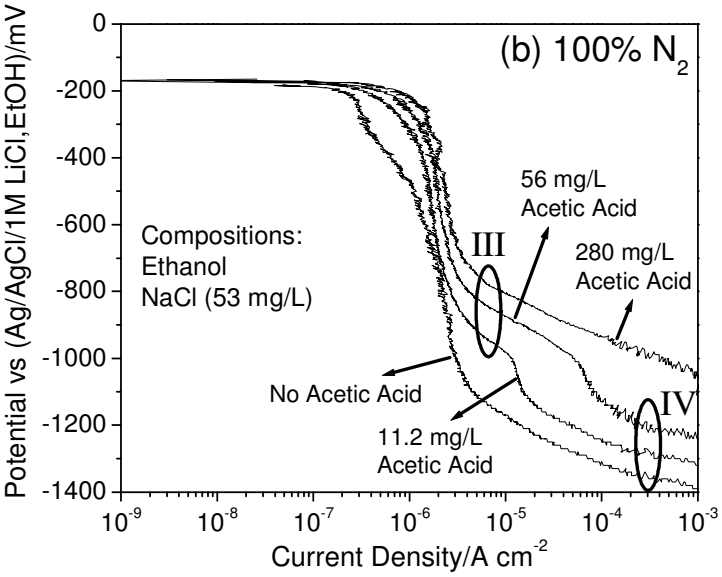

Figure 8-3. Cathodic polarization behavior of carbon steel in 200-proof ethanol with different acetic acid concentrations: (a) aerated condition (21% O_2+79% N_2); (b) deaerated condition (100% N_2)

The main difference between the tests for Figures 8-2 and 8-3 is the presence of water in SFGE. In Figure 8-2, SFGE contains 1 vol% water. Water exhibits a higher dissociation constant than ethanol. Therefore, in Reaction II, the dissociation of water is also possible and the reaction can be described as following:

$$O_2 + 2H_2O + 4e^- \Leftrightarrow 4OH^- \qquad (8\text{-}3)$$

Figure 8-3(b) shows the effect of acetic acid on the cathodic activity in 200-proof ethanol under de-aerated condition. The current values for the slope between -700 mV and -1000 mV vs Ref. increases as the acetic acid concentration increases. This slope represents the similar reaction as Reaction III in Figure 8-2. Without acetic acid, Reaction III disappears. These results indicate that the proton plays an important role in supporting Reaction III in ethanolic environments. Without oxygen, hydrogen reduction is a possible

cathodic reaction at the region with relatively high cathodic overpotential. Reaction III may be described by the following equation:

$$CH_3COOH + e^- \Leftrightarrow CH_3COO^- + H_{ads} \quad (8\text{-}4)$$

The adsorbed hydrogen atoms, H_{ads}, can subsequently combine to form H_2 molecules or diffuse into the metallic lattice, depending on the kinetics of these processes in certain environment. At a cathodic overpotential beyond -1200 mV vs Ref., the deficiency of acetic acid near the surface promotes a limiting reduction current and another reaction slope, which is similar to Reaction IV in Figure 8-2. Apparently, ethanol can be reduced under such a high overpotential. The reduction reaction is following:

$$C_2H_5OH + e^- \Leftrightarrow C_2H_5O^- + H_{ads} \quad (8\text{-}5)$$

It should be noted that hydrogen evolution in Equation (8-5) relies on the discharge of ethanol, which results in a reduction potential far below the free corrosion potential. Therefore, this process should not contribute to the corrosion process significantly. The verification of these hydrogen reactions will be discussed later using hydrogen permeation test.

Different from the 200-proof ethanol results in Figure 8-3(b), SFGE in Figure 8-2 contains 1 vol% water which may also contribute to the cathodic reduction reaction. In addition to the ethanol discharge described in Equation (8-5), water may also be reduced in Reaction IV to produce hydrogen at a high cathodic overpotential beyond -1000 mV vs Ref., as following:

$$H_2O + e^- \Leftrightarrow OH^- + H_{ads} \quad (8\text{-}6)$$

The cathodic activation slopes for the major reactions, β_c, have been summarized in Table 8-1 from Figure 8-3. The measurements of the activation slope in this table are

based on the curves with 280 mg/L and 0 mg/L acetic acid in Figures 8-3(a) and 8-3(b), which reduces the effects from the mass transport and mixed cathodic reactions. Generally speaking, oxygen reduction reactions exhibit higher activation slopes than hydrogen evolution reactions. Under aeration, oxygen reduction in Equation (8-1) shows a very similar slope as that in Equation (8-2). However, under de-aeration, hydrogen evolution through acetic acid discharge (Equation (8-4)) shows a smaller activation slope than that through ethanol discharge (Equation (8-5)). The activation controlled cathodic reaction slope, β_c, can be described using the following expression:

$$\left|\beta_c\right| = \frac{2.303RT}{\alpha nF} \tag{8-7}$$

where R is the gas constant, T is the temperature, α is the charge-transfer coefficient, n is the transferred electron number during reaction, and F is the Faraday's constant. Charge-transfer coefficient refers to the fraction of the interfacial energy that helps in lowering the activation energy barrier of a reaction. Clearly, oxygen reduction in Equation (8-1) has a similar α as that in Equation (8-2) if the number of electron is considered to be the same. But hydrogen evolution in Equation (8-5) has a lower α than that in Equation (8-4), which is primarily due to the difficulty in discharging an ethanol molecule. Of course, the way of the further hydrogen recombination can also affect the slope. Oxygen reduction transfers more electrons than hydrogen evolution, but still exhibits higher activation slopes than hydrogen evolution. This may suggests that transporting and decomposing O_2 in ethanol form a possible limiting step for cathodic reaction in ethanol.

Table 8-1. Measured activation slopes of different oxygen and hydrogen cathodic reactions in 200-proof ethanol based on Figure 8-3.

Reaction Type	Activation Slope (mV vs Ref. / decade)
Reaction in Equation (8-1)	191 ± 5
Reaction in Equation (8-2)	190 ± 7
Reaction in Equation (8-4)	145 ± 5
Reaction in Equation (8-5)	178 ± 8

8.3 Cathodic Activities under a Wide Range of pHe and Oxygen Concentration

Figure 8-4 shows the cathodic polarization curves of carbon steel in acidic, neutral and alkaline SFGE solutions under 21%, 5% and 0% oxygen-containing gas bubbling through the solution. OCPs of acidic SFGE and neutral SFGE are very similar though neutral SFGE shows a slightly more negative potential than acidic one. However, alkaline SFGE with 50 mg/L NaOH exhibits much lower OCP, which is mostly due to the change of redox reaction on the metal surface. The presence of acetic acid can promote Reactions I (Equation (8-1)) and III (Equation (8-4)) under the conditions with and without oxygen, respectively. Neutral and alkaline SFGEs present very similar cathodic reaction patterns under all oxygen partial pressures. Based on the existing knowledge for aqueous environments with different pH values, it can be reasonably inferred that the cathodic reactions in neutral and alkaline SFGE can be explained by Eqs. (2) and (3) for aerated condition and Equations (8-5) and (8-6) for de-aerated condition. The Reactions I-IV in Figure 8-2 are also labeled in Figure 8-4 based on the pattern and mechanism similarity. It should be noted that acidic, neutral and alkaline SFGEs show

very similar oxygen limiting current density under different dissolved oxygen concentrations, which suggests that the overall kinetics of oxygen reduction reaction in SFGE is similar under different pHe. At potentials close to the OCP, carbon steel in neutral SFGE (in Figures 8-4(a)-(c)) shows a current plateau with very low cathodic limiting current in the range of 10^{-7}-10^{-6} A/cm^2. The detailed reason for this reduction reaction will be discussed later.

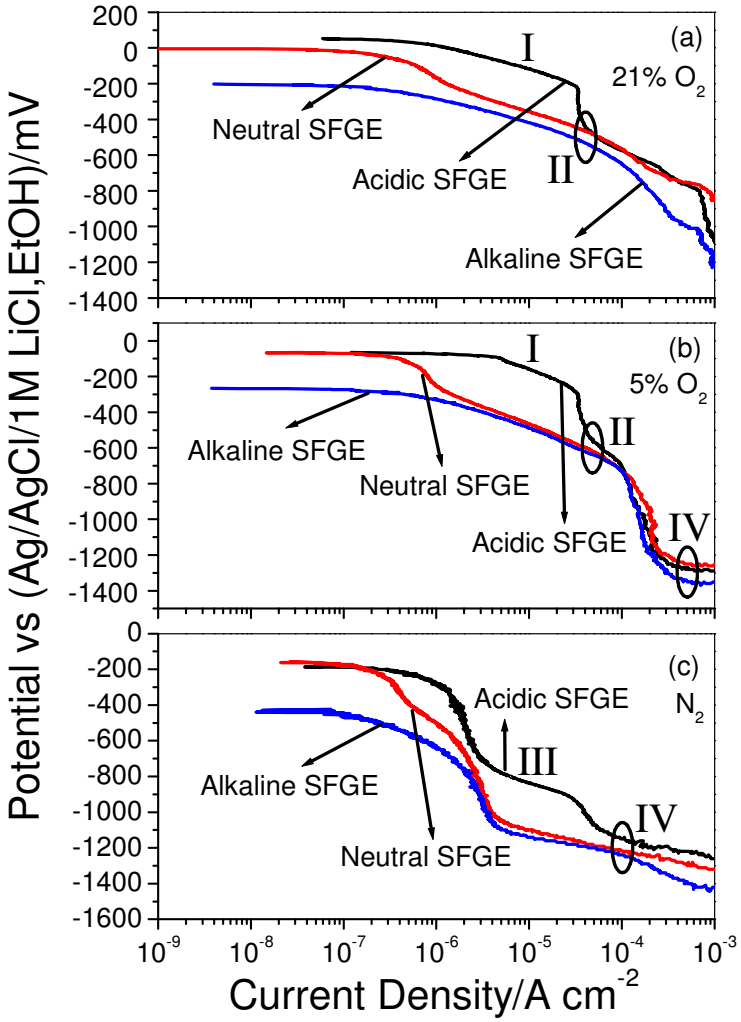

Figure 8-4. Cathodic polarization behavior of carbon steel in acidic (56 mg/L acetic acid), neutral and alkaline (50 mg/L NaOH) SFGE environments: (a) 21% O_2+79% N_2; (b) 5% O_2+95% N_2; (c) 100% N_2

8.4 Changes in Water Content and pHe due to Cathodic Reactions

Reactions from Equation (8-1) to Equation (8-6) show that the pHe and water content of the SFGE solutions should change, depending on the cathodic reactions involved. Table 8-2 shows the results from the pHe and water content analysis before and after 3 days' polarization tests at different conditions. According to the previous discussion, -260 mV vs Ref. in the acidified 200-proof ethanol (under 21% O_2) refers to the proton related oxygen reduction of ethanol described in Equation (8-1), where proton is consumed and water is produced as a result of this reaction. Whereas, -600 mV vs Ref. in neutral SFGE (under 21% O_2) refers to oxygen reduction of both ethanol and water which can be described using Equations (8-2) and (8-3), resulting in the production of hydroxyl ions. In comparison, -1180 mV vs Ref. in neutral SFGE (under 100% N_2) refers to the hydrogen evolution in both ethanol and water at very high cathodic overpotential, described in Equations (8-5) and (8-6). From the present results in Table 8-2, the changes in pHe and water content of SFGE show clear evidences of the changes predicted based on the proposed cathodic reactions. In the first situation, both pHe and water content increase during oxygen reduction, which confirms the consequences of the reaction in Equation (8-1). In the second and third situations of neutral SFGE, both pHe values increase mostly due to the production of OH^- in Equations (8-2), (8-3) and (8-6). An interesting phenomenon that should be noted is that water concentration always decreases with cathodic polarization in either the second or the third situation of Table 4. This suggests that water (Equations (8-3) and (8-6)) has higher reduction kinetics than ethanol (Equations (8-2) and (8-5)) in SFGE, which is primarily due to its higher dissociation constant and ease of discharge.

Table 8-2. The changes in water content and pHe as the result of cathodic polarization. Acidified ethanol contains 200-proof ethanol, acetic acid (280 mg/L), and NaCl (53 mg/L). Neutral SFGE contains ethanol (99 vol%), water (1 vol%), NaCl (53 mg/L). (Note: theoretically, 1 vol% water in ethanol is equally to 12640.5 ppm).

Testing Condition	Time	Water (ppm)	pHe
Acidified ethanol with 280 mg/L acetic acid, 21% O_2, -260mV vs Ref. (see Figure 8-3(a) for polarization curve)	before test	284.7	4.5
	after 3 days' test	1388.3	5.6
Neutral SFGE, 21% O_2, -600 mV vs Ref. (see Figure 8-4(a) for polarization curve)	before test	12625.8	6.2
	after 3 days' test	9324.3	7.4
Neutral SFGE, 100% N_2, -1180 mV vs Ref. (see Figure 8-4(c) for polarization curve)	before test	12820.4	6.3
	after 3 days' test	8534.5	8.7

8.5 Hydrogen Permeation Tests

Equations (8-4), (8-5) and (8-6) suggest that atomic hydrogen could be produced by the reduction reaction. If so, then the atomic hydrogen could also diffuse into the metal and affect its mechanical properties under these conditions. Hydrogen permeation tests were carried out to verify the hydrogen production during hydrogen evolution in ethanolic environments. Shown in Figure 8-5 is the uptake of hydrogen cathodic permeation current under some selected environmental conditions. The cathodic hydrogen current transients are visible for the proton reduction due to acetic acid (Reaction III) and hydrogen evolution due to ethanol and water discharge (Reaction IV), shown in Figures 8-5(b) and 8-5(c) respectively. Under the tested conditions in SFGE,

the permeation current density is around $2x10^{-7}$ A/cm^2, which is much smaller than the one normally reported in the aqueous environment for carbon steel. The difference between ethanolic environment and aqueous environment can be due to the slow cathodic kinetics and fast surface recombination rate for hydrogen on carbon steel in ethanol. The proton related oxygen reduction reaction, such as Reaction I in Figure 8-5(a), shows a continuous decrease in permeation current. This indicates that no measurable hydrogen is produced in the potential region where oxygen reduction Reaction I (or Equation (8-1)) is the predominant reaction, though proton consumption during Reaction I is detected in Table 8-2. It should be noted that no hydrogen gas bubble can be observed on the steel surface during the hydrogen evolution in ethanolic environment, which may be due to the unique surface tension properties in ethanolic environments.

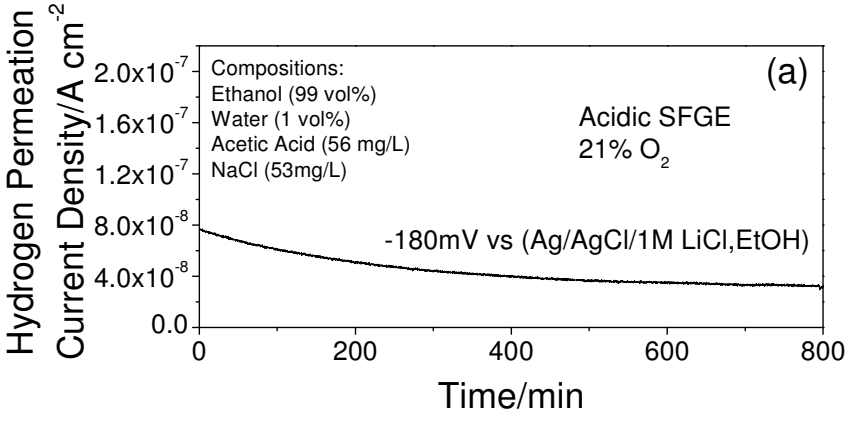

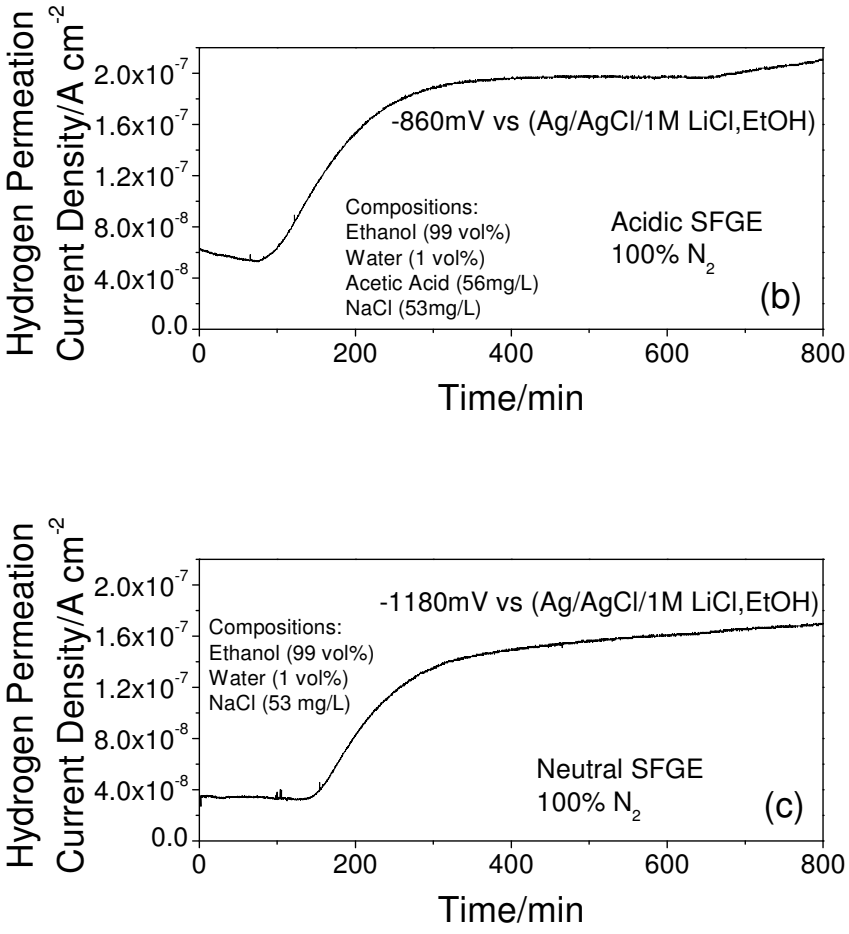

Figure 8-5. Hydrogen permeation current transient for a carbon steel membrane (thickness around 1.5 mm) exposed under different environmental conditions. (Time zero is cut from the original data and only chosen for better comparison): (a) Reaction I (see Figure 8-4(a)) in aerated acidic SFGE; (b) Reaction III (see Figure 8-4(c)) in de-aerated acidic SFGE; (c) Reaction IV (see Figure 8-4(c)) in de-aerated SFGE

8.6 Role of Water on the Cathodic Reactions of Carbon Steel in Ethanol

It has been widely reported that the addition of water plays an important role on the corrosion activities of metallic materials in alcohol [4, 5, 23, 36, 37, 51, 74]. In general, the presence of water in ethanol, even in a small amount, can significantly change the solvent structure and its physical properties, such as dielectric constant, oxygen content [82], and acidity [51]. Surface film characteristics can also be changed

due to the water [74]. However, few studies have been done to investigate the water effect on the cathodic activities of steel in ethanol. Figure 8-6 shows the cathodic polarization curves of carbon steel in 200-proof ethanol with different water contents. Both aerated and de-aerated conditions show a decrease in the OCP as water concentration in SFGE increases. In Figure 8-6(a), no significant change in the oxygen reduction (Reaction II) is visible as the water concentration in ethanol changes. However, in Figure 8-6(b), the hydrogen evolution (Reaction IV) shows a decrease in cathodic overpotential (or an increase in current density at a given potential) as the water concentration increases. The activation slope of Reaction IV also decreases slightly with the increase in water content. This may be due to the easier discharge of water than that of ethanol during the cathodic reaction. The ease of water discharge in ethanol can also lead to the fast consumption of water during cathodic reaction in SFGE, which is shown by the results in Table 8-2. However, with the addition of water into ethanol, no steep slope of limiting current is present in Figures 8-6(a) and 8-6(b) to separate the ethanol reaction and the water reaction. Clearly, ethanol and water share the same cathodic reaction slope. The mechanistic reason for this, which may be related to their reaction similarity and high miscibility of water and ethanol, is still not clear at this stage.

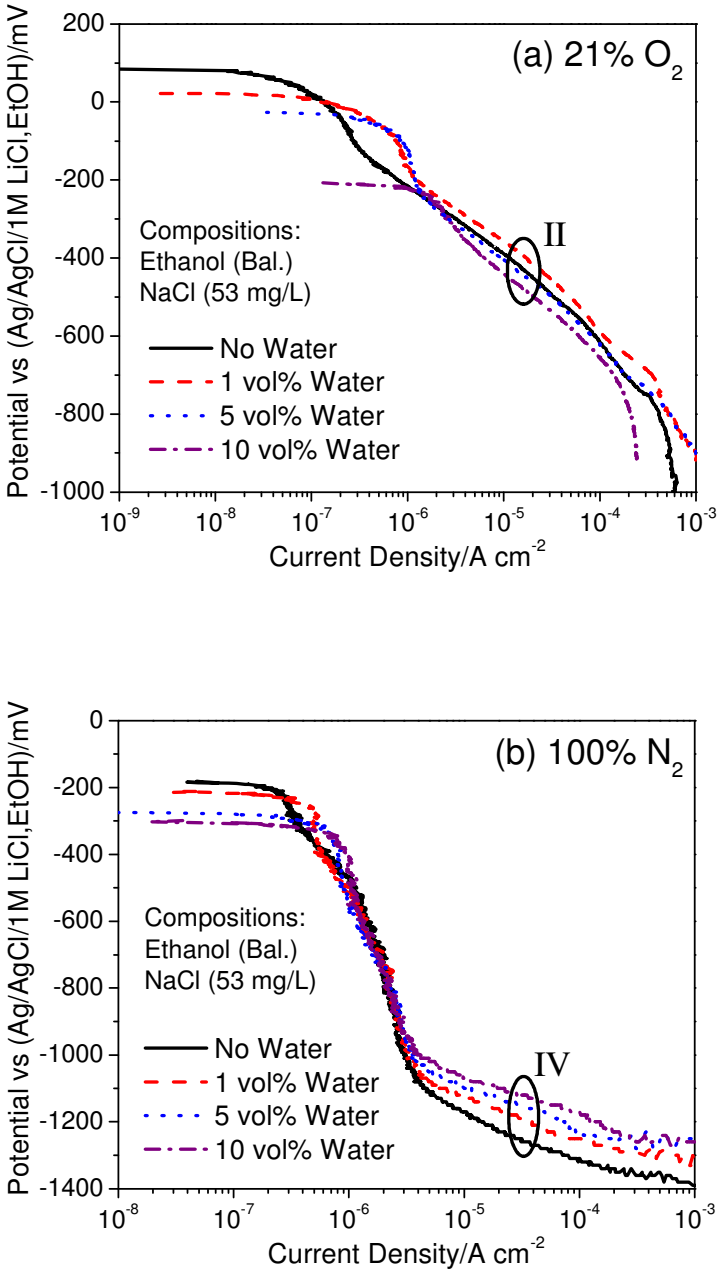

Figure 8-6. Cathodic behavior of carbon steel in 200-proof ethanol (ethanol (balanced), NaCl (53 mg/L)) with different water content: (a) 21 %O_2+79% N_2; (b) 100% N_2

The effects of water in acidic and alkaline ethanol are shown in Figure 8-7. In all tested conditions, OCP decreases with the increase in water content. In Figure 8-7(a), the cathodic current density in both aerated and de-aerated acidic ethanol increases as the

water content increases. Especially under de-aerated condition, proton reduction from acetic acid (Reaction III) shows a large decrease of its cathodic overpotential (or increase of current density at a given potential) with the addition of water in ethanol, which is most likely due to the easier dissociation and reduction of acetic acid in water than ethanol. The cathodic activation slope of acetic acid reduction in ethanol keeps similar before and after the water addition. In alkaline ethanol, as shown in Figure 8-7(b), the oxygen reduction (Reaction II) under aerated condition shows a slight decrease in current density due to the water addition. The hydrogen evolution due to the discharge of ethanol and water (Reaction IV) shows an increase in current density which is similar to the results in neutral condition, shown in Figure 8-6(b). Therefore, it can be concluded from Figure 8-7 that the presence of water can enhance the hydrogen reduction from both acetic acid and ethanol.

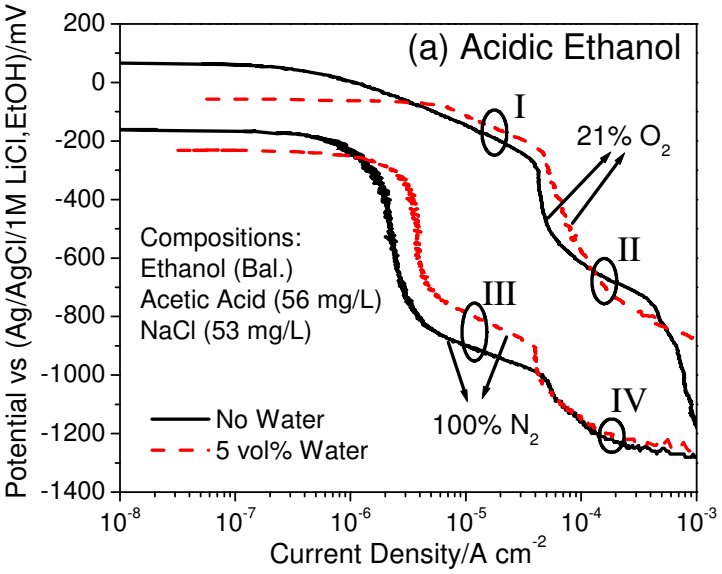

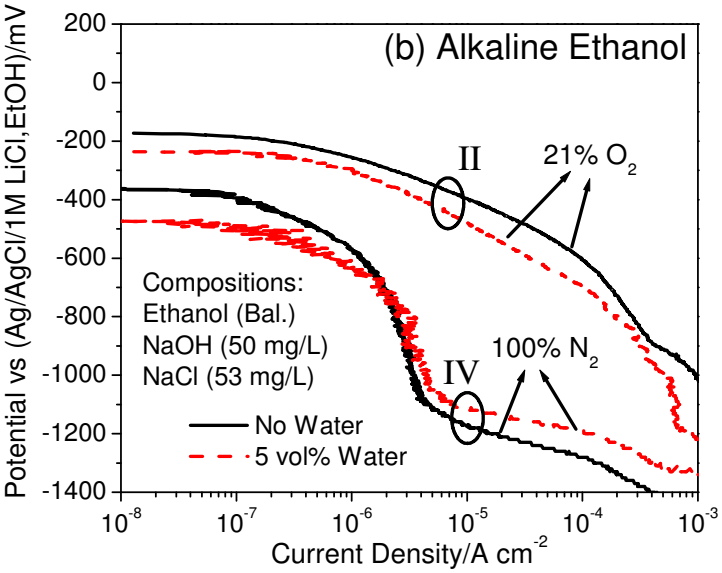

Figure 8-7. Effect of water on the cathodic behavior of carbon steel in (a) acidic ethanol and (b) alkaline ethanol

The addition of a small amount of water (e.g. 0.5 %) has been reported to decrease the free proton mobility in methanol, which possibly results in a decrease of corrosion rate [37]. Brossia et al. proposed that the reason for this is that the protonation of water can weaken the existing Grotthuss proton hopping mechanism in pure methanol, leading to the decrease in proton mobility. Their hypothesis is based on the results from the strong acid HCl in pure methanol. However, for the SFGE in the present study, a much weaker acid, acetic acid, is present in ethanol. Since acetic acid usually has higher acidity in water than in ethanol [51], the effect of the water addition in acidic SFGE highly depends on the competition between the kinetics of the dissociation of acetic acid and the protonation of water in ethanol. Figure 8-8 shows the change of the cathodic current as the water content is incrementally increased from 0 % to 5 %. Oxygen reduction in Reaction I (Figure 8-8(a)) and hydrogen evolution in Reaction III (Figure 8-8(b)) were selected as examples to study this effect. Clearly, the cathodic current in both

figures increase with the water content, suggesting an increase in the proton activity and availability. The decrease in proton mobility due to water protonation, which was reported in other system [37], is not visible in both oxygen reduction and hydrogen evolution in SFGE. In conclusion, in SFGE where acetic acid and ethanol are present, the reaction kinetics is mostly enhanced by the fast increase of acetic acid dissociation due to the water addition. The water solvation in ethanol can increase the free proton availability and reaction kinetics.

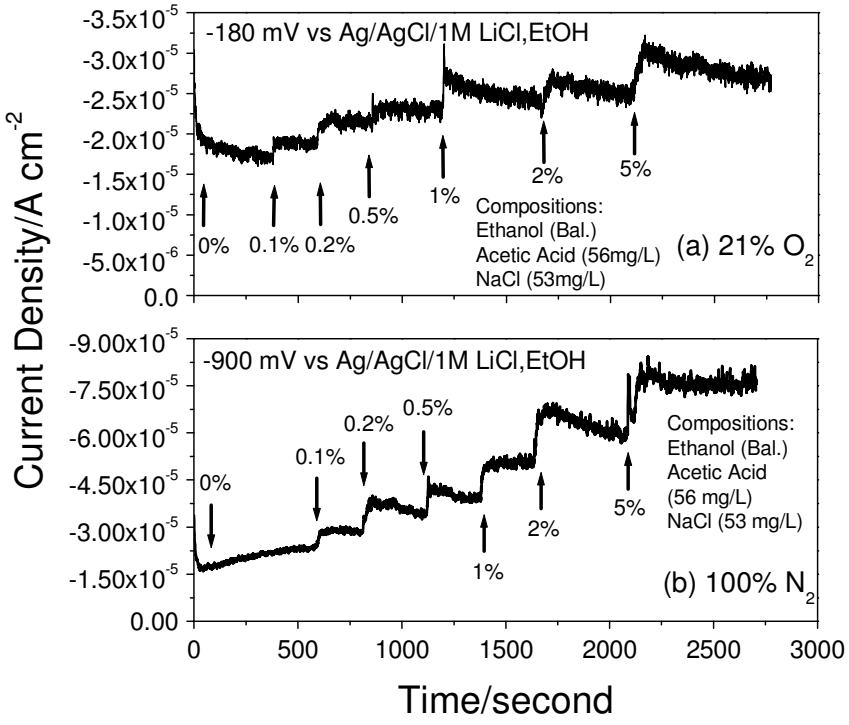

Figure 8-8. Effect of water addition on the cathodic current density from the proton related activities in the acidic SFGE: (a) 21% O_2+79% N_2, proton related oxygen reduction (Reaction I); (b) 100% N_2, hydrogen evolution from acetic acid (Reaction III)

8.7 Electrochemical Behavior in SFGE near Open-circuit Potential

Oxygen and hydrogen cathodic activities in SFGE have been thoroughly discussed in the previous sections. Some of these reactions require high overpotentials. In reality, general corrosion is mostly controlled by the electrochemical activities near OCP. As mentioned previously in Figure 8-4, a small plateau with a low cathodic limiting current in a range of 10^{-7}-10^{-6} A/cm^2 can be observed from the cathodic polarization curve in neutral SFGE. This phenomenon is also present in 200-proof ethanol, shown in Figure 8-6, no matter whether the ethanol is under aeration or de-aeration. Similar plateaus of cathodic current near OCP were also observed by Bellucci et al. [48], who attribute such a phenomenon to the reduction of pre-existing oxides based on Pourbaix diagram analysis. Figure 8-9 shows the enlarged cathodic polarization curves at the close-to-OCP region. In Figures 8-9(a) and 8-9(b), the solution is pure 200-proof ethanol without the water addition. In Figures 8-9(c) and 8-9(d), the water containing ethanol (5 vol% water) was also studied for comparison. Cathodic potentiodynamic polarization in Figure 8-9 was carried out in two ways: (1) in cathodic direction (from OCP to more negative cathodic overpotential); (2) in anodic direction (from negative cathodic overpotential to OCP). In both ethanol solutions, with or without water, the plateaus near OCP are present only when the polarization is in cathodic direction. With the polarization in anodic direction, no plateau of cathodic current is shown. The polarization in cathodic direction starts from an OCP equilibrium state where carbon steel surface may have metal oxides or other oxidized species. However, the anodic direction polarization starts from a highly negative reducing potential where fewer oxidation products are expected on the metal surface. The differences in the presence of the plateau region between cathodic

scan curve and anodic scan curve in the same potential range suggest that the reduction of surface pre-existing oxides and other oxidation products forms the first cathodic reaction in SFGE near OCP. In Figure 8-9, the current plateau formed under aeration is larger and more stable than the one formed under de-aeration, suggesting that oxygen plays an important role in the fast formation of pre-existing oxides and species on the carbon steel surface near OCP in ethanolic environments.

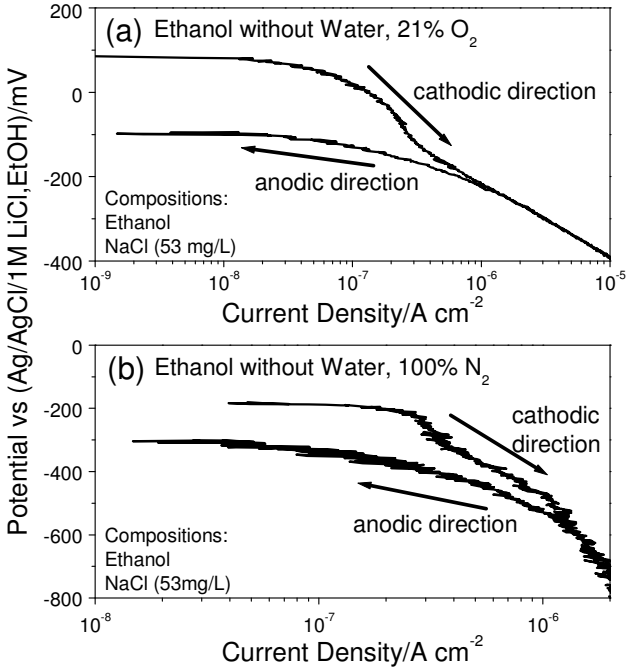

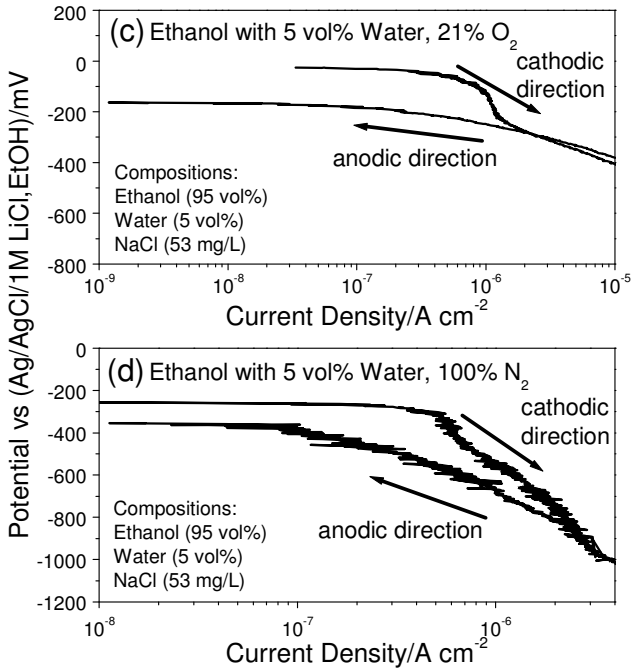

Figure 8-9. Cathodic activities near open-circuit potential: (a) ethanol with no water, 21% O_2+79% N_2; (b) ethanol with no water, 100% N_2; (c) ethanol with 5% water, 21% O2+79% N_2; (d) ethanol with 5% water, 100% N_2. (The cathodic direction means the polarization is from OCP to negative cathodic potential. The anodic direction means the polarization is from negative cathodic potential to OCP.)

The evolution of open-circuit potential reflects the surface electrochemical activity under free corrosion condition. Figure 8-10 shows the results of OCP measurements which were ended when a 0.05 mV/s drifting rate was reached. Under aeration, as shown in Figure 8-10(a), the initial OCP keeps increasing with time, which is primarily due to the formation of some oxidation products [52, 74, 85]. Based on others' in-situ surface study in methanol [40], these products may be ethoxy-iron [74]. Without water, time required to reach a stable OCP is about 900 seconds. As water content increases, the required time decreases. With 5 vol% water, less than 100 seconds are needed to reach a stable potential with drifting rate less than 0.05mV/s. The effect of water on OCP evolution in aerated ethanol suggests that the water can increase the

kinetics of oxide formation on carbon steel. Other studies also showed more stable hydroxide products can form, instead of oxides, in SFGE with high water content [74]. In comparison, under de-aeration in Figure 8-10(b), the initial OCP keeps decreasing with time before reaching a surface equilibrium. With the change of water content in ethanol, the time required to reach a stable OCP is similar, around 100 seconds. One explanation for this phenomenon is that the surface oxidation kinetics is strongly reduced by removing oxygen. Under de-aeration, the initial electrochemical activity of carbon steel is mostly limited by the cathodic reaction. Cathodic activity of carbon steel in ethanol becomes important especially under de-aeration. It should also be mentioned that the surface oxidation is not fully stopped by de-aeration. The potential will eventually increase after immersion for certain amount of time. Based on Figure 8-10, it can be concluded that the oxygen and water both play a critical role in the film formation kinetics on the steel's surface in SFGE.

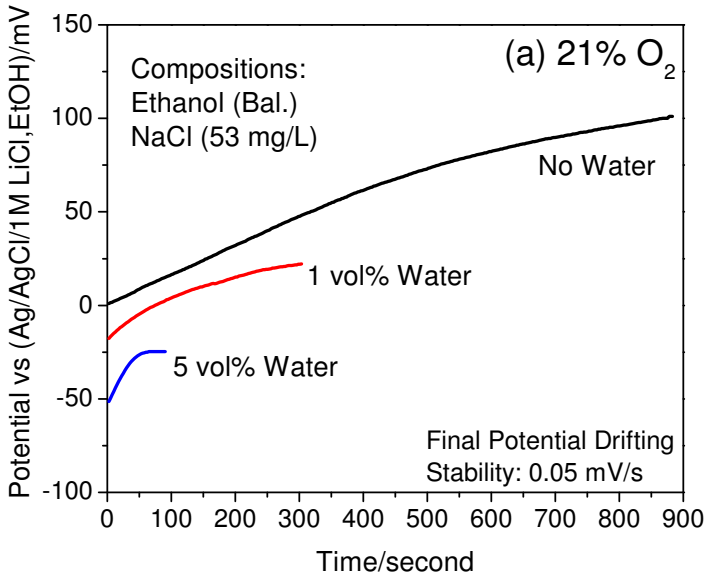

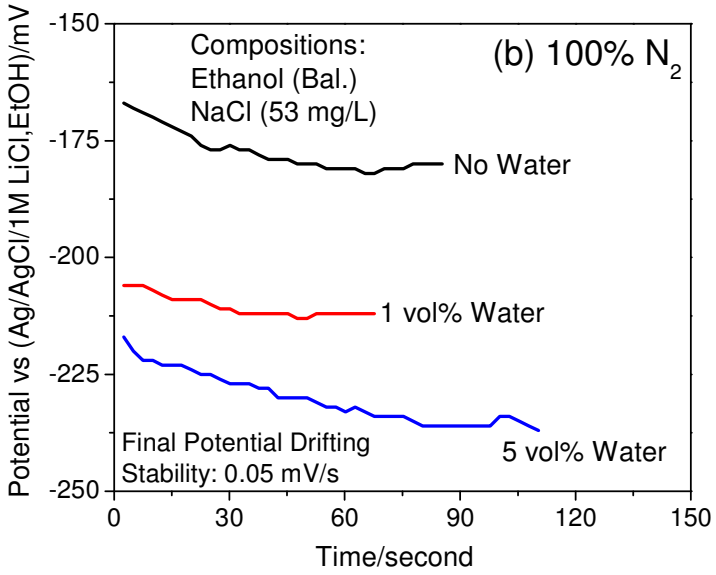

Figure 8-10. Time required to reach a stable open circuit potential in 200-proof ethanol with different water concentration. The stable OCP is defined at the moment where the potential drifting rate is 0.05 mV/s. (a) 21% O_2+79% N_2; (b) 100% N_2.

8.8 EIS Analysis on Oxygen Reduction in Acidic SFGE

Since oxygen is very important for both anodic and cathodic activities of carbon steel in SFGE, the detailed EIS analysis was carried out in acidic SFGE to obtain some mechanistic understanding of the oxygen reduction process. Figure 8-11(a) shows the equivalent circuit for oxygen reduction. R_S is the solution resistance. CPE stands for a constant phase element for double layer capacitance. R_{CT} is the charge transfer resistance for oxygen reduction. W is a Warburg impedance element which models the oxygen diffusion from the bulk solution to the surface. The admittance of CPE is as following:

$$Z_{CPE} = \frac{1}{Y_{dl}(i\omega)^{n_{dl}}} \qquad (8\text{-}8)$$

where Y_{dl} is a admittance like parameter with a unit of s^n/Ω, and n_{dl} is an adjusted exponent between 0 and 1. When $n_{dl}=1$, it represents a perfect capacitor; when $n_{dl}=0$, it represents a perfect resistor.

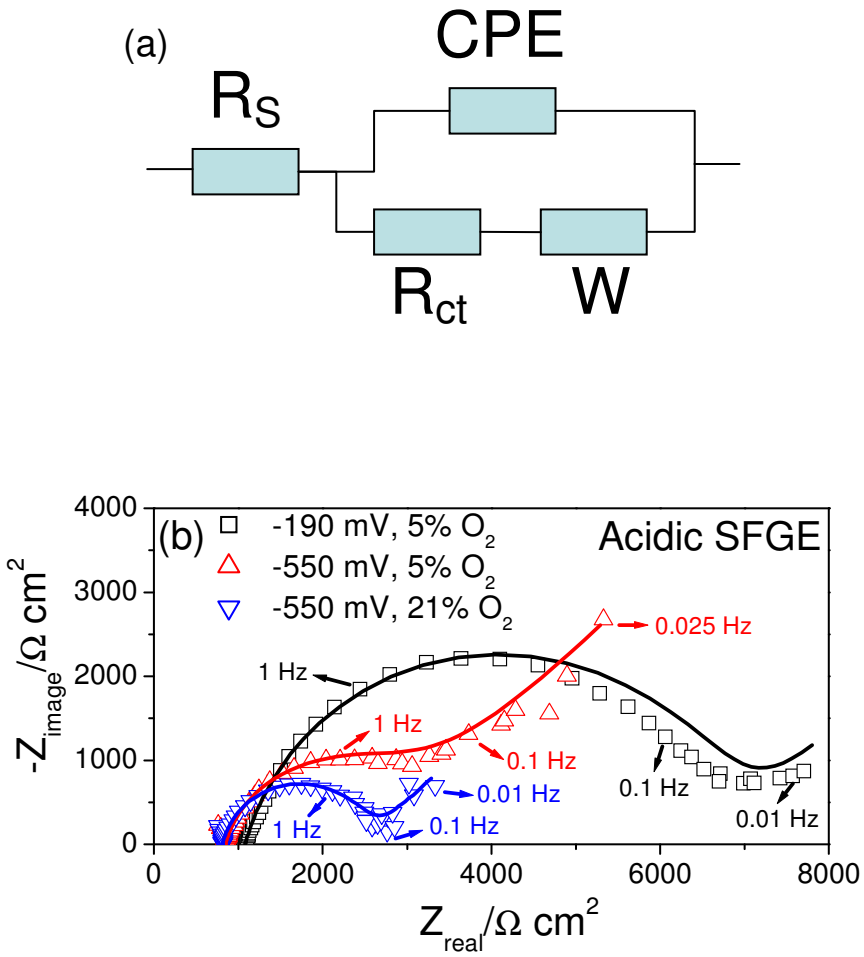

Figure 8-11. EIS analysis of oxygen reduction reaction on carbon steel in acidic SFGE: (a) equivalent electric circuit; (b) experimental (symbol) and fitted (line) Nyquist EIS spectra under different potentials and oxygen partial pressures. The potential is relative to Ag/AgCl/1M LiCl, EtOH.

The experimental and fitted impedance curves under selected conditions are shown in Figure 8-11(b). Oxygen reduction was studied with different oxygen partial pressures and applied cathodic potentials. The fitted curves show good agreements with

the experimental results. General fitting errors are less than 1%, although Warburg impedance fitting shows a little higher error around 5%. Some scattered data appears at the low frequency portion on the EIS spectra. The fitted values of EIS parameters are shown in Table 8-3. With the oxygen partial pressure of 5%, R_{CT} decreases from 5579.6 Ω cm^2 to 2222.6 Ω cm^2 when the cathodic overpotential increases from -190 mV vs Ref. to -550 mV vs Ref.. Higher cathodic overpotential enhances the overall charge transfer on the surface. At -190 mV vs Ref., the equivalent Warburg resistance R_W is only 232.3 Ω cm^2 $s^{-1/2}$, which is much smaller than R_{CT}. Therefore, oxygen reduction (Reaction I) under 5% O_2 is controlled by the charge transfer and does not experience a limiting effect from oxygen mass transport. However, at -550 mV vs Ref., R_W increases to 1196.8 Ω cm^2 $s^{-1/2}$. So the diffusion limit of oxygen plays a role in limiting the oxygen reduction kinetics. Therefore, at high cathodic overpotential, the oxygen reduction (Reaction II) under 5% O_2 is controlled by both charge transfer and oxygen diffusion to the metal surface. If the oxygen partial pressure in ethanol is increased to 21% at 550 mV vs Ref., both R_{CT} and R_W decrease. The charge transfer rate again becomes a major limiting factor. It has been well understood that oxygen has a similar diffusivity [86, 87], but a much higher solubility [82] in ethanol than in water. The higher solubility of oxygen in ethanol may reduce the concentration effect from mass transport. Therefore, the oxygen concentration polarization in ethanol only becomes dominant when the oxygen partial pressure is very low and the cathodic overpotential is very high.

8.9 The Cathodic Activities on Platinum in Ethanol

The comparisons between the cathodic reactions on platinum electrode and on carbon steel electrode in the slightly acidified 200-proof ethanol are shown in Figure 8-12. On platinum, similar cathodic reaction patterns can be identified under both aerated and de-aerated conditions. However, platinum shows more positive potential for both oxygen reduction and hydrogen evolution than carbon steel. The cathodic activation slopes of all the reactions are smaller on platinum than on carbon steel, suggesting faster and easier reaction kinetics on the platinum surface. Higher cathodic limiting current densities for all the reactions are seen on the platinum electrode compared to the carbon steel surface. The differences between platinum and carbon steel are mostly due to the higher catalytic activity on platinum electrode in ethanol [46, 47]. Therefore, the interpretation of corrosion rate on steel in SFGE using a platinum electrode may cause some variations.

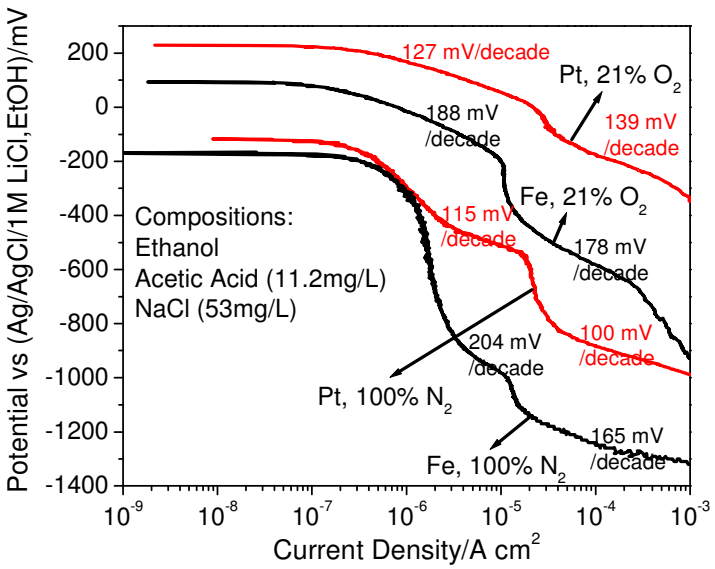

Figure 8-12. Cathodic polarization behavior of carbon steel and a platinum electrode in the slightly acidified ethanol (200-proof ethanol, acetic acid (11.2 mg/L), NaCl (53 mg/L)) under aerated (21% O_2+79% N_2) and deaerated (100% N_2) conditions (The cathodic activation slope for each reaction is marked on the curve)

8.10 Fracture due to Hydrogen Embrittlement

Although the hydrogen permeation current in SFGE is much smaller than that in aqueous environment, the production of hydrogen can still produce huge embrittlement fracture when the stress is applied. The SSRT test on notched tensile sample was used to study the hydrogen embrittlement under stress. As shown in Figure 8-13, the effects of Reactions III and IV were shown. In Figure 8-13(a), -860 mV vs Ref. was applied in acidic SFGE. And in Figure 8-13(b), -1180 mV vs Ref. was applied on the sample in alkaline SFGE. In both cases, clear brittle fracture morphologies are shown, suggesting strong hydrogen attack though the crack propagation path.

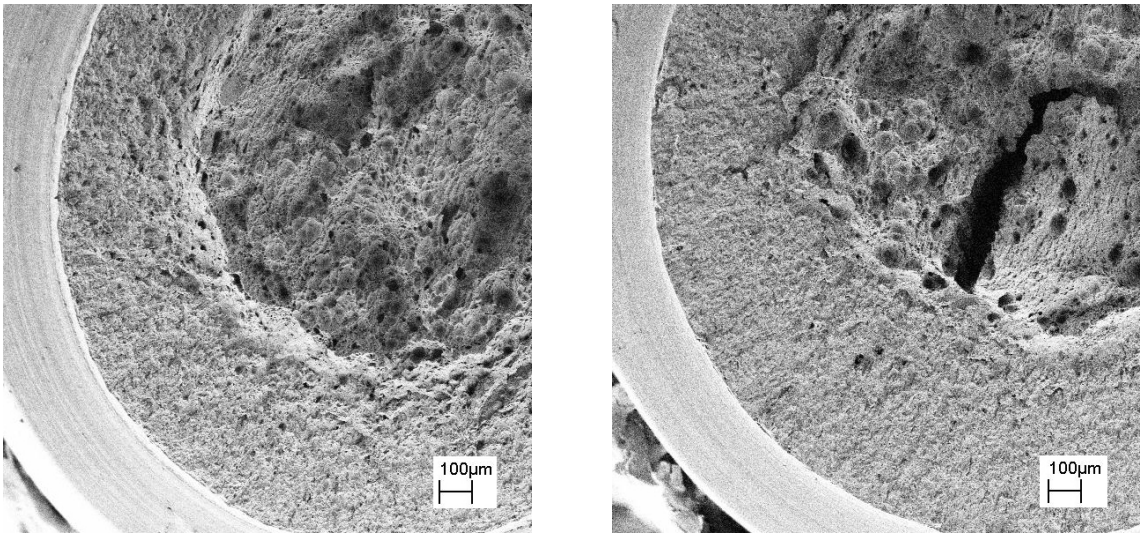

(a) -850 mV vs Ref. in acidic SFGE (b) -1180 mV vs Ref. in alkaline SFGE

Figure 8-13. Fracture morphology due to hydrogen embrittlement

8.11 Conclusions

The cathodic activities, especially oxygen and hydrogen, have been investigated in detail on carbon steel surface in SFGE. The results showed that carbon steel shows unique cathodic activities which can strongly influence the corrosion process.

1) Oxygen, even at 1% concentration in purge-gas, promotes the oxygen reduction. Oxygen reduction is a major cathodic reaction for normal condition.

2) Hydrogen evolution, from acetic acid, ethanol and water, needs a very high cathodic overpotential under de-aeration, which can be hardly achieved in normal corrosion process.

3) Acetic acid and water both increase the cathodic kinetics in SFGE.

4) Near the OCP, the reduction of surface pre-existing oxide and other oxidized species forms the first cathodic reaction in SFGE.

5) Cathodic reactions start to play important roles in controlling the corrosion potential when the system is under de-aeration and the anodic film formation is inhibited.

6) For normal corrosion process, the charge transfer kinetics is the major limiting reaction for oxygen reduction. Brittle fracture can take place once hydrogen production is possible in SFGE environment.

CHAPTER 9

GLOBAL PICTURE DERIVED FROM THIS RESEARCH AND RECOMMENDATIONS

9.1 Some Thoughts on Corrosion of Carbon Steel in Simulated Fuel-grade Ethanol

Corrosion behavior of carbon steel in FGE is chemically and electrochemically complex and very different from the aqueous systems. Complexity is due not only to the less known reactions between the metal and solvent, but also the unique physicochemical properties of the mixed-solvent itself. The electrochemical behavior of metal/solvent interface are governed by, but not limited to, the following phenomena: (1) Solution solvation and its related physical and chemical properties; (2) Close-to-wall double layer structure and its short range interaction; (3) Chemical and electrochemical reactions between the metal and solvent molecules.

FGE is not a single component liquid and generally contains ethanol, water, small amount of methanol, and other possible alcohols with higher molecular weights. The solvation in presence of mixed solvents generates a complex solution structure, which can affect the overall physical and chemical properties of the solution, such as dipole moment, dielectric constant, electrical conductivity, dissolved oxygen level, proton activity, etc. Therefore, corrosion susceptibility of iron in a mixed solvent, such as SFGE, depends on multiple effects due to the changes in their physical and chemical properties. For example, the increase in the water content in SFGE can decrease dissolved oxygen

level [64] and pHe [51], both of which can alter the electrochemical response, as shown in Figures. 5-18 and 5-10.

Anodic reactions of metals in alcoholic solvents have been widely reported, but the effects of alcohol molecules on mechanisms of charge transfer and surface products formation are still less understood. The results in this work showed an unstable passivation on the carbon steel surface in SFGE with low water content and slight acidity. No clear passivation is set up under the applied anodic overpotentials. A comprehensive discussion on these reaction mechanisms has been recently summarized by Banas et. al. [40]. So far, the research showed that the surface oxidation product forms a membrane type inhibition film rather than the passive oxide layer in pure alcohol at lower potentials [40, 70]. In SFGE with no water or limited amount of water, the formation of ethoxy-iron ($Fe(C_2H_5O)_2$) surface layer may be responsible for a decrease in the weight loss. Such metal-organic compound has been reported as an initial reaction layer in pure methanol elsewhere [40, 88]. Ethoxy-iron serves as a pseudo-passive layer, leading to an increase of OCP with time, as shown in Figure 5-4. However, this pseudo-passive layer is not stable, and can be easily destroyed by polarization (Figure 5-5). The reaction reaches the equilibrium as following:

$$Fe^{2+} + 2C_2H_5O^- \rightarrow Fe(C_2H_5O)_2 \qquad (9\text{-}1)$$

It was also proposed that such reaction product with a limited solubility can also possibly convert to iron oxide under lower oxidation state [88], which is unstable and unprotective against corrosion.

With a further addition of water in ethanol solution, both anodic and cathodic reactions are influenced to some levels. Regarding cathodic reactions, it has been

discussed that water content in alcoholic environments can influence the dissolved oxygen concentration [64] and proton activity [37, 51]. The changes in the proton availability and the dissolved oxygen level are major factors for the cathodic reaction in water-alcohol mixtures [37].

For the anodic reaction, the presence of water alters the oxidation reaction on metal. More iron oxide and hydroxide form under these conditions. Due to the limited amount of water, the hydroxide may form in such SFGE tends to be unstable and easy to dissociate into oxide form. Corrosion products with multiple oxidation states may be present in the form of oxide through the following reaction steps:

$$2Fe^{2+} + 3H_2O \Leftrightarrow Fe_2O_3 + 6H^+ + 2e^- \quad (9\text{-}2)$$

At higher water concentration (e.g. 50 vol%), more hydroxide products form on the surface, although iron oxides are still present in XRD analysis due to dehydration process.

$$Fe^{2+} + 3H_2O \Leftrightarrow Fe(OH)_3 + 3H^+ + 1e^- \quad (9\text{-}3)$$

$$2Fe(OH)_3 \Leftrightarrow Fe_2O_3 + 3H_2O \quad (9\text{-}4)$$

Thermodynamic calculations have already shown that the acidity strongly influences the oxidation reactions of iron in ethanolic solvents [3]. From the acidified ethanol to alkaline ethanol, the stable reaction products change from Fe^{2+} to Fe_2O_3, and finally $Fe(OH)_3$. In SFGE, better passivation is present in the alkaline condition, as shown in Figures. 5-7 and 5-8. Such an evolution in stable reaction products alters the surface from an unprotective ethoxy-iron layer to protective iron hydroxide layer. Therefore, by controlling environmental factors like acidity, water concentration, and chloride concentration, better corrosion and pitting resistance can be achieved for the carbon steel in SFGE environments.

9.2 A Physical Picture of Stress Corrosion Crack Behavior during SSRT on Carbon Steel in SFGE

Film breakdown and anodic dissolution is the most dominant mechanism in this process, although the surface film in the ethanolic environments may not be a stable passive film due to the limited amount of water. [36, 48] A slow film growth on carbon steel in SFGE takes place under low stress condition (below yielding). Film breakdown and crack initiation take place after the local yielding on the material. Once the stress corrosion cracks initiate, the fast anodic dissolution at the crack tip drives the crack growth into the material. The dissolution process significantly decreases the crack tip resistance. At the early stage, an increase in the crack density due to initiation promotes a fast increase in the crack tip corrosivity. With the strain reaching a certain level, small cracks coalesce and grow in a form of ring keep the crack propagation active. After the maximum stress, the corrosion activity from the SCC decreases. The crack blunting takes place due to final microvoid formation and coalescence, which form a ductile crack originating from the middle of the sample. Main crack and the ductile crack interact to form the final shear fracture, leading to the final failure. An increase in the capacitance on the crack wall may happen during the final fracture because of the dissolution and possible porous corrosion product formation.

9.3 Possible Influences of Cathodic Activities on Corrosion Process in SFGE

In most of the conditions, oxygen reduction is a major cathodic reaction to support the anodic corrosion activity. Hydrogen evolution is only predominant under de-aeration. Hydrogen evolution reactions in SFGE, either by acetic acid reduction or water

and ethanol reduction, also require a very high cathodic overpotential. This negative overpotential is usually in a range of -600 mV ~ -1000 mV vs Ref., depending on the tested pHe and oxygen concentration. Such a large overpotential is hardly considered possible in normal corrosion process. Therefore, under OCP, hydrogen is not expected to affect the mechanical behavior, i.e. hydrogen embrittlement, of carbon steel in SFGE. It has been reported that corrosion and stress corrosion cracking susceptibility are decreased in SFGE by de-aeration [3, 51, 74]. The decrease of cathodic activity by de-aeration may be one of the main reasons which cause the decrease in corrosion activity. Acetic acid donates protons which increase the cathodic current and decrease the cathodic overpotential. Therefore, regarding the cathodic activity, the presence of acetic acid assists the corrosion process. In comparison, neutral and alkaline SFGE, especially under de-aeration, can dramatically inhibit the cathodic reaction. The addition of water can accelerate the acetic acid dissociation in SFGE which can lead to a higher corrosion rate. Near open circuit potential, the first cathodic reaction which provides a small current density is the reduction of surface oxides and other oxidized species. Oxygen and water are both important in controlling the cathodic reaction kinetics. With aeration, the formation of surface film controls the overall corrosion potential. But with de-aeration, the film formation kinetics is reduced and the cathodic reactions become critical in the overall corrosion process. For normal corrosion process, the charge transfer kinetics is the major limiting reaction for oxygen reduction. The oxygen mass transport is usually not a limiting step unless the oxygen concentration is low and the overpotential is high.

9.4 Suggested Mitigation Methods for Corrosion and Stress Corrosion Cracking in Fuel-grade Ethanol

Although the development of the corrosion mitigation technology for carbon steel in fuel-grade ethanol is another topic which also needs further investigation, a guideline for this development can still be suggested based on the work that has been done in this thesis.

Stress corrosion cracking, pitting corrosion, and uniform corrosion on carbon steel all show strong dependences on the ethanol chemistry in fuel-grade ethanol. Therefore, controlling the chemistry in fuel-grade ethanol can be an effective way to inhibit the degradation from carbon steel. High pHe in alkaline region improves the passivity of carbon steel in ethanolic solution and mitigate both SCC and uniform corrosion. Ammonium hydroxide or other alkaline type inhibitor can be used to modify the fuel-grade ethanol. Surface adsorption type inhibitor cannot be used in FGE because such adsorption is not stable under flow condition in pipeline. Water is always present in fuel-grade ethanol. However, water concentration has to be controlled between 0.5 vol% to 1 vol% in order to achieve the best film stability in fuel-grade ethanol environment. Inorganic chloride which is an aggressive species in FGE should be minimized in ethanol fuel. Though methanol has shown to be more aggressive than ethanol by other studies [37], its effect on corrosion activity is still mild compared to other constituents. Therefore, the current ASTM standard for methanol content is still good for FGE.

De-aeration, which can also mitigate stress corrosion cracking in SFGE under some conditions, is not recommended based on this work. As shown previously in this thesis, oxygen is the major oxidizing species which enhances the film growth kinetics on

the surface of carbon steel in SFGE. Fast dissolution of ferrite is expected in SFGE under de-aeration condition, as shown in Figures 4-16 and 5-18. If inclusions are present on the pipeline steel surface, low passivity caused by de-aeration can cause the preferential dissolution of the inclusion particle from iron matrix. The removal of inclusion may serve as crack initiation site under stressed condition.

Operating stress condition for the carbon steel should be below the yield stress of the material. Tensile stress that is lower than the yield stress can hardly initiate cracks on carbon steel in fuel-grade ethanol. More attention should be given to the welding structure which may exhibit higher residual stress and different metallurgical microstructure and composition.

Cathodic polarization with a potential less than 500 mV vs Ref. can be applied on some structures in order to mitigate the possible corrosion and cracking activities. However, higher cathodic polarization may lead to hydrogen embrittlement in these environments. The application of cathodic protection needs careful monitoring.

9.5 Recommendations for Future Work in This Area

Though both phenomenological and mechanistic understanding of stress corrosion cracking and corrosion of carbon steel in SFGE has been obtained based on this research, more work needs to be done in order to understand the details of the materials degradation in ethanol system:

(1) In-situ and ex-situ surface characterization of film characteristics in this environment is necessary in order to understand the nature of the film on the metal surface.

(2) The detailed kinetics of the film growth under different environmental conditions should also be understood. This information will be very helpful to tailor the surface film structure in mitigation of corrosion and SCC.

(3) Correlation between the simulated fuel-grade ethanol and commercial fuel-grade ethanol needs to be investigated. The differences on corrosion and cracking susceptibility, electrochemistry, constituents, and surface film behavior should be studied.

(4) Though the general mechanism of SCC on carbon steel in SFGE is now understood, there are still many unknown metallurgical and environmental parameters in the stress corrosion cracking behavior of this system. Contradictions on cracking mode still exist in literature. The crack morphology observed in this work is dominantly transgranular type in all testing conditions and environments. However, intergranular or mixed type SCC has been reported in the same system [3]. Obviously, the cracking mode is very sensitive to the testing condition and the material pre-treatment. This difference leads to a serious question: what is the mechanism ahead of the crack tip which affects the crack propagation in the metal?

(5) Pipelines undergo fluctuations in their operating pressure. Effect of cyclic stresses in crack initiation and propagation in FGE environments needs to be studied.

REFERENCES

1. R. D. Kane, J. G. Maldonado, API Technical Report 939-D, American Petroleum Institute, Washington DC, USA (2003).

2. R. D. Kane, N. Sridhar, M. P. Brongers, J. A. Beavers, A. K. Agrawal, L. J. Klein, Mater. Perform. 44 (2005) 50.

3. N. Sridhar, K. Price, J. Buckingham, J. Dante, Corrosion 62 (2006) 687.

4. Z. Szklarska-Smialowska, J. Mankowski, Corros. Sci. 22 (1982) 1105-1112.

5. E. Cavalcanti, V. G. Wanderley, T. R. V. Miranda, L. Uller, Electrochim. Acta 32 (1987) 935-937.

6. Photo Courtesy of Metallurgical Technologies, http://www.met-tech.com/metallography.htm.

7. J. L. Luo, B. T. Lu, Corrosion 62 (2006) 723-731.

8. G. S. Frankel, J. Electrochem. Soc 145 (1998) 2186-2198.

9. R. Nishimura, Y. Maeda, Corros. Sci. 46 (2004) 769.

10. P. Combrade, In: P. Lacombe, B. Baroux, G. Beranger, Editors, Les Editions de Physique, Les Ulis (1993), p. 329.

11. D. A. Jones, Corrosion 52 (1996) 356-362.

12. R. N. Parkins, Corrosion 52 (1996) 363-374.

13. A. Turnbull, Corrosion 66 (2010) 055001.

14. J. Lufrano, P. Sofronis, H. K. Birnbaum, J. Mech. Phys. Solids 44 (1996) 179.

15. C. D. Beachem, Metall. Mater. Trans. B 3 (1972) 441.

16. H. K. Birnbaum, P. Sofronis, Mater. Sci. Eng., A 176 (1994) 191.

17. P. Sofronis, Y. Liang, N. Aravas, EUR J MECH A-SOLID 20 (2001) 857.

18. ASTM-G-148-97, Annual Book of ASTM Standards, ASTM International, West Conshohocken, PA, USA (2003).

19. Y. Roques, G. Mankowski, G. Chatainier, F. Dabosi, Electrochim. Acta 32 (1987) 971-976.

20. C. A. Farina, U. Grassini, Electrochim. Acta 32 (1987) 977.

21. D. J. Simbi, J. C. Scully, Corros. Sci. 34 (1993) 1743.

22. D. J. Simbi, J. C. Scully, Corrosion 53 (1997) 298.

23. E. Heitz, Adv. Corros. Sci. Technol. 4 (1974) 149.

24. R. C. Newman, Corrosion 64 (2008) 819.

25. Y. Jiang, Y. Wu, K. Wang, Mater. Corros. 57 (2006) 418.

26. K. R. Cooper, R. G. Kelly, Corros. Sci. 49 (2007) 2636.

27. Z. Y. Liu, X. G. Li, C. W. Du, G. L. Zhai, Y. F. Cheng, Corros. Sci. 50 (2008) 2251.

28. R. C. Newman, C. Healey, Corros. Sci. 49 (2007) 4040.

29. S. L. Asher, B. Leis, J. Colwell, P. M. Singh, Corrosion 63 (2007) 932.

30. X. D. Liu, G. S. Frankel, B. Zoofan, S. I. Rokhlin, Corros. Sci. 46 (2004) 405.

31. R. K. Singh Raman, A. Saxena, J. Electrochem. Soc. 154 (2007) C451.

32. J. J. Park, S. I. Pyun, K. H. Na, S. M. Lee, Y. T. Kho, Corrosion 58 (2002) 329.

33. T. Shibata, Corros. Sci. 49 (2007) 20.

34. I. U. Toor, J. Kwon, H. Kwon, J. Electrochem. Soc. 155 (2008) C495.

35. W. Zheng, D. Hardie, Corros. Sci. 32 (1991) 23.

36. J. Banas, Electrochim. Acta 32 (1987) 871-875.

37. C. S. Brossia, E. Gileadi, R. G. Kelly, Corros. Sci. 37 (1995) 1455-1471.

38. F. Bellucci, G. Capobianco, G. Faita, C. A. Farina, G. Farnia, F. Mazza, S. Torchio, Corros. Sci. 28 (1988) 371-384.

39. J. B. Wang, J. M. Wang, H. B. Shao, J. Q. Zhang, C. N. Cao, J. Appl. Electrochem. 37 (2007) 753.

40. J. Banas, B. Stypula, K. Banas, J. Swiatowska-Mrowiecka, M. Starowicz, U. Lelek-Borkowska, J. Solid State Electrochem. 13 (2009) 1669.

41. A. Kriaa, N. Hamdi, K. Jbali, M. Tzinmann, Corros. Sci. 51 (2009) 668.

42. T. Ramgopal, S. Amancherla, Corrosion 61 (2005) 1136.

43. M. Kabasakaloglu, I. Kalyoncu, T. Kiyak, Appl. Surf. Sci. 135 (1998) 188-192.

44. M. G. Athayde, O. R. Mattos, L. Sathler, Electrochim. Acta 32 (1987) 909-913.

45. H. B. Shao, J. M. Wang, X. Y. Wang, J. Q. Zhang, C. N. Cao, Electrochem. Commun. 6 (2004) 6.

46. J. S. Spendelow, A. Wieckowski, Phys. Chem. Chem. Phys 9 (2007) 2654.

47. B. Lim, M. J. Jiang, P. H. C. Camargo, E. C. Cho, J. Tao, X. M. Lu, Y. M. Zhu, Y. Xia, Science 324 (2009) 1302.

48. F. Bellucci, G. Faita, C. A. Farina, F. Olivani, J. Appl. Electrochem. 11 (1981) 781-785.

49. ASTM-G-129-00, Annual Book of ASTM Standards, ASTM International, West Conshohocken, PA, USA (2006).

50. ASTM-D-4806-01a, Annual Book of ASTM Standards, ASTM International, West Conshohocken, PA, USA (2001).

51. X. Y. Lou, D. Yang, P. M. Singh, Corrosion 65 (2009) 785.

52. X. Y. Lou, D. Yang, P. M. Singh, J. Electrochem. Soc. 157 (2009) C86.

53. N. A. Noda, M. Sera, Y. Takase, Int. J. Fatigue 17 (1995) 163.

54. J. A. Dean, Editor, Lange's Handbook of Chemistry (15th edition), McGraw-Hill Professional (1998).

55. C. S. Brossia, R. G. Kelly, Electrochim. Acta 41 (1996) 2579.

56. ASTM-D-6423-08, Annual Book of ASTM Standards, ASTM International, West Conshohocken, PA, USA (2008).

57. P. Luhring, A. Schumpe, J. Chem. Eng. Data 34 (1989) 250.

58. R. N. Parkins, Corros. Sci. 20 (1980) 147.

59. P. L. de Anna, Corros. Sci. 25 (1985) 43-53.

60. T. Mussini, F. Mazza, Electrochim. Acta 32 (1987) 855.

61. S. Trasatti, Electrochim. Acta 32 (1987) 843.

62. W. Oelssner, F. Berthold, U. Guth, Mater. Corros. 57 (2006) 455.

63. J. D. E. McIntyre, W. F. Peck, J. Electrochem. Soc. 117 (1970) 747.

64. S. A. Shchukarev, T. A. Tolmacheva, J. Struct. Chem. 9 (1968) 16.

65. I. Frateur, C. Desloius, M. E. Orazem, B. Tribollet, Electrochim. Acta 44 (1999) 4345.

66. D. G. Kolman, J. R. Scully, Philos. Mag. A 79 (1999) 2313.

67. A. P. Jivkov, Theor. Appl. Fract. Mech. 42 (2004) 43.

68. G. J. Brug, A. L. G. Van Den Eeden, M. Sluyters-Rehbach, J. H. Sluyters, J. Electroanal. Chem. 176 (1984) 275.

69. S. P. Harrington, T. M. Devine, J. Electrochem. Soc. 155 (2008) C381.

70. J. Swiatowska-Mrowiecka, J. Banas, Electrochim. Acta 50 (2005) 1829.

71. M. C. Petit, M. Cid, M. Puiggali, Z. Amor, Corros. Sci. 31 (1990) 491.

72. R. W. Bosch, F. Moons, J. H. Zheng, W. F. Bogaerts, Corrosion 57 (2001) 532.

73. R. W. Bosch, Corros. Sci. 47 (2005) 125.

74. X. Y. Lou, P. M. Singh, Corros. Sci. 52 (2010) 2303.

75. R. de Levie, Adv. Electrochem. Electrochem. Eng. 6 (1967) 329.

76. R. Oltra, M. Keddam, Corros. Sci. 28 (1988) 1.

77. J. Bisquert, Phys. Chem. Chem. Phys 2 (2000) 4185.

78. J. Bisquert, G. Garcia-Belmonte, F. Fabregat-Santiago, A. Compte, Electrochem. Commun. 1 (1999) 429.

79. P. L. Andresen, L. M. Young, Corrosion 51 (1995) 223.

80. K. R. Cooper, R. G. Kelly, J. Chromatogr. A 850 (1999) 381.

81. Q. J. Peng, G. F. Li, T. Shoji, J. Nucl. Sci. Technol. 40 (2003) 397.

82. J. Tokunaga, J. Chem. Eng. Data 20 (1975) 41.

83. C. Franco, J. Olmsted, Talanta 37 (1990) 905.

84. ASTM-D-4806-06c, Annual Book of ASTM Standards, ASTM International, West Conshohocken, PA, USA (2006).

85. X. Y. Lou, P. M. Singh, Electrochim. Acta (2010), doi:10.1016/j.electacta.2010.07.024.

86. A. Schumpe, P. Luhring, J. Chem. Eng. Data 35 (1990) 24.

87. I. M. Krieger, G. W. Mulholland, C. S. Dickey, J. Phys. Chem. 71 (1967) 1123.

88. M. Sakakibara, N. Saito, H. Nishihara, K. Aramaki, Corros. Sci. 34 (1993) 391.

VITA

XIAOYUAN LOU

Xiaoyuan Lou was born in Nanjing, Jiangsu, China. He received a B.S. in Physics from Nanjing University, Nanjing, China in 2002. After that, his interest changed from physics to engineering. He went to US and got his M.S. in Materials Science and Engineering from The Ohio State University, Columbus, USA under the guidance of Dr. Robert H. Wagoner. From 2006 to 2010, he pursues his doctorate degree in Materials Science and Engineering at Georgia Institute of Technology, Atlanta, USA. He has worked on solid oxide fuel cell in Dr. Meilin Liu's group and is currently working on materials degradation in bio-ethanol under the guidance of Dr. Preet M. Singh for his Ph.D. degree.